HEAT TRANSFER AND FLOW VISUALIZATION IN NATURAL CONVECTION IN RAPIDLY SPINNING SYSTEMS

by

LAWRENCE D. SOBEL

B.S. Swarthmore College
(Mechanical Engineering, 1977)

M.S. Massachussetts Institute of Technology
(Mechanical Engineering, 1980)

Submitted to the Department of
Mechanical Engineering
in Partial Fulfillment of the
Requirements for the
Degree of

DOCTOR OF PHILOSOPHY

at the

MASSACHUSETTS INSTITUTE OF TECHNOLOGY

May 1984

Signature of Author..
Department of Mechanical Engineering
May 28, 1984

Certified by..
Prof. Maher El-Masri, ME Department
Thesis Supervisor

Certified by..
Prof. Joseph L. Smith, ME Department
Thesis Supervisor

Accepted by..
Prof. Warren M. Rohsenow, ME Department
Chairman, Department Committee on Graduate Students

HEAT TRANSFER AND FLOW VISUALIZATION IN NATURAL CONVECTION IN RAPIDLY SPINNING SYSTEMS

by

LAWRENCE D. SOBEL

Submitted to the Department of Mechanical Engineering
on May 30, 1984 in partial fulfillment of the
requirements for the Degree of Doctor of Philosophy.

Horizontal plumes in rapidly spinning vertical rotors have been examined in an effort to improve the cooling systems of rapid spin-up airborne superconducting rotors. Using water as the primary working fluid, plume trajectories have been observed and surface heat transfer coefficients measured. It is found that natural convection plumes in strongly rotating systems are two dimensional whereas an equivalent non-rotating high Rayleigh number plume will create a three dimensional entrainment flow field. A starting plume is thus found to generate the thermal equivalent of a Taylor column. The surface heat transfer coefficient is measured and found to be independent of fluid viscosity. The Nusselt number in the rotating system correlates well with $(RaPr)^{.33}$. Pictures of plumes and a plot of rotational heat transfer data are presented.

Flow fields and plume behaviour have also been observed in vertical, non-axisymmetric rotors accelerated to high rotational speeds. The flow field during spin-up is characterized by strong vortices which quickly develop in corners of the rotor, gather kinetic energy from the interior irrotational fluid motion and then move into the interior flow regions. Surface heat transfer coefficients during the spin-up are estimated based on a model for the instantaneous relative motion flow field and are shown to underestimate the measured heat transfer coefficients.

Thesis Supervisor:	Dr. Maher El-Masri
Title:	Asst. Prof. of Mechanical Engineering
Thesis Supervisor:	Dr. Joseph L. Smith
Title:	Prof. of Mechanical Engineering

Acknowledgements

There are three people who deserve a great deal of credit for the successful completion of this thesis research. David Otten of the EPSEL Lab at MIT designed and constructed the rotating data acquisition used in these experiments. The data acquisition system has now been operating flawlessly for 6 years and this is a remarkable testament to Dave's skill as an engineer. His assistance and advice in all matters electrical and mechanical were invaluable. His own modesty keeps him from admitting the significance of his work and as he has never let me thank him in person, I will print my gratitude here instead.

The photographs shown in this thesis were often taken by, and always developed by Gail Gordon. I wish to thank her for the long and productive hours that she spent in the darkroom. Many of these pictures were taken with very little light and some considerable skill was required to make the photographs intelligible.

I also owe a great debt to James Wreski who constructed the support structure and turntable for the rotating apparatus. His ebullience, enthusiasm and mechanical skill helped me through a very difficult time. Jim is another example of someone whose modesty is exceeded only by his considerable competence. I wish, again, to let him know how much I appreciated the time we spent together.

I wish to acknowledge my two thesis advisers: Prof. Joseph L. Smith and Prof. Maher El-Masri. To say that they are largely responsible for the work completed and reported here and for the knowledge I have gained while at MIT is obviously an understatement. I am not exactly certain how to thank my advisors being smart men.

This thesis ends a long adventure at Building 41. It is most important that I also acknowledge the very competent machinists and technicians in our lab: Karl Benner, Bob Gertsen and Mike Demaree.

And last of all, I want to thank my roommates and friends for their many years of company: Tony, Gary, Carl, Eric, Jocelyn, Ruth H. and F., Lynn and Moses.

to

my mother and father,
Fred and Vera Orthlieb,
and Frank Rumore

TABLE OF CONTENTS

LIST OF TABLES

LIST OF FIGURES

List of symbols

a	outer radius
A	area (cm^2)
b	plume width, particle radius
c	characteristic length scale
c_p	specific heat (J/gm/C)
e_r, e_R	unit vector in radial direction
e_θ, e_ϕ	unit vector in tangential direction
e_x	unit vector in x direction
e_y	unit vector in y direction
erf	error function
erfc	complementary error function
KE	kinetic energy
E	energy
F	force
F_r	force in the rotating frame in the radial direction
F_θ	force in the rotating frame in the tangential direction
F_o	surface heat flux (W/cm^2)
F_e	surface heat flux error (W/cm^2)
g	acceleration, gravity (980cm/s^2), or rotational acceleration
h	length scale in direction parallel to axis of rotation, heat transfer coefficient, (W/cm^{2}C)
h_{tr}	transient heat transfer coefficient (W/cm^{2}C)
k	thermal conductivity (W/cm/C)
l	heater length scale
m	mass (kg)
n	unit normal

p, P	pressure
PE	potential energy
q	relative velocity in rotating frame (cm/s)
r	radius
r_m	minimum radius
r_c	radius of cylindrical wave front during spin-up
R	radial distance to centroid of off-axis geometries
R_c	radial distance to center of object moving in rotating fluid
R_o	radial distance to outer lexan window in rotating test bed
s	arc length or distance traveled
S	bounding surface of some area
T	temperature
T_s	surface temperature
T_a	ambient temperature, initial temperature
ΔT	temperature difference
ΔT_{ss}	steady state temperature difference
U_p	particle velocity relative to rotating coordinate system (cm/s)
U_I	inertial velocity (cm/s)
u	relative velocity in radial direction
u_p	relative particle velocity in radial direction
v	relative velocity in tangential direction
v_p	relative particle velocity in tangential direction
w	relative velocity in axial direction
w_E	axial velocity into the Ekman layers
W	work

Greek symbols

α	density fraction ρ/ρ_a, angle between particle velocity and e_θ, thermal diffusivity (cm^2/s)
α_0	initial density fraction
β	coefficient of thermal expansion (1/K), angle between normal to surface and e_r
δ	boundary layer thickness, variational operator
δ_t	thermal boundary layer thickness
δ_v	fluid momentum boundary layer thickness
ε	entrainment coefficient (dimensionless)
ν	kinematic viscosity (cm^2/s)
μ	viscosity (gm/cm/s)
τ	time constant (s), dimensionless time (ωt)
τ_E	Ekman time constant: $h/(\sqrt{\nu\omega})2$, (s)
τ_{ht}	dimensionless time during transient heat transfer experiments ($\delta/(\sqrt{Pr})/\delta_t$)
τ_α	acceleration time: $\Delta\omega/(\alpha)$, s
ψ, Ψ	stream function
Φ	potential function
ρ	density
ρ_a	ambient density
$\omega^2 r$	rotational gravity
ω	rotational speed (rpm, rad./s)
ω_1	initial rotational speed
ω_2	final rotational speed
ξ	vorticity

∇	del operator

Dimensionless groups

Ek	Ekman number $(\nu/\omega h^2)$
Nu	Nusselt number (hl/k)
Pr	Prandtl number $(\mu cp/k)$
Ra	Rayleigh number based on rotational acceleration $(\omega^2 R\beta\Delta T l^3 Pr)/\nu^2$
Re	Reynolds number $(U_p b/\nu)$
Ro	Rossby number $(U_p/(\omega b))$

CHAPTER 1

OVERVIEW

The work reported in this thesis examines natural convection plume heat transfer in rapidly spinning containers of various geometries. This chapter summarizes the full thesis, broadly outlining the issues addressed and their relevance to the cooling systems of superconducting rotors.

I.A. Purpose of research

The operation of a superconducting generator requires the removal of large quantities of heat from within the rotating machine. These generators have a rotating field winding wound from superconducting wire immersed in a liquid helium bath. During normal steady state generator operation the heat generated within the field winding will initiate a bouyancy driven helium circulation- the heat convected inwards ultimately removed by boiling in regions close to the axis of the spinning machine. Work has now begun on a prototype airborne superconducting generator which will be operated only intermittantly. This generator will be spun to rated speed only when there is a need for power and then operated for a short period of time. The rotor will normally be idled at a much lower speed. The demands on the cooling system for such a machine are naturally more severe than those of a conventional rotor because coolant flow and thermodynamic transients are coincident with significant transient heating in the field winding itself. The rotor must be fully operational in a time that is short compared with conventional rotor cooling system time constants.

The overall helium cooling system of a superconducting rotor is composed of several smaller subsystems, one of which is the primary concern of the present research. The work reported here is most relevant to large pool natural convection initiated by isolated small thermal sources in rapidly spinning systems . The details of superconducting rotor cooling systems will be deferred until the next chapter. At this point it suffices to sketch in general terms the geometry characteristic of the water filled experimental apparatus used to model the transient thermal and fluid behaviour of a helium filled system. Figure 1.1 is an example of the geometry shared by the various rotating apparatus. Shown in Fig. 1.1 is a right circular annular cylinder filled with fluid. The cylinder is fitted with two radial baffles . A small heater is affixed to the outer cylinder wall and the heater surface is parallel to the axis of rotation. (The heater dimensions are not necessarily small compared to the dimensions of the container). In the succeeding chapters pictures and surface heat transfer coefficient data will be presented which characterize the resulting flow in the container when the heater is turned on.

Natural convection flows have been observed in two different situations. In one mode of testing the heater was turned on a long time after the fluid in the container had come to be in solid body rotation- (the fluid was motionless relative to the walls of the container). In the second testing mode the heater was energized and the fluid filled container impulsively accelerated to a higher rotation rate. The purpose here was to assess the impact of the motion of the fluid relative to the walls of the container on the surface heat transfer coefficient. The former class of experiments will be refered to as quasi-steady heat transfer tests in the discussion to follow in chapters 4 and 6. The flow was quasi-steady because the bulk fluid in the container absorbed all the

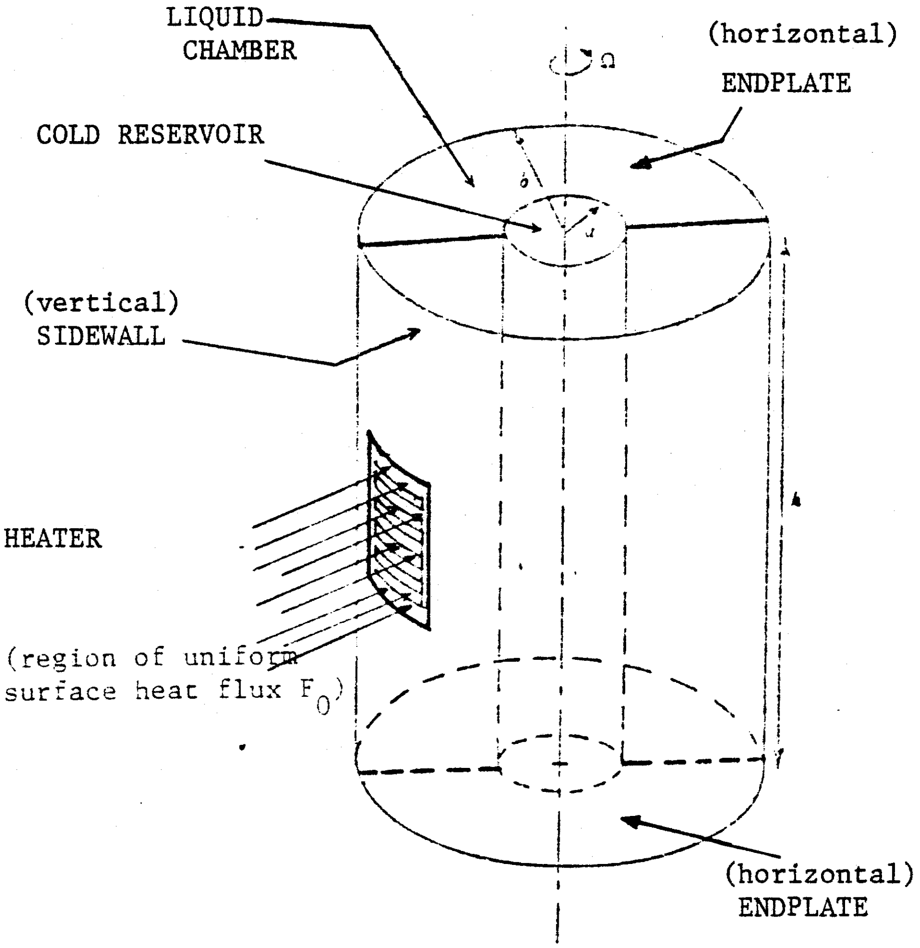

Figure 1.1 Sketch of annular liquid reservoir with radial baffles and small heat source at the outer radius. Heater surface is parallel to the axis of rotation.

heater power- though the test duration was short enough (less than a minute in the longest test) to make bulk water temperature changes negligible. The latter class of tests will be referred to as transient spin-up heat transfer tests. In this testing mode, heat transfer was a combination of natural convection and forced convection. The motion of the container radial walls imparted some initially irrotational motion to the fluid and this augmented the surface heat transfer coefficient. These results are discussed in Chapters 7 and 8. The range of centrifugal accelerations in these experiments extended from 27 to 120 times the earth's gravity and acceleration rates of order 100rpm/s. Except where otherwise noted, the dynamics of the system were unaffected by the earth's gravity field. (Experiments with rotors spinning on horizontal axis revealed some interesting phenomena associated with air bubbles acted on by both gravity and rotational acceleration. These phenomena are described in Chapter 9.)

I.B. Quasi-steady heat transfer flow visualization

Fig. 1.2a shows a right circular cylinder with a 6 in. i.d. and 6 in. axial length. The cylinder is fitted with a single, removable baffle. A small 40 ohm flat surface heater is taped to the outer wall. The container is filled with water to which a small amount (a thumbnails worth) of mica flakes coated with shiny titanium oxide have been added. These mica flakes are roughly 4μ in diameter and tend to align themselves with strong shear stresses in the fluid within the container. The water filled container is chucked up in a horizontal lathe and heater power is supplied via slip rings attached to the lathe spindle. The lathe is then spun to

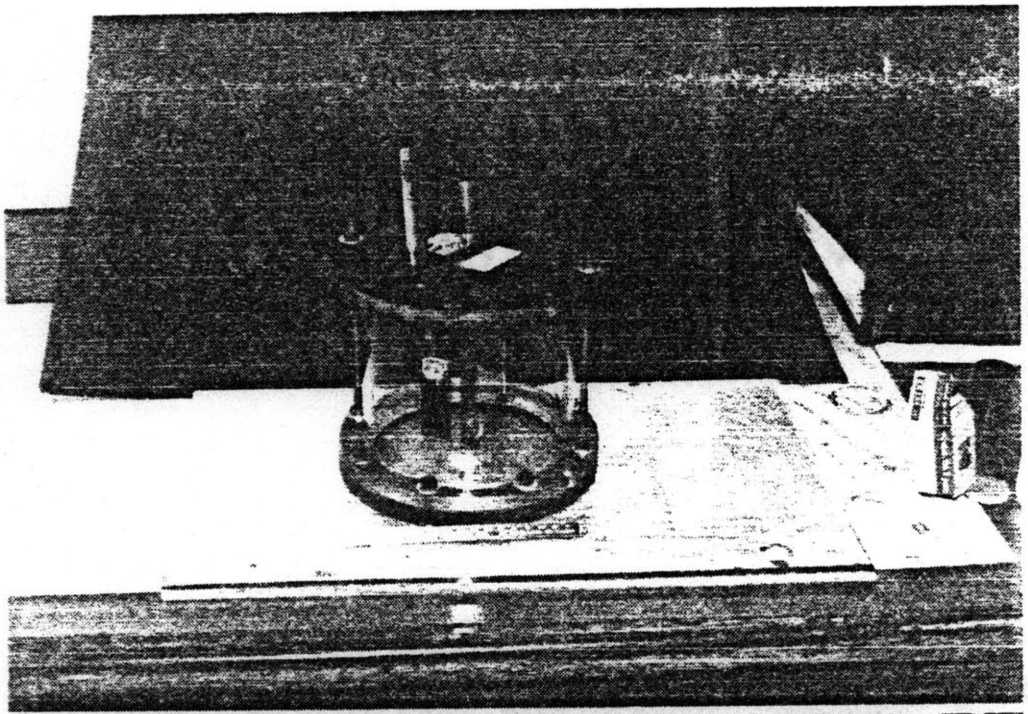

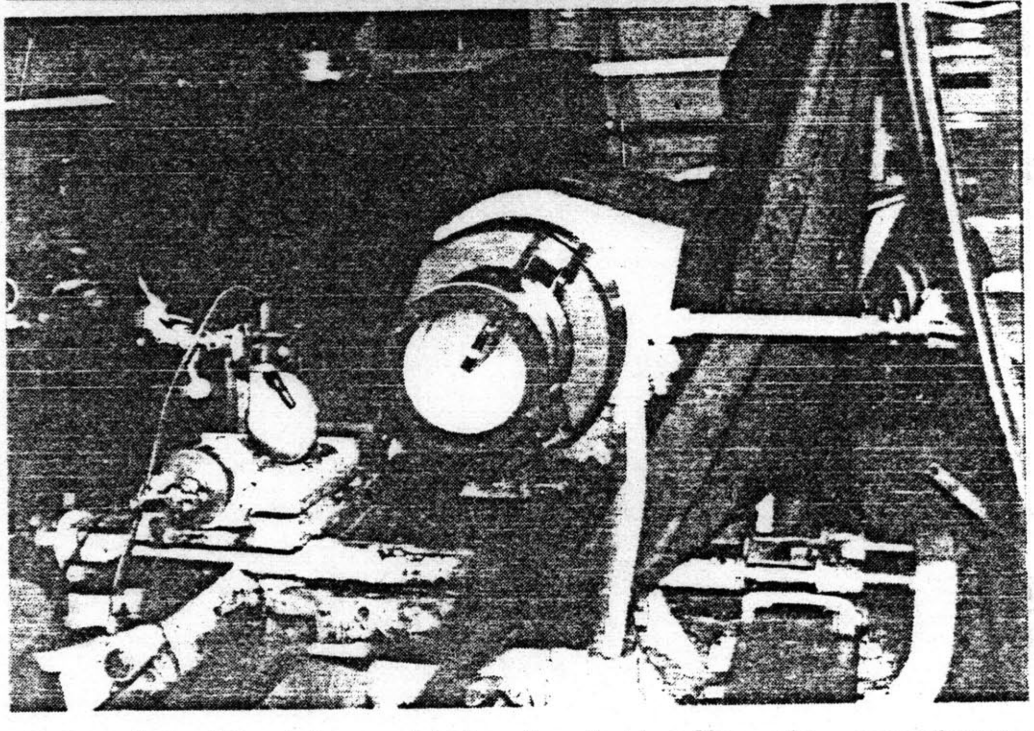

Figure 1.2a Plexiglas cylinder for lathe flow vis. experiments
Figure 1.2b (below) Cylinder mounted in horizontal lathe

531 rpm and the container motion is frozen by the strobe shown in the front of the lathe. When the fluid within the container is finally in solid body rotation the heater is turned on.

Figure 1.3 shows the starting plume as it accelerates away from the heater surface. Fig. 1.4 shows the same plume a few moments later after the plume has reached the center of the container. Now these rather simple looking plumes are quite extraordinary. It is surprising, first of all, to find that the plume is visible at all. The pictures shown in Figs. 1.3 and 1.4 are of fluid motions as seen through the front end plate of the rotating cylinder. The heater, however, is taped to the cylinder wall near the middle of the container (Fig. 1.2a). Figs. 1.3 and 1.4 therefore indicate that the hot fluid leaving the surface of the heater is dragging along a column of fluid that extends to the cylinder end plates (where it can be seen and photographed). The hypothesis, subsequently proven with dyed fluid, was that a small slowly moving buoyant thermal creates a Taylor column [1], that is, a small amount of buoyant fluid will pull a column of non-buoyant fluid inwards just as if the heater had extended the full axial length of the container. The fact that no fluid moves over or under the thermal (that no fluid changes in elevation) as the thermal moves inwards can be physically explained as follows. Individual fluid filaments (imagine a thread of fluid extending from one horizontal endplate to the other) that are rotating rapidly posses a kind of gyroscopic stiffness. In response to small forces perpendicular to the axis of rotation (such as a buoyant spherical lump of fluid moving inwards) the fluid filaments will not bend, but rather, move around the obstacle keeping their original length unaltered.

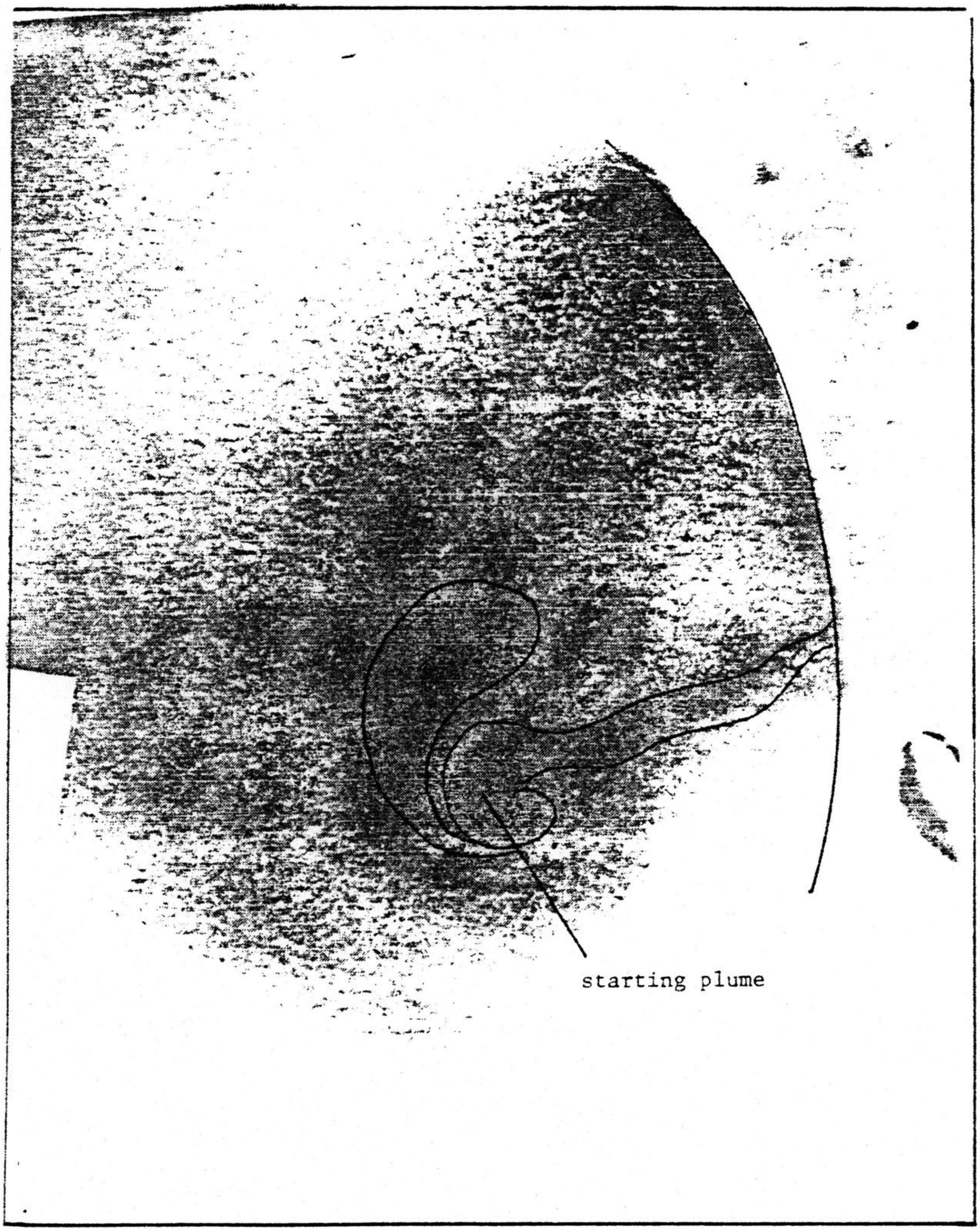

Figure 1.3 Starting plume from small heater affixed to outer wall of plexiglas cylinder. Note plume front which consists of pair of eddies, and the plume itself which narrows towards the wall at the heater surface. Heater is less than 1/2" wide. Speed is 531 rpm.

Figure 1.3

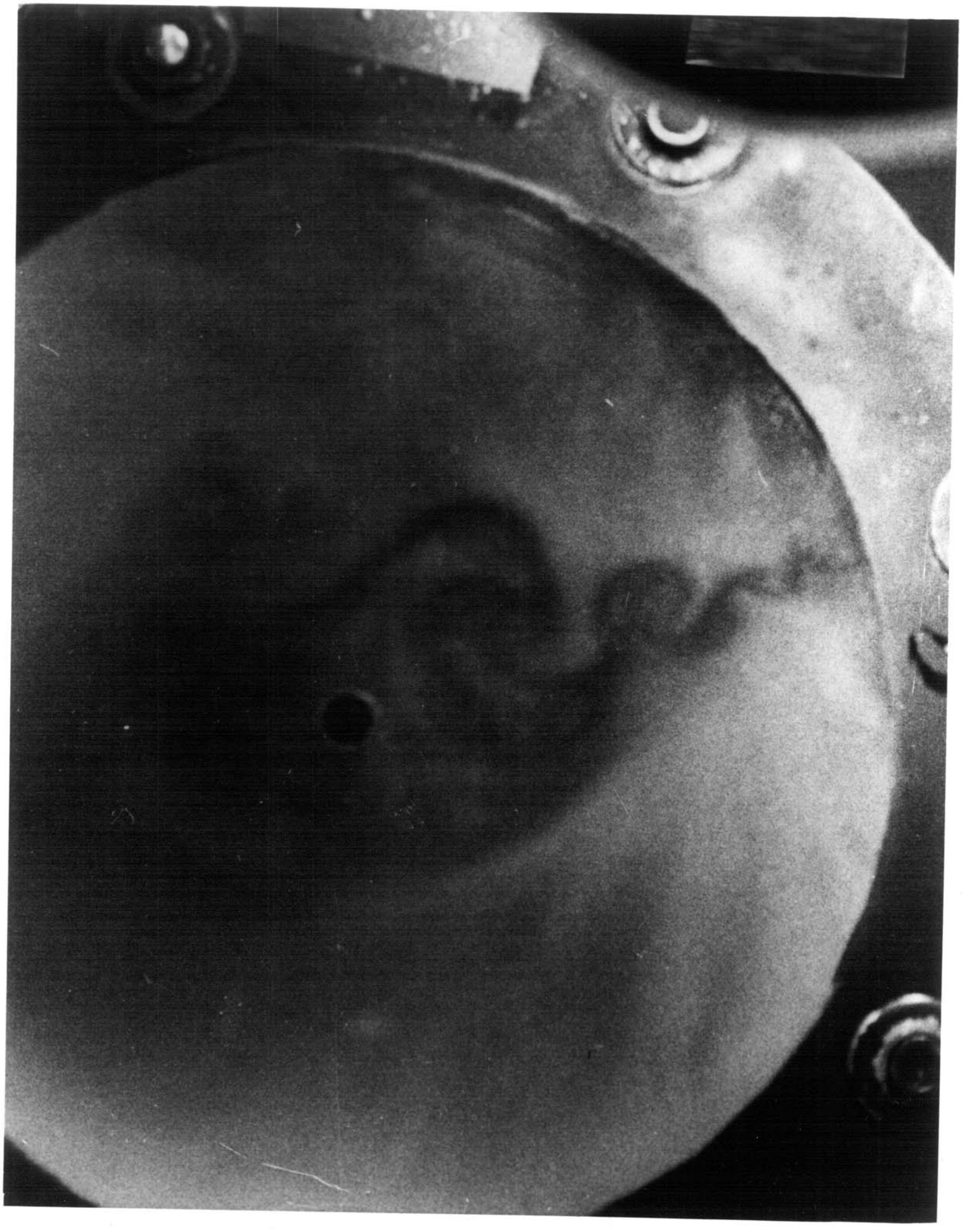

Figure 1.4 Picture of plume a long time after plume front has reached the centerline.

The second extraordinary feature of the plume photographed is that the trajectory is radial. A radial trajectory in a rapidly spinning system is only possible if there is a net force acting on moving fluid particles at right angles to their motion. This net force keeps the fluid within the plume from accelerating azimuthally relative to the walls of the container inorder to conserve angular momentum. Many flow visualization experiments were performed with baffled as well as unbaffled cylinders (Figs. 1.3 and 1.4 show a plume in an unbaffled cylinder) and the plume trajectories have been the same. The trajectory is not a consequence of geometry. The external force acting on the buoyant column, it turns out, is supplied by the pressure field of the cold fluid streaming around the thermal.

Flow visualization experiments have also been performed with heaters of widely different shapes and crossections. Although the plume trajectories were not radial in all cases (for sufficiently small heaters and sufficiently high surface heat fluxes- the trajectories curve inwards towards the centerline) it has not been possible to generate a single three dimensional convection flow field with a heat source fixed to the outer container wall. The interesting conclusion of these experiments is that fluid motions generated by bouyancy forces in rapidly spinning fluids tend to be two dimensional. This phenomena is a characteristic of strongly spinning fluid systems which is independent of the fluid itself.

I.C. Quasi-steady heat transfer

A fully instrumentated rotational test bed has been constructed for measuring surface heat transfer coefficients at high rotational speeds.

Fig. 1.5 shows a pie shaped container mounted on a rotating test bed. The container is a water tight aluminum frame with lexan windows on 3 sides. Heaters of various shapes are mounted on the inside of the container outer lexan window. There are thermocouples attached to the heater surface and in the interior bulk fluid region. The thermocouple output is used to obtain surface heat transfer coefficients as a function of heat flux, fluid properties and rotation rate. An onboard rotating data acquisition system multiplexes 11 analog thermocouple voltages from within the container, converts each analog signal to a digital signal which is serially transmitted out of the rotating system with optical slip rings.

Over 150 quasi-steady heat transfer tests have been performed. Surface heat transfer coefficients as a function of heater power and rotation rate have been obtained for glycerine and alcohol as well as water. The range of centrifugal Rayleigh numbers (rotational acceleration, $\omega^2 r$, substituted for g) covered in these tests is 10^6 to 10^{11}. The heat transfer data has been found to follow a relationship of the form:

$$Nu=.107(RaPr)^{.33} . \tag{1.1}$$

Fig. 1.7 is a log-log plot of all the heat transfer data collected (water, water/glycerine,alcohol). The data includes tests with heaters of large and small axial extent (the dimension parallel to the axis of rotation) and heaters mounted in different places on the outer wall. Fig. 1.6 is the water data only compared with the standard laminar and turbulent natural convection correlations again, based on centrifugal acceleration. A linear regression for this data alone yields a relationship of the form:

$$Nu=.23Ra^{.32} . \tag{1.2}$$

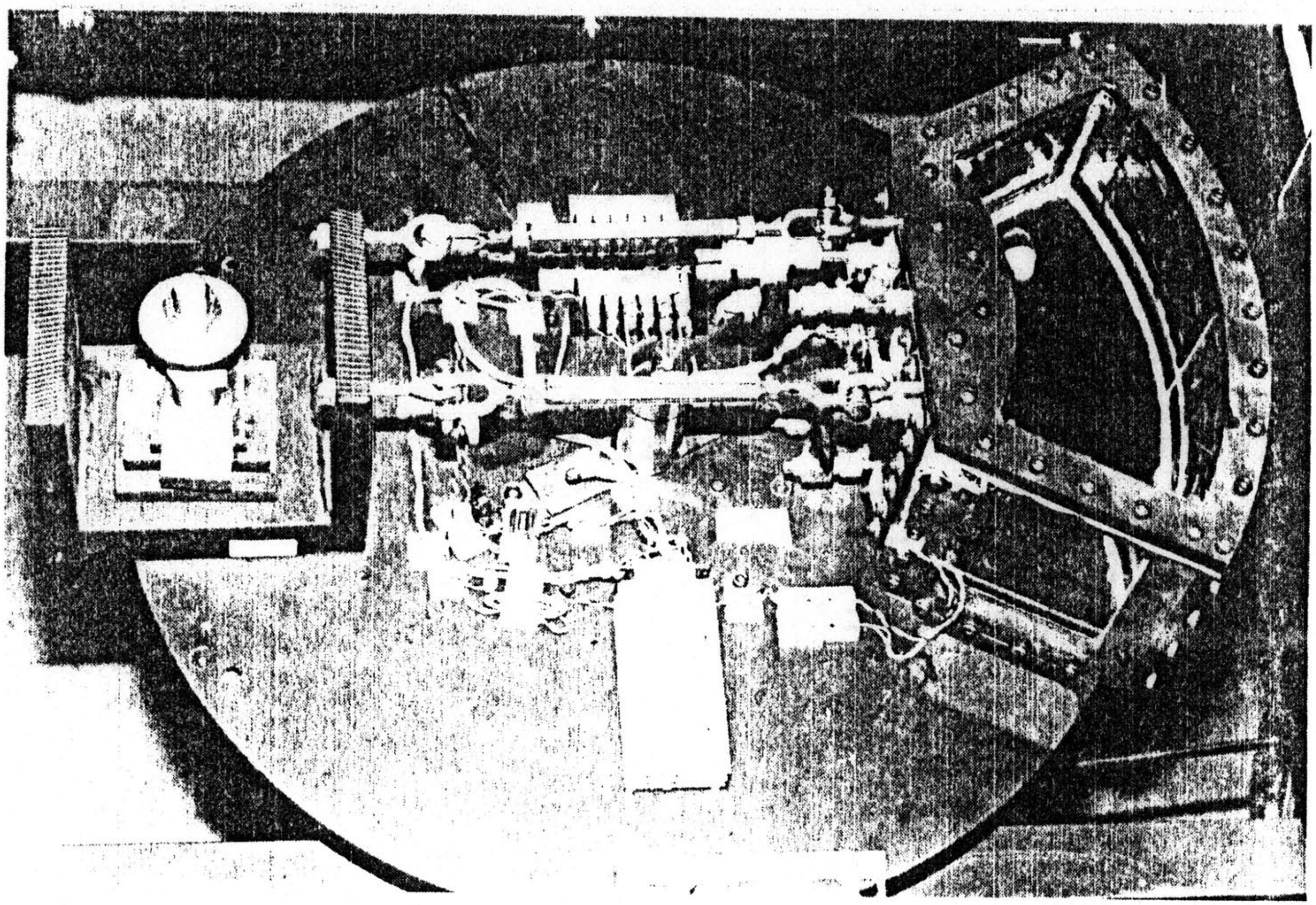

Figure 1.5 Rotating test bed consisting of pie shaped lexan/aluminum container, counterweight, and rotating electronics package. Turntable radius is 12".

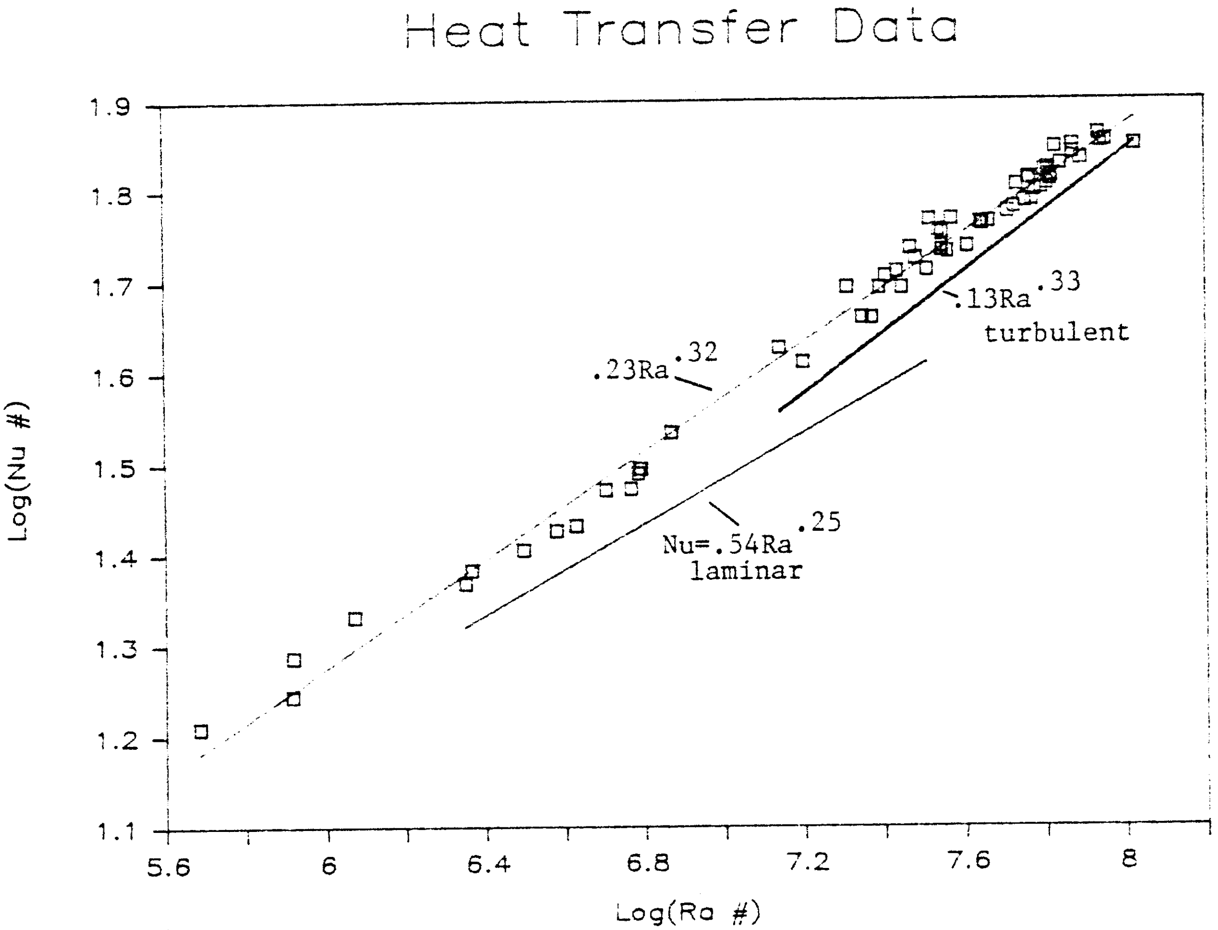

Figure 1.6

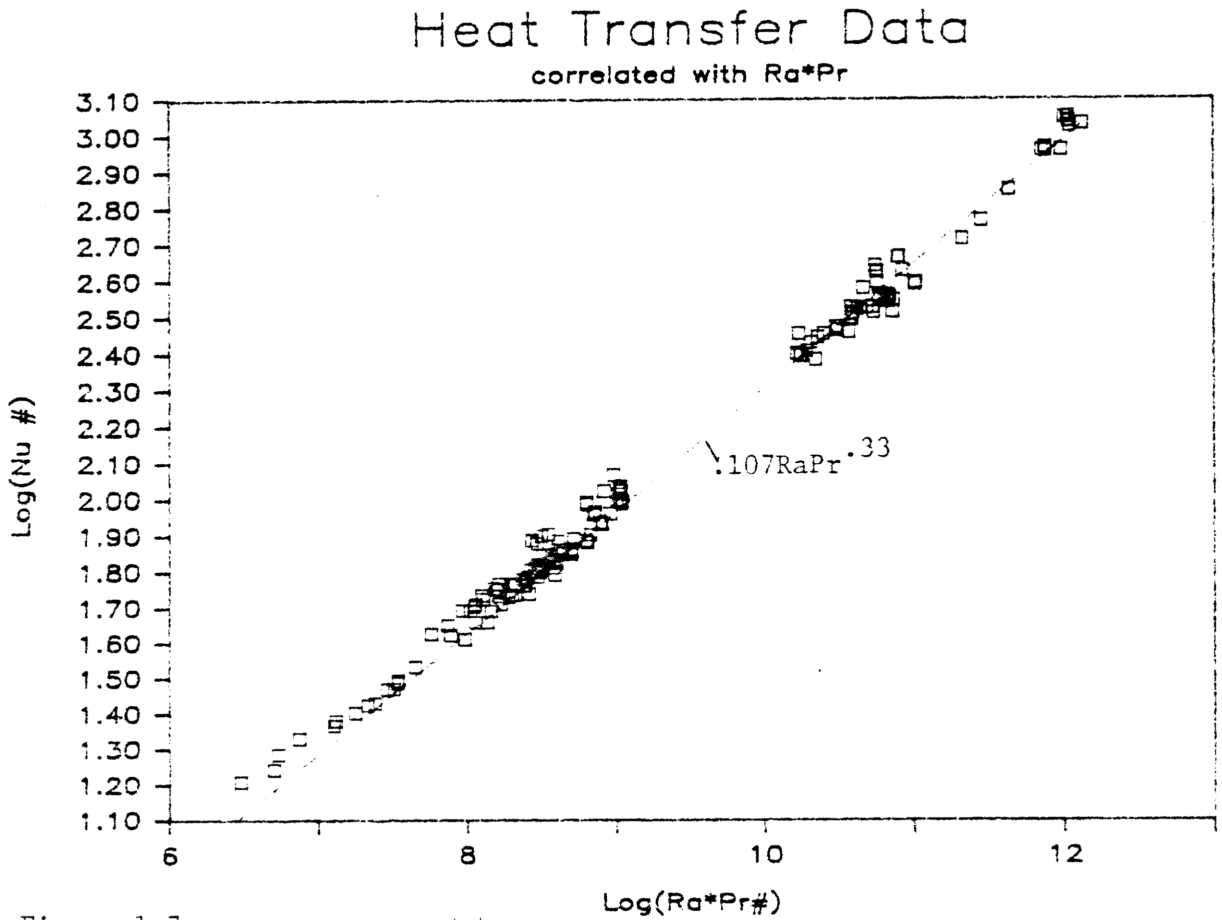

Figure 1.7

The interesting implications of these two correlations (Eq. 1.1 and 1.2 are as follows:

1. the conduction boundary is so thin at these high Rayleigh numbers that the surface heat transfer coefficient is not affected by the trajectory of the plume or the additional fluid dragged inwards by the buoyant fluid,
2. the Nusselt number is apparently independent of fluid viscosity, indicating a conduction dominated process of a sort associated with low Prandtl number fluids in Benard like convection,
3. the surface h measured in water is 50% greater than expected, attributable to the nearly constant heat flux boundary condition obtaining in the tests reported here.

I.D Spin-up of a homogenous fluid in a non-axisymmetric geometry

An airborne superconducting generator will operate at rated speed only for short periods of time. The rotor, normally idling at low speed, will be accelerated at a rate of 6000rpm/s for 1 second when there is a sudden demand for power. Now it takes a finite amount of time for the on-board helium supply to come into solid body rotation. While the fluid is being spun up the natural convection heat transfer coefficient will be smaller than the steady state value since the fluid pressure gradient is not yet fully established. However, the relative motion of the fluid during spin-up- a function, it will be shown, of reservoir geometry, will augment the natural convection h to an extent and in a manner that will be described below. The purpose of the investigation into spin-up flows in general and the effect of fluid relative motion on the surface heat transfer coefficient in particular is thus to determine whether it is advantageous to exploit fluid relative motion with a generator reservoir design that inhibits fluid spin-up.

When a right circular cylinder without radial baffles is suddenly rotated about its vertical axis the fluid comes to know of the motion of the cylinder because an imbalance in centrifugal pressure forces exists in different regions of the fluid. Unless the container geometry is small, spin-up is not a diffusive (viscous) process. As the container begins to rotate fluid close to the top and bottom horizontal endplates of the cylinder is thrown radially outwards . New fluid must then be drawn into the two endplate boundary layers from the interior fluid regions. To complete the flow circuit fluid is drawn away from the outer wall region and into the interior . The latter fluid, however, is spinning -it has come from regions close enough to the wall to have been acted upon by viscous stresses, and as the spinning fluid moves inwards it spins faster. The spin-up is completed when the fluid in the interior is spinning at the same rate as the container. A schematic of this flow process is shown in Fig. 1.8. The time required for spin-up is consequently determined by the time required to flush all of the interior region fluid through the endplate boundary layers and replace it with fluid drawn inwards from the boundary layers on the vertical sidewalls of the cylinder. These sidewall boundary layers are indicated in Fig. 1.8. This time is the Ekman time:

$$\tau_E=(h/2)(\nu\omega)^{-.5} \qquad (1.3)$$

where h is the distance between the two horizontal end-plates, ν is the kinematic viscosity and ω is the final speed of rotation.

The spin-up process can be neatly visualized in an experiment designed by Prof. Greenspan [2]. A right circular cylinder is seeded with shiny mica flakes and rotated on a vertical turntable (represented schematically in Fig. 1.9). A thin collimated light source is projected

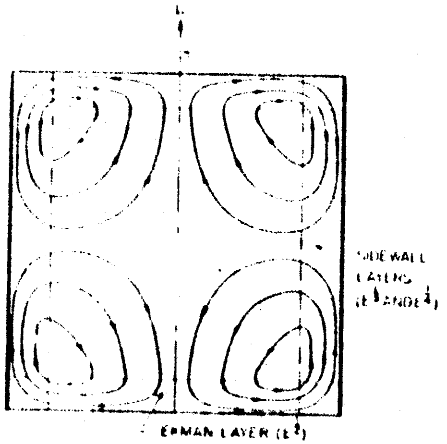

Fig. 1.8 Streamlines of spin-up flow field. Fluid acquires rotation after being flushed through Ekman layers on endplates.

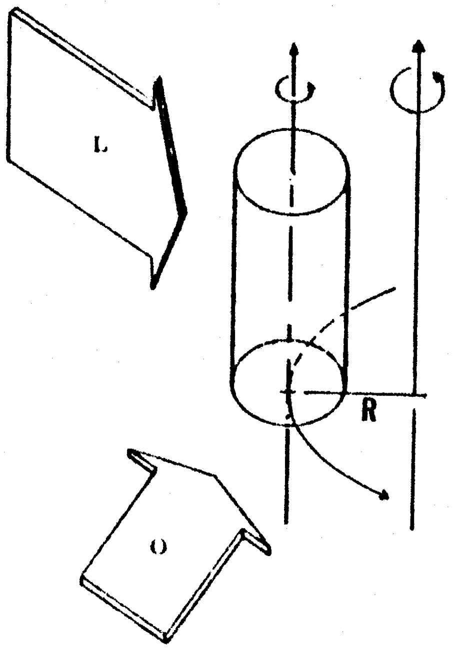

Figure 1.9 Schematic for visualizing columnar evolution of fluid rotation. Observer is at right angle to vertical slit source of light. Container can be spun-up on axis or off axis and observer will see no difference, except that spin-up off axis is visible only once per rev.

thru the container, with the camera and the viewer positioned infront of the container and at right angles to the light source. Fig 1.10 is a sequence of photos illustrating a spin-up using such an arrangement. The shiny column of fluid in the interior of the container is fluid that is non-spinning and is being slowly drawn into the top and bottom end plate boundary layers. The rest of the fluid in the container is spinning . The mica particles in this region are aligned with the rotation and are not visible to the observer. These particles reflect the incoming light back to the light source. A fraction of the the incoming light, however, is not reflected back at the light source and is reflected from the interior in the direction of the camera, showing the slowly diminishing core of non-spinning fluid.

Suppose instead that the same circular cylinder is made to rotate about a vertical axis not coincident with its vertical axis of symmetry . It turns out that the spin-up process is still the same. (Fig. 7.6 shows an apparatus constructed for performing off-axis spin-up tests. The sequence of pictures in Fig. 1.10 actually show an off axis spin-up). The distance of the cylinder on the turntable from the axis of rotation affects only the pressure forces on the walls of the container. Pressure forces acting on a homogeneous fluid (no density gradients in the fluid) cannot create a torque on a fluid element, and so cannot by themselves impart rotation to the fluid. Furthermore, though the pressure forces in the fluid are different in an off-axis spin-up, the net pressure imbalance, the imbalance which drives the secondary flow, is the same as in an on axis spin-up.

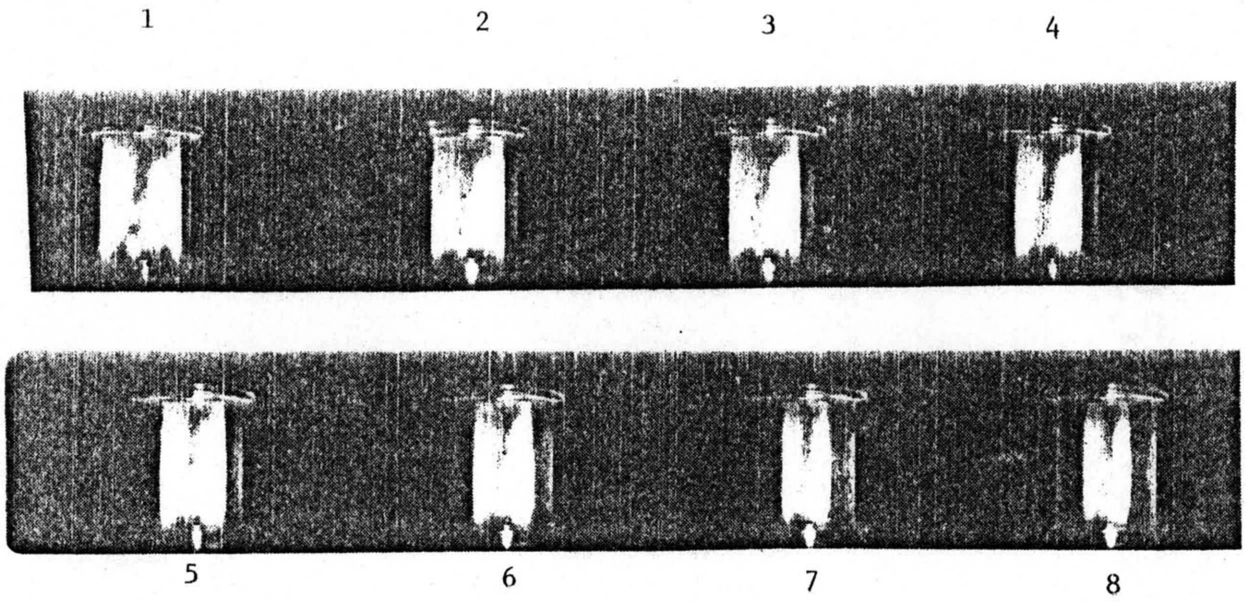

Figure 1.10 Sequence of pictures taken during <u>off</u> axis spin-up. Note column of interior fluid getting thinner as spin-up evolves. The last two pictures (7,8) were taken with the turntable stopped. Unstable spin-down is characterized by roll cells on outer container wall.

A homogeneous fluid acquires rotation then as it is slowly pumped into the viscous dominated endplate boundary layers. For very small times fluid motion in the regions away from the endplates and sidewalls must be irrotational. This is true regardless of the shape of the container. When a right circular cylinder is impulsively accelerated to speed ω the fluid initially appears in the reference frame of the container to counterrotate relative to the walls of the container at a rate equal to $-\omega$. Similarly, if a container of any shape is impulsively accelerated to some speed ω the fluid will always appear to counterrotate along streamlines having the horizontal contour of the fluid container itself at a rate equal to $-\omega$. The sum of this relative fluid rotation and the container rotation is zero, and the inertial motion of each fluid element is irrotational. This result will be derived in Chapter 8.

The relative motion of the fluid in an arbitrarily shaped container thus scales with $\Delta\omega c$, where $\Delta\omega$ is the impulsive change in rotation rate, and c is a characteristic radius of the container (see Figure 7.3). This result can be used to estimate the relative motion heat transfer enhancement. However, the inviscid irrotational flow just described is unstable for container geometries that are not circular. Deccelerating boundary layers near the horizontal boundaries of the container will separate . Fig. 1.11a shows the pie shaped container of Fig. 1.5 seeded with mica flakes and impulsively accelerated from rest to 20rpm. The direction of rotation is from right to left. Within two revolutions, the fluid in Fig. 1.11b can already be seen to have separated in the two opposing corners. Kinetic energy will be fed into the corner regions from the original irrotational flow field in each succeeding revolution until

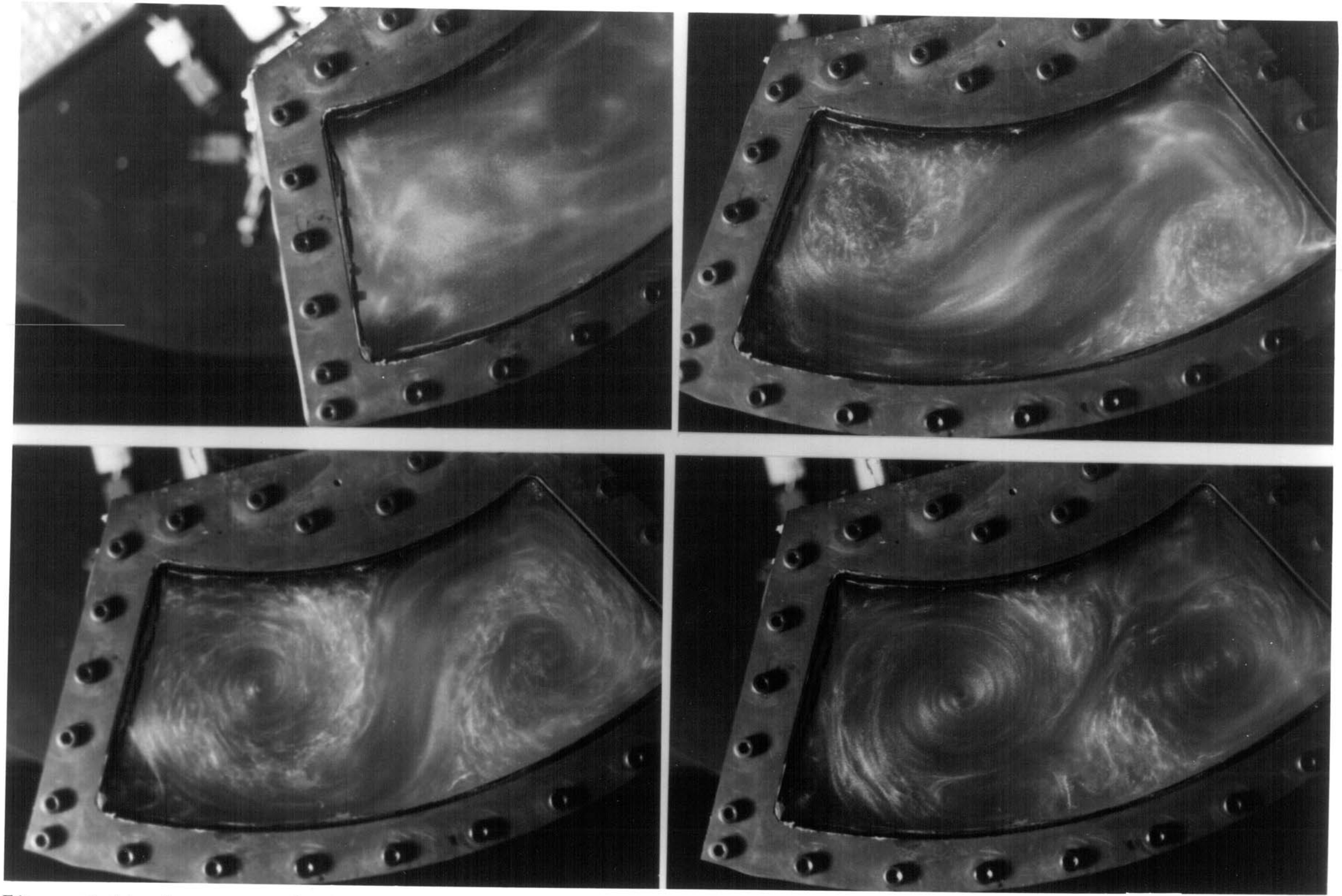

Figure 1.11 Sequence of pictures taken of spin-up in pie shaped container of Figure 1.5. The upper left hand corner picture shows the container impulsively accelerated from right to left to 20 rpm. Fluid attempts fo counterrotate along horizontal contour of container but adverse pressure gradient causes boundary layer flow to seperate in the corners. The two corner eddies continue to grow drawing kinetic energy out of the interior fluid. The eddies are rotating in the same direction.

the vortices in the corners are of sufficient size to move out of the corners and into the interior of the container. It is most interesting to note that the initial flow field quickly evolves (within 2 revolutions) into two irrotational vortices which are now spinning in the same direction as the container. (A region of concentrated vorticity is clearly visible at the center of each of the 2 primary vortices). These vortices continue to interact (shown in Figures 7.13-7.16) until the spin-up evolves. Though the container in these pictures was rotating slowly, the flow field for impulsive accelerations to 500 rpm is not appreciably different. The number of eddies and their interactions are a function of container geometry and speed of rotation, (in the singly baffled container of Fig.1.12 there are 4 large eddies). However, a most important result of observations of spin-up in non-axisymmetric containers is that the spin-up is still an essentially two-dimensional process with a time constant of the same order as that in an unbaffled, symmetric container.

I.E Transient Heat Transfer Tests

The effect of this energetic relative motion on the surface heat transfer rate has been measured . The pie shaped rotor shown in Fig. 1.5 was idled at rougly 250 rpm until the fluid was in solid body rotation. The heater was energized and the rotor impulsively accelerated to, say, 550 rpm. The rotor reached 90% of its final rotation rate in less than 2 seconds (6 revs). (The spin-up time constant for the fluid within this

Figure 1.12 Spin-up in a baffled plexiglas cylinder.

container is 13 seconds and the acceleration could be considered impulsive.)

Figure 1.13 is a recorded plot of the temperature history on the surface of a heater following an impulsive acceleration. Also shown in Fig. 1.13 is a plot of surface temperature during a quasi-steady test at 550 rpm. The heater power in both tests was the same. Figure 1.13 clearly shows that there is improvement in the heat transfer coefficient for some length of time, although that time is still short compared to the spin-up time of the fluid in the container.

The unusual result that a quasi-steady heat transfer state is reached while there is still considerable relative motion in the interior of the container is explained as follows. The local surface heat transfer coefficient is determined by the buoyancy based upon the local gradient in pressure and not upon the global pressure gradient. Although it takes a considerable amount of time to produce rotation in the interior of the container, a significant gradient is established early on in the regions very close to the sidewalls because of viscous diffusion. At high acceleration rates the local thermal boundary layer is also so small that it is quickly embedded within the spin-up wall boundary layer and as the spin-up boundary layer grows outward the net relative motion mass flux in the vicinity of the heater diminishes as well. The appropriate dimensionless time with which to scale the transient heat transfer data is thus found to be:

$$\tau_{ht}=\sqrt{\nu t}/[(\sqrt{Pr})\delta_t] \ . \tag{1.4}$$

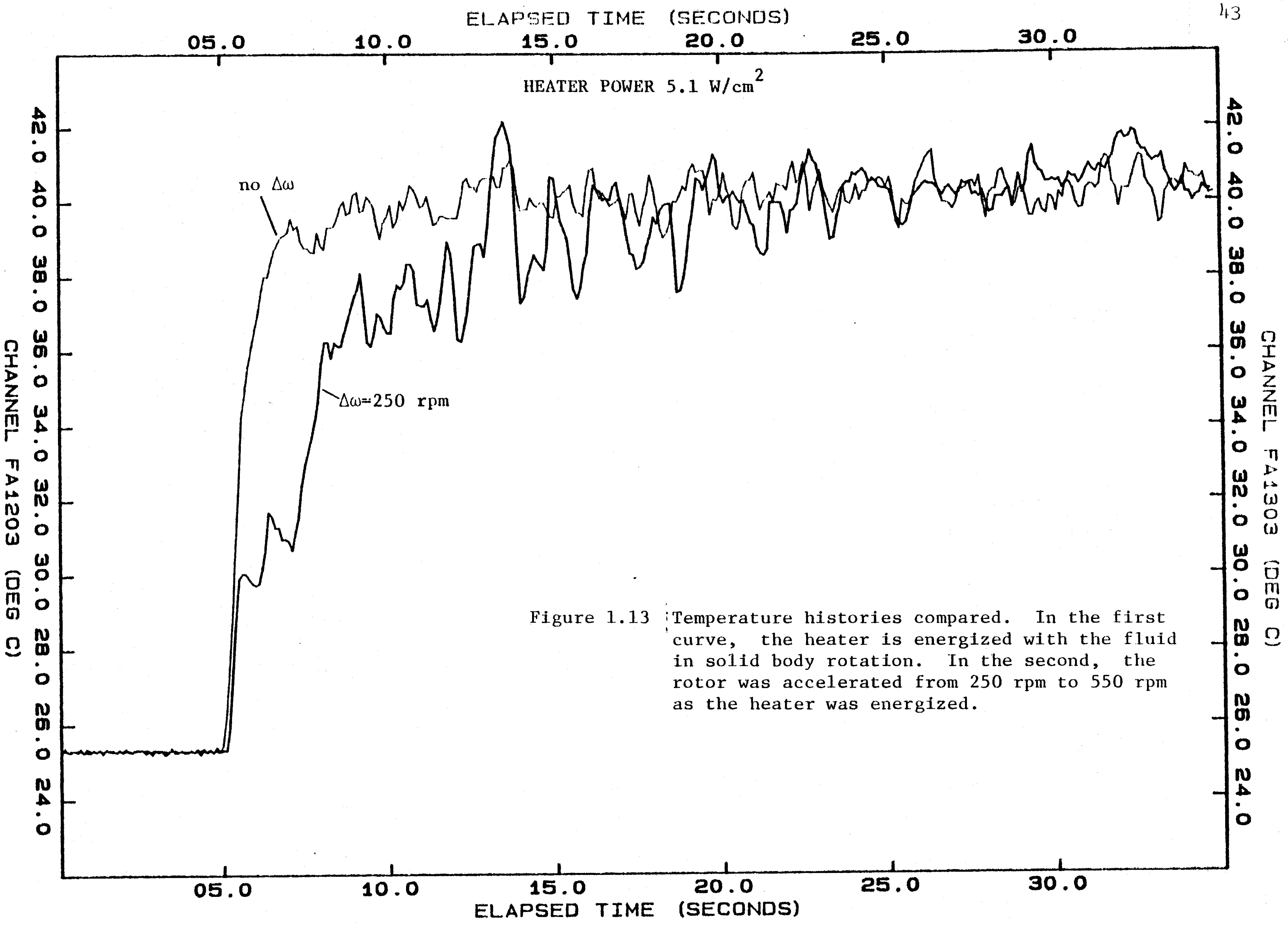

Figure 1.13 Temperature histories compared. In the first curve, the heater is energized with the fluid in solid body rotation. In the second, the rotor was accelerated from 250 rpm to 550 rpm as the heater was energized.

Equation 1.4 is the ratio of the momentum boundary layer thickness from ordinary diffusion divided by $\sqrt{Pr}$ times the steady state thermal boundary layer thickness at the final rotational speed. A nondimensional temperature history is shown in Fig. 1.14. Using a plot of this form it is possible to reduce the transient data for a range of Prandtl number fluids for the same step change in rotation rate to a single curve. The nondimensional time in Eq. 1.4 is independent of fluid viscosity and roughly represents the time required for a quasi-steady thermal conduction boundary layer to develop. It could not be established with the apparatus available exactly how the time required to establish a thermal boundary layer depends on the relative fluid motion in regions very close to the wall. A greater impulsive change in speed will produce a longer period of heat transfer enhancement. But it also seems that the bumps and dips in the temperature curve of Fig. 1.13 are due to the swirling vortices which are interacting and scouring the container walls at the beginning of the spin-up. This tends to suggest that a disordered spin-up is preferable for heat transfer purposes, and that reservoir baffles have an important role in enhancing heat transfer during spin-up.

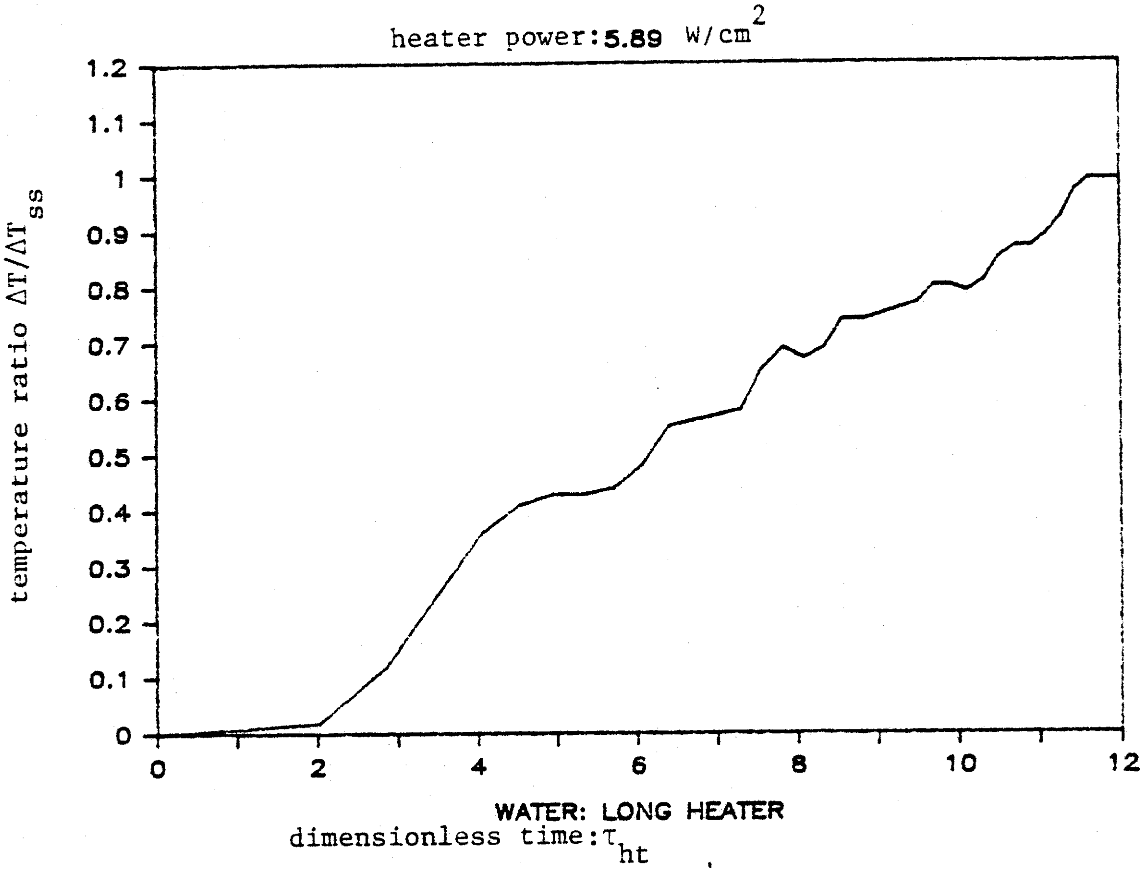

Figure 1.14 Nondimensional temperature ratio plotted against dimensionless time τ_{ht}. When dimensionless time is roughly 10, the complex interior fluid motion no longer affects surface heat transfer coefficient.

CHAPTER 2

SUPERCONDUCTING GENERATORS

II.A Background on MIT generator program

The work presented in this thesis is intended to support the development of an improved cryogenic cooling system for airborne and conventional superconducting generators. The experiments described in the opening chapter are explorations of fundamental phenomena characteristic of rapidly spinning systems. For simplicity, water experiments were designed to simulate certain aspects of actual cryogenic generator operation. Compared to water, helium is an essentially inviscid, compressible fluid with poor thermal conductivity. In Chapter 5 when the details of the construction of the water filled apparatus are discussed, a comparison will be made of relevant characteristic nondimensional numbers for the experimental apparatus and the GE airborne superconducting generator.

The Cryogenic Engineering Laboratory in collaboration with the Electric Power Systems Engineering Laboratory and with financing from DOE is presently constructing a 10MVA superconducting generator. The program is a showcase for certain advanced concepts in superconducting generator design. The machine presently under construction incorporates advances in (1) electromagnetic shielding for the superconducting field winding, (2) superconducting winding design and rotor design, (3) high voltage armature design and (4) cryogenic cooling systems. The background material to follow on the operation of a superconducting generator will emphasize the role of rotor cooling in the overall generator operation.

The principle of operation of a superconducting generator is the same as that of a conventional generator with a rotating field winding [3].

However, the field winding in a superconducting generator is made from superconducting wire which must be maintained at cryogenic temperatures. The field winding is immersed in a liquid helium bath which is connected to the central liquid helium reservoir by a manifold of small radial fluid passages and radial copper conduction bars (Fig. 2.1). During normal generator operation any heat evolved in the field winding generates bouyancy driven circulation currents within the narrow passages of the field winding structure. This small scale circulation transfers heat to the copper conduction bars which extend into the larger central field winding helum reservoir. (The copper conduction bars also serve as liquid isothermalizers removing some of the compression temperature rise in the liquid.) The small scale circulation also drives a large scale circulation which brings colder fluid to the field winding space through the fluid passages connecting the bath and the liquid reservoir. The fluid convection through the radial channels augments the radial conduction through the copper bars.

The rotating field winding is also enclosed within two rotating, helium temperature electromagnetic shields. These shields screen the field winding from AC fields arising from non-synchronous space harmonics . The innermost shield is a high conductivity copper tube. The second shield is the damper shield. The damper shield is a two phase winding of finely stranded and transposed high conductivity normal (non-superconducting) conductor (Fig. 2.2). The screening is effected by currents induced in the damper shield winding and by eddy currents induced in the high conductivity copper can shield.

The transient heat generated by these shielding currents must be prevented from diffusing into the field winding structure. The damper shield thus sits upon a thermal isolation layer of low thermal diffusivity

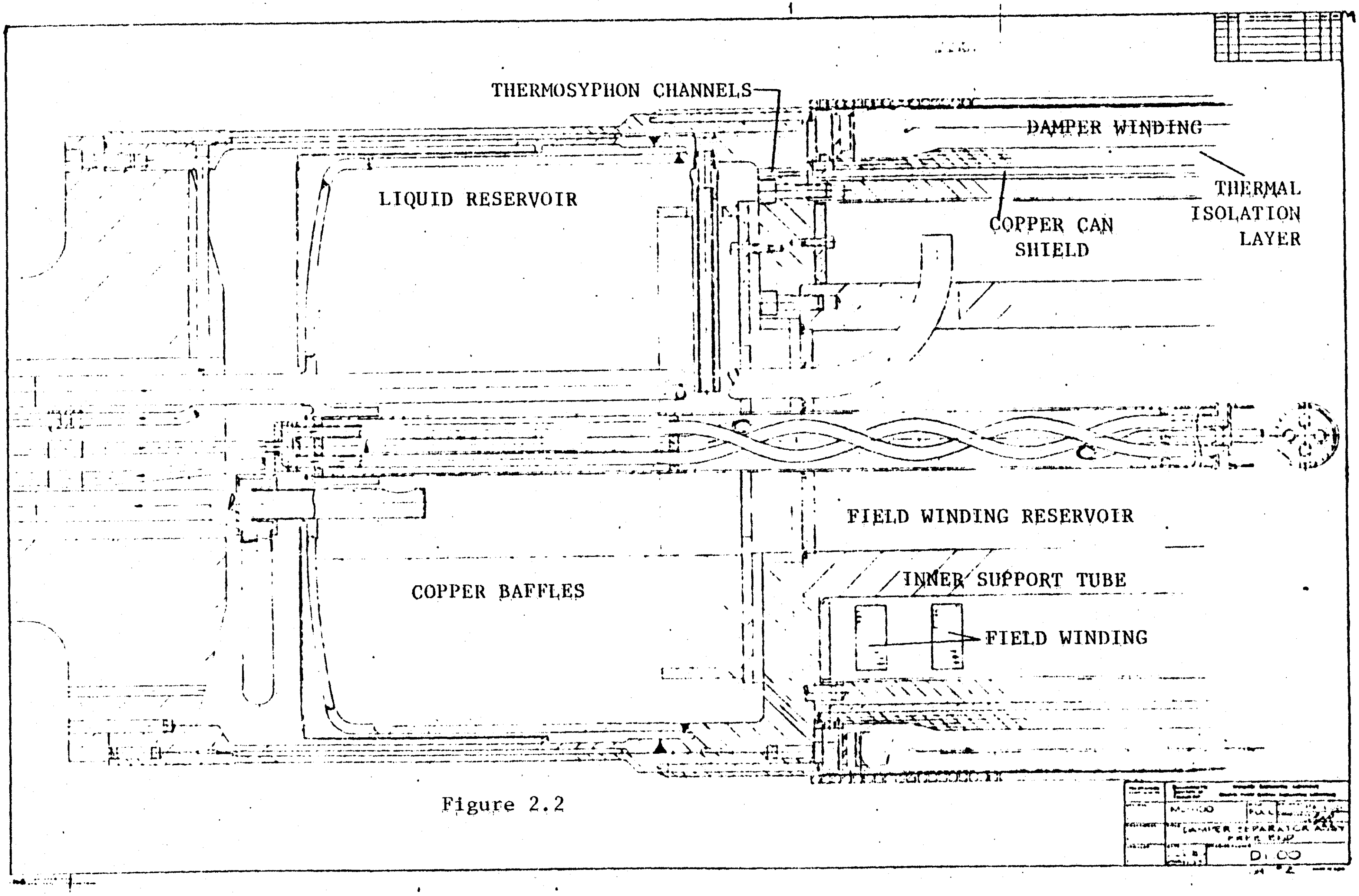
THERMOSYPHON CHANNELS
DAMPER WINDING
THERMAL ISOLATION LAYER
LIQUID RESERVOIR
COPPER CAN SHIELD
FIELD WINDING RESERVOIR
INNER SUPPORT TUBE
COPPER BAFFLES
FIELD WINDING
FULL
DAMPER SEPARATOR ASSY
FREE END

Figure 2.2

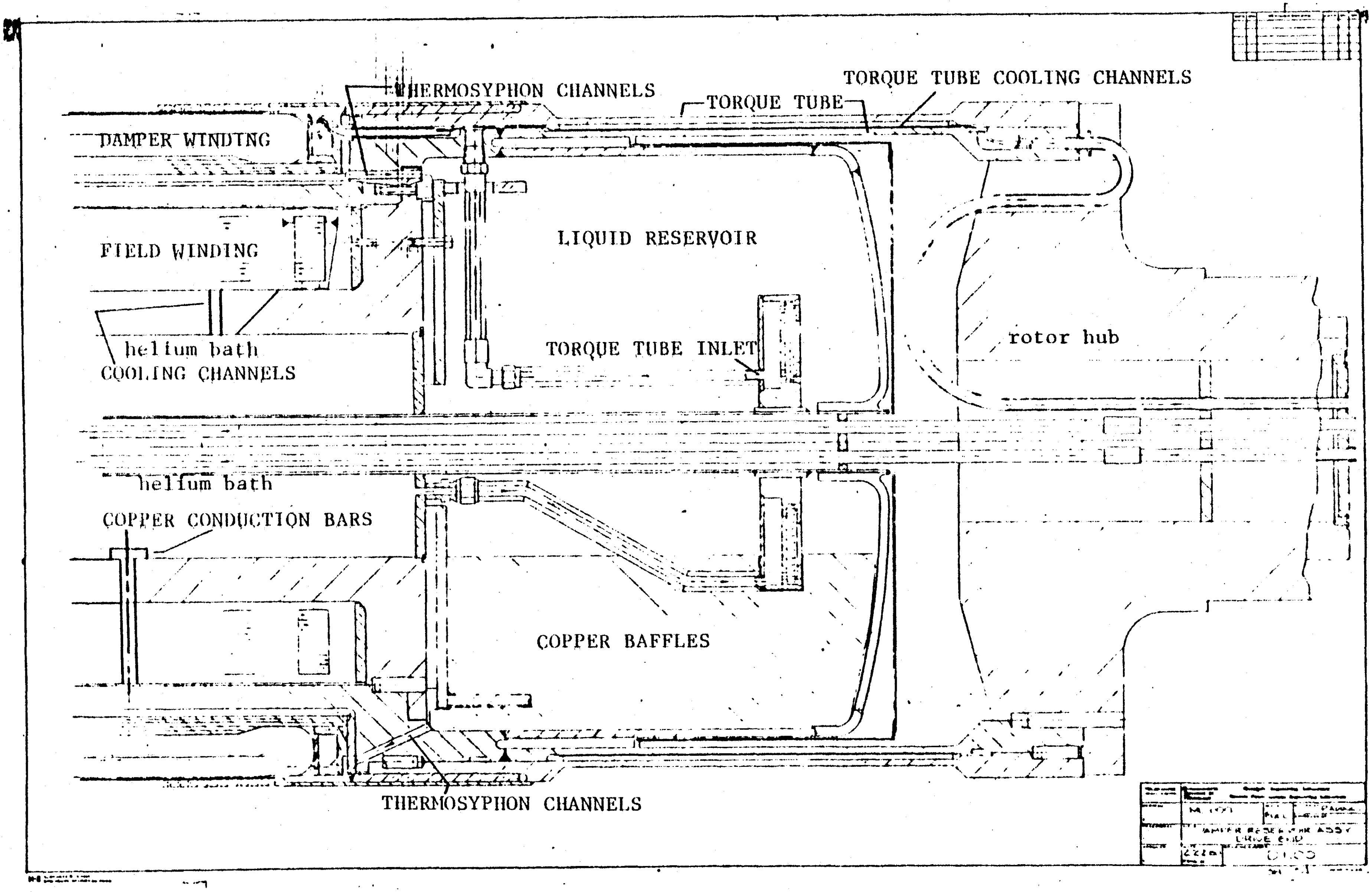

Figure 2.1 Drive end of rotor

material which is shown in Fig. 2.2. The can shield is at the inner radius of the thermal isolation layer. Both the can shield and the damper winding structures have numerous axial cooling passages . These helium filled passages communicate with two large-volume liquid reservoirs on either end of the rotor. The generation of heat within either shielding structure starts a thermosyphon which transfers this internal heating to the two liquid helium baths. Surface evaporation at the liquid surface in the reservoirs ultimately removes the heat from the rotor.

The rotor has been designed on the assumption that any hot bouyant fluid deposited at the periphery of the liquid helium pool will quickly rise to the liquid surface where boiling occurs. In the current rotor design, the two liquid helium reservoirs supplying liquid for the electromagnetic shield cooling thermosyphon are fitted with four radial baffles, two of which are shown in the reservoir schematic of Fig. 2.2. Figure 2.3 is another schematic of a rotor reservoir fitted with four radial baffles and showing actual rotor dimensions. Figure 2.4 is a picture of the copper endplate for the baffle structure. This copper plate bolts to the wall of the reservoir as illustrated in Fig. 2.2, the additional length of copper baffling required to span the reservoir length is then attached onto this end plate. It has already been mentioned in Chapter 1 that the baffled reservoir geometry shown here led to the design of the rotating apparatus of Fig. 1.5. In the absence of any external reservoir heat input, the purpose of these baffles is twofold. These baffles keep the two phases of helium well seperated within the reservoir. Liquid helium foams very easily, and these baffles insure that any turbulent foaming is kept to a minimum. The baffles are also reservoir isothermalizers eliminating or reducing the temperature rise in the liquid as it is compressed in the centrifugal field [4]. Isothermalizing the

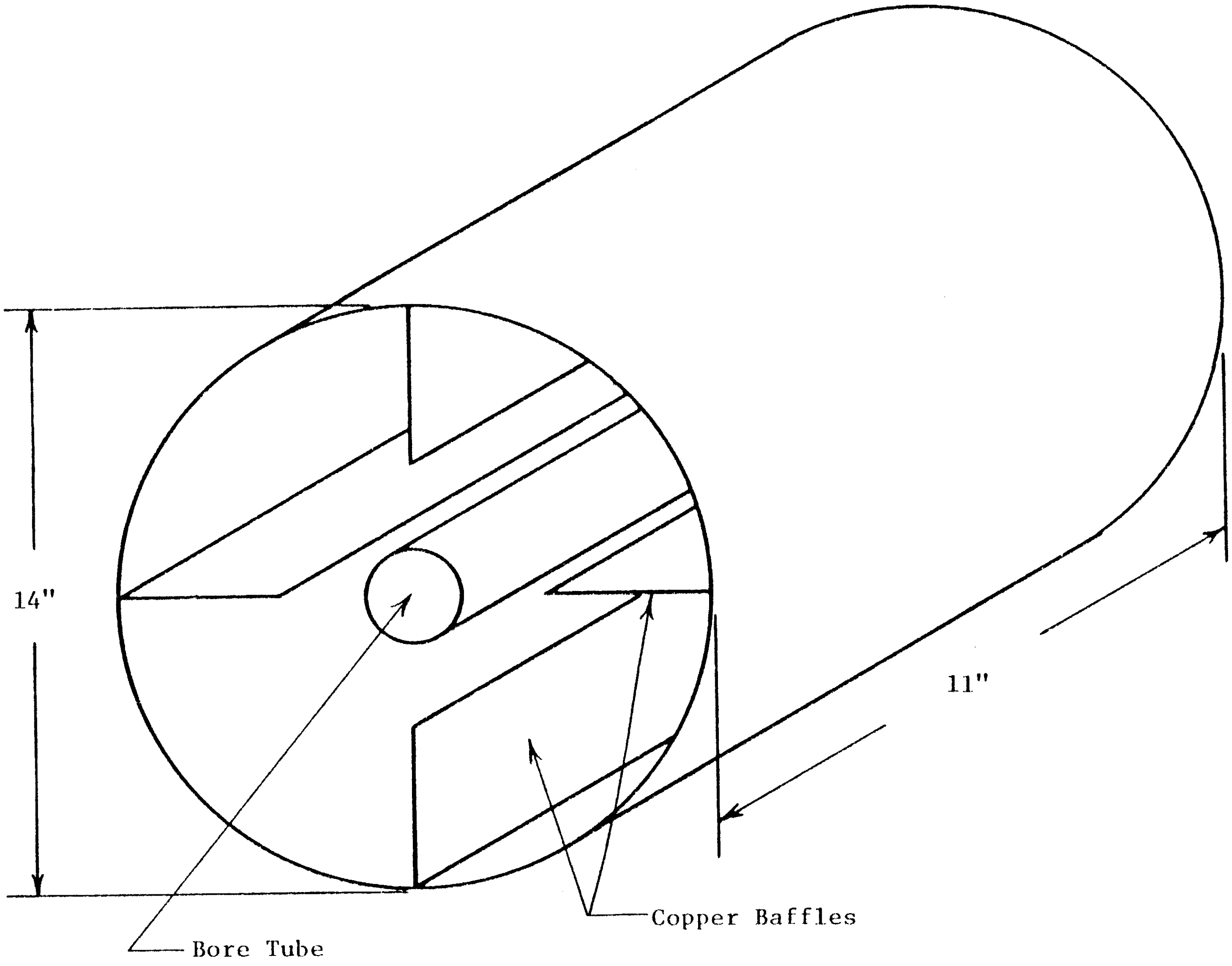

Figure 2.3 End Reservoir

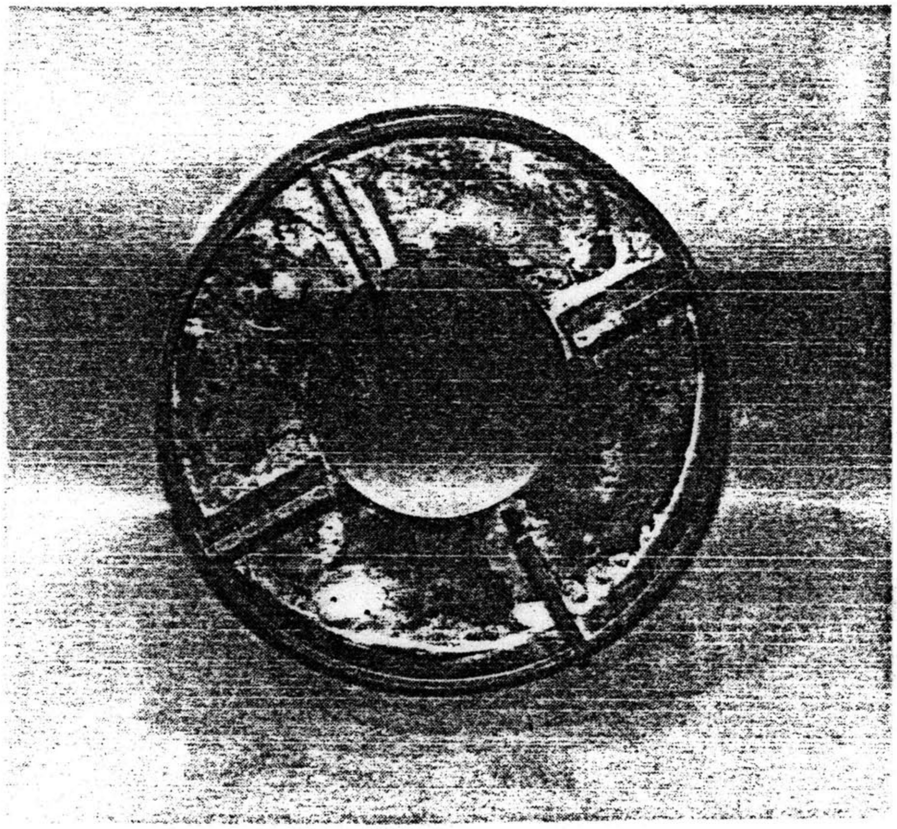

Figure 2.4 Part of copper isothermalizer for large helium reservoir.

reservoir liquid lowers the temperature at the periphery of the reservoir where there are various axial thermosyphon inlets and outlets- but at the expense of higher reservoir pressures. During normal generator operation, however, the baffles were intended to aid in the transport of hot fluid inwards. The baffles were thought to produce a beneficial ordering of the convective flow. Any hot fluid deposited in the outermost radii of the reservoir which started to accelerate inwards would be deflected by coriolis forces to the trailing baffle wall, where it would continue to move towards the vapor liquid interface. Similarly, a cold stream moving radially outwards would be deflected to the leading, high pressure side of the baffle. The boundary layers on the radial walls were thus assumed to involve only a very small portion of the fluid in the reservoir. The fluid seperating the warm ingoing fluid on one baffle from the cold outgoing fluid on the other baffle would tend to remain in solid body rotation and in isothermal equilibrium. It is interesting to note that some of the results reported in this thesis suggest that those hot plumes of fluid issuing axially into the reservoir at the outermost radius will have no difficulty moving towards the rotor axis.

Other notable features of the rotor cooling system are the vapor cooled torque tubes. Figure 2.1 shows that torque is transmitted to the field winding support structure from the rotor shaft through a thin, stainless steel torque tube structure. The torque tube thickness is minimized (to limits set by fault torque transmitting requirements) to keep the conduction heat leak from the room temperature rotor shaft to the cryogenic field winding structure as small as possible. This axial conduction heat leak can be effectively eliminated by countercooling the torque tube with boiloff vapor from within the rotor itself. A large fraction of the vapor evolved in the rotor reservoirs from heat generated in the damper winding or field winding or from the radiation heat load is routed from the central vapor core in the end reservoirs to the torque tube cooling channels through the torque tube inlet tubes shown in Figure 2.1. The vapor then warms as it travels through the torque tubes and returns to the centerline through the S shaped tubing shown in Fig. 2.1 to be ultimately exhausted from the rotor to the helium recovery system. This process of cold vapor compression in the torque tube inlets, nearly constant pressure heat addition in the torque tube cooling channels and warm vapor expansion in the torque tube outlets creates a vacuum on the centerline of the rotor. The vapor cooling loop thus serves to self pump the rotor with liquid from the supply dewars. It is worthwhile mentioning that should these inlet tubes fill with liquid- the vacuum created within the rotor can pull all the liquid rapidly from the stationary storage dewar supplying the rotor. Protection against liquid fill is especially important in the design of the airborne rotor to be discussed next.

For the past 12 years, the Air Force has been funding the developement of a 20MW, lightweight, superconducting generator to be used in airplanes [5]. Work is nearly completed at GE on such a machine . Westinghouse is also conducting research on certain aspects of airborne generators as will be discussed later. This thesis, as mentioned previously, is in support of the helium rotor research being conducted by Westinghouse.

Fig. 2.5 is a schematic of an airborne powerplant. Several crossectional views of the actual GE powerplant are shown in Figures 2.6,2.7 and 2.8. The generator is designed to produce 20MW of DC power at a voltage of 20-40KV . Furthermore, the rotor is designed with as low a rotational inertia as possible so that it can be accelerated to 6,000 rpm in roughly 1 second. The rotor operates like a conventional powerplant ,

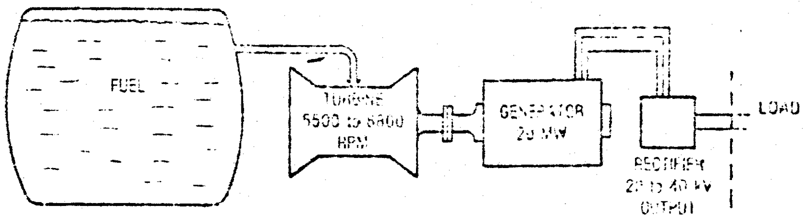

Airborne high-power system.

Figure 2.5

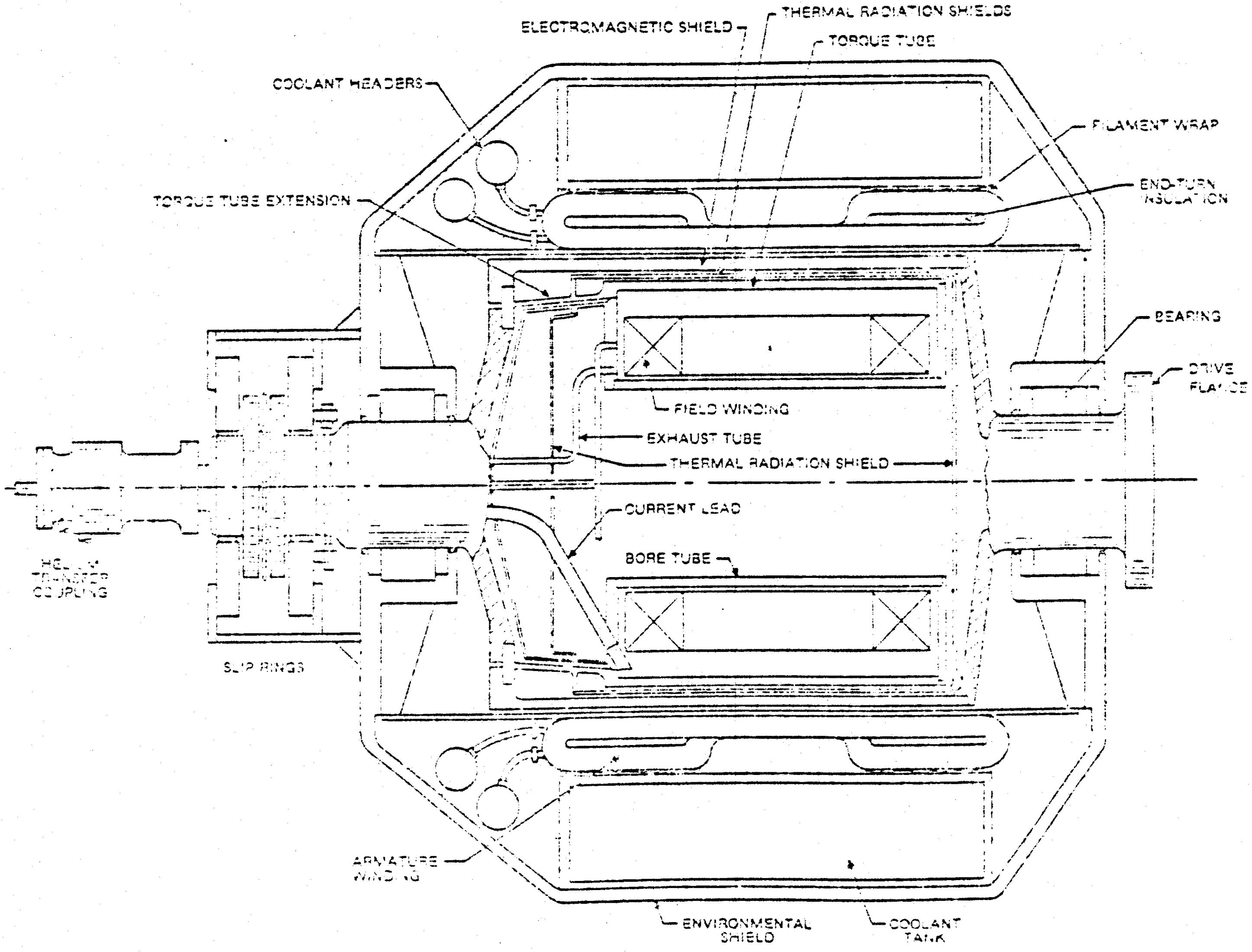

Figure 2.6

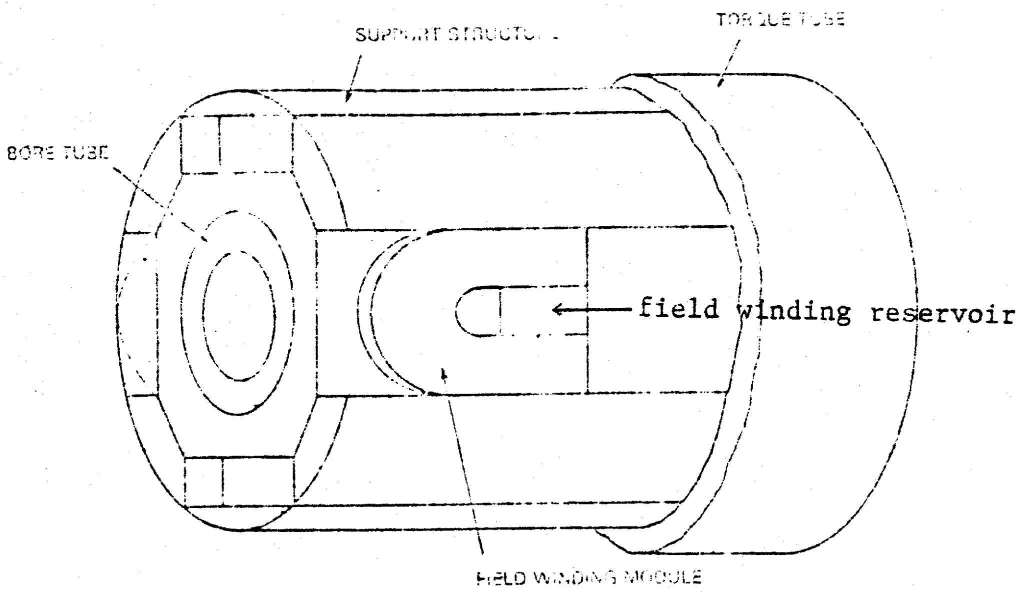

Figure 2.7

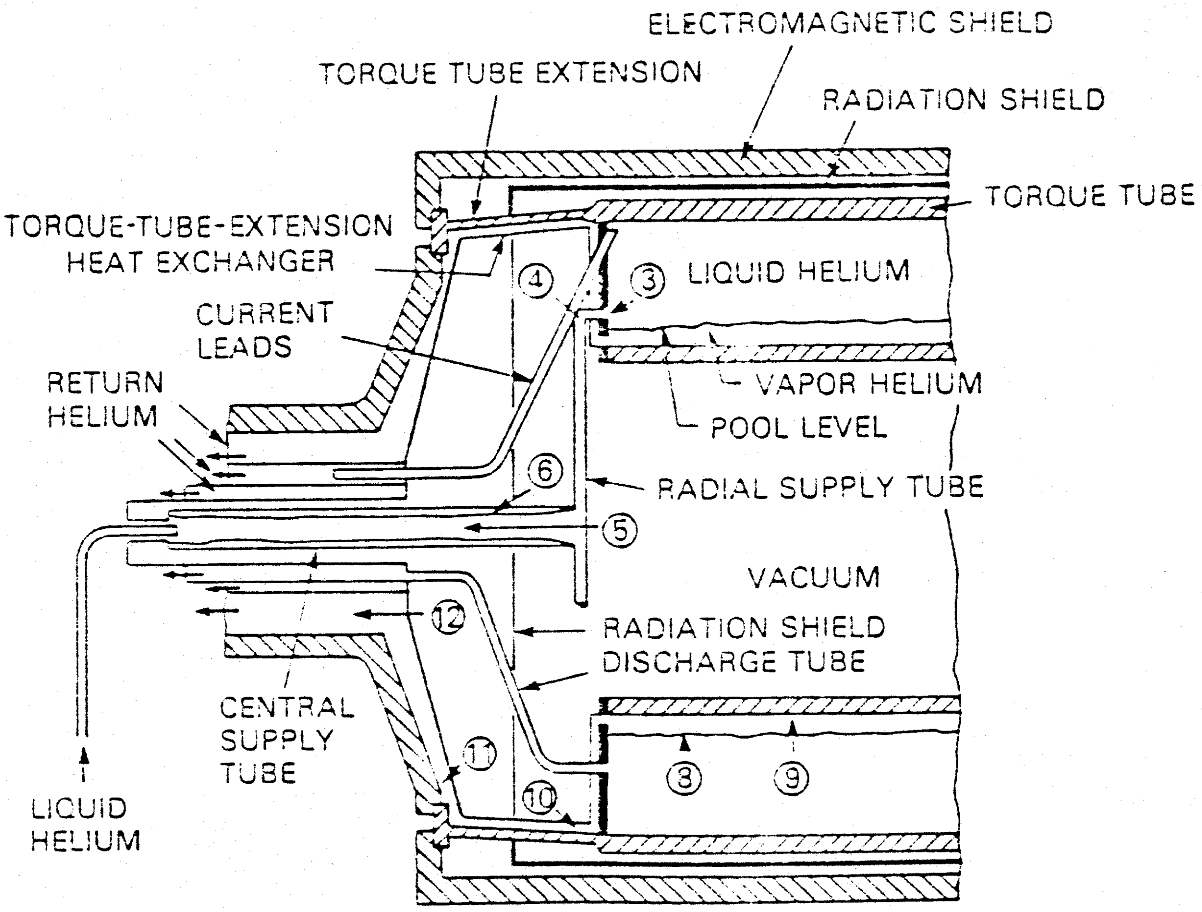

Figure 2.8

except that it must be operational in very short period of time. Since the rotor is generating power within a time short compared to fluid transient decay times- cooling system optimization is much more critical to this design. During tests of a prototype rotor developed by Westinghouse Electric Corp. it was found that even moderate speed changes (40 rpm/s) caused the rotor field winding to go normal [6]. Rapid speed changes may result in frictional heating due to relative motion between the winding module and the support structure and between the superconducting wires themselves. The body forces in the superconductors following a rapid field excitation may also cause conductor to conductor slip. GE hopes to solve the problem by using a teflon interface between the field winding and the support structure. Conductor relative motion, on the other hand, will be eliminated by fully potting the superconductor into rigid epoxy. Figure 2.9 shows a superconductor, epoxy module of the sort envisioned by GE. Radial cooling slots will be formed directly into the structure. The winding module is mounted onto the support structure as shown in Fig. 2.7. The superconductor winding in the MIT machine has teflon slip planes wound in between the adjoining layers of superconductor. The winding itself is supported in discrete yoke-like structures which are able to pivot and twist on pins which position the yokes on the inner suport tube [7]. These pivoting yokes, hopefully , will torsionally uncouple the superconductor module from the field winding support structure. The advantage of supporting the superconductor in these yoke-like structures instead of enclosing them within rigid epoxy is the enhanced conductor cooling. Since radial thermosyphon heat transfer coefficients are high, the dominant thermal impedence in the GE design is the epoxy support structure. The disadvantages of the yoked winding comes from the difficult fabrication and

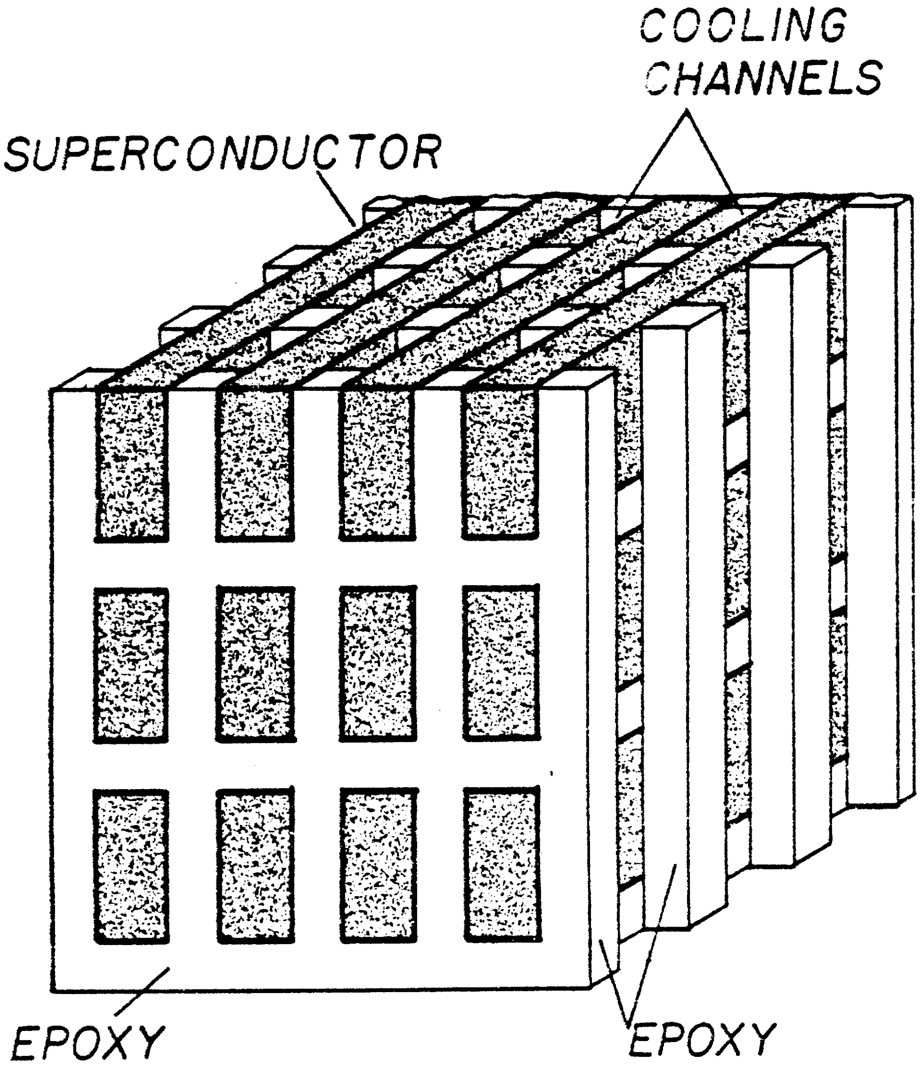

Figure 2.9 Potted superconductor winding with cooling channels.

mounting process and from the fact that there is still conductor relative motion.

In summary, the heat transfer processes occuring in a superconducting generator may be thought of as interacting phenomena at three different size scales :

1. local conductor flow pattern and heat transfer
2. intra rotor circulation system flow
3. supply and vent system behaviour.

At the local scale, the potted superconductor winding with its built in radial cooling channels supports thermosyphon cooling loops. Westinghouse is conducting a lengthy series of tests with helium thermosyphons in simulated conductor cooling slots. Since these channels are small and the helium flow fully developed and most likely turbulent, the orientation of the coriolis vector with respect to the hot walls of the cooling channel determines the heat transfer coefficient. These tests are essentially to examine the effect of coriolis induced secondary flow instabilities on heat transfer in fully developed channel flows. A secondary focus of this research is to determine the time constants for these thermosyphon loops. These small scale thermosyphons are found to have response times in the ms range [8].

The local conductor thermosyphons ultimately communicate thermally with the large helium reservoirs (the bore reservoir in the airborne machine, the three large reservoirs in the MIT rotor). The thermosyphon jets either spill out directly into the large pools or the heat is conducted from a thermosyphon loop into the open pool by copper conduction bars. Heat transfer on this level of rotor cooling falls within the intra-rotor circulation system, or large reservoir cooling system. The work in this thesis is most relevant to this level of the cooling system. The problem addressed in this thesis is that of open-pool convection initiated by an ensemble of small heat sources located at the outermost radii of a rotating reservoir. Convection was studied both during a fluid spin-up and with the fluid in solid-body rotation. It should be noted that the Ekman spin-up time constant for the bore fluid in the GE airborne superconducting rotor is roughly 13s, and the rotor is to be fully operational in roughly 1s. The bulk fluid is clearly not in solid body rotation as the rotor first becomes operational.

The final level of rotor cooling is the supply and vent system. There are considerable problems associated with filling and venting a rotor with helium at high rotation rates and these are being studied at both GE and Westinghouse. Some of the experiments reported in this thesis may be relevant to supply system problems , such as observations of frothing in unbaffled horizontal axis rotors with a large ratio of air to water as well as observations of surface waves in baffled rotors. But it is certainly clear that phenomena associated with the coupling of gravity and centrifugal acceleration in horizontal rotors, previously overlooked, need to be examined further.

II.B. Previous work on rotating convection

The cooling systems of superconducting rotors have been shown to be part thermosyphon, part open pool convection. There is a great deal of previous work and ongoing research in the area of rotating thermosyphons and forced convection flow in rotating channels and tubes [9]. There is even a considerable amount of work in this area where helium was the working fluid [10]. A thesis by Schnapper [11] shows how the radial temperature distribution in a small i.d. rotating cylindrical tube whose axis is perpendicular to the axis of rotation and which connects with a large reservoir of fluid near the centerline can be calculated using an argument based on entropy fluxes. Scurlock and Thornton [12] made heat transfer measurements in a similar geometry. Scurlock's work in particular indicates that free convection in rotating helium filled radial cooling channels at critical and subcritical pressures follow a correlation of the form: $Nu = 0.29Ra^{.29}$. As mentioned previously, there is ongoing research at Westinghouse where measurements are being made of heat transfer coefficients in the narrow radial cooling passages of superconductor field windings. They have found significantly higher heat transfer rates than previously reported, of order $Nu=.03Ra^{.4}$. It can thus be reasonably assumed that even though the exact secondary flow field is not known, there are enough correlations extant to adequately design this portion of the rotor cooling system. A summary of helium data from free convection experiments is also shown in Fig. 2.10. The water data obtained from open-pool convection studies reported in Chapter 6 are also shown on this curve. This is not meant to suggest that this data is relevant to thermosyphons since there is no geometrical similarity between the water filled apparatus and the radial tubes and thermosyphons of these other experiments.

While a great deal of work has been done to determine the heat transfer coefficients in rotating narrow enclosures- there has been very little work in the area of large pool plume behaviour, or even Benard convection at high rotational speeds. Large Rayleigh number natural convection in stationary systems, though, has received a great deal of attention [13], [14]. Work by Hudson [15], Homsy [16] and Abell [17] extends the research done in stationary enclosed systems by measuring the heat transfer rates in similar geometries which are rotating . Fig. 2.11 shows the geometries studied. Notice that the heat input occurs on surfaces which are perpendicular to the axis of rotation and that the density

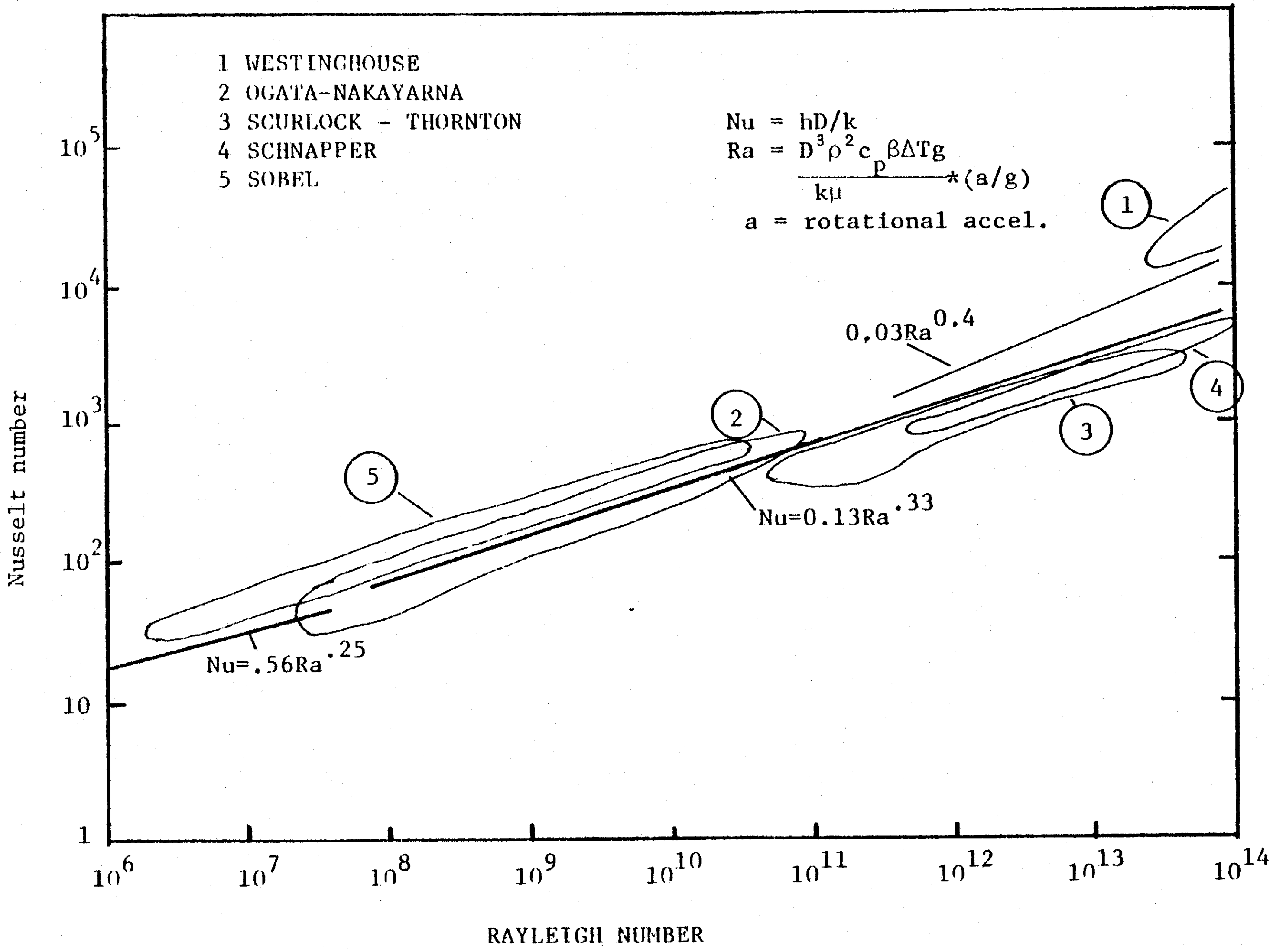

Figure 2.10

FREE CONVECTION DATA IN ROTATING SYSTEMS

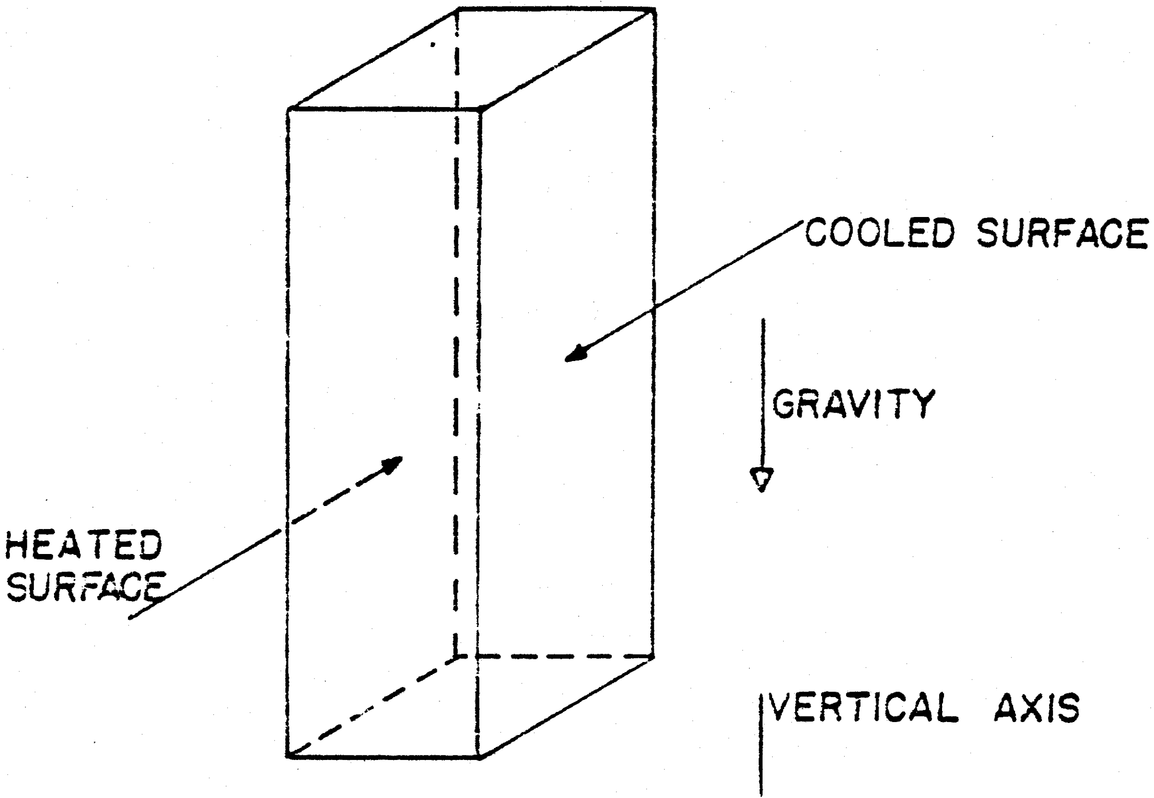

Figure 2.11a Stationary vertical cavity (Gill)

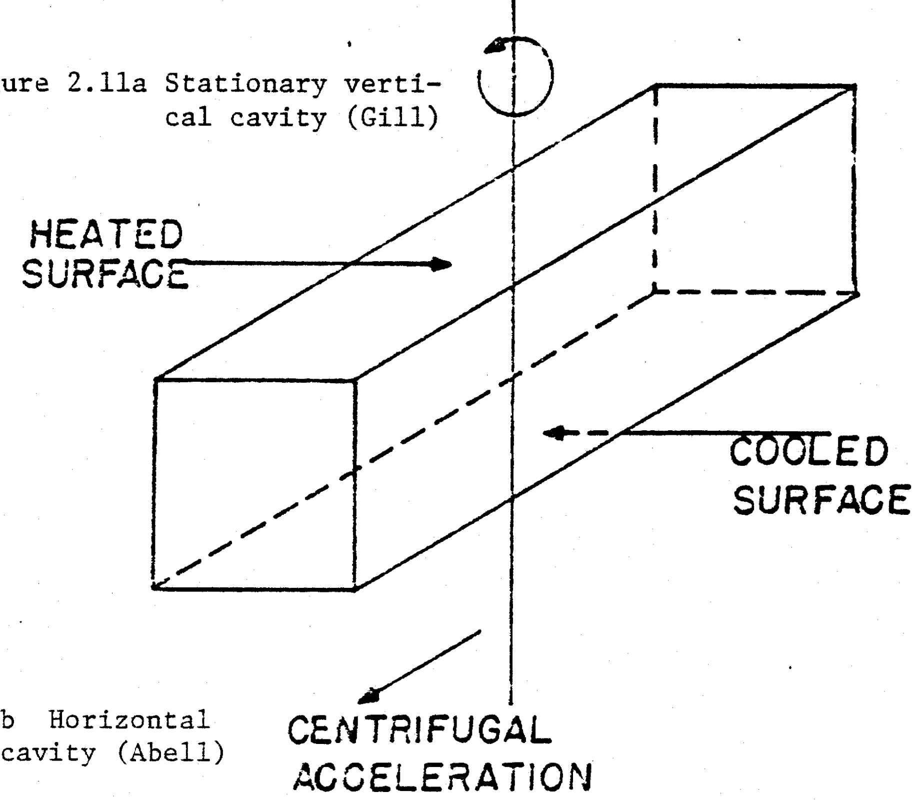

Figure 2.11b Horizontal rotating cavity (Abell)

circulation. When the convection of heat within these enclosures occurs primarily in thin boundary layers on the hot and cold surfaces, the heat transfer coefficient in the rotating enclosure can be related to that in the nonrotating enclosure by substituting the rotational acceleration for gravity in the Rayleigh number. That is not the case, however, if the rectangular enclosure in Figure 2.11b is a circular cylinder with a heated upper plate and a cooled lower plate (the circular cylinder of Fig. 1.1 with no baffles, and the top and bottom plates maintained at different temperatures.) In such a geometry, the heat transfer rate at the same ΔT between the two endplates is actually inhibited. The mechanism for heat transfer in such a geometry is Ekman pumping of hot fluid from a boundary layer on the top plate down to a cold boundary layer on the lower plate. There is, infact, a strong azimuthal motion in the interior fluid regions. This azimuthal flow is in one direction near the top plate, zero at container midheight, and equal in magnitude and opposite in direction at the cold bottom plate. This motion is a thermal wind like flow caused by the coupling of a centrifugal pressure gradient in the radial direction and a density gradient in the z direction. The circulation produced in the regions outside the endplate boundary layers is in the radial direction because of the dominance of the coriolis terms in the inviscid interior. These strong azimuthal flows are blocked in a rotating channel (Fig. 2.11b) and the flow field in the fluid regions outside the boundary layers on the top and bottom endplates resembles that of its stationary counterpart- Fig. 2.11a.

Although the heat transfer studies just mentioned illustrate interesting phenomena unique to rotating systems they are not directly relevant to the experiments reported here. The geometry under consideration (Fig. 1.1) shows that the heater surface is parallel to the axis of rotation and therefore, the density gradient established when the heater is first turned on is parallel to the local acceleration vector and thus cannot generate large scale circulation. The problem is thus related to flow from a small heated horizontal plate facing upwards within an enclosure except for the fact that the rotation of the fluid system completely alters the nature of the radial plume. The closest relevant work in the literature has to do with a study by Gray [18] of heat transfer in rotating boilers. Although Gray concentrated on measuring enhanced boiling heat transfer coefficients and showed no interest in explaining the resulting fluid motion, the author does note with some surprise that the bubbles generated at the outer radius of this boiler tended to move radially inwards to the liquid/vapor interface.

CHAPTER 3

PARTICLE DYNAMICS IN SPINNING SYSTEMS

The dynamics of fast and slow moving buoyant particles in rapidly spinning systems are considered in order to interpret flow visualization experiments with thermals and starting plumes.

III.A Accelerating buoyant particles in spinning systems

The dynamics of small particle motion in rapidly spinning fluids are considered in this chapter and some simple models are developed which demonstrate the dynamical forces unique to spinning systems. The analysis was initially motivated by the presumption that an isolated heat source is a generator of buoyant thermals which will alternately form on the surface of the heater, break away and move inwards towards the centerline. The motion of three dimensional particles (i.e., a small buoyant sphere) in a rotating coordinate system will be considered at two extremes: nearly steady, slow motions, and fast, unsteady or accelerating motions. Slow motions imply that the Rossby number, $U_p/\omega b$, is much less than 1. The Rossby number is the ratio of inertial forces to coriolis forces acting on a particle of characteristic width b and velocity U_p in a system rotating at speed ω. Whether the Rossby number is small or large determines whether a particles' motion is nearly steady or whether the particle deflects tangentially relative to the container in a rotating system. Steadiness in the rotating frame therefore implies that particle inertia is negligible compared to coriolis terms in both the radial and tangential directions. This distinction between steadiness and unsteadiness arises because an assymetry is created when simple motions are superimposed on a rotational flow field which has the effect of creating lift like forces at right angles to the motion. That is to say, if the motion of a particle due to some applied force is slow (Rossby number << 1), the force acting on the particle due to the pressure field in the surrounding fluid as it moves around the particle equals the coriolis acceleration of the particle and there is no imbalance in forces at right angles to the particle motion. The particle velocity thus remains in the direction of the originally applied small force. Indeed, a slowly moving three dimensional particle will actually generate a two-dimensional flow in a rotating container. This phenomena is known as a Taylor column. An even more unusual result will also be derived that the trajectory of a two-dimensional object such as a cylinder whose height extends the full height of the container is not affected at all by the rotation of the system, regardless of its' Rossby number. At the other extreme of particle motion, however, the trajectories of fast moving particles (Rossby number >> 1) are very much affected by the rotation of the system. This is because the pressure field in the surrounding fluid cannot balance both the coriolis and inertia forces acting on the particle and the particle accelerates in the tangential direction. Although the fast motion of a particle also creates a pressure field in the surrounding rotational fluid, that pressure field is ignored in the present analysis. The model instead allows for drag forces to act on the particle as the particle accelerates relative to the fluid around it. When the drag acting on the particle is large enough the motion becomes steady (friction forces rather than pressure forces balance the coriolis forces) and in this sense, adding drag connects the analysis to the inviscid, low Rossby number motions mentioned previously. Both the analyses presented are relevant to observable phenomena in spinning systems. The starting plumes (buoyant thermals with a plume as a wake) behave very much like slow moving solid particles. When enough heat is pumped into the rotating fluid over a small enough area, the plume behaviour falls somewhat between the two extremes of particle motions to be described.

As is often the case in this thesis, the analysis presented draws from and elaborates on the work of G.I. Taylor [19,20]. G.I. Taylor found that an inviscid steamtube of light fluid (essentially a three-dimensional steady plume of fluid whose crossection varies slowly) that is released from rest at the outer radius of a rotating cylinder will have a streamline identical to that of a buoyant particle released from rest. Such a streamtube might originate as an outlet jet of warm fluid issuing into a large reservoir, or as a thermal generated by a very small heat source (so long, as the pictures in Chapter 4 will show, as the heat flux is sufficiently great). However, it should be made clear that the analogy between streamtubes and buoyant particles is mathematical and not literal. (It is much simpler to analyze buoyant particles than it is to analyze buoyant plumes). A buoyant thermal would neccessarily push ambient fluid out of its' way along a given trajectory and the accelerating ambient fluid would generate lift forces. (In stationary systems an added mass is considered in the dynamics of the buoyant thermal and accounts for an apparent drag associated with accelerating ambient fluid). Since a streamtube by definition has no normal velocity there is no additional external pressure distribution set up in the surrounding fluid. The only constraint on the analysis of a streamtube (which may also be entraining fluid) is that the pressure must be continuous at the boundary between the two fluids.

Consider then a spherical blob or particle of fluid (a thermal) of some initial particle radius b, and initial density $\alpha\rho_a$ where ρ_a is the density of the ambient fluid. When released from rest at the outer wall the particle will be drawn inwards because of its density deficiency. In the absence of drag forces or any pressure distribution in the surrounding liquid creating a net force at right angles to the particle motion the particle will conserve its original angular momentum and acquire some azimuthal velocity relative to the fluid. The increase in azimuthal velocity tends to throw the particle back outwards. The radial and azimuthal velocities are thus coupled together and the overall motion of the particle as seen from the rotating frame is elliptical. A trajectory for this inviscid particle motion is shown in Fig. 3.1. It is important to note that the buoyant particle never reaches the centerline. In fact, the particle never gets any closer to the centerline than $\sqrt{\alpha}$ times the initial radius. This important result can be derived by considering the energy of the buoyant particle under certain constraints. When the particle is released from rest (relative to the walls of the container) it is acted on by a central force equal to $\rho(\omega^2 r)$ (not $(1-\alpha)\rho(\omega^2 r)$) and possesses the following energies per unit mass in the rotating coordinate system relative to a zero energy state at the centerline of the rotating system.:

$$KE = \alpha\omega^2 a^2/2 \tag{3.a.1}$$

$$PE = \omega^2 a^2/2 \tag{3.a.2}$$

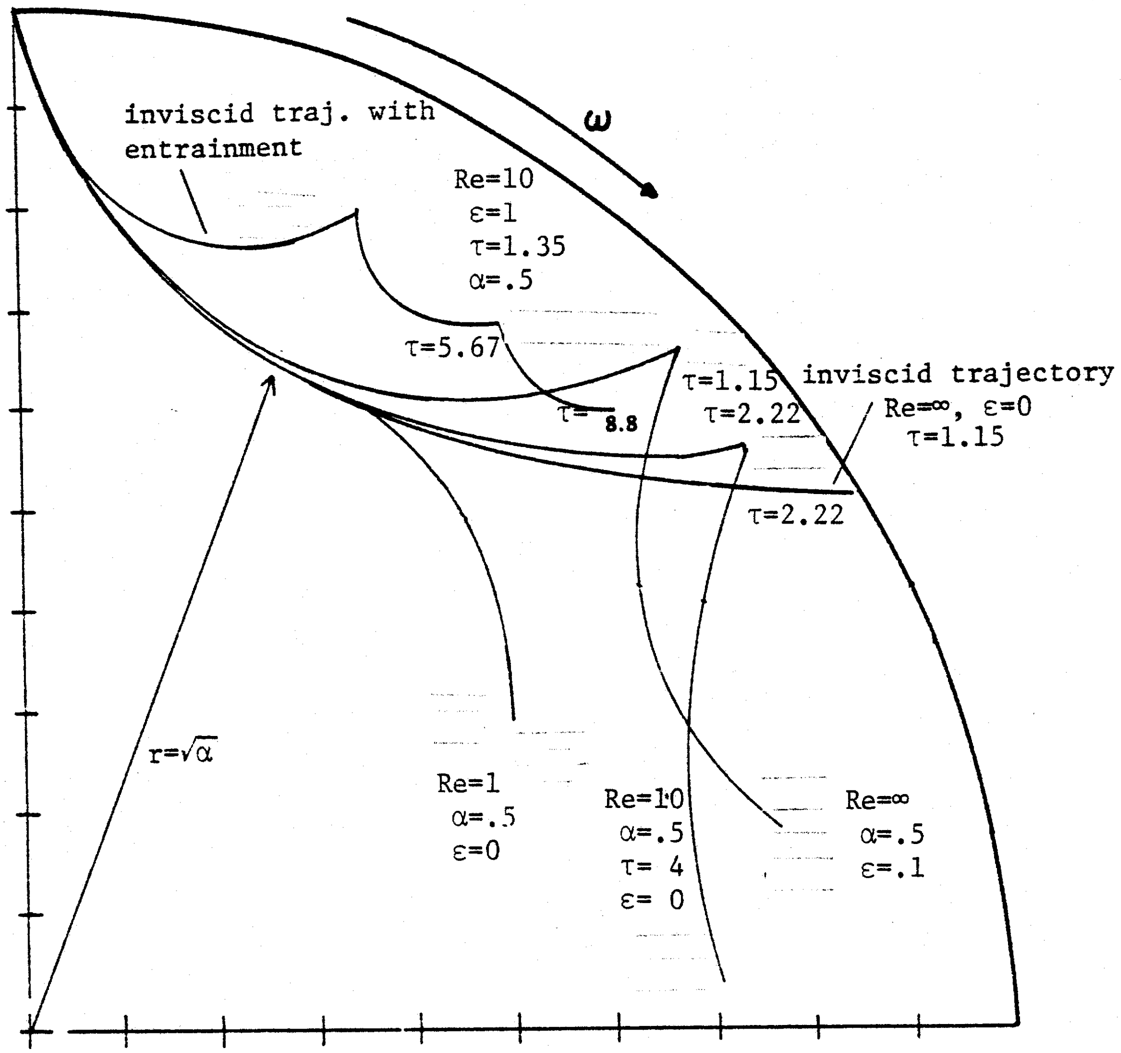

Figure 3.1 Trajectories of bouyant particles in rapidly spinning containers.

where a is the radius from the axis of rotation to the initial location of the particle. The energies shown above are obtained by calculating the total work required to place a particle of density fraction α at a radius a with a tangential velocity constrained to be always equal to ωr within a gravitational field of magnitude $\omega^2 r$. (The pressure field is established by the ambient fluid which is in solid body rotation. Changes in the moment of inertia of the ambient fluid surrounding the particle as the particle moves about are not considered here since the mass of the particle is a negligible fraction of the total mass of the system. The only coupling between the ambient fluid and the buoyant particle is the radially directed pressure gradient $\omega^2 r$ acting through the centroid of this particle. It is as if the particle is in a vacuum, acted upon by a body force proportional to r.) The work is composed of two parts: the integral of the torque required to change the angular momentum of the particle, $\alpha\omega^2 a^2$, and the integral of the net radial force required to displace the particle each increment in radius out to the outer radius a. The latter force is $(1-\alpha)\omega^2 r$ since the particle is assumed to be constrained to have velocity ωr at each radius and the integral is $(1-\alpha)\omega^2 a^2/2$. The total energy of the particle at radius a is thus $(1+\alpha)\omega^2 a^2/2$. Since the kinetic energy of the particle at this radius is obviously $\alpha\omega^2 a^2/2$, the PE of the particle is the remainder: $\omega^2 a^2/2$. (The potential energy of a particle with density α is thus the integral of the external pressure force $\omega^2 r$ established by the constant rotation of the ambient fluid from $r_1=0$ to a, independent of the path of the particle). As the particle accelerates away from the outer radius, some of its potential energy is converted into kinetic energy since the particle now has relative velocity in both the radial and tangential directions. At the minimum radius (r_m) of the particle's trajectory, however, the velocity in the radial direction is zero and the azimuthal velocity is obtained from conservation of angular momentum assuming that there are no forces acting on the particle in the θ direction, namely

$$v_p r_m = \omega(a^2-r_m^2) \quad . \tag{3.a.3}$$

The energies/unit mass at this new radius are equal to

$$KE = \frac{\alpha(v+\omega r_m)2}{2r_m^2} = \frac{\alpha(\omega a^2)^2}{2r_m^2} \tag{3.a.4}$$

$$PE = \omega^2 r_m^2/2 \quad . \tag{3.a.5}$$

Equating energies at r_m and at r=a yields:

$$r_m/a = \sqrt{\alpha} \tag{3.a.6}$$

which is the result mentioned previously.

Now consider a buoyant thermal which entrains fluid at a rate proportional to the instantaneous speed of the thermal q. This is the assumption most often seen in analyses of turbulent plumes and jets (Turner [21]). If a thermal has radius b, and volume $(4/3)\pi b^3$, then

$$\frac{d(4/3\pi b^3)}{dt} = \varepsilon q 4\pi b^2 \tag{3.a.7}$$

or the rate of change of particle volume is equal to the inflow velocity times the surface area of the thermal. The inflow velocity is some empirical constant ε times the velocity of the thermal. Eq. 3.a.7 can be further simplified to:

$$\frac{db}{dt} = \varepsilon q \quad . \tag{3.a.8}$$

Since q=ds/dt where s is the distance traveled by the thermal, the entrainment assumption can be integrated to give

$$b = b_1 + \varepsilon s \tag{3.a.9}$$

$$b/b_1 = 1+\varepsilon s/b_1 \quad . \tag{3.a.10}$$

When the particle has traveled a distance b_1/ε the radius has doubled and the volume has increased by a factor of 8.

As a consequence of the entrainment of colder fluid the density of the thermal increases and its buoyancy decreases. To relate the buoyancy of the thermal to its radius the energy equation is used to calculate the average temperature of the thermal. The energy of the thermal at any point along its trajectory is $\rho(c_pT({}^4/{}_3)\pi b^3)$, where all properties are calculated at the mean temperature and the intensive energy is presumed equal to c_pT. The rate of change of energy is equal to the flux of energy into the thermal by entrainment, namely:

$$\frac{d(\rho c_p T4/3\pi b^3)}{dt} = \rho_a c_p T_a \frac{d(4/3\pi b^3)}{dt} \quad . \tag{3.a.11}$$

The density is related to temperature through the Boussinesq approximation:

$$\rho = \rho_a + (\partial\rho/\partial T)(T-T_a) \tag{3.a.12}$$

$$\alpha = \rho/\rho_a = 1-\beta\Delta T \quad . \tag{3.a.13}$$

Since $d({}^4/{}_3\pi b^3)/dt$ is the inflow velocity into the thermal per unit surface area of the thermal (Eq. 3.a.7), combining Eqs. 3.a.8, 3.a.11, and 3.a.13 gives the following integrable relation:

$$\frac{d(1-\alpha)}{dt} = -(1-\alpha)3\frac{d(\ln(b))}{dt} \tag{3.a.15}$$

or $\alpha=1-(1-\alpha_0)/b^3$, where b is normalized to be equal to 1 when $\alpha=\alpha_0$. Equation 3.a.15 now relates the instantaneous density to instantaneous thermal radius ratio b.

The actual equations of motion in a rotating coordinate system can now be derived. The sum of the forces equals the change in the particle's momentum:

$$\Sigma F = \frac{d(mU_p)}{dt} \qquad (3.a.16)$$

where m is the instantaneous mass of the particle which changes as the particle entrains fluid and U_p is the particle vector velocity. Since the pressure gradient in the fluid is assumed to be purely radial the motion of the particle is best described in cylindrical coordinates in a rotating reference frame. The full equations of motion in the radial and azimuthal directions for a particle of density fraction α are:

$$\left(\frac{d(u_p)}{dt} - \frac{v_p^2}{r} - 2\omega v_p - \omega^2 r\right) = -\frac{\omega^2 r}{\alpha} - u_p\frac{3\varepsilon q}{\alpha b} - \frac{9\mu u_p}{2(\rho_a b^2 \alpha)} \qquad (3.a.17)$$

$$\left(\frac{d(v_p)}{dt} + \frac{u_p v_p}{r} + 2\omega u_p\right) = -v_p\frac{3\varepsilon q}{\alpha b} - \frac{9\mu v_p}{2(\rho_a b^2 \alpha)} \; . \qquad (3.a.18)$$

The last terms in Eqs. 3.a.17 and 3.a.18 represent the drag force on a particle of radius b in a fluid of viscosity μ (Stokes drag). The velocity q, where it appears in Eqs. 3.a.18 and 3.a.17 is the scalar sum of u_p and v_p, $(\sqrt{(u_p^2+v_p^2)})$. The terms on the right of equations 3.a.17,18 proportional to ε follow from the change in mass of the particle due to entrainment. Using Eq. 3.a.7, dm/dt is calculated to first order by the following relationship:

$$\frac{d(m)}{dt} = \rho_a 4\pi b^2 \varepsilon q \qquad (3.a.19)$$

where q is the scalar velocity $\sqrt{U_p^2}$. The first term on the right hand side of Eq. 3.a.17 is the centrifugal pressure gradient in a fluid of density ρ_a due to solid body rotation, divided by the particle's density. Eqs. 3.a.17 and 3.a.18 are then nondimensionalized as follows:

$$\begin{aligned}
&t=\omega t \qquad (3.a.20)\\
&q=q/\omega a\\
&u=u/\omega a\\
&v=v/\omega a\\
&b=b/b_1\\
&\alpha=\rho/\rho_a\\
&r=r/a\\
&Re=(2\rho_a\omega b_1^2)/(9\mu)
\end{aligned}$$

$$\frac{d(u_p)}{dt} = \frac{v_p^2}{r} + 2v_p - u_p\frac{3\varepsilon q}{\alpha b} + \frac{(\alpha-1)r}{\alpha} - u_p/(Re\alpha b^2) \qquad (3.a.21)$$

$$\frac{d(v_p)}{dt} = -\frac{v_p u_p}{r} - 2u_p - \frac{v_p}{\alpha}\frac{3\varepsilon q}{b} - v_p/(Re\alpha b^2). \qquad (3.a22)$$

The set of equations above were integrated numerically for various combinations of Reynolds number and ε, and $\alpha_0=0.5$. The results are shown plotted in Figures 3.1 and 3.2 Some the more important conclusions from the numerical integration are as follows. In the inviscid case with no entrainment, as has already been mentioned, the minimum radius of the particle trajectory is proportional to $\sqrt{\alpha}$. This result suggests that radial baffles need to be placed at the outlet ports of thermosyphons to direct a warm jet inwards and prevent warm fluid from mixing with cold fluid at the thermosyphon inlet. If the particle entrains fluid the original trajectory has a minimum of roughly the same value ($\sqrt{\alpha}$) but unlike the non-entraining particle, the entraining particle eventually

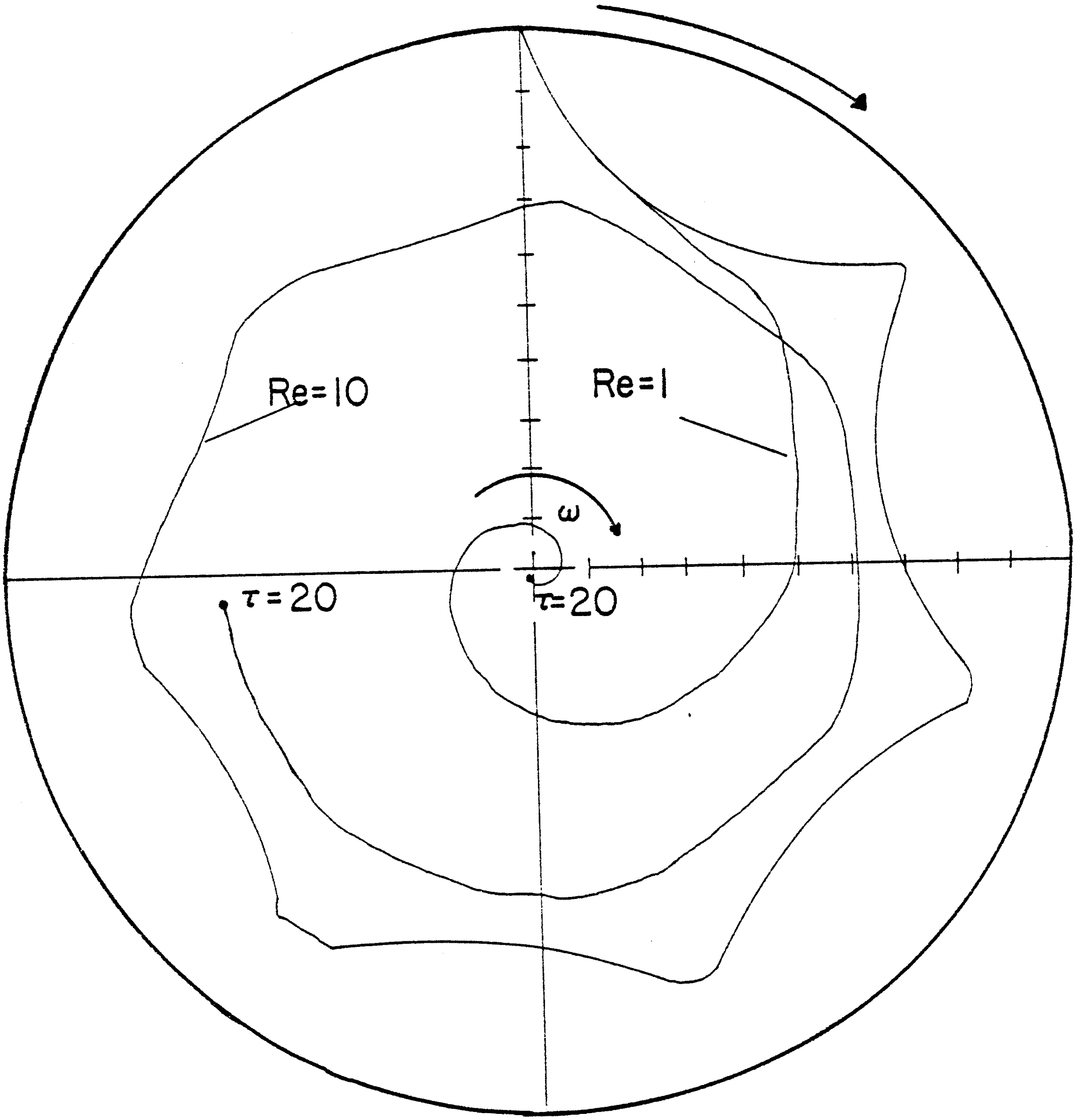

Figure 3.2 Trajectories of bouyant particles with drag.

comes to rest at a smaller radius. The reason for the nearly similar trajectory is that while entrainment increases the average density of the thermal it does not dissipate any kinetic energy and the particle conserves its' angular momentum. The trajectory is shallower though because at every increment of distance traveled by the thermal its bouyancy is less than that of its' non-entraining counterpart. Because the net force acting on the thermal is less, one would not expect this thermal to move inwards quite as far.

If there is drag on the particle and no entrainment, the particle will always find its way to the center. When the Reynolds number (based on particle diameter b_1) is sufficiently small (of order 10 or less) and for dimensionless times t greater than 1 the particle no longer accelerates and the equations of motion become:

$$(\alpha-1)r/\alpha - u/(\alpha Re) + 2v = 0 \qquad (3.a.25)$$

$$v = -2Re\alpha u \quad . \qquad (3.a.26)$$

Equations 3.a.25 and 3.a.26 can be integrated to give:

$$r = e^{(t/\tau)} \text{ where } \tau=((\alpha-1)/(4\alpha^2 Re))^{-1} \qquad (3.a.27)$$

$$v = ((\alpha-1)/(4\alpha))e^{(t/\tau)} \quad . \qquad (3.a.28)$$

The solution describes a spiral trajectory which slowly approaches the centerline. The trajectories for two different small Reynolds numbers are shown in Fig. 3.2.

The nondimensional times listed in Figures 3.1 and 3.2 can be related to revolutions of the containment vessel by dividing by 2π. For Re=10, the last data point shown occurs in 3.18 revolutions of the apparatus, which is quite fast. It takes roughly 100 revolutions of the container before the particle can be said to have effectively reached the centerline.

In summary, then, particle motions in the absence of fluid lift forces are fast- even with considerable drag and entrainment. More importantly, the inviscid trajectories are shown to become shallower as the initial density ratio decreases (α goes to 1). One might expect to find that a plume with a small bouyancy would hug the outer wall. This turns out to be exactly the opposite of what occurs. As the initial bouyancy in the thermal decreases, the character of the flow changes dramatically. This change in character is the result of the neglected lift forces. The neglected pressure distribution at right angles to any motion of a solid can be easily calculated if the moving object is circular and two-dimensional although the result is independent of the two-dimensional shape. This will be done next. The results are not also applicable to the motion of a three-dimensional object, however, unless the motion is slow and steady (Rossby number << 1).

III.B. Slow, steady motions in a rotational fluid

The two most striking observable characteristics of slow plumes in a rotating container are the radial trajectory and the two-dimensionality of the flow. To understand this phenomena it must first be understood how a two-dimensional object (i.e., a cylinder with the same axial length as the container) sets up a pressure distribution in a streaming flow. The analysis will also show that when a solid object of infinite height (the cylinder just mentioned, although the object could be of any shape) is moved about in a rotating fluid of the same density as the object itself and in a direction perpendicular to the axis of rotation, a pressure field is created by the streaming flow which identically balances the coriolis acceleration of the solid cylinder. The resulting motion is thus unaffected by the rotation of the system as a whole and in contrast to the trajectory of a buoyant particle in the previous section the object moves only in the direction of an applied force.

Consider an infinitely long solid cylinder of the same density as the fluid moving with speed U_p relative to the fluid which is in solid body rotation (Fig. 3.3). This motion is resolved into components in the local coordinate system centered at the origin of the cylinder as follows:

$$U_p = -U_p(\cos\alpha)e_\theta + U_p(\sin\alpha)e_r \qquad (3.b.1)$$

where e_r is aligned with a radial line from the center of the spinning container and α is the angle of cylinder motion as shown in Figure 3.3 relative to the local r,θ coordinates. The fluid is incompressible and flow is two dimensional and a stream function exists whose derivatives are everywhere related to the fluid relative velocity . The normal velocity is constrained at the surface of the cylinder to be equal to:

$$\frac{-\partial\psi}{c\partial\beta} = U_p\sin\alpha\cos\beta - U_p\cos\alpha\sin\beta \qquad (3.b.2)$$

where ψ is the inviscid stream function and $cd\beta$ is an arc length along the cylinder. The equations of motion of the fluid in the rotating coordinate system is:

$$\frac{d(q)}{dt} - \omega^2 re_r - 2\omega ve_r + 2\omega ue_\theta = \frac{-\nabla p}{\rho} \qquad (3.b.3)$$

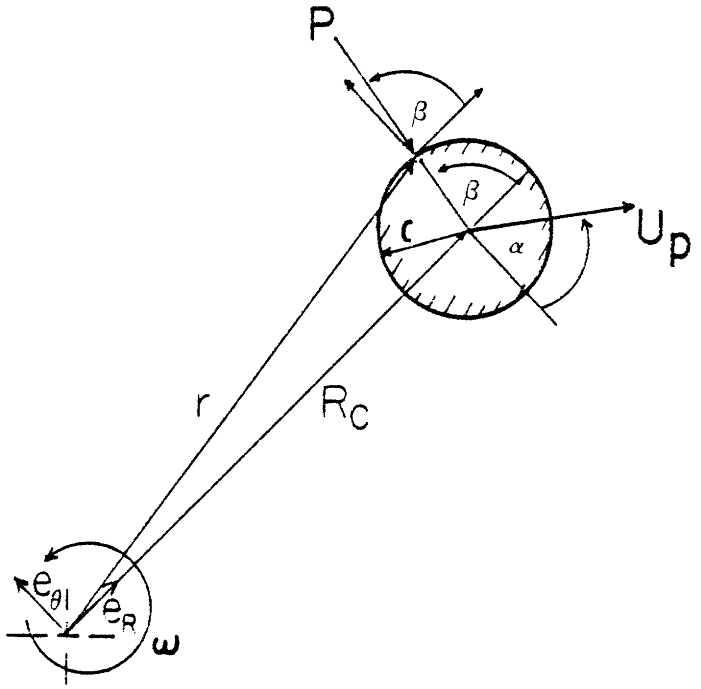

Figure 3.3 Motion in an unbounded rotational fluid

$$u = \frac{-\partial\psi}{r\partial\theta} \qquad (3.b.4)$$

$$v = \frac{\partial\psi}{\partial r} \qquad (3.b.5)$$

such that

$$\frac{d(q)}{dt} = -(1/\rho)\nabla(P-2\omega\psi-\omega^2r^2/2). \qquad (3.b.6)$$

At this this point it is convenient to divide the pressure term into two components. Let $P=P_1+P_2$ where:

$$-\nabla(P_1)/\rho = d(q)/dt \qquad (3.b.7)$$

$$-\nabla(P_2)/\rho = -(2\omega\psi+\omega^2r^2/2), \qquad (3.b.8)$$

$$\nabla P_2/\rho = 2\omega\psi+\omega^2r^2/2 + C.$$

Looking at Eqs. 3.b.7,8 it is evident that P_2 is that part of the pressure distribution that results from the rotation of the system as a whole, but P_1 is not a function of rotation. These last two equations can then be integrated around the perimeter of the cylinder to calculate the forces acting on the cylinder as it pushes ambient fluid out of the way. The net forces in the r and θ directions due to P_2 are:

$$F_r = -\int P_2\cos\beta c d\beta = \int \rho(-2\omega\psi\cos\beta-(\omega^2r^2/2)\cos\beta)cd\beta) \qquad (3.b.9)$$

$$F_\theta = -\int P_2\sin\beta c d\beta = \int \rho(-2\omega\psi\sin\beta-(\omega^2r^2/2)\sin\beta)cd\beta) \qquad (3.b.10)$$

where it should be noted that c is the radius of the cylinder and the countour of integration is the boundary of the cylinder. The distance of any point on the perimeter of the cylinder to the center of rotation is related to the radius of the cylinder and β in the local coordinate system by the relationship:

$$r^2 = R_c^{\,2} + c^2 + 2R_c c(\cos\beta) \tag{3.b.11}$$

where R_c is the distance to the center of the cylinder from the origin. Using Eq. 3.b.11, the contributions of the centrifugal acceleration term $(\omega^2 r^2)/2$ in the r,θ directions in Eqs. 3.b.9,10 (called F_{r1}, $F_{\theta 1}$), are found by integrating around the countour $cd\beta$:

$$F_{r1} = -\rho\omega^2 R_c \pi c^2 \tag{3.b.12}$$

$$F_{\theta 1} = 0. \tag{3.b.13}$$

The former equation represents a force directed radially inwards of magnitude $m\omega^2 R_c$ where m is the mass/unit length of fluid displaced by the cylinder.

The integration of ψ around the countour in Eqs. 3.b.9 and 3.b.10, however, can not be done directly because ψ has not been determined. Since the derivative of ψ along the cylinder countour is known (it is the velocity of cylinder normal to the boundary of the cylinder) it is possible to integrate by parts. A differential length on the contour ds is just $cd\beta$ and working with Eq. 3.b.9 first, since $\cos\beta d\beta = d(\sin\beta)$ the first term in this equation integrates to:

$$-\int \rho 2\omega\psi\cos\beta c d\beta = -\rho 2c\omega\psi\sin\beta \Big|_0^{2\pi} + \rho 2\omega c^2 \int_0^{2\pi} \sin\beta(\partial\psi/\partial\beta)d\beta. \tag{3.b.14}$$

The first term on the right of Eq. 3.b.14 is zero and a substitution of Eq. 3.b.2 into the second term results in the following integral:

$$\rho 2\omega c^2\int_0^{2\pi}\sin\beta(\partial\psi/\partial\beta)d\beta = (\rho 2\omega U_p c^2)\int_0^{2\pi}\sin\beta(-\sin\alpha\cos\beta+\cos\alpha\sin\beta)d\beta \tag{3.b.15}$$

of which only the second term matters. Thus it is found that the lift force in the radial direction is:

$$F_{r2} = \rho 2\omega\pi c^2 U_p\cos\alpha. \tag{3.b.16}$$

Similarly, the stream function term in Equation 3.b.10 can be integrated by parts to give the lift force in the tangential direction:

$$F_{\theta 2} = \rho 2\omega\pi c^2 U_p\sin\alpha. \tag{3.b.17}$$

Taken together, Equations 3.b.16 and 17 represent a force directed at right angles to the motion of the cylinder and proportional to $2m\omega U_p$, where m is again the mass/unit length of the displaced fluid. If ω is counterclockwise, this force opposes a motion of the cylinder to its' right. Eqs. 3.a.12 and 3.a.13, on the other hand, represent a centrifugal force of magnitude $m\omega^2 R_c$ acting at the center of the cylinder and pointing towards the center of rotation.

The significance of these results become apparent when the equations of motion for the cylinder itself are written out. Referring to Fig. 3.3, if the cylinder has a relative motion velocity $v_p=-U_p\cos\alpha$ and $u_p=U_p\sin\alpha$ in the radial and azimuthal directions respectively, it can be shown that the inertial acceleration of the particle is:

$$\frac{dmU_p}{dt} = \Big[\Big(\frac{du_p}{dt} - 2\omega v_p - \frac{v_p^2}{R_c} + \omega^2 R_c\Big) e_r + \Big(\frac{dv_p}{dt} + \frac{u_p v_p}{R_c} + 2\omega u_p\Big) e_\theta\Big] \rho \pi c^2 \; . \qquad (3.b.18)$$

Comparing Eqs. 3.b.18 and Eqs. 3.b.17 and 16, it is apparent that the force distribution caused by the motion of the fluid around the cylinder is exactly equal to those inertial terms proportional to the rotation rate ($2\omega U_p$, $\omega^2 R_c$), provided that the mass of displaced fluid and the mass of the cylinder per unit length are equal. The conclusion is that a neutrally buoyant cylinder moves in response to a centrally applied force in a rotating system exactly as it would if the same force were applied in a fluid system that was not rotating at all.

The previous result can also be used to explain the Taylor–Proudman theorum. If the infinite cylinder of the previous analysis is replaced by a sphere which is slightly buoyant and released from rest at some radius then initially, at least, $U_p/\omega b \ll 1$. An order of magnitude analysis of the pressure forces P_1 and P_2 in Eqs. 3.b.7 and 3.b.8 shows that $P_1 \ll P_2$ (the inertial terms/coriolis terms $\ll 1$). If one now takes the curl of the dominant terms in Eq. 3.b.3 and recognizing that the curl of the pressure term is zero in an incompressible fluid, the result is the following:

$$2\omega \nabla x(-ve_r + ue_\theta) = 0 \qquad (3.b.19)$$

such that;

$$\frac{\partial v}{\partial z} = \frac{\partial u}{\partial z} = 0 \qquad (3.b.20)$$

and

$$\partial w/\partial z = 0 \text{ by continuity.} \qquad (3.b.21)$$

Eqs. 3.b.20 and 21 together require that the solution to the flow around this sphere must be a fluid motion that cannot change in the z direction . Now a sphere, unlike a cylinder, has a surface normal with a component in the z direction. In order to satisfy the Taylor-Proudman constraint (Eqs. 3.b.21,20) two distinct flow regions will form in response to the motion of the sphere which will keep the fluid above and below the sphere distinct from the rest of the fluid. As the sphere moves it will appear as if a cylinder of fluid were moving with it. The motion imparted to the fluid by the buoyant sphere will be the same as the flow generated by a slightly buoyant solid cylinder of infinite extent. However, as soon as the spherical particle begins to accelerate the fluid motion is no longer constrained to be two dimensional, the pressure forces cannot balance the inertial forces acting on the fluid in the Taylor column and the column of fluid moving with the sphere will be left behind. In fact, the sphere itself will begin to accelerate at right angles to the applied force with a trajectory as shown in the previous section because the lift forces corresponding to a three dimensional flow are not the same as those previously calculated for the cylinder.

It is now possible to see how rotating fluid can be thought of as possessing stiffness in the axial direction. Just as gyroscopes resist overturning so to does any given filament of fluid in solid body rotation resist bending and lengthening up to a point. When the fluid is pushed out of the way by a three-dimensional object moving at a slow, steady rate, no fluid will move over or under the object, the filaments of fluid will stay straight and move around instead.

Consider also the sequence of events which occur when heat is generated on the surface of a small heater on the outer wall of a spinning container. For small time, heat is being pumped into the fluid near the wall and some amount of buoyant and non-moving fluid is collecting. When enough bouyancy has accumulated the thermal begins to move off the surface, moving slowly at first because it takes time for the thermal to accelerate. If the background vorticity is large enough, that is, if the dimensions of the thermal are sufficiently large so that the Rossby number based on thermal width and velocity is small, a Taylor column is set up around the thermal by inviscid pressure waves. When the thermal does break away, a column of fluid extending to the endplates is dragged along.

It is interesting to note in light of the previous discussion, that once a buoyant thermal begins to accelerate it will acquire a velocity not in the direction of rotation but in the opposite direction. The fluid forces acting on the thermal are of the order of the ambient density times the coriolis acceleration. The coriolis acceleration of the buoyant fluid however is some fraction of this since the density is lower. The streaming flow of ambient fluid would cause the thermal to accelerate to its' left if the rotation was counterclockwise. This effect has not been observed. This is probably because the buoyancy defficiency within the thermal is too small to have any effect, in fact, the bouyancy defficiency must be based on the average density of the whole Taylor column. But when the heat flux was increased a hundredfold and the dimensions of the heater reduced, the curved trajectory that resulted was still in the direction of rotation. Furthermore, the flow was still two-dimensional. Since it is clear that an imbalance in forces in the tangential direction exists (otherwise the trajectory would be radial) and since the fluid in the Taylor column is on average lighter than the surrounding fluid- it is felt that the trajectory is the result of an assymetry in the flow field around the head of the thermal. (Assymetrical wakes have been observed in the lee of towed Taylor columns [1,22] as the Reynolds number of towing was increased). What is even more interesting about these curved plume trajectories is that they were still two-dimensional. This suggests that there is an intermediate regime where a kind of unsteady Taylor-Proudman theory is applicable.

CHAPTER 4

FLOW VISUALIZATION EXPERIMENTS

Natural convection from small heat sources in rapidly spinning systems is shown to be slow and two-dimensional. Experiments with mica flakes and dye demonstrate that bouyant plumes are a thermal analogue to a Taylor column.

IV.A Background on flow visualization experiments

The instrumented rotating test bed described briefly in the first chapter was designed for flow visualization experiments as well. The technique used to make either a spin-up flow field or a convection flow field visible was to seed the water filled container with small, shiny flat particles. These mica flakes are coated with titanium oxide and are manufactured by a cosmetics firm for use in eye shadow. The tiny flat particles (4μ in diameter) tend to align with strong shearing flows. If the motion of a rapidly spinning container is frozen with a single strobe or several strobes synchronized together, particle alignment makes strong fluid motions visible. In regions where the particles are randomly oriented they reflect a large amount of incident light. Where the particles are aligned because of a locally strong shear flow, they will not reflect much light. A picture of a particle seeded container reveals contrasting regions of light and shadow which can then be interpreted as a qualified view of a given flow field. The word qualified is used because such a picture, especially when looking into a rotating container from above , is only an image of what is happening in the vicinity of the endplate. It turned out, infact, that the results of particle visualizations were so unusual that a second flow visualization experiment was designed and experiments were done with dye as well.

The first succesful natural convection flow visualization experiments were performed in the container of Fig. 1.5 with a long thin heater taped to the outer lexan window. The heater was meant to be a vertical line source generating a thin plume extending fully from one endplate to the other (see Fig. 5.9). With the container rotating at the relatively low speed of 300 rpm (to increase the centrifugal settling time of the particles) and the heater energized, a slow radial thermal was visible ambling inwards. The observation was made looking down into the end plate from atop the turntable. The result was surprising for several reasons. As described in the previous chapter, it was assumed (based upon work of G.I. Taylor) that a streamtube of warm fluid would tend to accelerate relative to the walls of the container producing a curved trajectory. Furthermore, the time scale for bouyant particle motions in an inviscid fluid was shown to be of order of the tip speed rather than the few cm/s observed. The radial trajectory and the slow plume speed led inexorably to the notion that this two-dimensional starting plume might be a thermal equivalent of the famous experiment by G.I. Taylor [1] where a long, cylindrical column was towed radially inwards by a string. Thus a new flow visualization test was performed with a smaller heater having the same width (in the azimuthal direction) as the original heater but having a length 1/5 as great (in the direction parallel to the axis of rotation). The heater was taped at midheight on the outer lexan window. The trajectory for the plume coming off the small heater was once again radial and slow. It should not go unmentioned, once again, that it was surprising to find that any flow was visible at all. The observer is looking down into the container and only the motion near to the surface is visible. Fluid could easily be moving underneath a layer of non-moving fluid and this would go undetected. The notion that a bouyant thermal generated at container midheight could be dragging along a column of fluid that extended to the top endplate was, again, difficult to believe.

At this point it was decided that a new experiment was required to verify the presumed nature of the flow field observed. Although it appeared that the plume motion was two dimensional it was not possible to say for sure that a different flow didn't exist further down in the container. Furthermore, because the experiments had been performed in a container with radial side walls which could support an azimuthal pressure gradient, it was not known what role container shape played in determining the trajectory of the plume.

IV.B Flow visualization experiments

To resolve these questions as well as to provide a more amenable environment for picture taking, the experimental container shown in Fig. 4.1 was built. Shown here is a plexiglas cylinder with 3 in. radius and 6 in. axial length with an endplate that has a removable baffle. A small heater can be seen taped to the container side wall at roughly midheight. The container was filled with mica flakes and water and chucked up in a lathe. The lathe had a disk clutch that easily allowed for impulsive container accelerations to 531 rpm. A strobe, pulsed by a photoelectric pickoff shown in Fig. 4.4 froze the motion of the spinning container so that observation of particle orientation could be made. Power to the

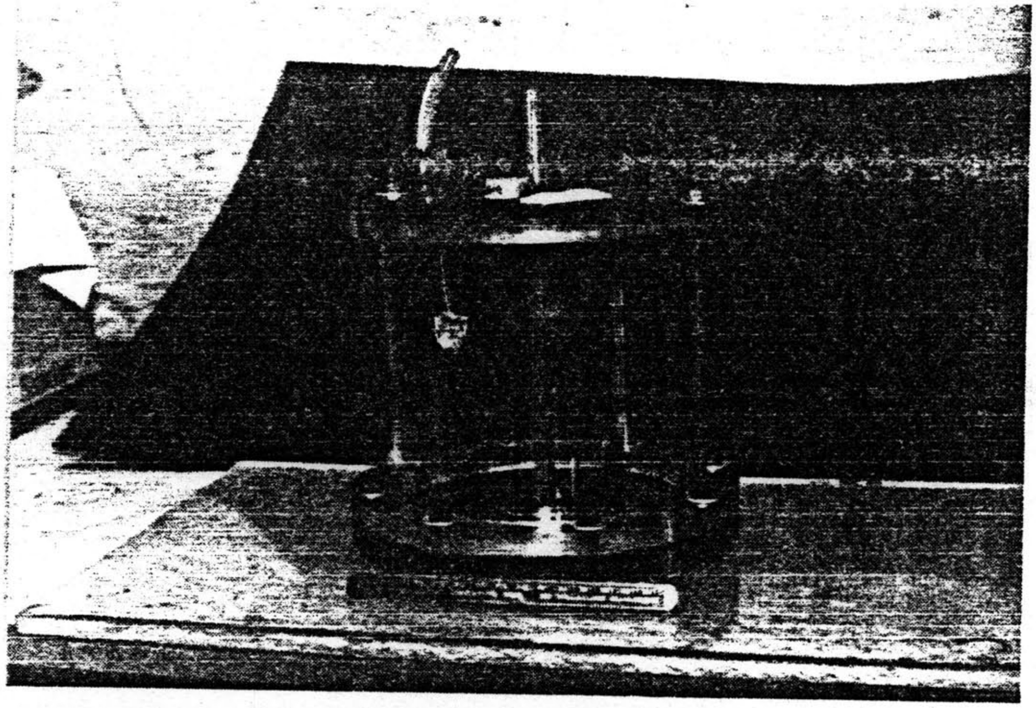

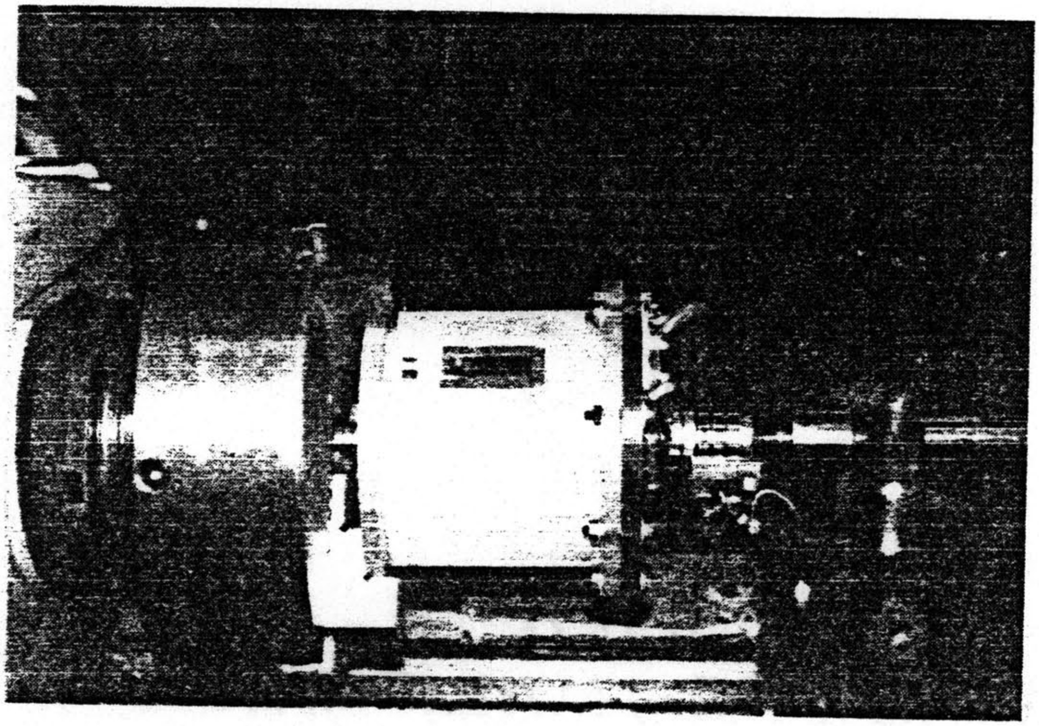

Figure 4.1 (above) Plexiglas cylinder for horizontal lathe flow visualization studies. Cylinder radius is 3", axial length is 6".

Figure 4.2 (below) Cylinder chucked up in lathe. Power to heater is supplied through slip-rings mounted on the front plate of cylinder.

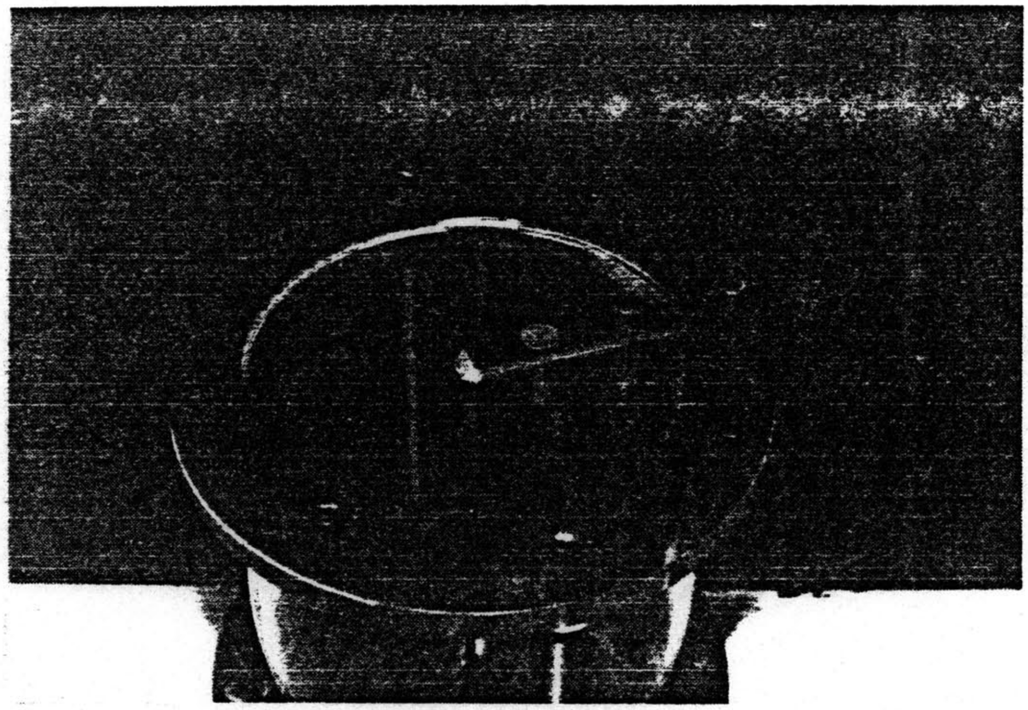

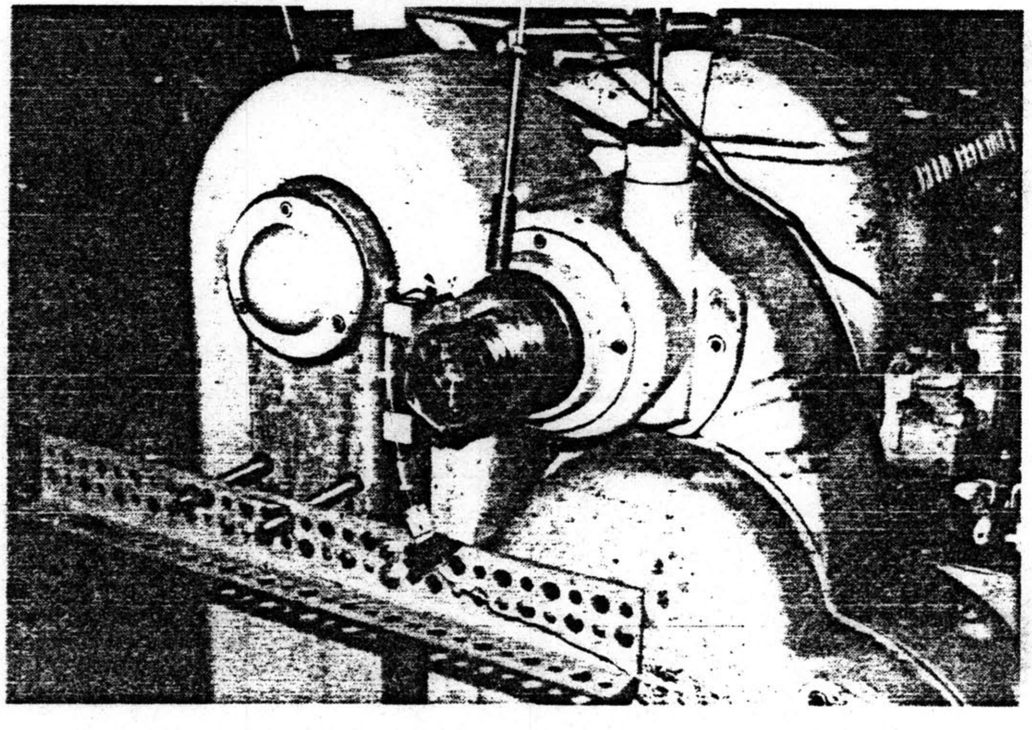

Figure 4.3 (above)
Figure 4.4 (below)

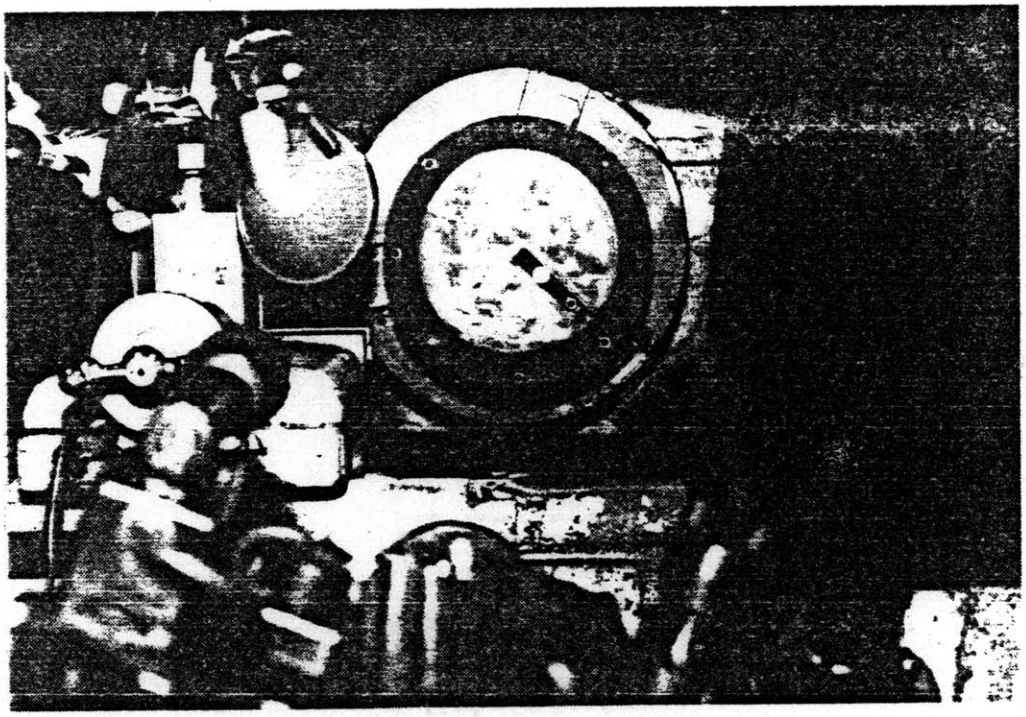

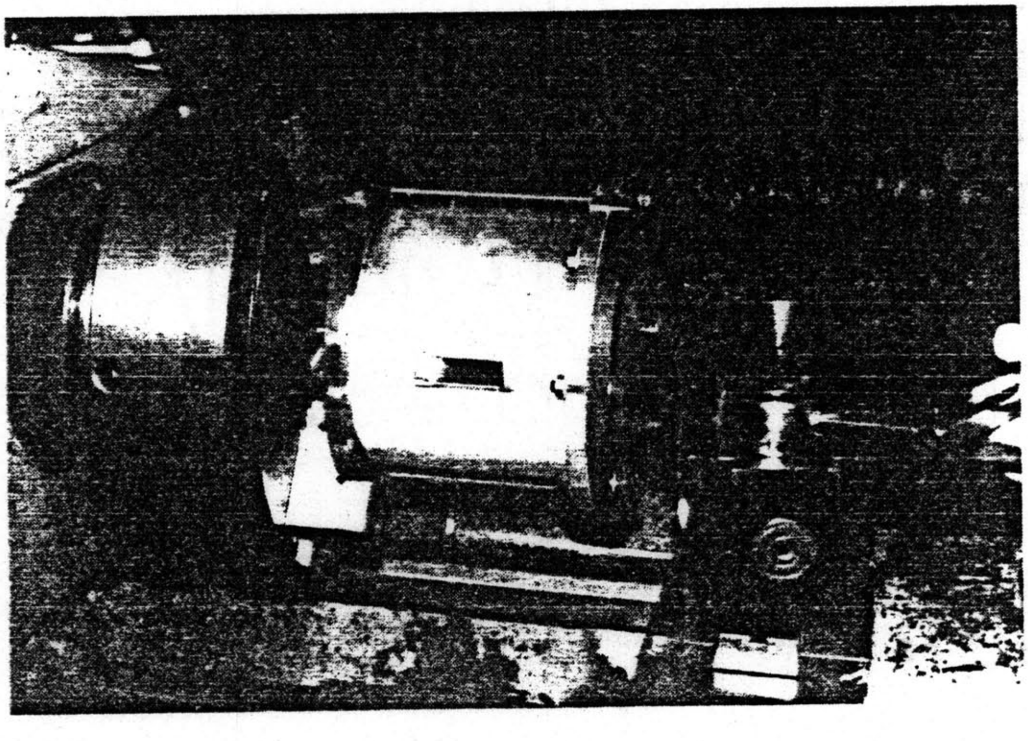

Figure 4.5 (above)
Figure 4.6 (below)

heater was supplied through a slip ring assembly which was originally attached to the front end of the container (Fig. 4.2) and later moved to the rear of the lathe spindle (Fig. 4.4) so that an unobstructed picture through the container endplate could be taken.

Figure 1.3 is a photograph of a starting plume in this rotating cylinder. Several features of this picture deserve mention. In this picture the cylinder does not have a radial baffle. It turns out that the trajectory of the plume is the same whether the cylinder is baffled or unbaffled. As explained in Chapter 3, there is no imbalance in forces acting on the plume fluid. The coriolis acceleration of the plume is balanced by pressure forces in the fluid outside the plume, a consequence of the rotational stiffness of the fluid. It should be noticed as well that the width of the plume is very thin near the heater but grows out to the plume front which is considerably wider. It is presumed that the width of the plume front is the characteristic length on which to base the plume Rossby number helping to explain the two-dimensionality of the flow. If the structure of the plume is similar to its non-rotating two-dimensional counterpart then the plume front is moving slower than the plume behind it and is drawing in bouyancy as it expands through entrainment. The plume front itself seems to consist of two eddys, one eddy appearing to be slightly further ahead of the other, again, resembling a two-dimensional vortex pair. A self-similar plume structure is confirmed in successive photos of the starting plume as it progresses inwards (Figure 9.6). It is also interesting to note the sinuousness of the longer plume (Figure 1.4) and the eddies alternately shed along the radial trajectory. This sinuousness is probably related to the shear instability of the plume in the enclosed rotating fluid, since fluid is moving outwards as the plume moves inwards, although why the eddies are alternately shed is a mystery.

To investigate the two-dimensionality of the plume, a means of tagging the fluid pathlines at various axial locations was necessary. The mica flakes are dispersed evenly throughout the container and it is only possible to see the motion of particles near to the endplate of the cylinder. Another technique which allows the flow to be observed at all levels within the container involves the use of a thymol blue dye water solution [23]. This technique is succesful here because the plume velocity is so small (less than 2 cm/s). A water solution of thymol blue is prepared and titrated to a Ph of 8 with NaOH. The solution is now a deep, dark blue. This solution is then made slightly less basic by adding HCl drop by drop until the solution turns amber. When thin platinum wires (0.002 in.) are placed in the solution and made to conduct electricity through the water to a nearby copper cathode, the yellow water changes color to dark blue in the vicinity of the platinum wire. Figure 4.7 shows the heater and a grid of platinum wires also taped onto the outer wall. When the wire is made to conduct electricity the dye is formed as shown in the darkening of the fluid around the wires in Figure 4.8. The conduction of current through these wires also generates a little bit of heat and the dyed fluid is slightly bouyant. This bouyant dyed fluid moves inward very slowly in a clearly two-dimensional manner as shown in Figures 4.9 and 4.10. (It is very interesting to compare the shape of the front of the lines of dye with a picture of incipient Benard convection cells- Fig. 4.11). The platinum wires are discretely spaced to illustrate this effect. The sequence of photographs in Figures 4.12a, c show what happens when the

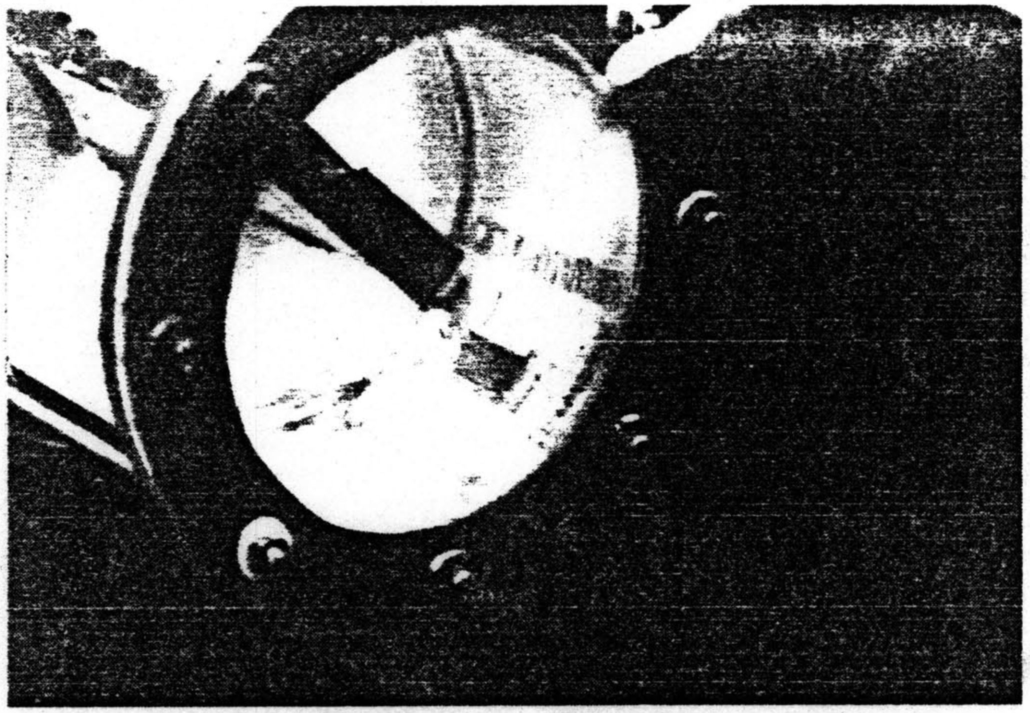

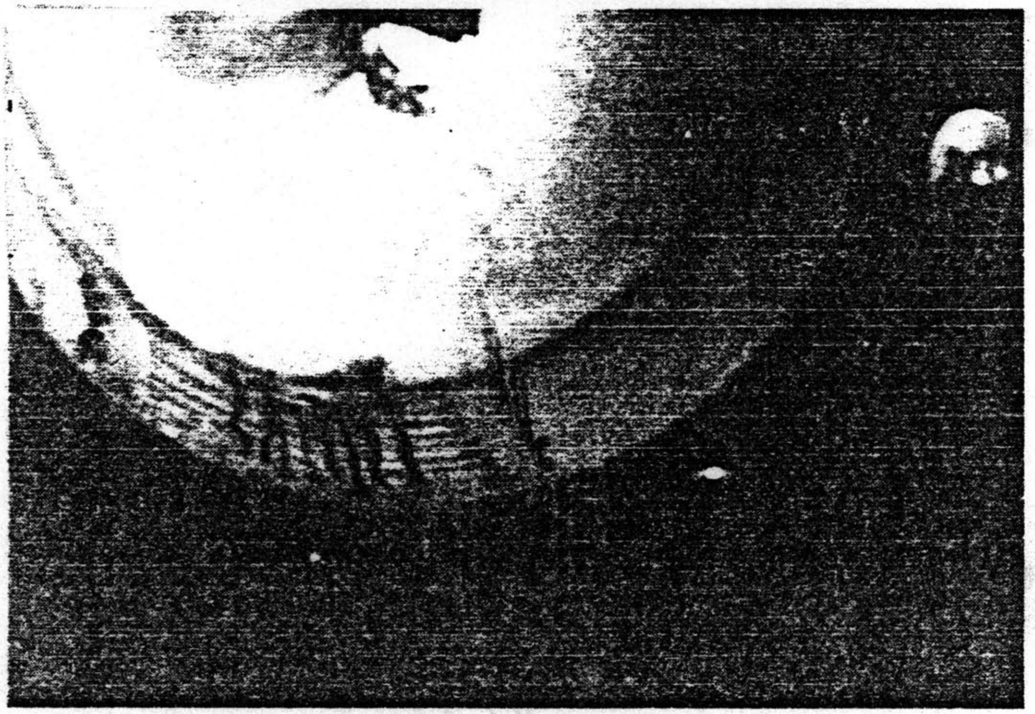

Figure 4.7 (above) Stationary container showing heater taped to outer wall and array of thin platinum wires for generating dye. Container is filled with thymol-blue water solution.

Figure 4.8 (below) Conduction of current through water causes water color to change locally to blue. Plastic foam is taped to the inner radius of the baffle to prevent air bubbles from bouncing around and disturbing plume motion.

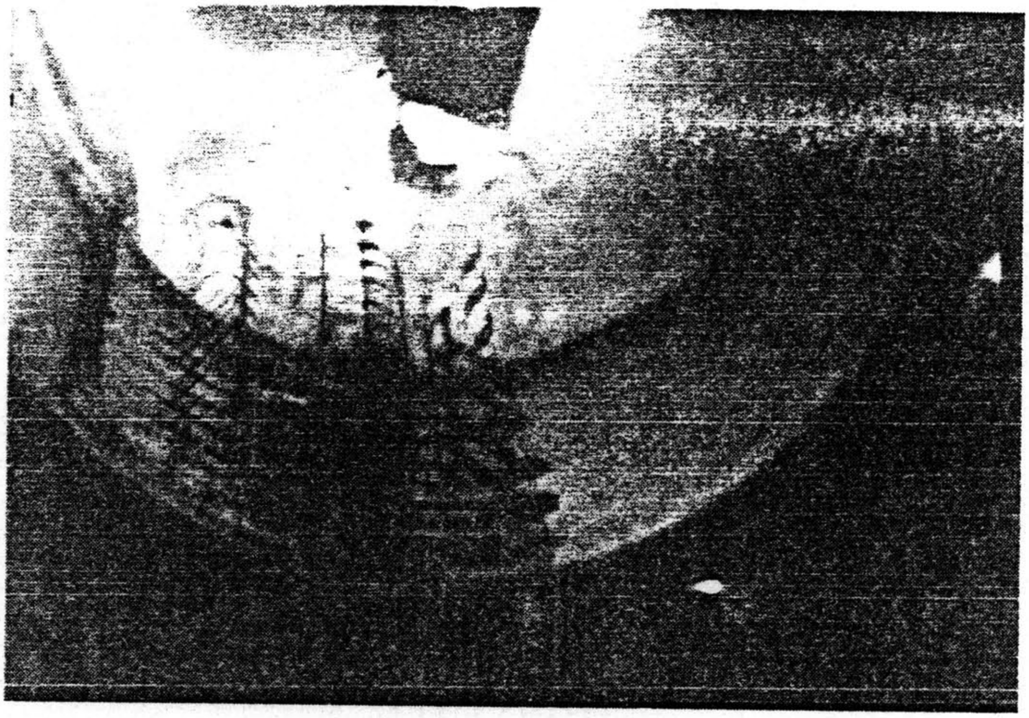

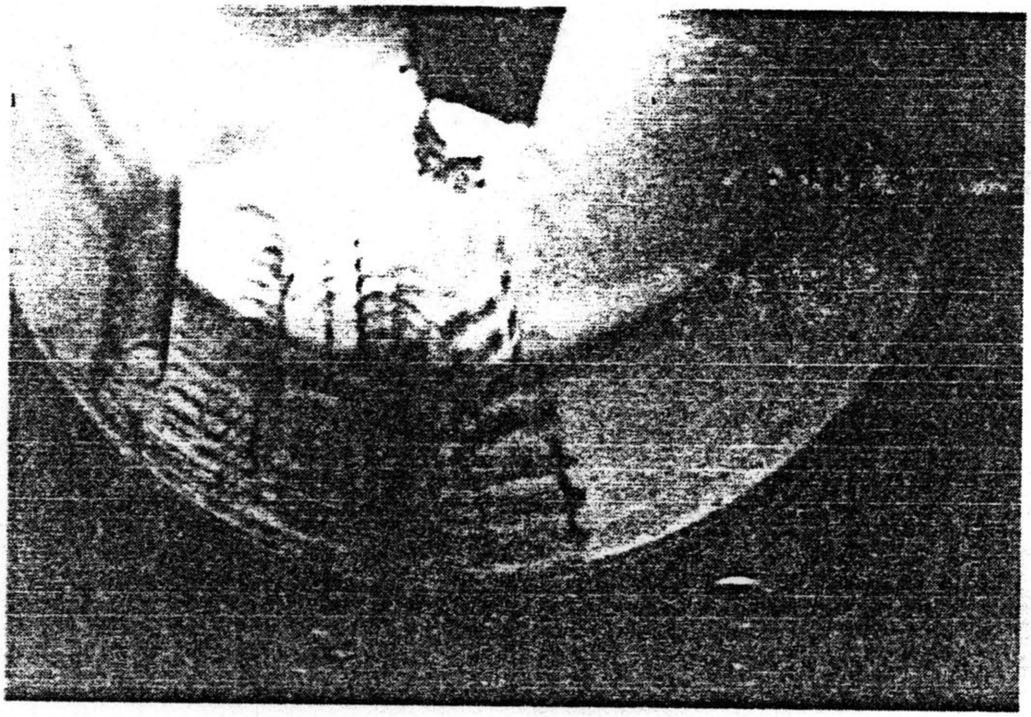

Figure 4.9 (above), Figure 4.10 (below) Dyed water is slightly bouyant and moves inwards slowly. Even this flow is strongly two-dimensional.

real heater is energized. The container used when these pictures were taken was fitted with radial baffle (with foam taped at the centerline to trap air bubbles) and the heater is diagonally across from the baffle. Fluid immediately rises off the heater and draws in fluid off the outer wall. Notice how the lines of dye start to bend towards the heater as the plume starts to rise (Fig.4.12b). If the flow off the heater was not two-dimensional then the lines of dye on either side of the heater would not be pulled into the plume at equal rates in the axial direction nor would they appear to bend uniformly along their length. Figures 4.12a,c also clearly show the starting plume itself with its mushroom shaped front and a characteristic pair of alternating eddies. The angle of the photograph plainly shows that this pattern is continuous in the axial direction demonstrating directly the two-dimensional character of the flow.

Once the dye experiments verified the orderly nature of a plume coming off a small heater, different shaped heaters were taped to the outer wall of the plexiglass cylinder. Figure 4.13 shows a long (5 in. X1/2 in. wide heater) taped to the side wall. Figures 4.14, 4.15 and 4.16 are a sequence of photographs taken a few moments after energizing the heater. It appears at first (Figure 4.14) that several radial plumes have risen off the heater surface. Very soon after, however, the various plumes coalesce and form a strong central plume which tends to rise inwards in the middle of the heater (Figure 4.16). The trajectory, again, is nearly radial. This long thin heater was then removed, and a much larger heater was taped to the outer wall. This second heater is shown in Fig. 4.17. The resulting flow is shown in Figures 4.18 and 4.19. In Fig. 4.18, the disparate plumes are shown emerging off the heater surface. A few moments

Figure 4.11 'Thermals' rising from a heated horizontal surface under a layer of water. (From Turner [21])

Figure 4.12a. First in a sequence of three pictures of plume rising off of a small heater. Container is spinning at 531 rpm. Plume is on diameter of container baffle, and is circled in the next figure.

Figure 4.12b

Figure 4.12c

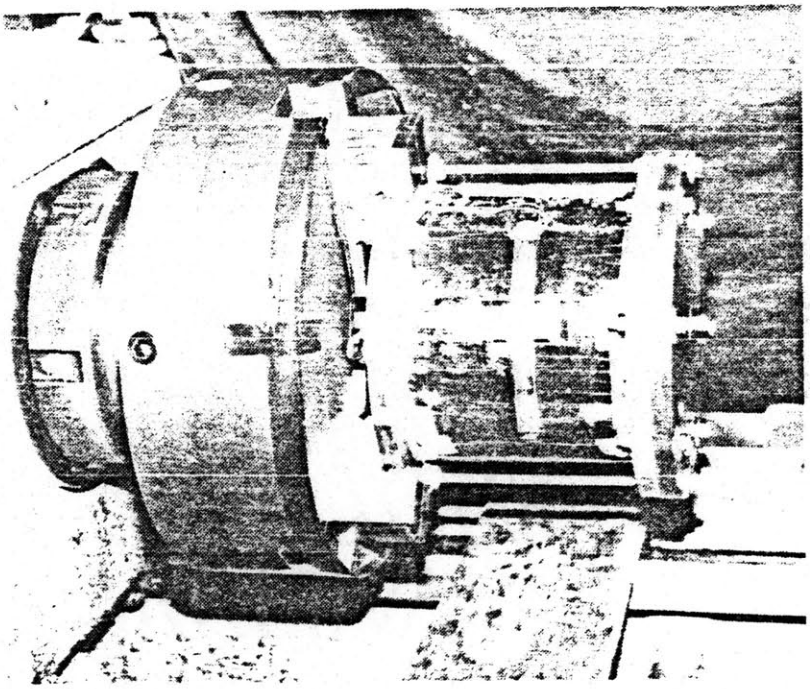

Figure 4.13 Thin heater taped to outer container radius. Axial platinum wires for generating dye also shown.

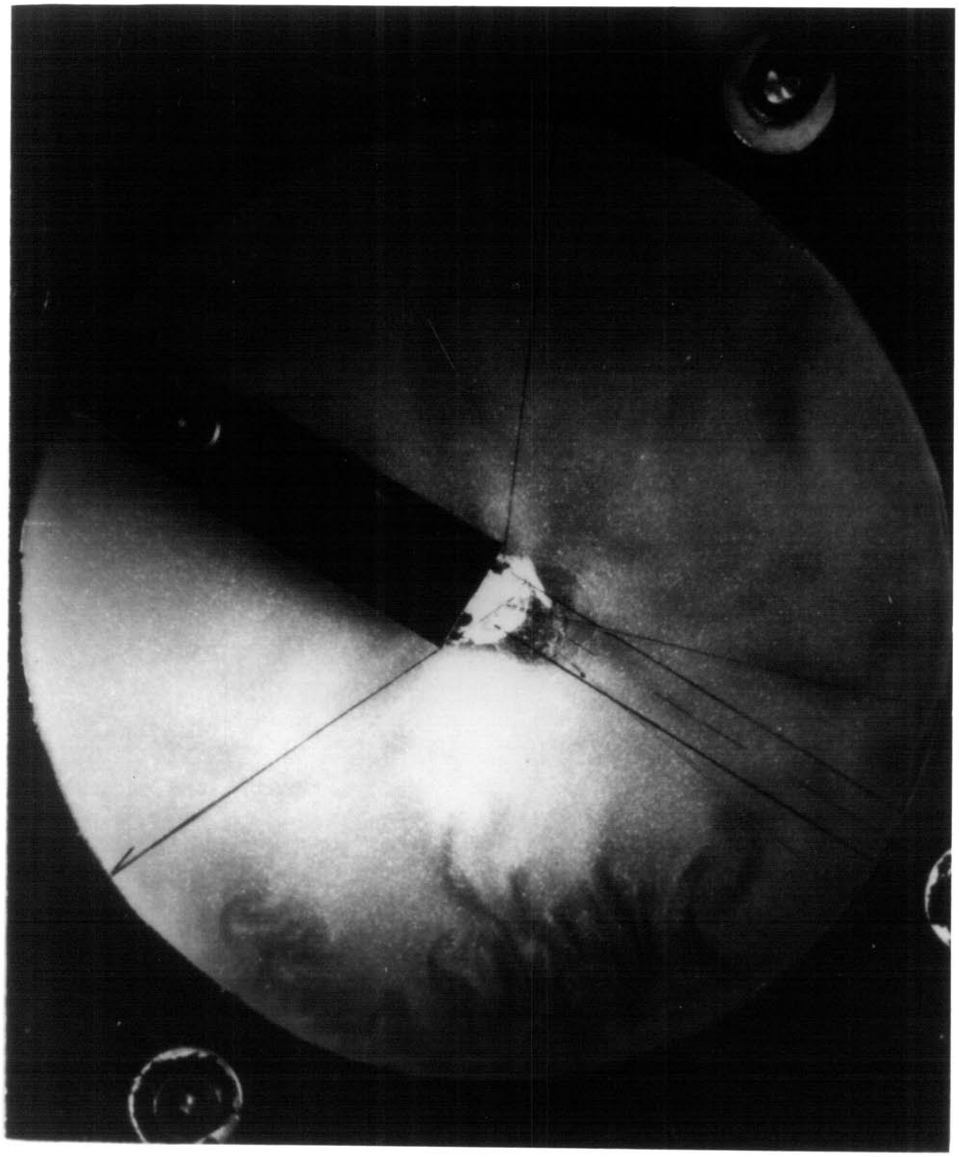

Figure 4.14

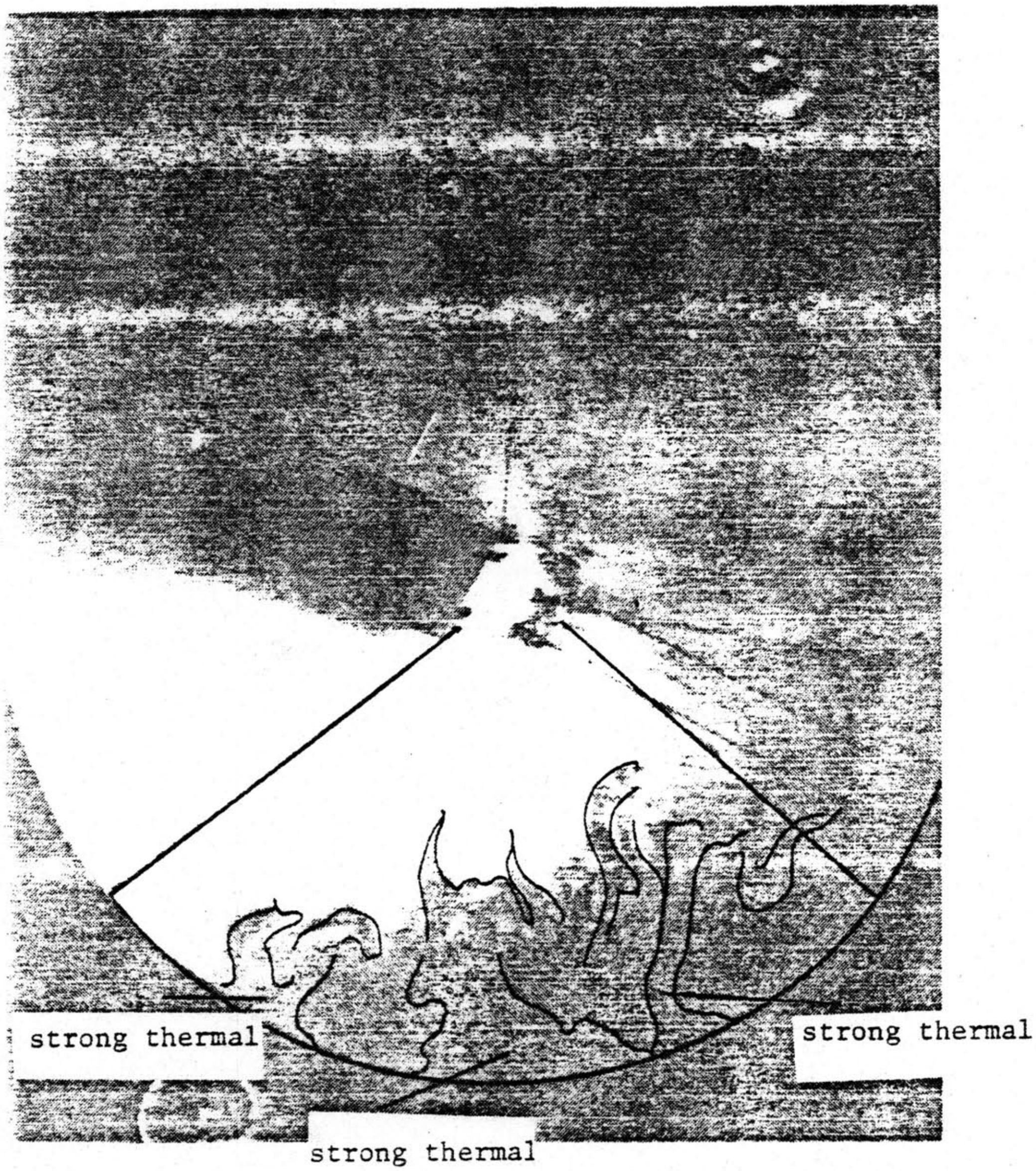

Figure 4.15

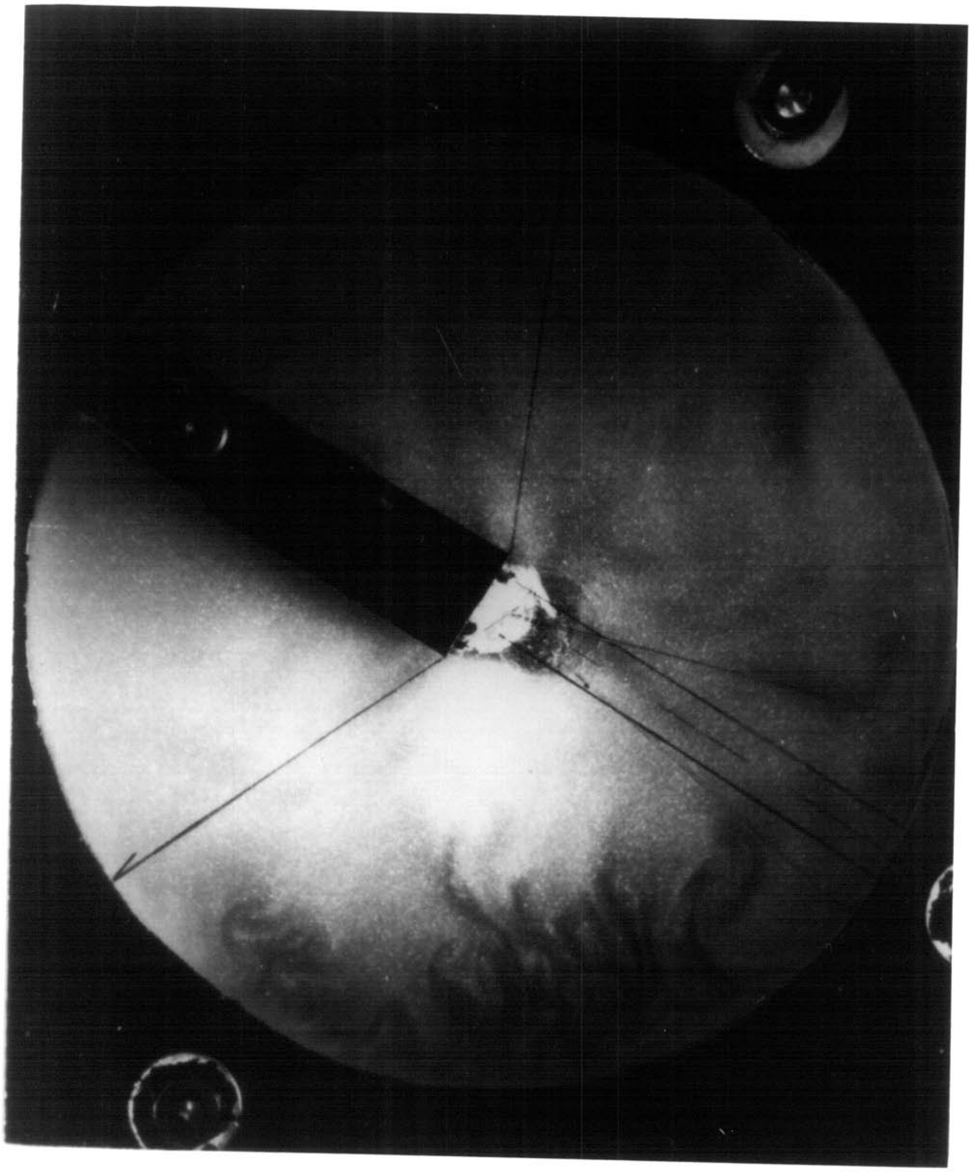

Figure 4.15

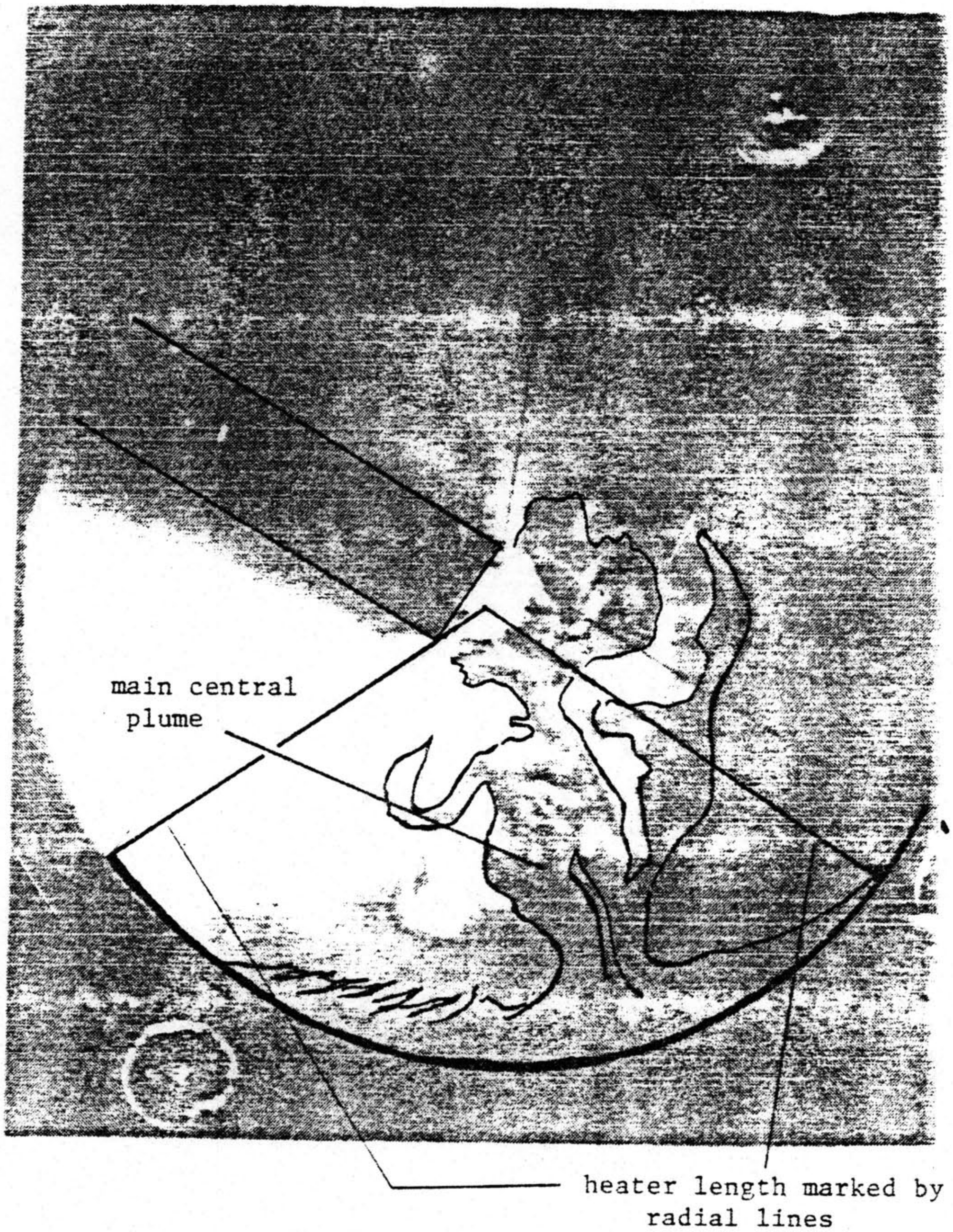

Figure 4.16 Thermals have merged into a strong thermal plume centered approximately at the middle of the heater.

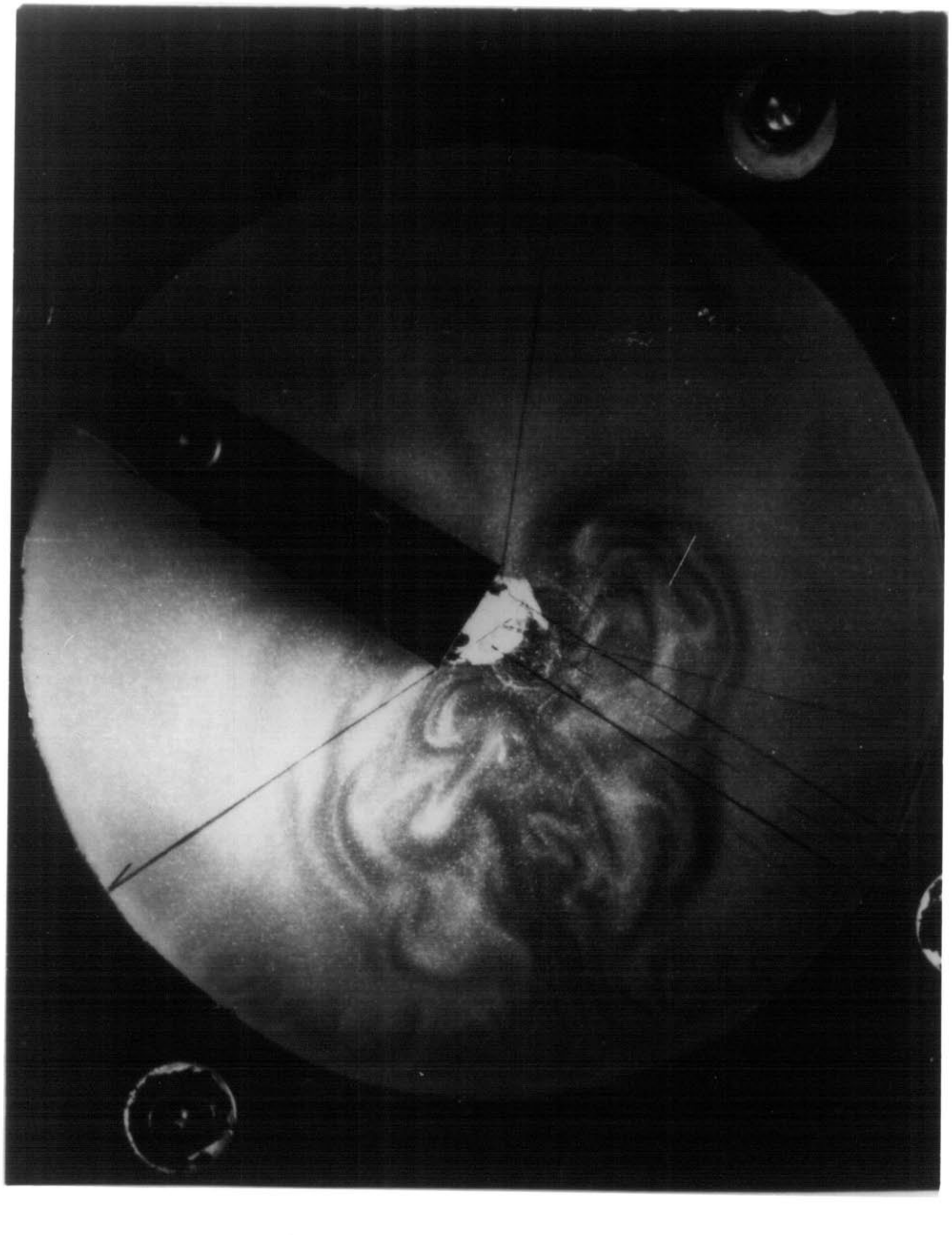

Figure 4.16

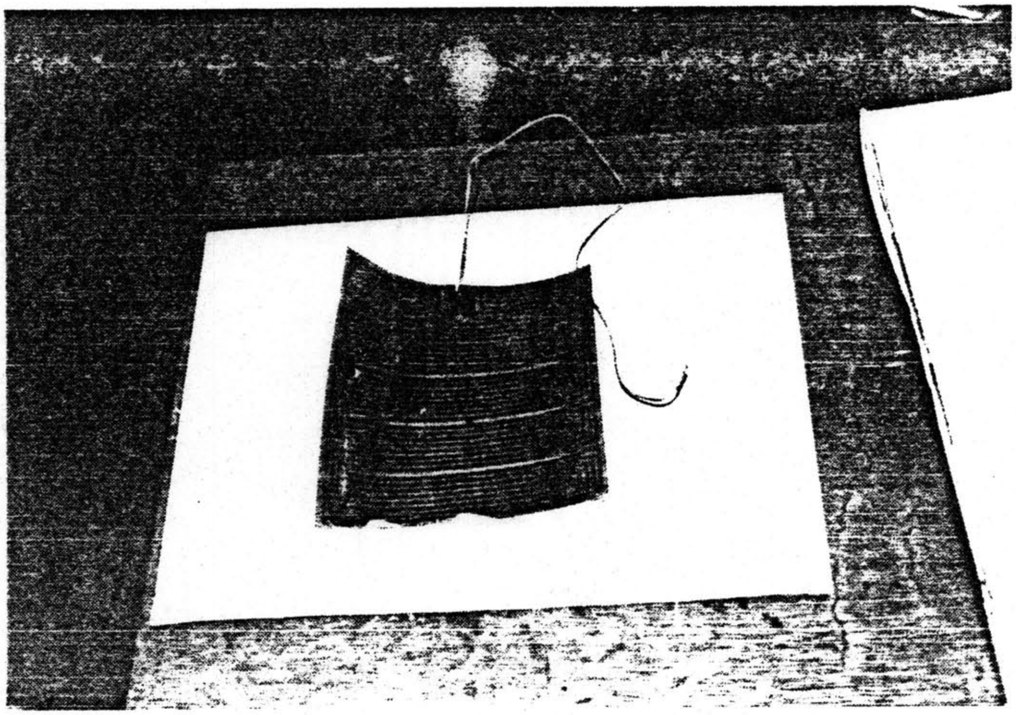

Figure 4.17 Large heater to be taped to container radius, replacing heater in Figure 4.13

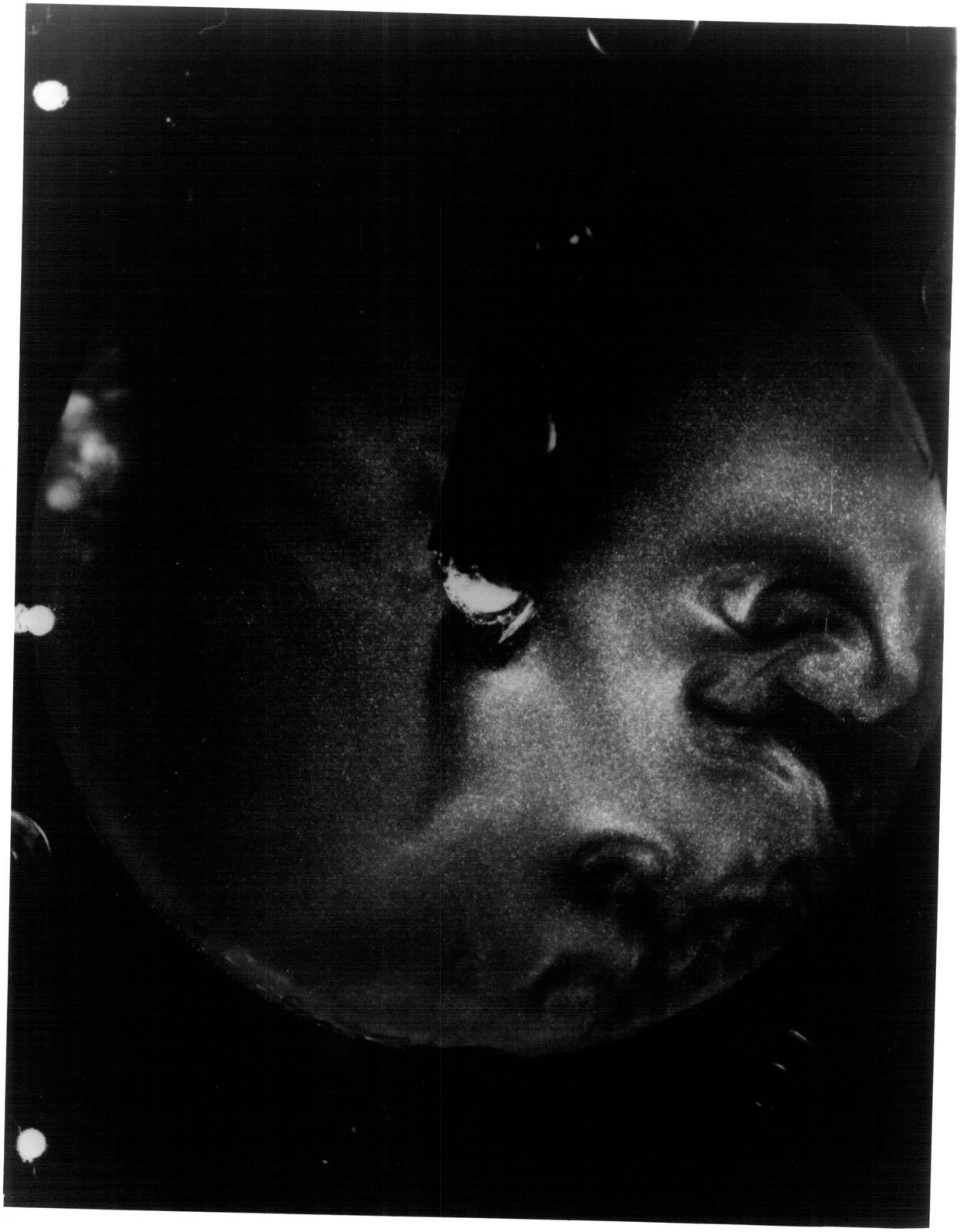

Figure 4.18

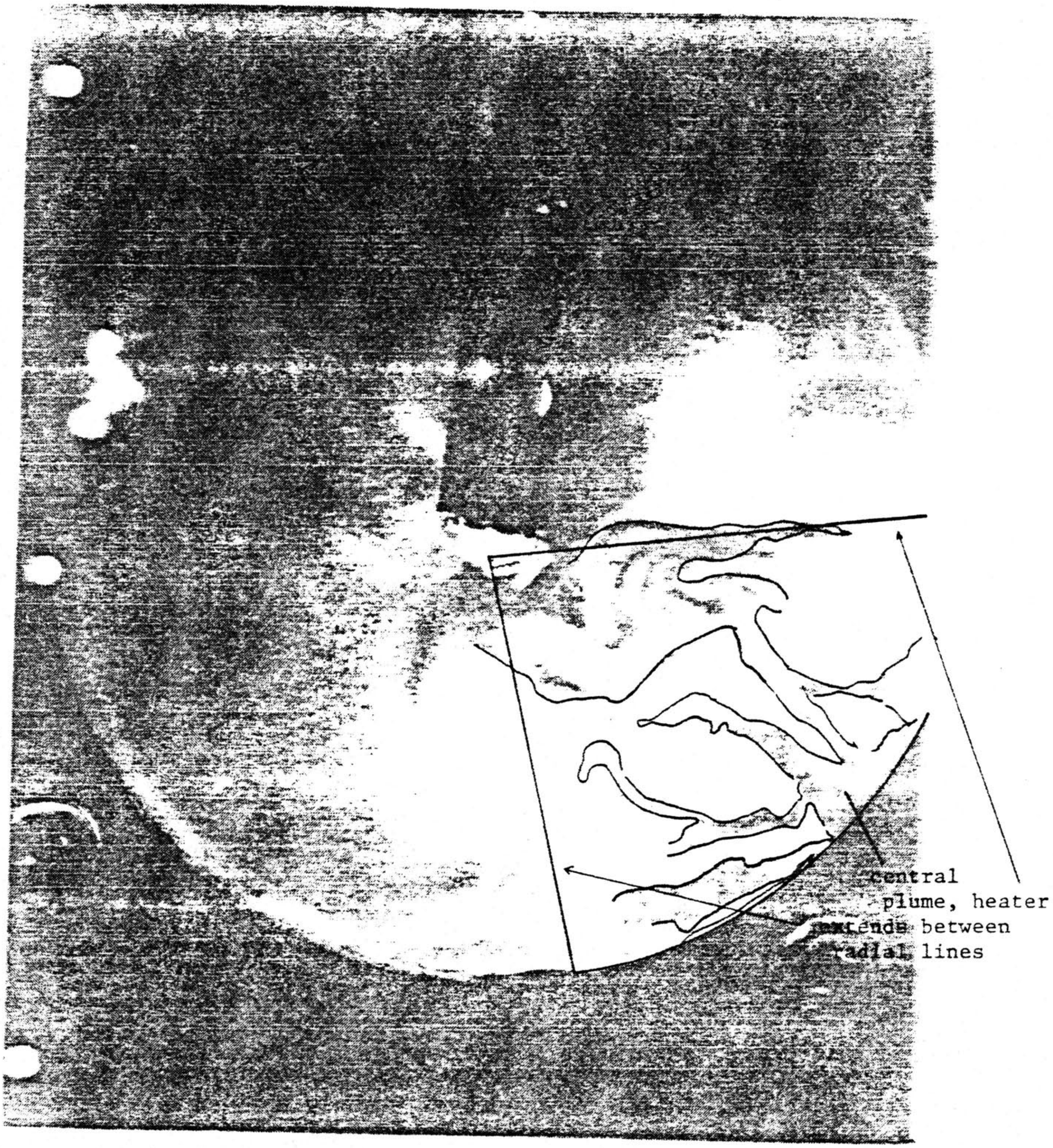

Figure 4.19 Thermals off of large heater tend to coalesce into a strong central thermal.

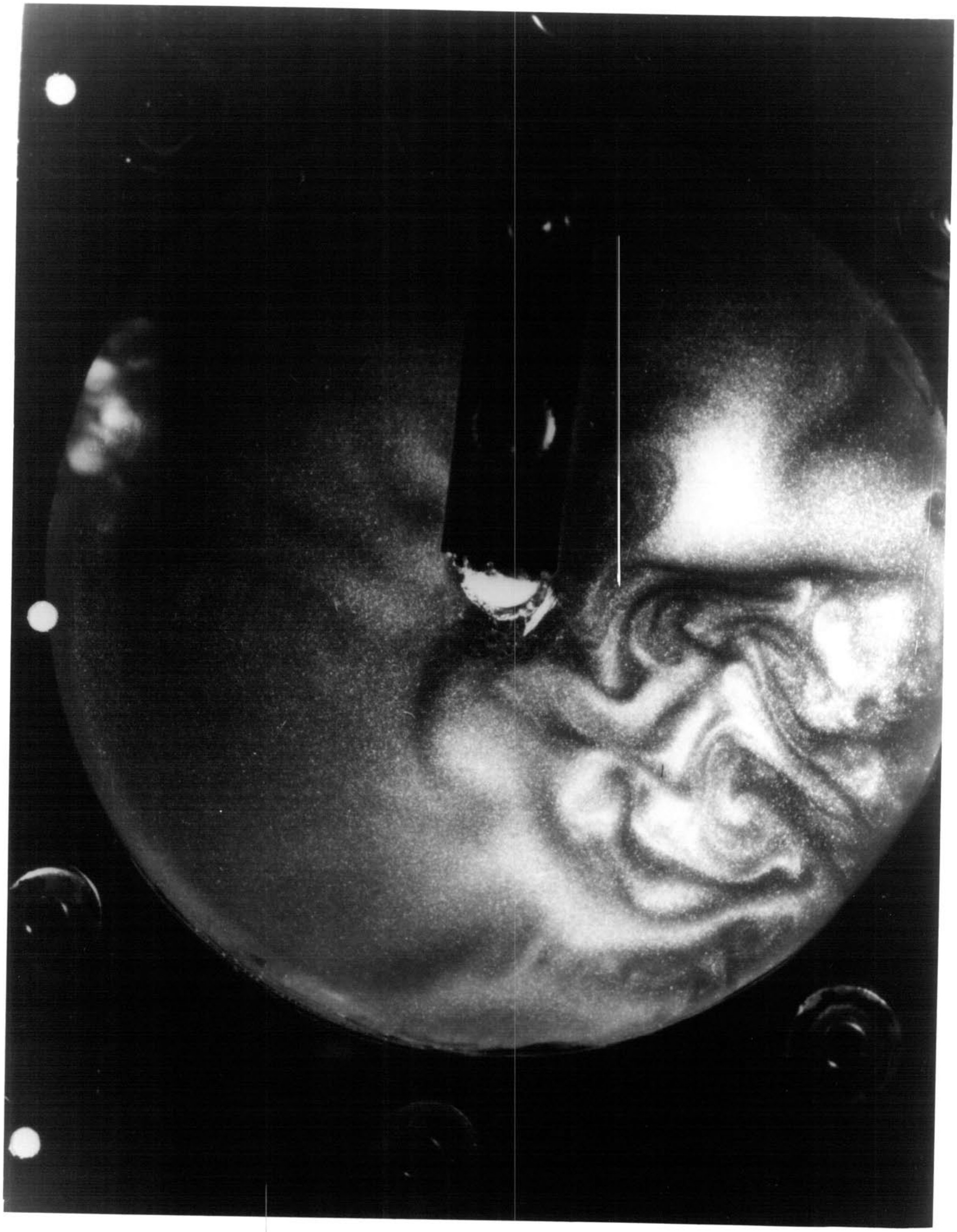

Figure 4.19

later, those seperate plumes have merged into the larger central plume shown in Figure 4.19. The similarity between Figures 4.19 and 4.16 is remarkable.

Flow observation using mica flakes offers an explanation for the absence of a length scale dependence in the surface heat transfer coefficient mentioned in Chapter 1 and discussed further in Chapter 5. Initially, at least, hot fluid tends to rise off the heater surface in cells with a characteristic length determined, one supposes, in the same way as the cell width in horizontal Benard convection. Over time, the assymmetric entrainment of these little cells competing for the same ambient fluid causes them to organize into a strong central plume centered roughly at the middle of the heater. By this time, however, the plume has little effect on the surface heat transfer coefficient, and surface temperature is quasi-steady.

Having found that the trajectories from all the flat surface heaters were radial an attempt was made to generate some curved trajectories. By analogy with Taylor's experiments, it seemed that if enough heat could be generated over a small enough area giving a small thermal a large bouyancy then a curved trajectory should result. A small resistor (1 in. long, 0.1 in. id) was taped to the outer wall inplace of the flat surface heater used previously. With surface heat fluxes of up to 100 W/cm^2, as opposed to the 5 W/cm^2 available with the flat heater, the ensuing thermal did move off in a curved trajectory but the plume was still two dimensional. (The experiments with the resistor were first done with dye to be sure the flow was two-dimensional). Figures 4.20 and 4.21 show the plume coming off of the resistor. When the direction of container rotation was changed the

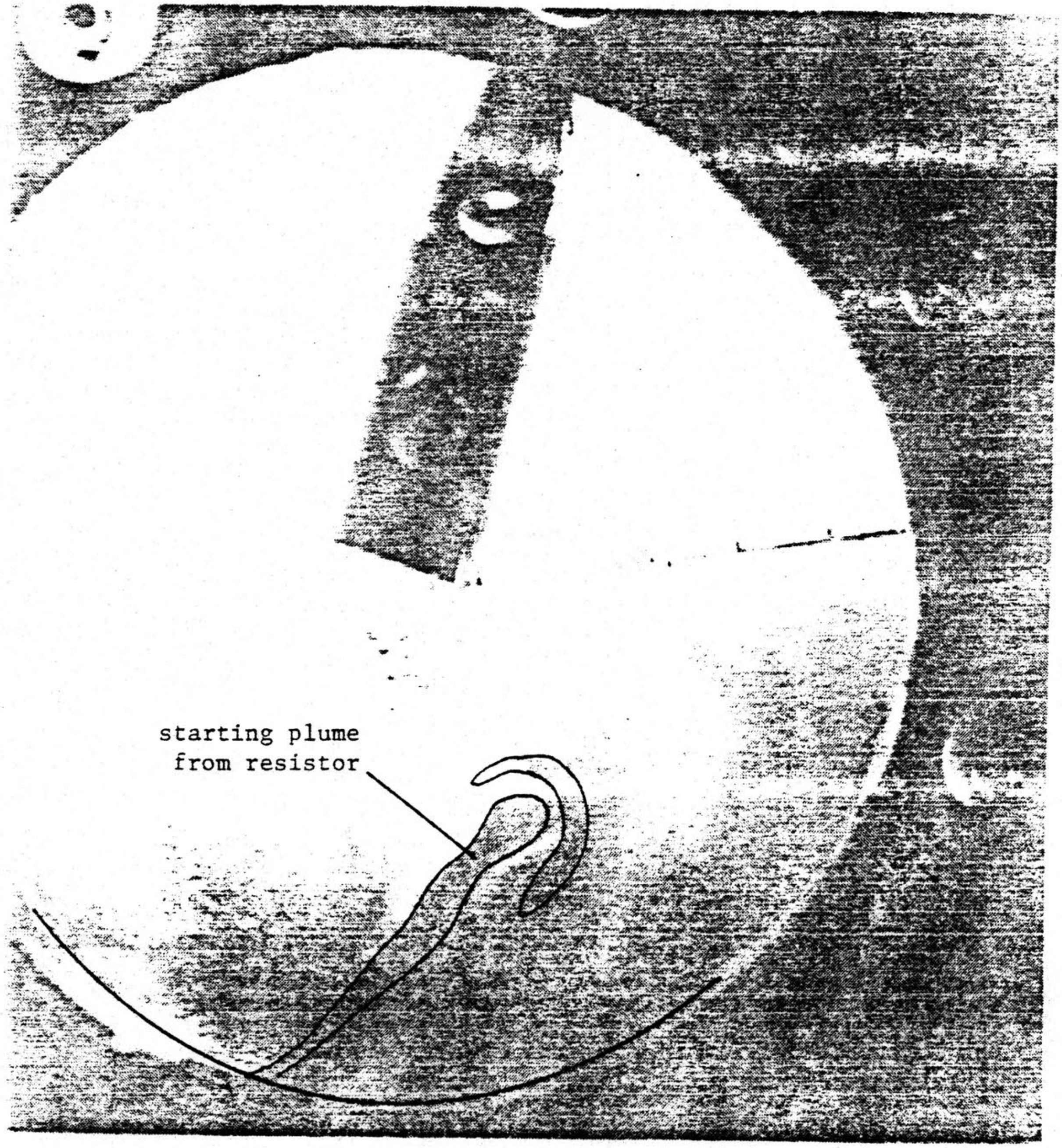

Figure 4.20 Thermal rising off of small heat source taped to outer wall directly across from baffle. Heat source is a small 100 ohm resistor, 0.1" o.d. Heater power is of order 50 W/cm^2. Trajectory is curved in the direction of container rotation.

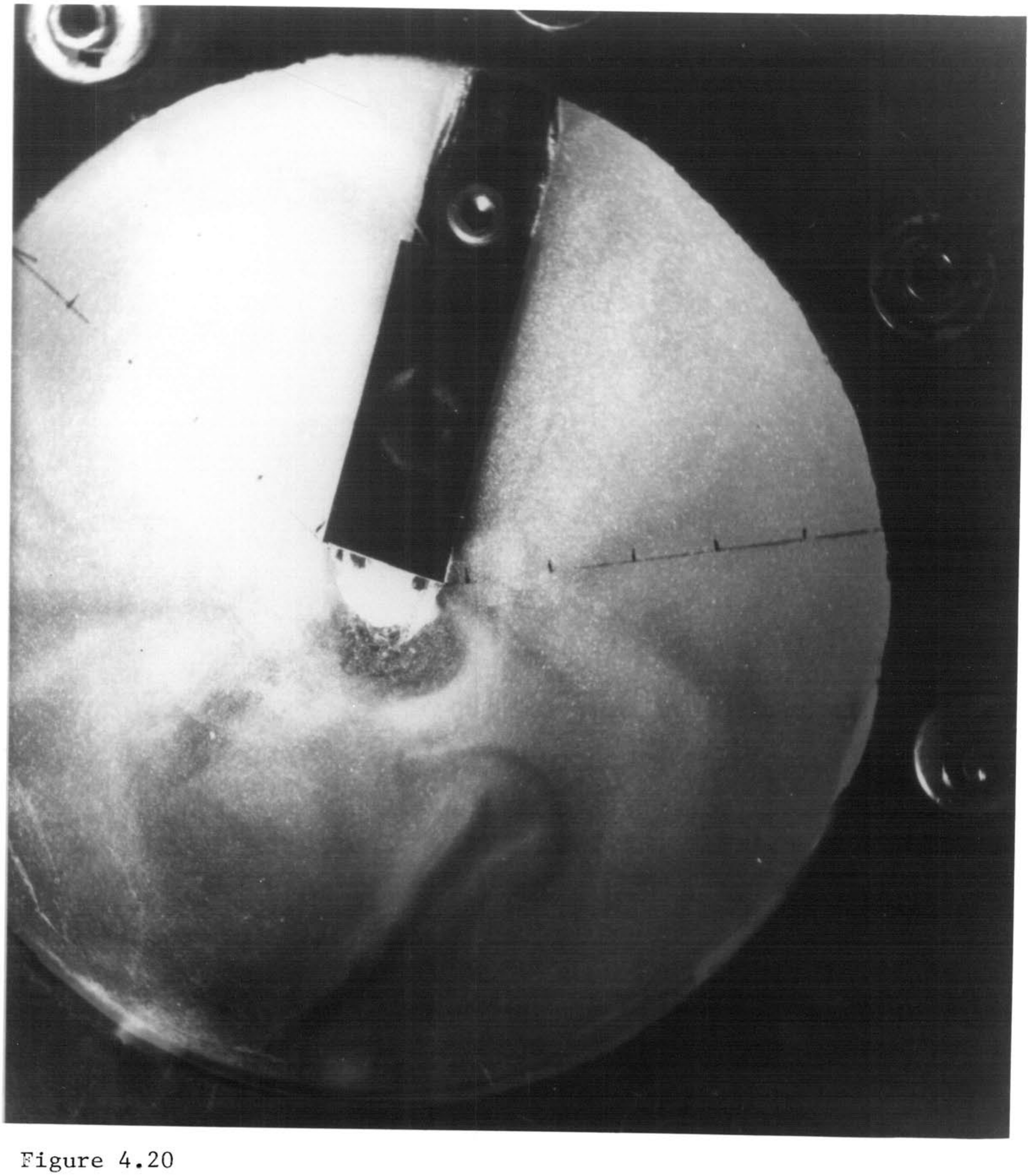

Figure 4.20

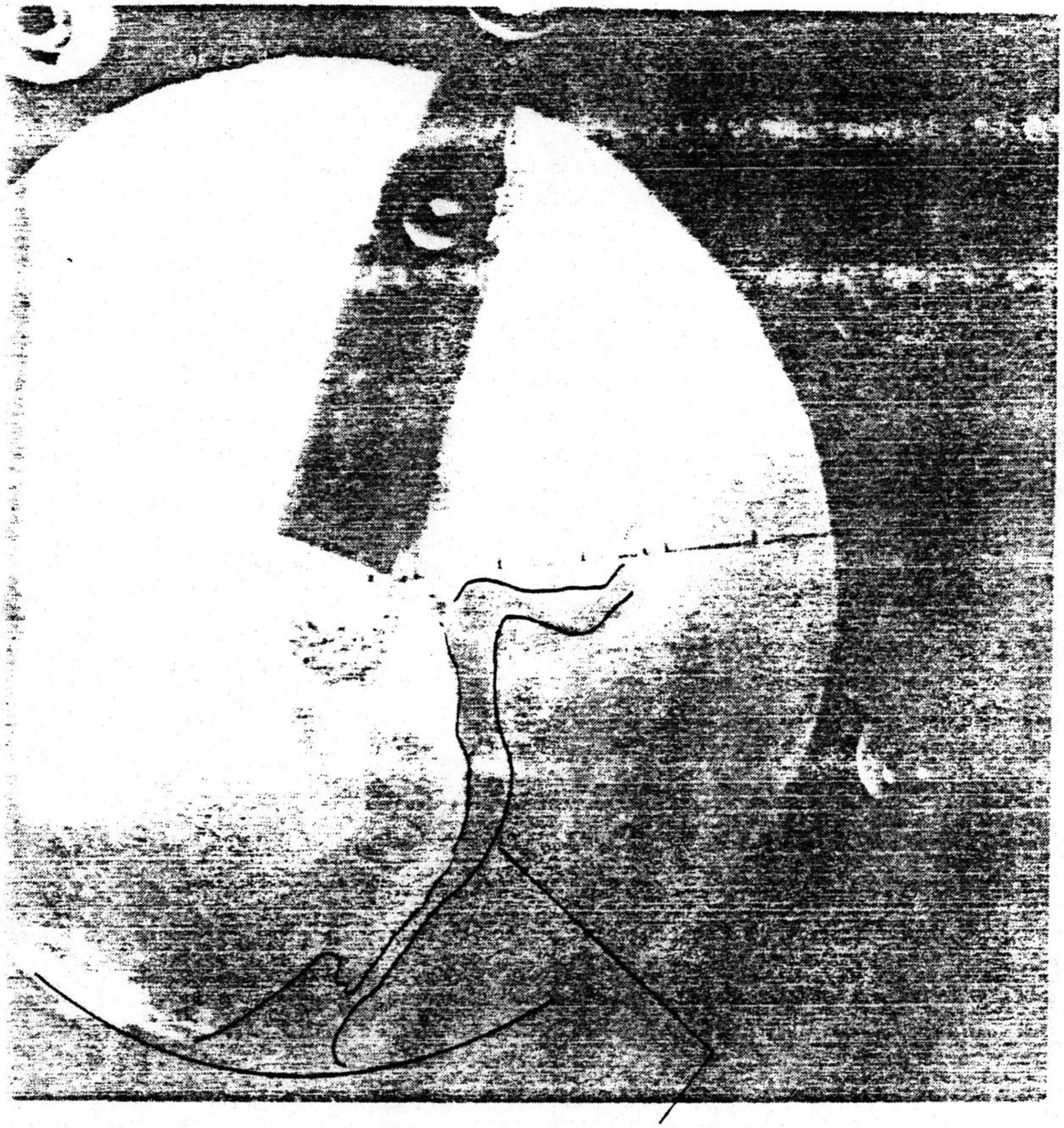

plume rising off of resistor

Figure 4.21

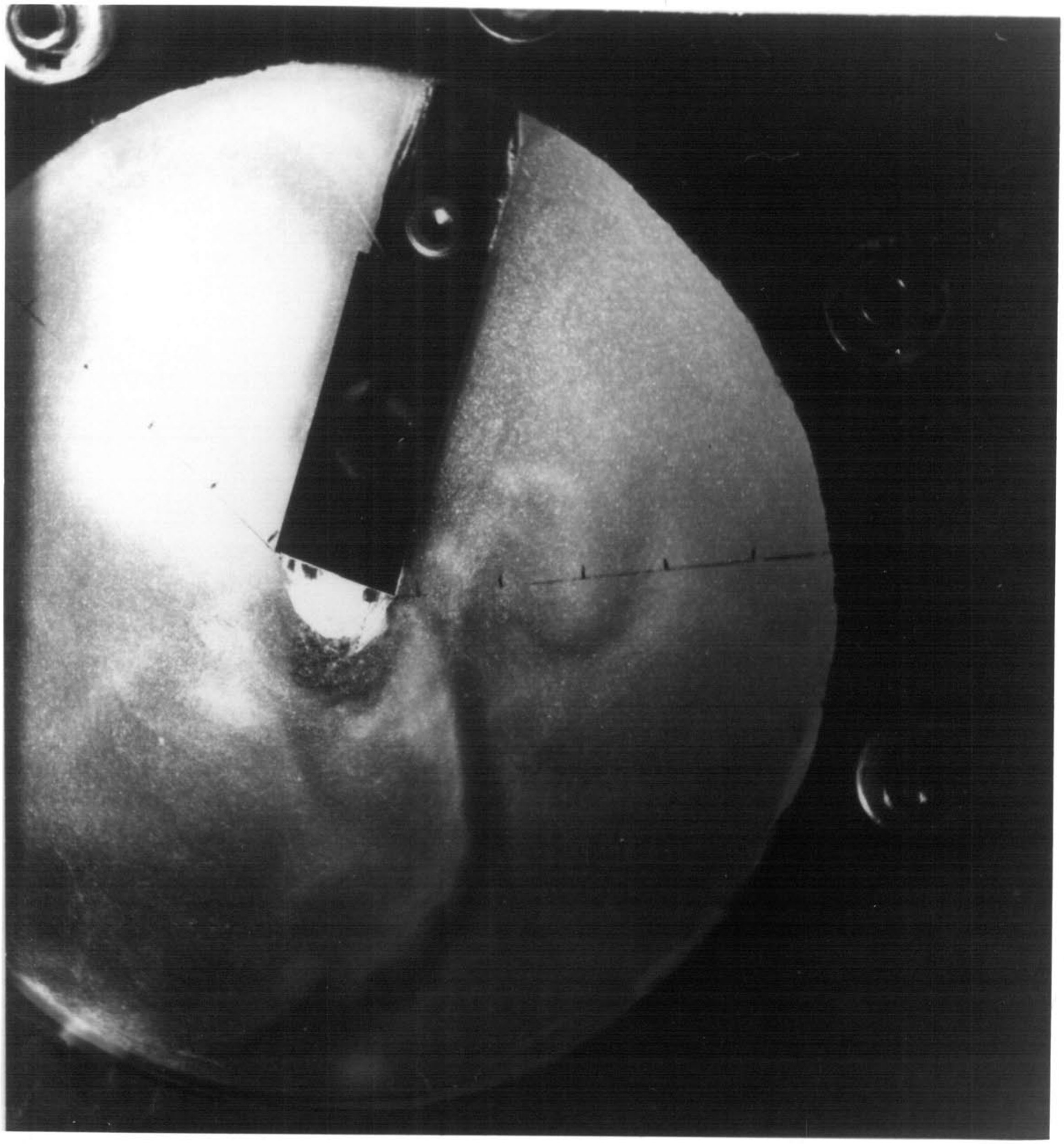

Figure 4.21

trajectory curved in the opposite direction, indicating that the plume was moving fast enough to be affected by inertial forces. It is quite apparent that the thermal flow is now in an intermediate regime where the flow is unsteady, but not unsteady enough to generate a three dimensional flow field. It is felt that assymetry of the separated flow around the fast moving thermal front causes the imbalance of forces in the azimuthal direction which results in the particle acceleration in that direction.

CHAPTER 5

DESIGN AND CONSTRUCTION OF ROTARY APPARATUS

V.A Overview of test apparatus

A rotating apparatus was built to allow for both flow visualization and surface temperature measurements in a container during natural convection experiments at high Rayleigh numbers. The fluid container designed resembles a baffled liquid helium reservoir found in a superconducting generator (see Fig. 2.3). Fig. 5.1 shows the fully assembled test bed. This chapter includes a description of the essential features of the rotary apparatus, some details of the construction of the fluid container, the specifications of the rotating data acquisition system and the placement of heaters and thermocouples within the container.

Table 5.1 is a sketch of the pie shaped container including a tabular listing of the dimensions of the container. Table 5.2 is a list of some characterictic dimensionless groups relevant to this particular container geometry. Table 5.3 compares the dimensionless groups characterizing the experiment and the GE prototype airborne generator. The container height of 14.6 cm. was chosen to satisfy the conflicting requirements of slow spin-up and high turntable speeds. The spin-up time for the container scales with the container height. If the fluid has a long spin-up time it becomes easier to satisfy the requirements for an impulsive acceleration. However, increasing the height of the container also lowers the critical speed of the apparatus. With a 3hp DC motor and a tight V belt (Fig. 5.2), the fully loaded turntable shown in Fig. 5.1 could be accelerated from

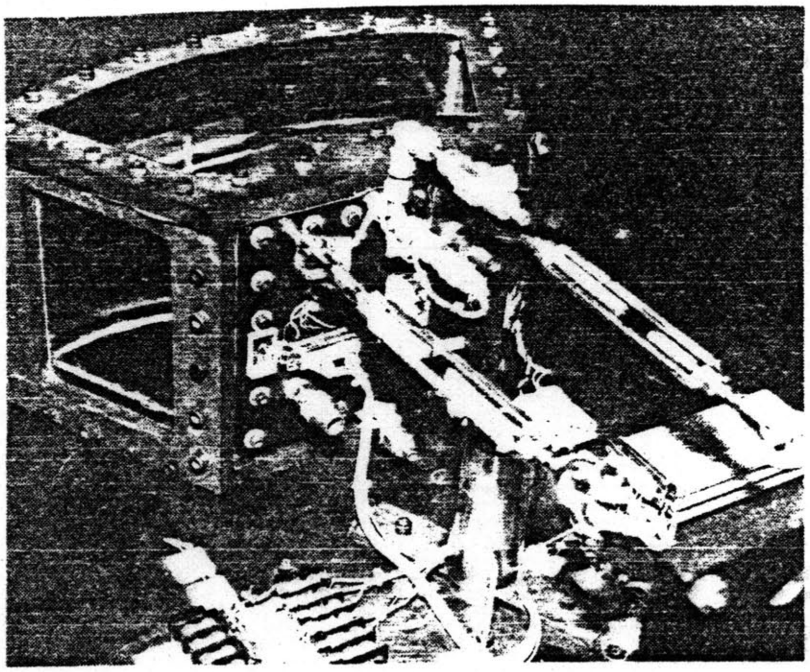

Figure 5.1 Another view of rotating test bed. Valves in rear of container allow container to be filled with water. Additional pipe fittings are for filling rear reservoir with water. Stainless structure on centerline is to position a rotating union which would be used to recirculate cooling water through the rear reservoir during a long heat transfer test.

Table 5.1 Experiment parameters

water volume		4.3 l
rear reservoir vol.		1.46 l
total water volume		5.76 l
weight: container, bolts, top plate-		9.54 kg.
total weight	33 lbm.	15.3 kg.
outside radius	12"	30.5 cm.
inside radius	7.25"	18.4 cm.
sector angle	1 rad	
axial height	5.75"	14.6 cm.
DC motor power	3 hp	
max. rotational speed	600 rpm	
max. input heater power	30 W/cm^2	
total power	80 W	

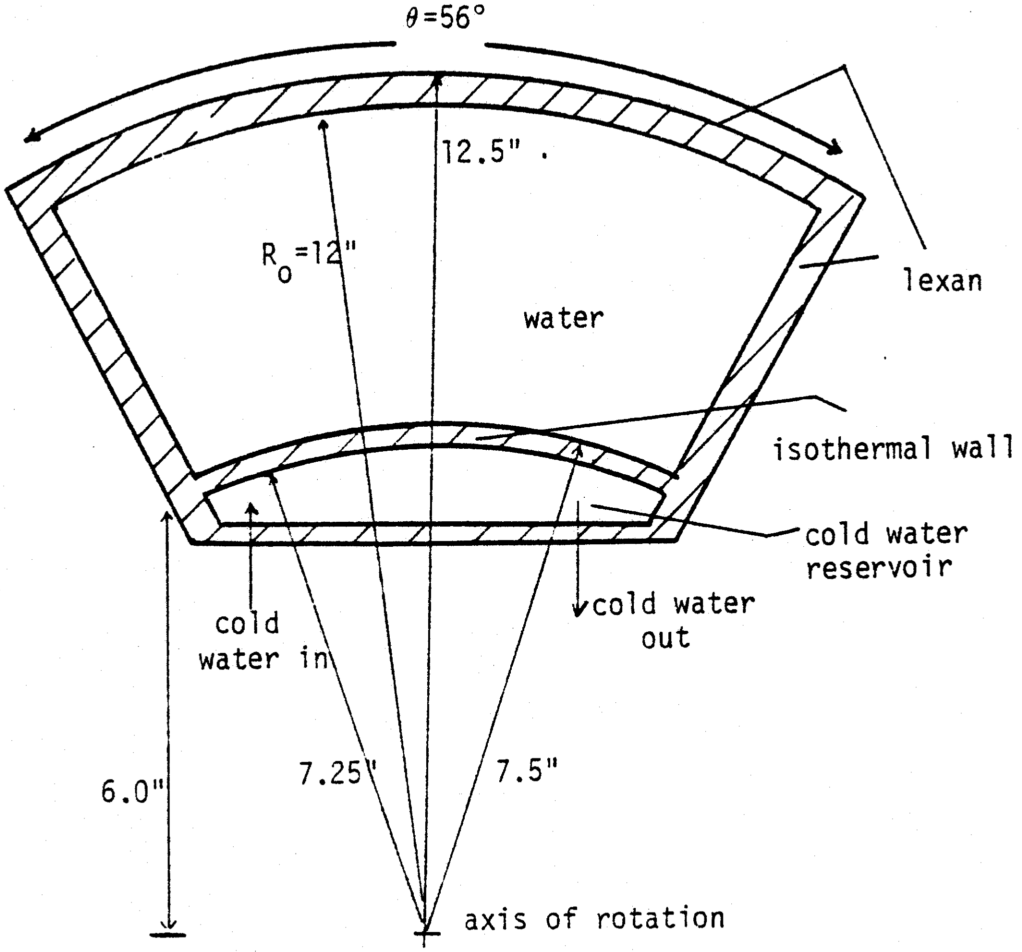

HORIZONTAL CROSS SECTION OF INSTRUMENTED CONTAINER

Table 5.2 Important dimensionless numbers

Dimensionless number or or characteristic time	Water (300K)
spin up time constant $h/2\sqrt{(\nu\omega)}$	
50 rpm	41s
500 rpm	12.8s
1000 rpm	9.1s
Ekman number $\nu/(\omega h^2)$	
50 rpm	5.5X10-6
500 rpm	5.5X10-7
1000 rpm	2.7X10-7
Rayleigh No.[1]	
$\frac{(Pr)(\beta\Delta T)\omega^2 R_o (R_o)^3}{\nu^2 8}$	$=4.7X10^{11}$
	$(\beta\Delta T)$ =0.01
	R_o =30.54
	ω =600 rpm
convective time scale[2]	
$\frac{(Pr)(R_o)(\Delta r)}{2Nu(\nu)} = \frac{\rho c_p(\Delta r)}{h}$	
Nu = 10	3.4 hr
= 100	20 min.
= 1000	2 min.

[1] length scale for Rayleigh number is half the width of the outer lexan window, $R_o/2$ since the window sector angle is 1 radian.

[2] time to establish a steady state temperature distribution in the bulk fluid using the rear reservoir as a heat sink and assuming uniform heat generation over entire outer window surface area. This number roughly estimates the time constant to raise the bulk fluid temperature to the mean temperature $T_a+\Delta T/2$. Δr is the container outer radius minus the inner radius, h is the surface heat transfer coefficient and R_o is the outer radius.

Table 5.3 Comparison of experiment and GE airborne rotor

	GE airborne rotor[1]	Experiment
rotational speed	6000 rpm	500 rpm
acceleration rate	5000 rpm/s	100 rpm/s
surface heat flux	20 mw/cm^2	20 w/cm^2
spin-up time constant	30 s (bore fluid)	18 s
Rayleigh no.	10^{13}	$10^6 - 10^{11}$
transient Reynolds no.	10^8	10^5
axial length	23 cm.	14.6 cm.
$\beta \Delta T$	10^{-2}	10^{-3}

[1] numbers based on dimensions of bore reservoir in the prototype GE machine, Fig. 2.7

200rpm to 500 rpm in less than 3 seconds with a step change in DC motor armature voltage. Since the spin-up time constant at 500 rpm is roughly 10 seconds, the acceleration can be considered impulsive. Rayleigh number estimates listed in Table 5.1 are an optimistic maximum based on a heater covering the entire outer wall. The estimate is based on a $\beta\Delta T=\Delta\rho/\rho$ of 0.012, or the largest bouyancy possible before boiling occurs. Again, The Rayleigh number estimate is misleading because it will be shown later on that the surface heat transfer coefficient is independent of heater length.

V.B Turntable and support structure

Fig. 5.2 shows the welded steel support structure for the rotating apparatus[24]. A 3 hp DC motor with DC motor controller (not shown in this picture) and a 3:1 speed ratio single V-belt drive allows turntable speeds of up to 600 rpm with an overhanging mass (consisting of a water filled container and a counterweight) of roughly 70lbs. The large step down in speed between the motor and the turntable is required for rapid turntable acceleration rates approaching 100 rpm/s. The two bearing vertical shaft system with a smaller overhanging mass mounted on the turntable can be safely run to speeds in excess of 2000 rpm. A welded steel structure provides rigid support and easy access to the motor, bearings and slip ring assembly. A five slip ring and brush assembly (the slip rings are shown in Fig. 5.2b) connects electrical power to the system for both the heater and a rotating electronics package mounted on the turntable. The rotating electronics in conjunction with an optical data telemetry system on the turntable shaft is used to pass data from the rotating experiment to

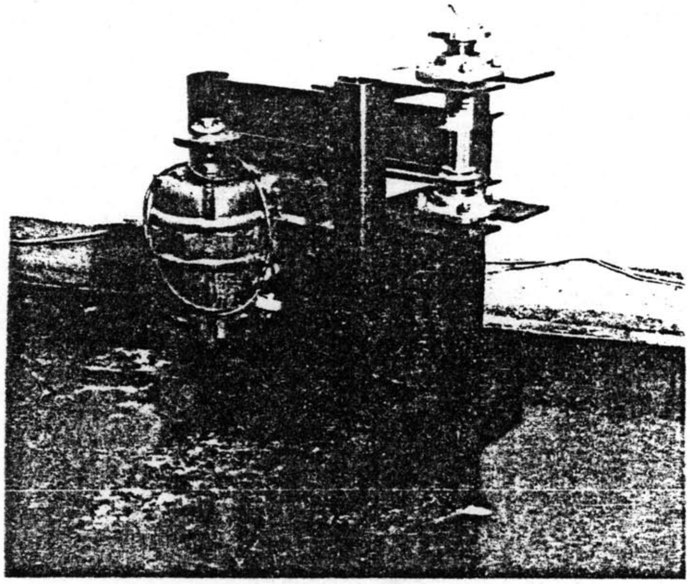

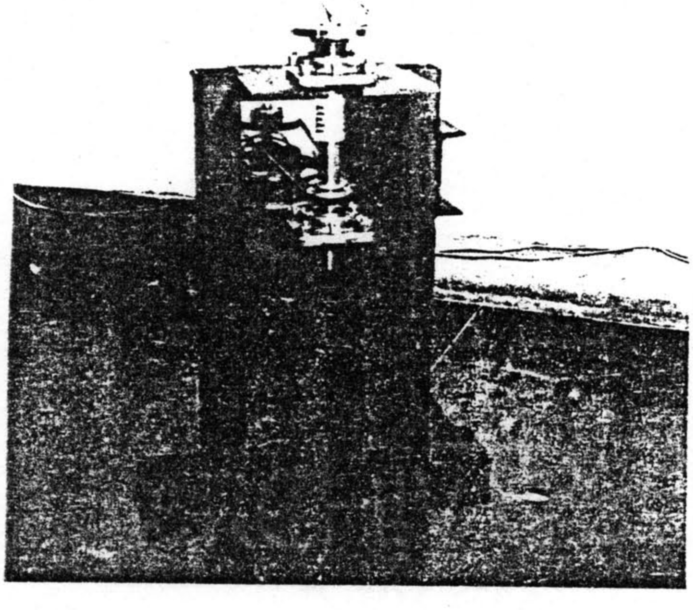

Fig. 5.2a (above)

Fig. 5.2b (below) Support structure for rotating test bed. Shaft-bearing system visible in 5.2b.

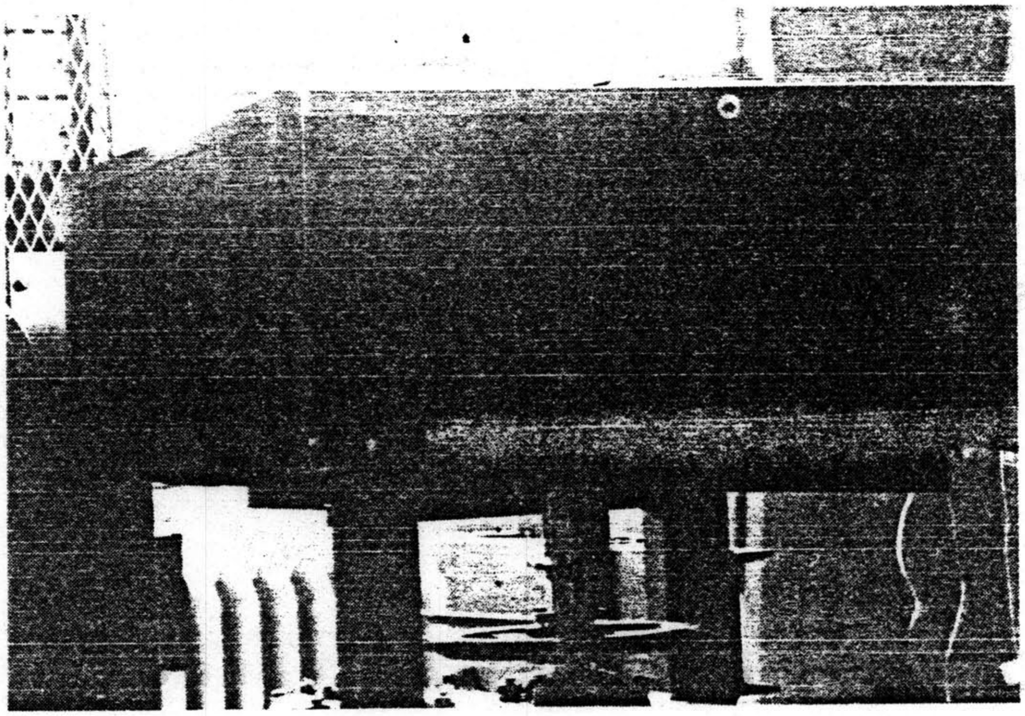

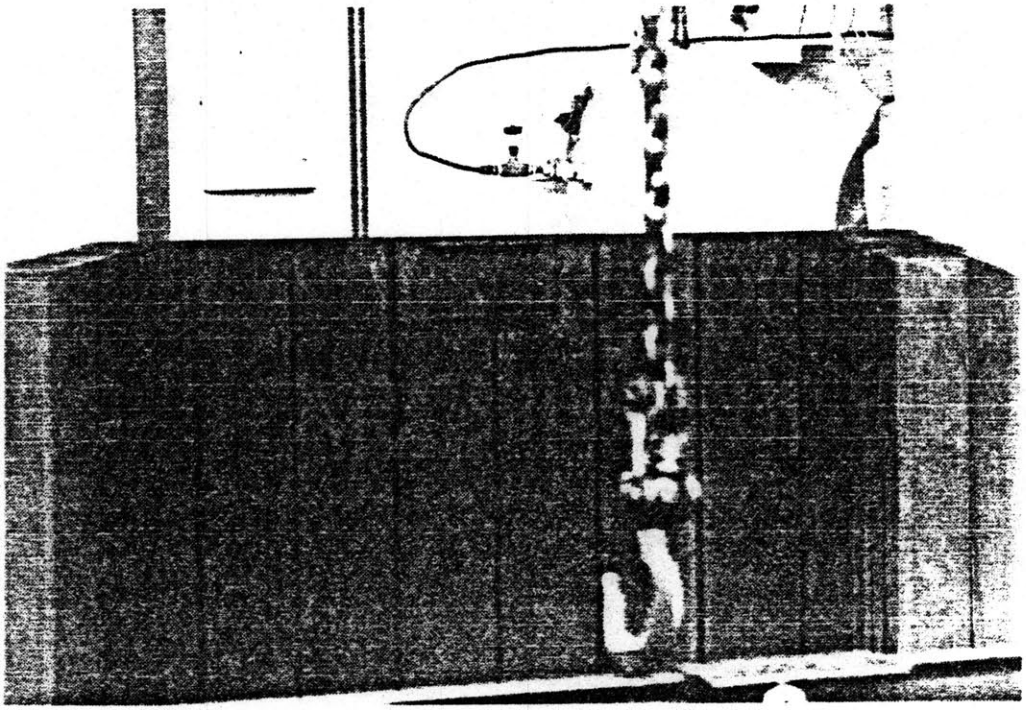

Figure 5.2c (above)
Figure 5.2d (below) Plywood enclosure affixed to rotating test bed. Movable plywood and oak enclosure for additional protection is shown in Figure 5.2d.

the stationary frame. Figure 5.2c shows the slip rings, one of two slip ring brush holder pieces, and a micarta ring glued to the shaft beneath the slip rings which holds the leds used in optical data transmission. A steel frame housing 4, 1/2 in. plywood boards encloses the turntable. Additional safety protection in the event of a catastrophic material failure of any piece of the rotating test bed is provided by the movable plywood and oak enclosure shown in Fig. 5.2d. The enclosure is made from 4 in. X 6 in. beams attached to sheets of 3/4 in. plywood sheet using 3 in. lag bolts. This additional structure is on casters and is rolled around the experiment for high speed tests.

V.C Liquid container

The fluid filled container itself is pie shaped. It is a bolted aluminum structure which holds three lexan windows in place. A picture of the container in an early stage of contruction is shown in Fig. 5.3a. The container was built with windows in the front, in the top plate and on the two sides because it was not clear at first how best to view the natural convection flow field within the container. (However, the maximum internal pressure is limited by the stresses in the outer curved lexan plate and this design prevents testing with high vapor pressure Freon 12.) The aluminum structure consists of five pieces: a 1 in. thick base plate, a back wall machined out of a solid block of aluminum which also has a machined out chamber for a cold water reservoir , two side plates and a curved outer plate. These pieces all bolt together and clamp the various lexan windows tightly in place. A cover plate of aluminum with another lexan window bolts to the top of the container. Liberal amounts of RTV

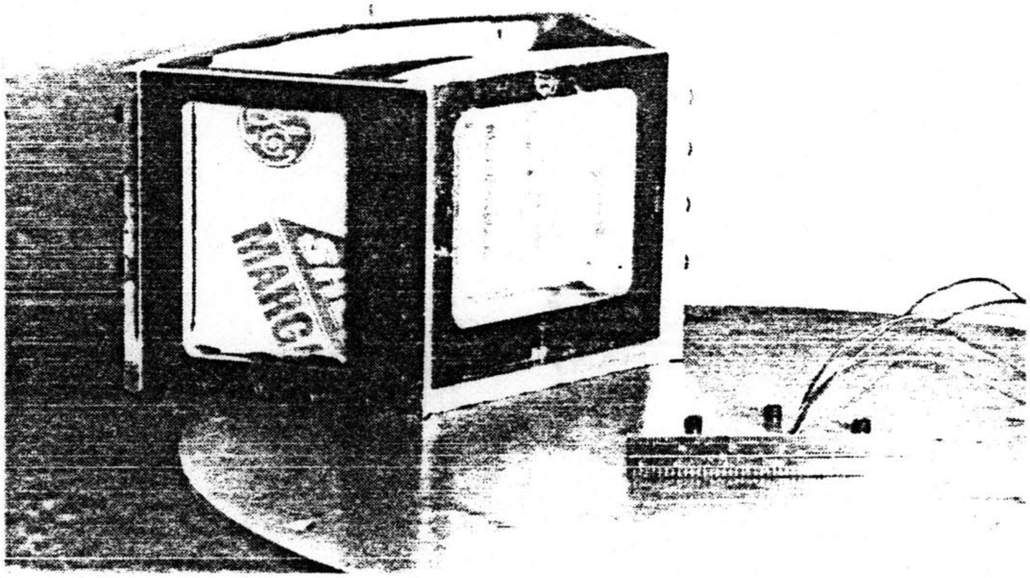

Figure 5.3a Container at an early stage of construction. Wires shown emerging from center of turntable come from slip-rings.

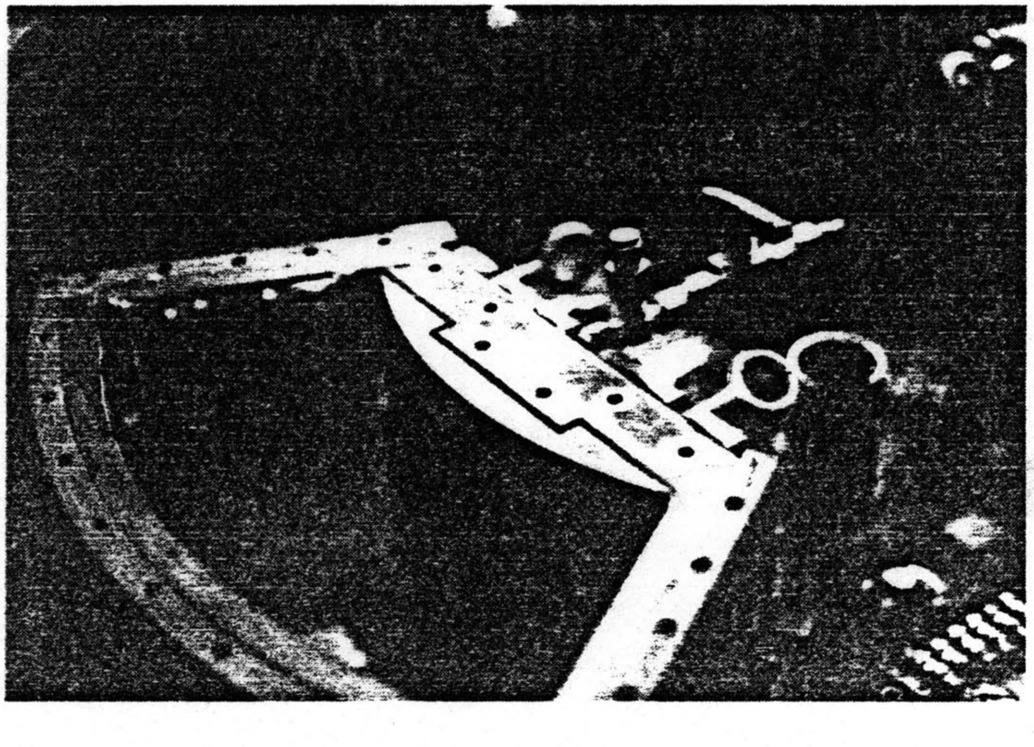

Figure 5.3b View of container without top plate. Grooves cut in top of rear reservoir aluminum block allow the container to be filled with water without trapping air inside. Container is filled off of turntable, with the inlet valves facing upwards.

silicon rubber are used to make a liquid seal between the lexan and aluminum and between the curved lexan window and side lexan window. A gasket of neoprene is used between the top cover plate and the container body.

The container is removed from the turntable whenever it is refilled with water, retrofit with new heaters or thermocouples and whenever the particle smeared windows are cleaned. The container bolts to the turntable with 5, $^1/_4$ in. bolts and 2, $^1/_2$ in. shear pins fix the position of the container at a precise location. Figure 5.3b shows grooves cut in the top of the rear wall of the container. The grooves allow the container to be filled with water or any other fluids without having air bubbles trapped inside. Fig. 5.3b shows the two valves and associated tubing which communicate with the large reservoir chamber and through which the container is filled.

All the aluminum used in this container is 6061-T6. The outer curved piece of aluminum was cut from a piece of rolled cylinder of 5052-H32 al. with a 25 in. id. The aluminum pieces were anodized before the final container assembly. The container windows are made of lexan. This polycarbonate is reasonably strong and ductile. The particular grade of lexan used is MR4000 which has a mar-resistant coating which makes the lexan difficult to scratch and less susceptible to crazing in an alcohol environment. The mar-resistant coating however, does reduce the transparency somewhat. The outer, 1/2 in. thick curved window was thermoformed to a 12 in. curvature by first heating an appropriately sized piece of lexan in a furnace and then bending the hot lexan over a wooden mold of slightly smaller curvature.

V.D Rotating electronics package and stationary data acquisition

The analog output from the various thermocouples within the liquid container are digitized in an electronics package mounted on the turntable and then transmitted serially through optical slip rings to a micro computer in the stationary frame. The rotating electronics package can be seen in Figure 5.4. Important characteristics of the rotating data acquisition system are summarized in Table 5.4[25]. Figure 5.5 shows the Imsai 8080 processor, the Compupro disk drives, Tektronix terminal and the television screen which together form the stationary part of the data acquisition system. Figure 5.6 is a close up of the television screen. The various channels displayed show the output of the themocouples and voltage taps installed in the rotating container. Although there are 16 channels displayed on the screen, only 11 of these are avilable for use. There are 4 channels grounded internally in the rotating data acquisition box in order to provide a zero reference for the other signals. Another channel measures the output of an absolute temperature' sensor. This sensor comes in a five pin can package and is soldered into the upper cinch connector of the electronics package. This sensor is shown in Fig. 5.4. There is a single copper/constantan reference junction for all the thermocouples inside the container and this junction is soldered to the case of the absolute temperature sensor. The data acquisition system thereby measures not only the ΔT between the experiment thermocouples and the reference junction, it also records a signal which is proportional to the actual temperature of the reference junction as well. All the signals measured are filtered through an RC filter with a rolloff frequency of

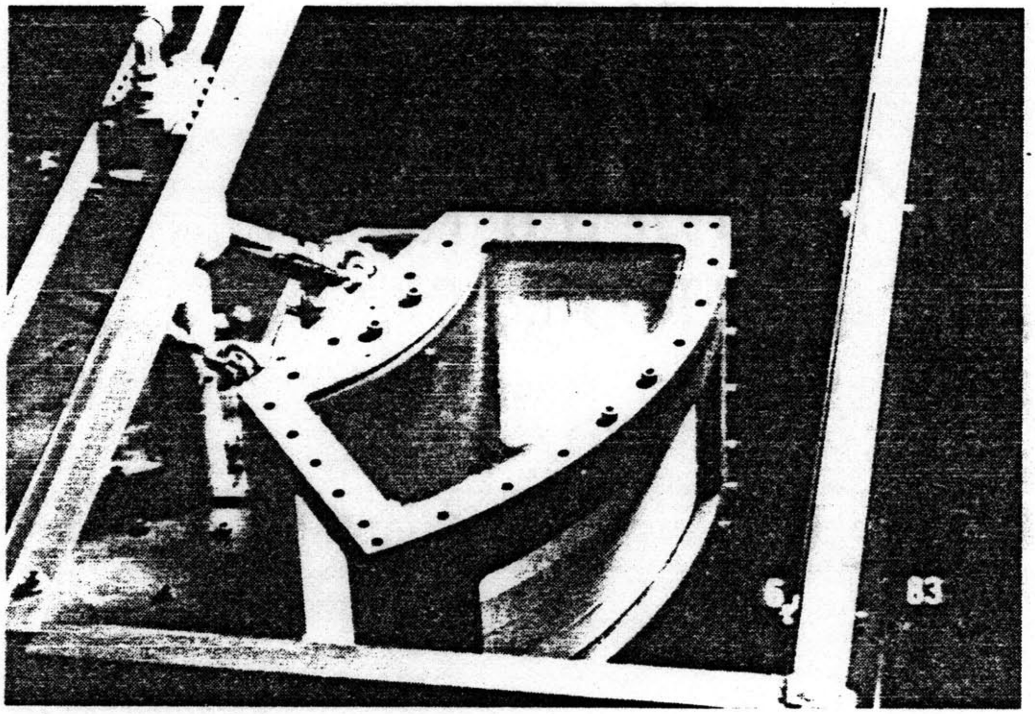

Figure 5.4 Container shown affixed to turntable. Rotary union at turntable centerline allows water to be pumped through container rear reservoir. This union was never used because no steady state heat transfer tests were performed.

Table 5.4 Electronics Box electrical Design Parameters [25]

1. 16 differential channels with a full scale range of 5mV and a common mode range of 10 volts (4 channels internally grounded).

2. Each input channel has a single pole low pass filter with a rolloff at 0.8Hz.

3. An absolute temperature thermometer is provided to measure the reference junction temperature of any thermocouples used.

4. All signals are multiplexed at low levels with solid state CMOS multiplexors.

5. A monolothic instrumentation amplifier with a voltage gain of 1000 is used to amplify all signals prior to digitization.

6. All signals digitized with a 12 bit A/D converter, this gives a maximum resolution of appr. +-5µv.

7. Parallel data from the A/D converter along with the channel number are converted to serial data and transmitted to the stationary frame through an optical slip ring with a self-clocking frequency-independent scheme. All logic is CMOS to minimize power dissipation.

8. Built in voltage regulators and charge storage capacitors help to minimize the effects of slip ring bounce.

9. 11 channels are available to measure any voltages needed, 4 of the 16 channels are internally grounded and 1 channel is connected to a matched pair of NPN transistors configured as an absolute temperature thermometer.

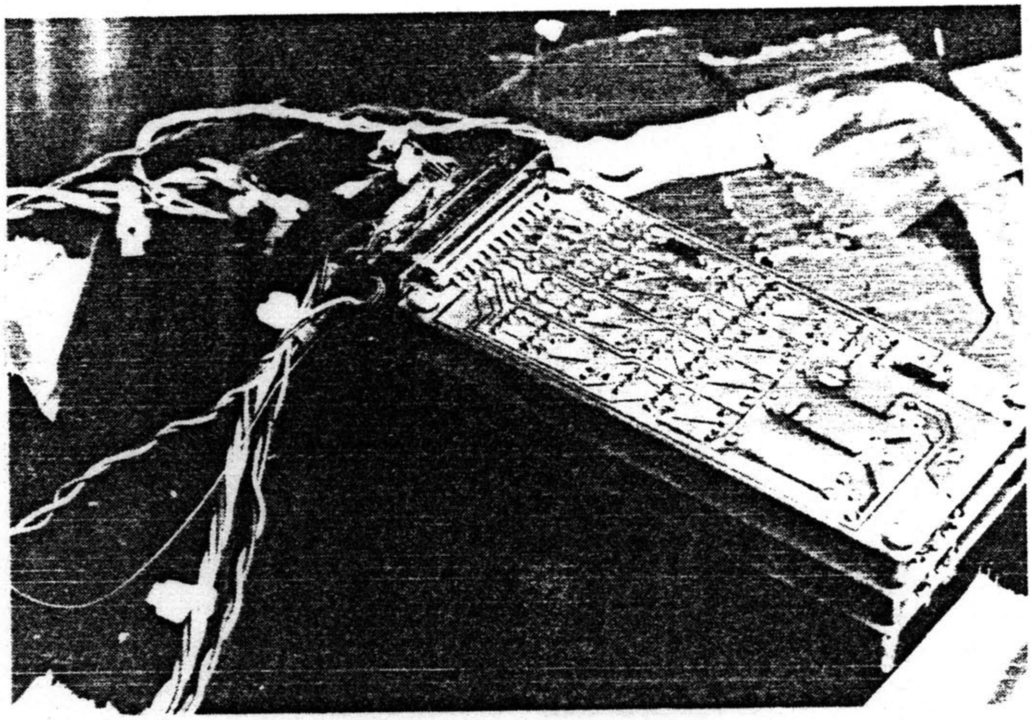

Figure 5.5 Rotating electronics package with absolute temperature sensor shown soldered to appropriate connector. The reference junction for all thermocouples is soldered to the outside of the can of this absolute temperature sensor.

Figure 5.6 Stationary data acquisition system.

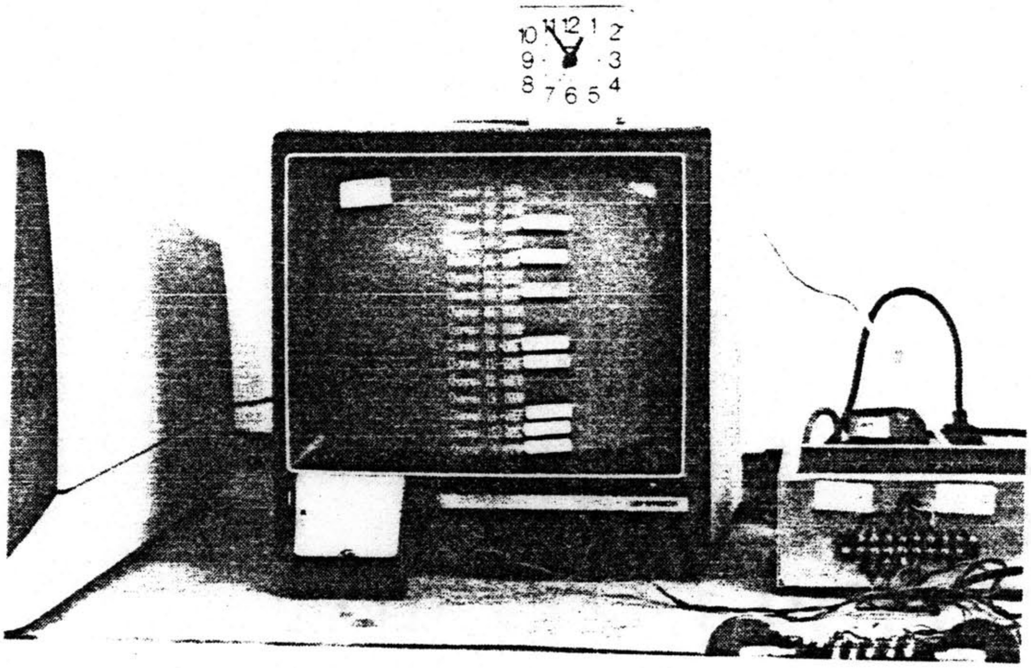

Figure 5.7 Data is simultaneously displayed on monitor and stored in computer RAM. Data is transferred to disk after test is completed.

0.8Hz. A 16 channel multiplixer steps through each input channel, 12 signals plus 4 ground signals. The signal is then amplified by an extremely stable (0.5μv/°C) monolithic instrumentation amplifier. The analog output is then digitized with a 12 bit A/D convertor. The amplifier gain is set at 1000 with a full scale output voltage of 5V, allowing inputs at each of the 16 channels of up to 5mV. The maximum resolution of the system is thus $5mV/(2^{12})$ (where 2^{12} is the resolution of the last bit of the 12 bit A/D convertor) =1.22μV. The copper constantan thermocouples have a sensitivity of roughly 40μV/°C . The data acquisition system is thus theoretically able to resolve temperatures to within 0.03°C, though the accuracy of the thermocouples themselves is only 0.5°C. Note, however, that the signal input filters limit the realistic frequency response of the system to less than 0.5Hz. Since 500 rpm, the experiment design speed, corresponds to 8Hz., events occuring within the container at frequencies on the order of the frequency of rotation will certainly be missed by the data acquisition system. The same statement is true, however, of any noise. Finally, the parallel output of the A/D convertor along with a coding signal to mark the channel number are converted into a serial data string and transmitted to the stationary frame through an optical slip ring. The power to drive the rotating electronics and the heater are supplied via regular slip rings.

V.E Heaters

Thin, flexible Minco heaters were taped or glued onto the inside of the outer, curved lexan window. Fig. 5.9 shows one of the heaters used. The leads of the heater were drawn out of the container in grooves cut into the top of one of the side aluminum plates. The heater leads can be seen in Fig. 5.3c. This particular Minco heater is similar to the others used in the experiment and is a sandwich made of an inconel heater element (0.008 in. thick, 0.020 in. wide) vulcanized to a kapton/teflon film. The lines of the inconel heating element are clearly visible in this photograph. There are two surface thermocouples (0.2 mil thick at the junction, 2 mil thick leads) glued down onto the surface. The thermocouples were laid on top of a thin layer of clear acrylic paint newly sprayed on the heater surface. A second layer of clear acrylic paint was then sprayed over the thermocouple. The overall paint thickness was less than a mil. This heater has only two thermocouples glued to the surface. In other tests using this heater there were four thermocouples on the surface. The junction of one of these thermocouples is always placed directly over a strip of inconel, (which is 0.020 in. wide) , and another thermocouple is placed in the space between two inconel strips. It turns out that there is some variation in surface temperature due to the discreteness of the inconel in the heating element, the thin thermal boundary layer thickness in high Rayleigh number convection, and the thermosphysical properties of kapton/teflon insulation in the heater. The average of these two surface thermocouples is taken to be representative of the surface temperature. In several tests gradients in temperature on the surface of the heater were reduced (at the expense of heater thermal inertia) by gluing a thin copper strip across the heater. The thermocouples were then insulated with acrylic and laid down onto the copper. Thermocouple placement was certainly taken into account when surface temperature were correlated to heat transfer coefficient. (It is more reasonable to consider these heaters as an ensemble of convection elements rather than as a continuous heat source).

The heaters originally designed into the experiment were very thin pieces of glass with a few hundred angstroms of SnO sputtered onto the surface. The heaters proved too fragile to allow for repeated repositioning within the container. Minco heaters were chosen because of their ruggedness and because the lead wires were insulated. When power leads are exposed in the water there are considerable thermocouple errors associated both with direct current conduction through the thermocouples to the electronics ground and capacitive coupling between the sensors and the power leads.

Table 5.3 shows the dimensions and placement of the heaters used in the experiments. Figure 5.9 shows a heater similar to that of Fig. 5.8 taped to the lexan window. Fig. 5.10 shows two thermocouples glued to the heater surface and an array of copper/constantan thermocouples supported by a piece of stainless steel welding rod. These thermocouples were used to measure fluid temperatures near to the wall on either side of the heater, and to track the path of the plume away from the wall.

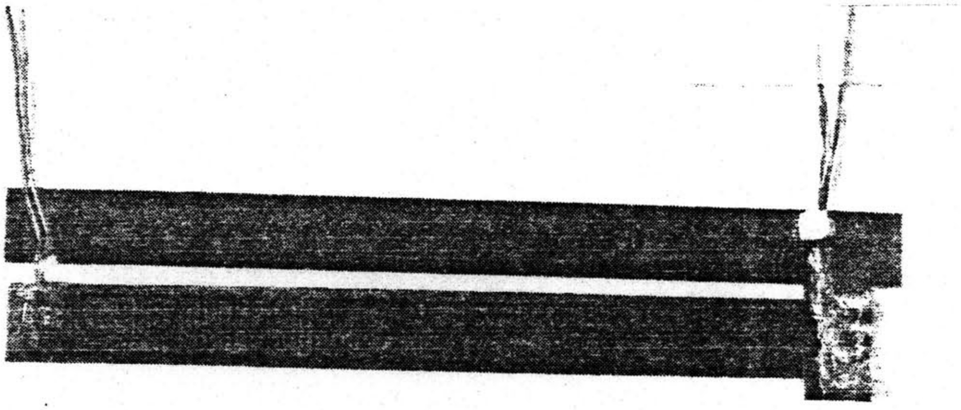

Figure 5.8 Minco heater with pair of thermocouples attached to surface. One thermocouple is placed ontop of heater element, one is placed in the space between.

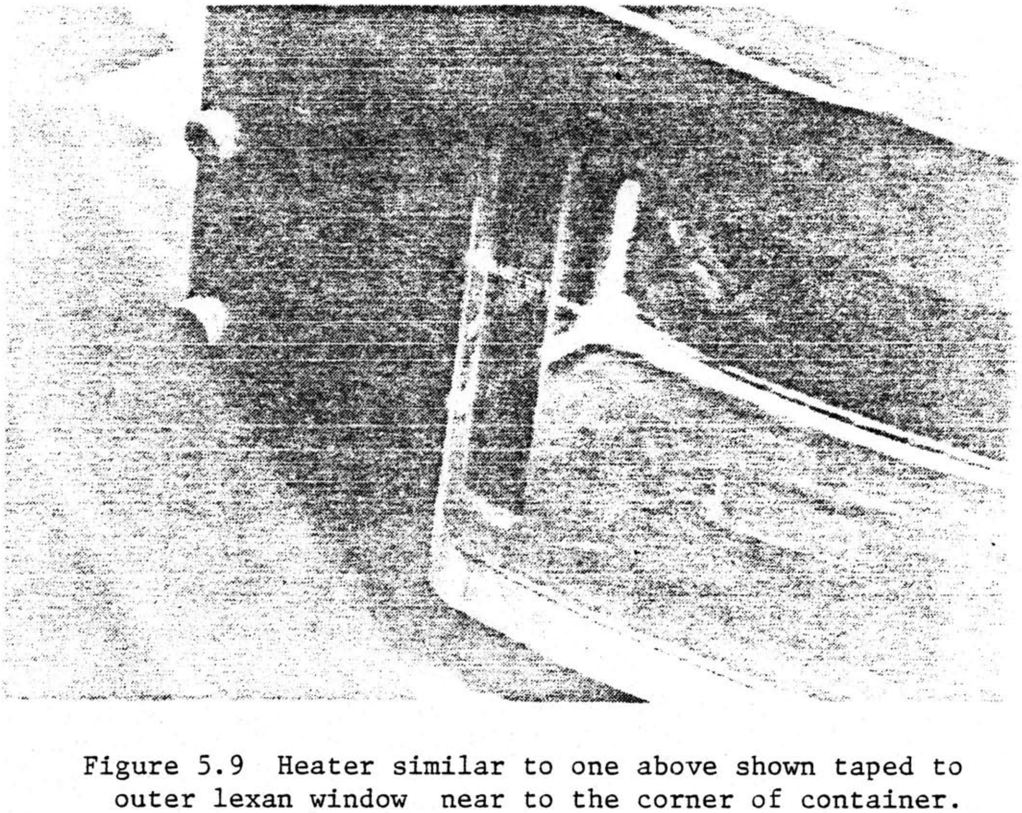

Figure 5.9 Heater similar to one above shown taped to outer lexan window near to the corner of container. In this configuration, heater simulates a vertical line heat source.

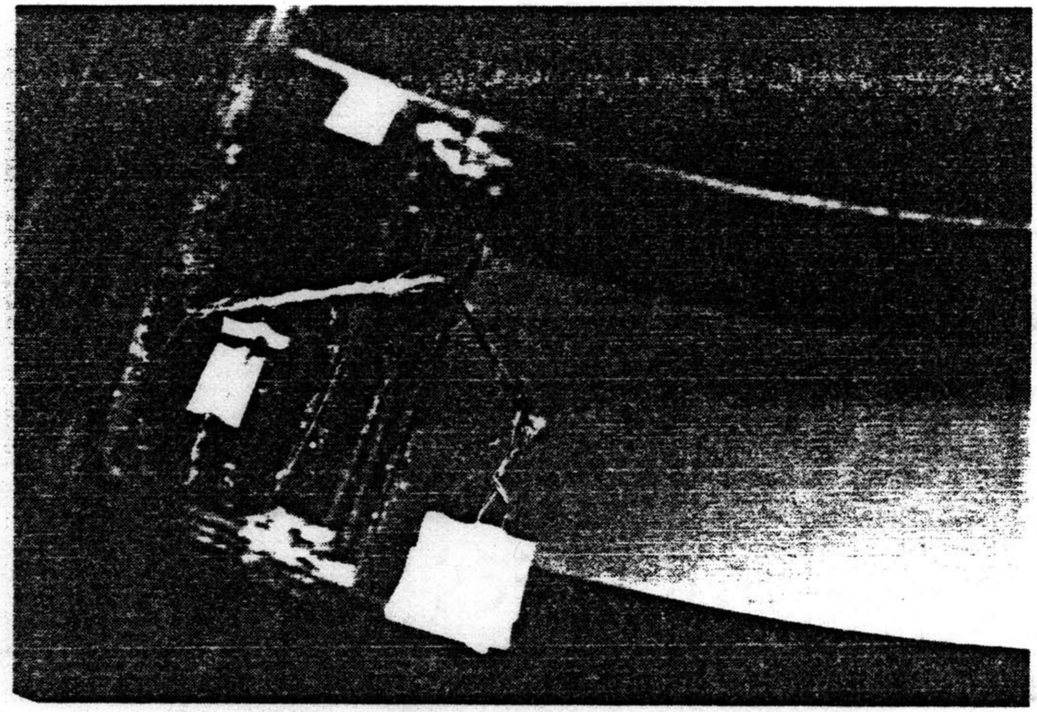

Figure 5.10 Heater of previous figure and array of thermocouples to track trajectory of plume. There are two thermocouples on either side of heater attached to the lexan and a fan of three thermocouples mounted on a piece of stainless steel welding rod.

CHAPTER 6

QUASISTEADY HEAT TRANSFER TESTS

This chapter includes a discussion of quasi-steady heat transfer test procedures, and measured surface heat transfer coefficients. Surface h was found to be independent of heater length and of fluid viscosity. Appropriate correlation of Nu is found to be: $Nu = .107(RaPr)^{.33}$.

VI.A Testing Procedures

The quasi-steady thermal tests were a series of 156 experiments designed to measure the surface heat transfer coefficient associated with free convection from small heaters of various crosssections. Heat transfer measurements are discussed apart from the plume flow visualization studies of Chapter 4 because the surface heat transfer coefficient is apparently unaffected by the trajectory of the plume or the direction of rotation of the container. The data to be presented here includes tests with heaters mounted near to the radial side walls of the container where the resulting plumes have been observed to attach themselves to the nearest radial wall, as well as tests where the plumes have been observed to move in radially. The thermal boundary layers are found to be conduction dominated, quite a bit smaller than the observable fluid momentum boundary layers. This point will be discussed at length later in this chapter.

The tests described in this chapter are called quasi-steady because there is no cold reservoir in the container other than the bulk fluid itself (including a small reservoir of fluid in a chamber in the rear wall of the container). The duration of the tests were short enough so that the slow increase in bulk fluid temperature during the test did not introduce errors into the calculation of the ΔT for heat transfer. At the maximum heater input power of roughly 40 Watts the rate of change of bulk fluid temperature in the container was 0.005°C/s, 0.3°C/min.

The quasi-steady heat transfer experiments involved the following sequence of events. The turntable was accelerated to some rotational speed between 300 and 600 rpm and allowed to idle without any heater power for roughly 3 to 5 minutes. This idling time at steady speed insured that the container fluid was in solid body rotation. The idling time at high rotational speed also insured that the multiplexer chip in the rotating data acquisition system was isothermal. The rotating electronics package generates a considerable amount of heat which is removed by forced convection on the turntable surface as it rotates. Temperature gradients in the multiplexer chip tend to introduce errors in the measured thermocouple voltages. Whenever the turntable is accelerated from a low rotational speed some time must be allowed for thermal transients to disappear in the electronics before testing begins. With the fluid in solid body rotation and all installed thermocouples indicating the same fluid temperature, the software used to store data in computer memory was then enabled. A few seconds later the heater power was turned on. The heater was left on for roughly a minute and then turned off. Data collection was disabled at this time . The data in memory was converted to engineering units such as temperature or voltage and then transferred from computer memory onto disks to be analyzed and plotted at a later time. The rotor was then deccelerated to some lower speed to facilitate turbulent mixing of the bulk fluid. When temperatures throughout the container were more or less uniform, the experimental procedure was repeated.

Fig. 6.1 shows the thermocouple output from a sample data run. The few seconds of data at the beginning of the plot were taken in the period of time between enabling the data collection software and energizing the heater. The data collected in this short period is averaged to represent ambient fluid conditions in the ΔT for the heat transfer coefficient. As soon as the heater is turned on the temperature on the heater surface begins to rise. The time constant for the temperature rise on the surface is limited by the thermal inertia of the heater and the surface heat transfer coefficient. There is also a small amount of heat conduction back into the lexan wall but with such high heat transfer coefficients on the wetted surface this error is negligible. An appendix at the end of this thesis estimates the conduction error. It is apparent from the plot shown in Fig. 6.1 that a quasi-steady state is established quickly on the heater surface. The oscillatory nature of the recorded surface temperature can be explained from observations of dye on the heater surface. The fluid flow off the surface of the heater appears like that of a laminar boundary layer on a hot plate facing upwards. Two thin boundary layers begin on either side of the heater and meet at the center of the heater. Here the two boundary layers merge to form a plume which moves radially inwards. Boundary layer instabilities of the sort associated with convection off of horizontal surfaces were not observed [26], but it was noticed that the dye was swept off of the heater surface in waves rather than a continuous flow. It was also observed that the point where the plume turned to move radially inwards tended to wander about on the heater surface. It is fair to assume that these effects are related to the vacillations in surface temperature.

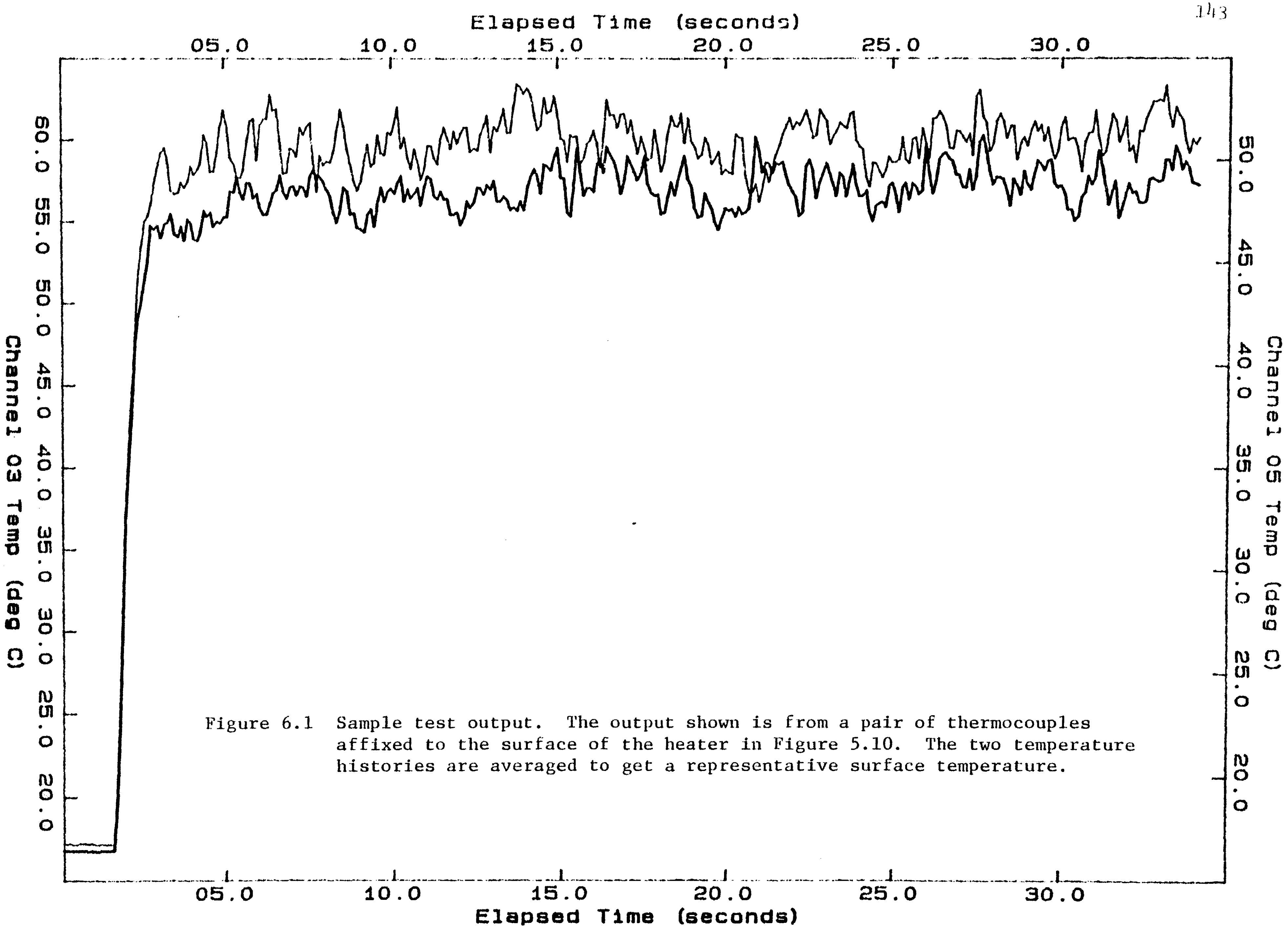

Figure 6.1 Sample test output. The output shown is from a pair of thermocouples affixed to the surface of the heater in Figure 5.10. The two temperature histories are averaged to get a representative surface temperature.

An average surface temperature was calculated by time averaging the various thermocouple outputs over periods of from 5 to 10 s.

There were between three and four thermocouples placed on the surface of each of the heaters used. The temperature difference, $T_s - T_a$, used to calculate the surface h was based on a weighted average of these thermocouple measurements. As mentioned previously, the discreteness of the heater strip elements in the kapton heater package resulted in gradients in surface temperature. The surface temperature was therefore taken to be the average of a thermocouple directly over a heater strip and one placed in the space between. The thermocouples were placed near to the middle of the heater element where the two fluid boundary layers merged and flowed radially inwards. In tests using the heater with a copper isothermalizer strip on the heater surface the average of all the surface temperatures was used in calculations.

VI.B Test results

Of the 156 heat transfer tests, over 100 experiments were performed using triple distilled water as the working fluid. Surface temperature data was gathered using four different heater configurations, rotational speeds from 300 rpm to 600 rpm and surface heat fluxes from $0.2 W/cm^2$ to $20 W/cm^2$. The maximum surface ΔT above ambient was on the order of 50°C insuring that no boiling had occured. A surface heat transfer coefficient was established using the following formula:

$$h=Q/(A\Delta T) \qquad (6.b.1)$$

where input heat flux is calculated from a measured heater voltage and ΔT is based on a weighted average of surface temperatures measured minus the surface temperature at the beginning of the test. The surface heat transfer coefficient was then formed into a Nusselt number with a length scale based on half the heater width in the azimuthal direction. The Rayleigh number for each test is of the form

$$Ra=\omega^2 R_o \beta \Delta T (l/2)^3 Pr/\nu^2 . \qquad (6.b.2)$$

The Rayleigh number is calculated based on measured rotational speed, a length $l/2$ equal to the half width in the azimuthal direction, R_o of 30.5cm. (the inner radius of the outer lexan wall), and fluid properties based on the mean of the surface and ambient temperatures. The results are shown plotted in Fig. 6.2. The data over this whole range of Rayleigh numbers from 10^5 to 10^{10} falls most nearly on a curve of the form:

$$Nu= .23Ra^{.32} . \qquad (6.b.3)$$

Fig. 6.3 shows the same data plotted along with the most commonly found laminar and turbulent Rayleigh number natural convection correlations.

At this point several comments should be made. The data shown here represents tests with a long heater mounted vertically (heater #2 in Table A.I.1, $l/2$=0.57cm.), a long heater mounted azimuthally (heater #3, $l/2$=6.45cm.), and short heaters (heater #1,4 l=1.79,2.36cm.) as well. The fact that all the data falls so neatly onto the same curve does not by itself imply that that the convection field is two dimensional- since the length dependence nearly vanishes in the correlation of Eq. 6.b.3. It does show that the surface heat transfer coefficient is not adversely affected by the additional fluid dragged inwards by the bouyant fluid. The two-dimensionality of the flow itself is based only on observation. The lack of a clearly defined laminar, turbulent transition in the plotted data

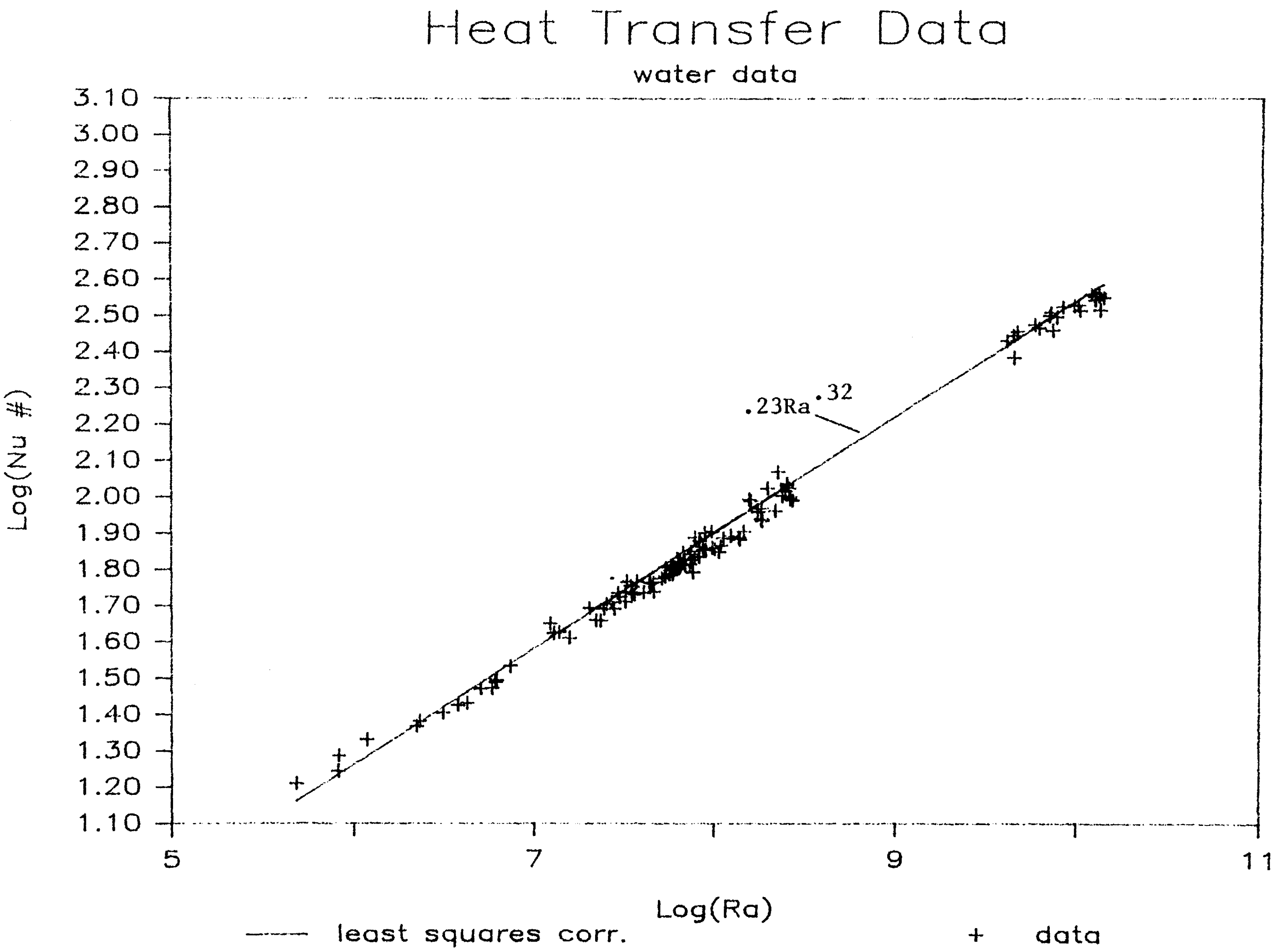

Figure 6.2 Water data only, graphed vs. Rayleigh Number.

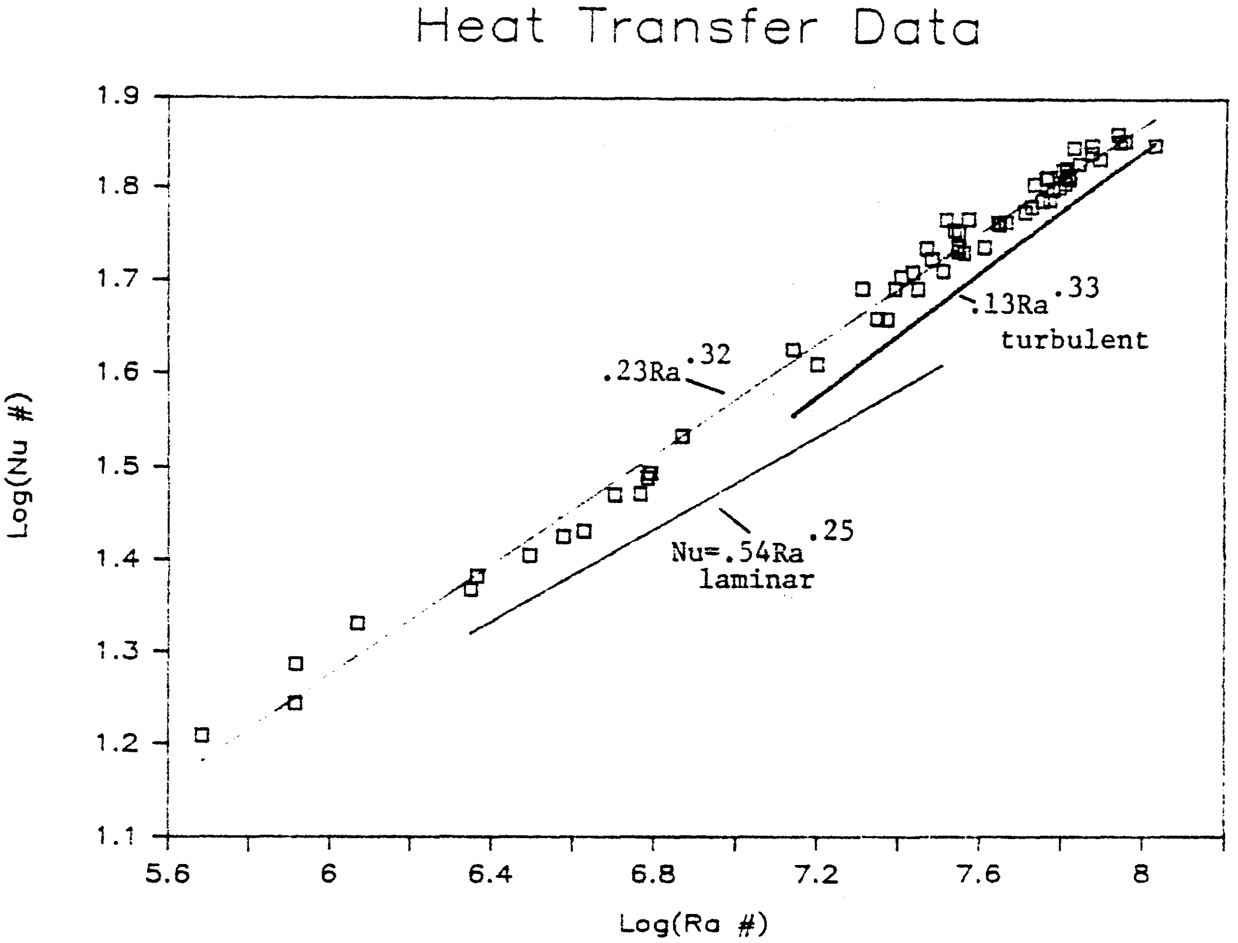

Figure 6.3

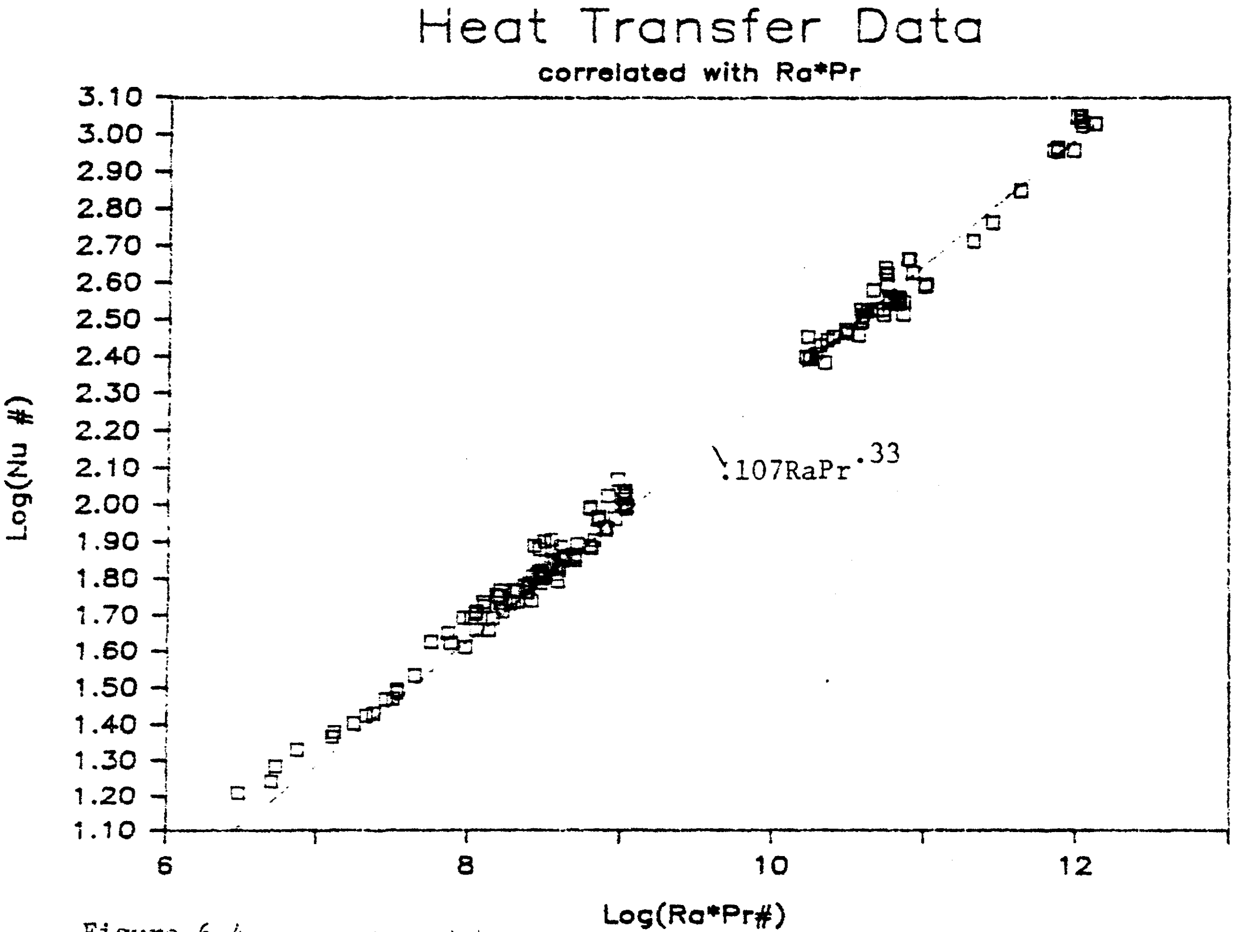

Figure 6.4

does tend to confirm the visual observation of a stable, non-bursting fluid boundary layer. Furthermore, the data includes tests with the container rotating both clockwise and counterclockwise and with the heater mounted both near to and far from the radial walls- with no apparent effect on surface heat transfer coefficient. Measurements were made, however, to determine that the flow was two-dimensional in fluid motion but three dimensional in temperature distribution. Fluid in the moving plume was shown to vary in temperature in the z direction by placing thermocouples on the outer lexan wall above and below a small heater and in the bulk fluid in a plane above and below the heater. No measurable temperature change could be detected in the fluid in these regions. Thermocouples mounted in the interior fluid in the same horizontal plane as the heater registered distinct changes in temperature once the plume had swept by.

VI.C Experiments with glycerine/water and alcohol

To study the effect of Prandtl number on the surface heat transfer characteristics the container was filled with two other fluids: a 31% glycerine/water solution, and isopropyl alcohol. Quasi-steady heat transfer tests similar to the ones performed with water resulted in the data shown in Figures 6.6 and 6.7. The Nusselt number and Rayleigh number were calculated as before but it was clear that the heat transfer correlation obtained previously was not universal. The thermal properties for a 31% glycerine solution were obtained by interpolating between published data for a a 20% and 40% glycerine solution (Appendix III.2). Although the viscosity and thermal conductivity of a mixture are not simple

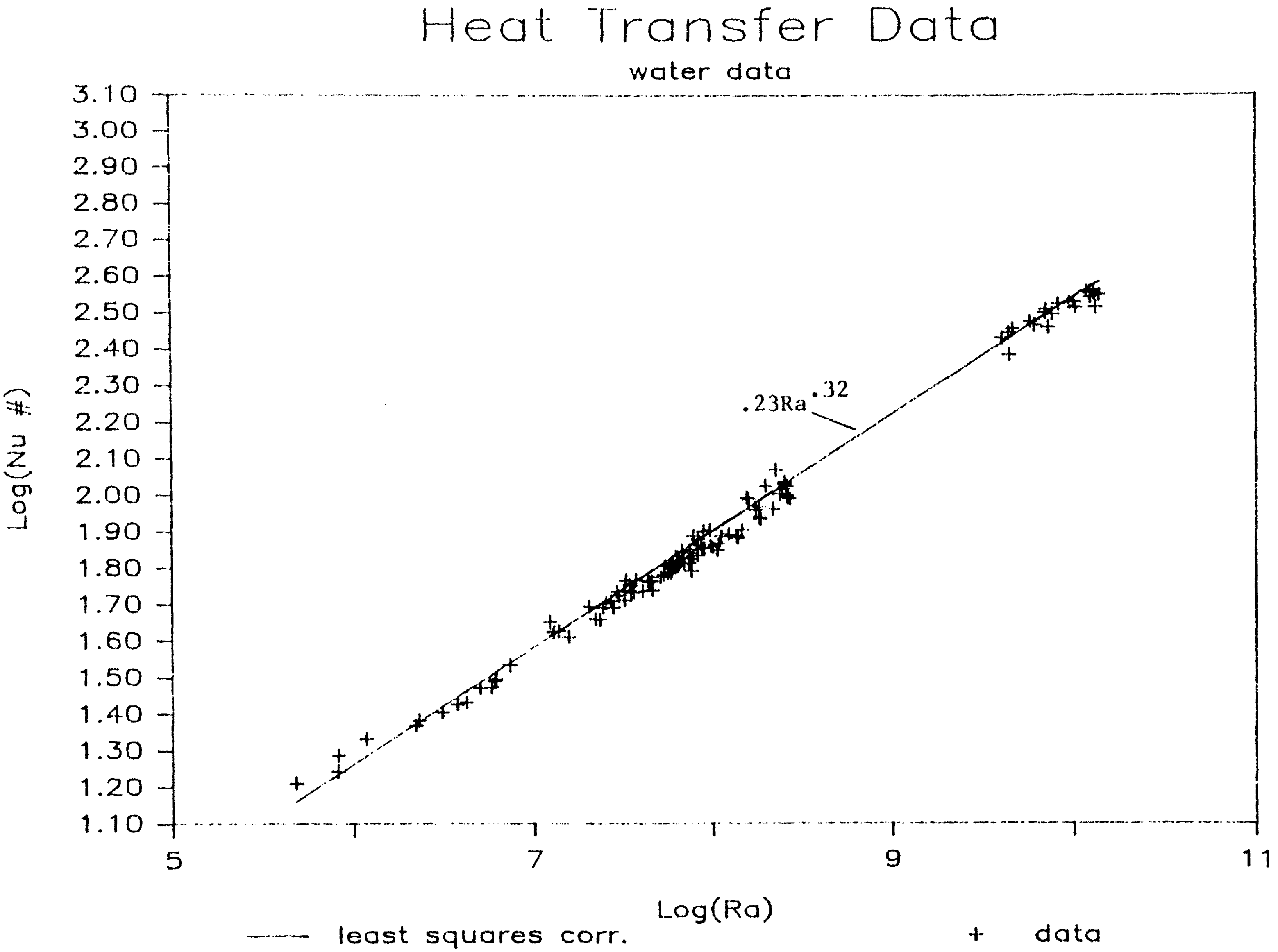
Heat Transfer Data
water data
3.10
3.00
2.90
2.80
2.70
2.60
2.50
2.40
2.30
2.20
2.10
2.00
1.90
1.80
1.70
1.60
1.50
1.40
1.30
1.20
1.10
Log(Nu #)
.23Ra.32
5
7
9
11
Log(Ra)
least squares corr.
+ data

Figure 6.5

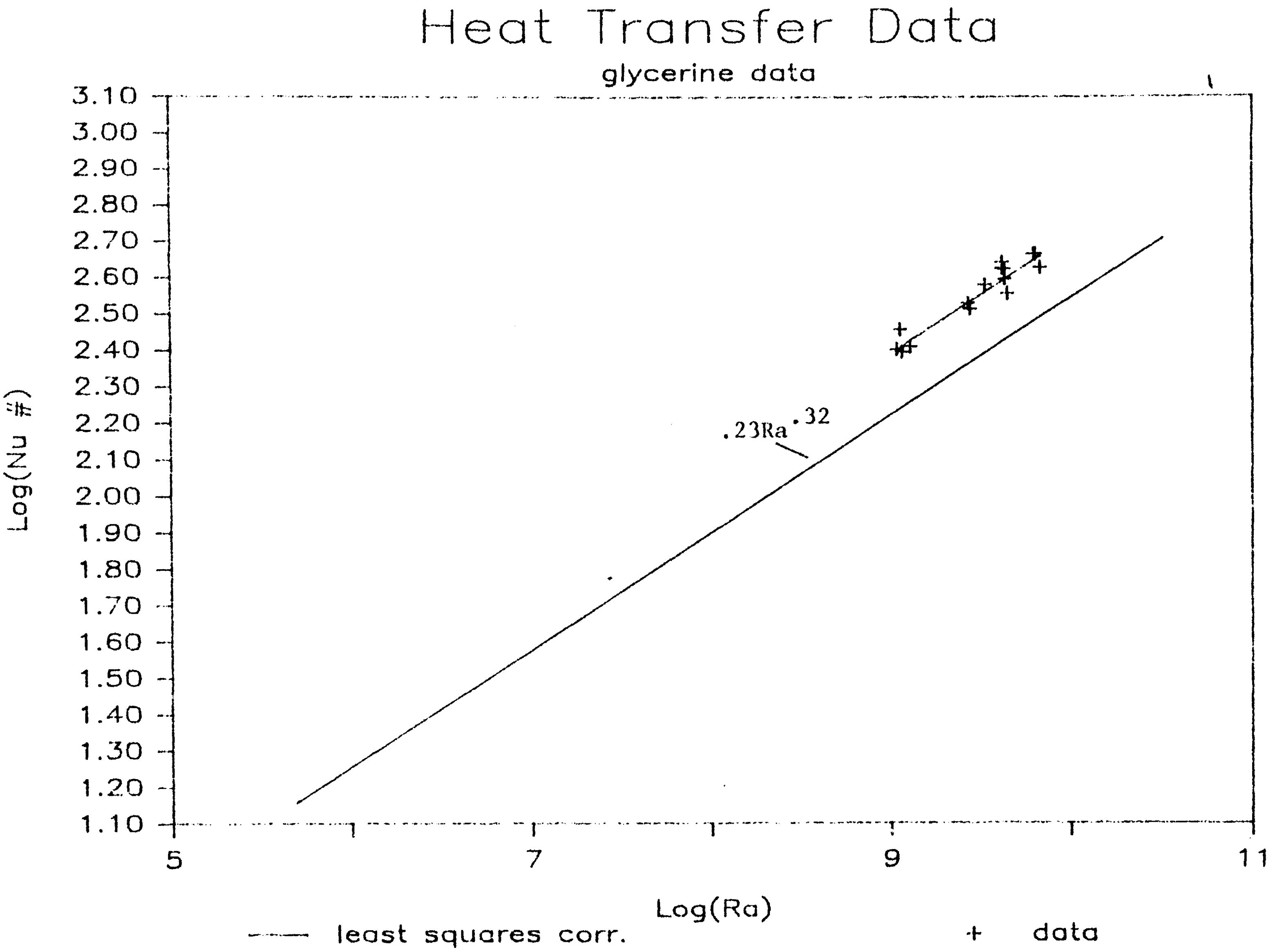
Heat Transfer Data
glycerine data
Log(Nu #)
3.10
3.00
2.90
2.80
2.70
2.60
2.50
2.40
2.30
2.20
2.10
2.00
1.90
1.80
1.70
1.60
1.50
1.40
1.30
1.20
1.10
5
7
9
11
Log(Ra)
.23Ra.32
least squares corr.
+ data

Figure 6.6

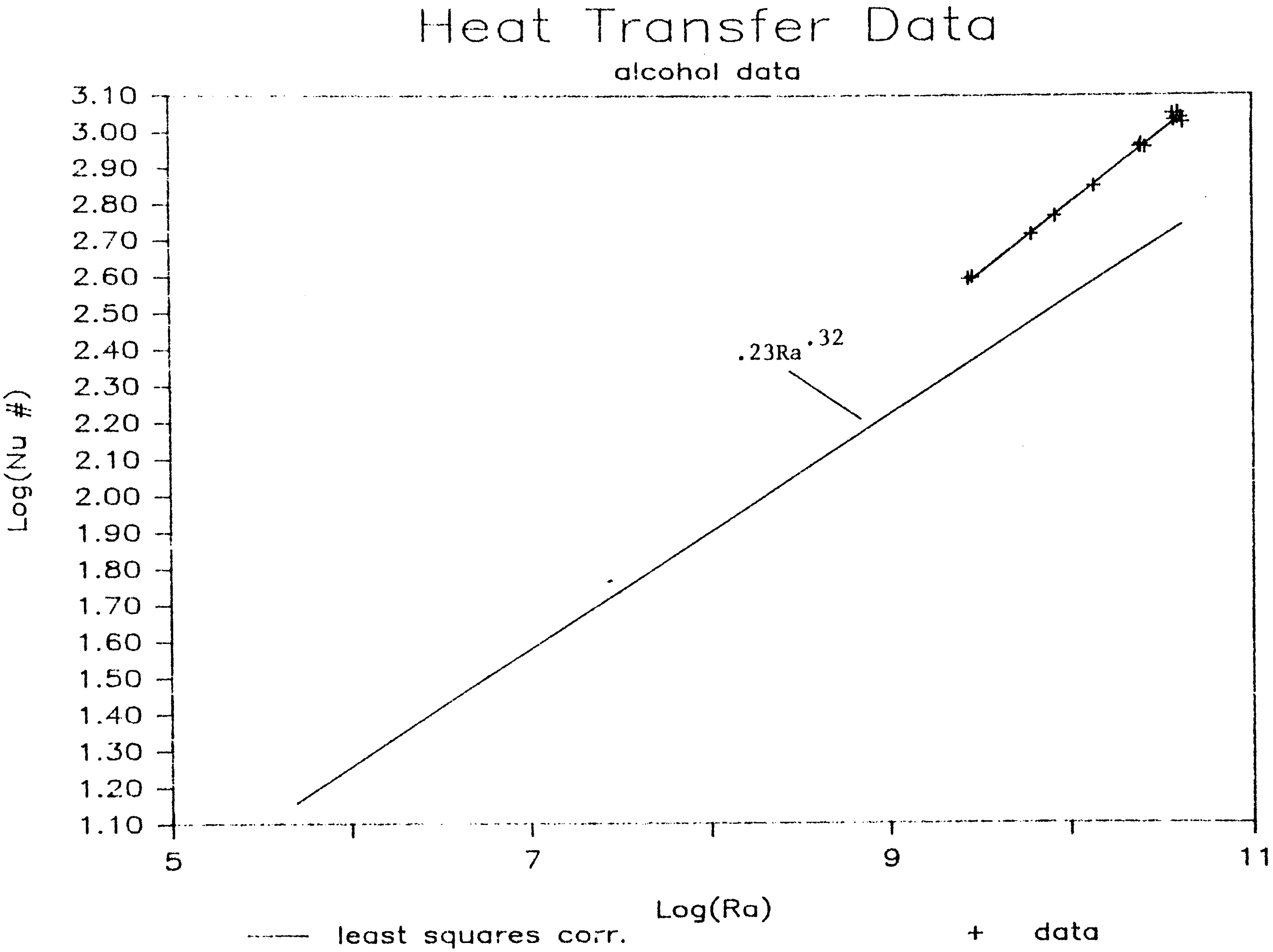
Heat Transfer Data
alcohol data
3.10
3.00
2.90
2.80
2.70
2.60
2.50
2.40
2.30
2.20
2.10
2.00
1.90
1.80
1.70
1.60
1.50
1.40
1.30
1.20
1.10
Log(Nu #)
5
7
9
11
Log(Ra)
.23Ra^.32
least squares corr.
+ data

Figure 6.7

functions of composition (unlike density and specific heat), the former properties are relatively slowly changing functions of composition for glycerine percentages under 40%.

The appropriate dimensionless group for correlating the new data was suggested by comparisons of the ratio of $(Nu/Ra^{.33})$ for each of the glycerine and alcohol data, and some high Rayleigh number water data . This is a technique commonly used in analysing natural and forced convection data to determine the effect of Prandtl number on the heat transfer coefficient. It turned out, surprisingly, that:

$$(Nu/Ra^{.33})_{al}/(Nu/Ra^{.33})_{w} \sim Pr_{al}/Pr_{w} \tag{6.b.4}$$

$$(Nu/Ra^{.33})_{gl}/(Nu/Ra^{.33})_{w} \sim Pr_{gl}/Pr_{w} \tag{6.b.5}$$

where the subscripts refer to the liquids involved (al=alcohol, gl=glycerine and w=water). This result immediately suggested a correlation of the heat transfer data of the form:

$$Nu=a(RaPr)^{b}. \tag{6.b.6}$$

The data was regraphed using Log(RaPr) as the abscissa and the result is shown in Figs. 6.8, 6.9, 6.10 (Figure 6.4 shows all the data on a single curve). A least squares correlation of the data resulted in the relationship:

$$Nu=.107(RaPr)^{.33}. \tag{6.b.7}$$

This result has several implications. The heat transfer coefficient is independent of a heater length scale. In addition, the surface heat transfer coefficient is also independent of fluid viscosity . A correlation of this form suggest that heat transport occurs in a conduction

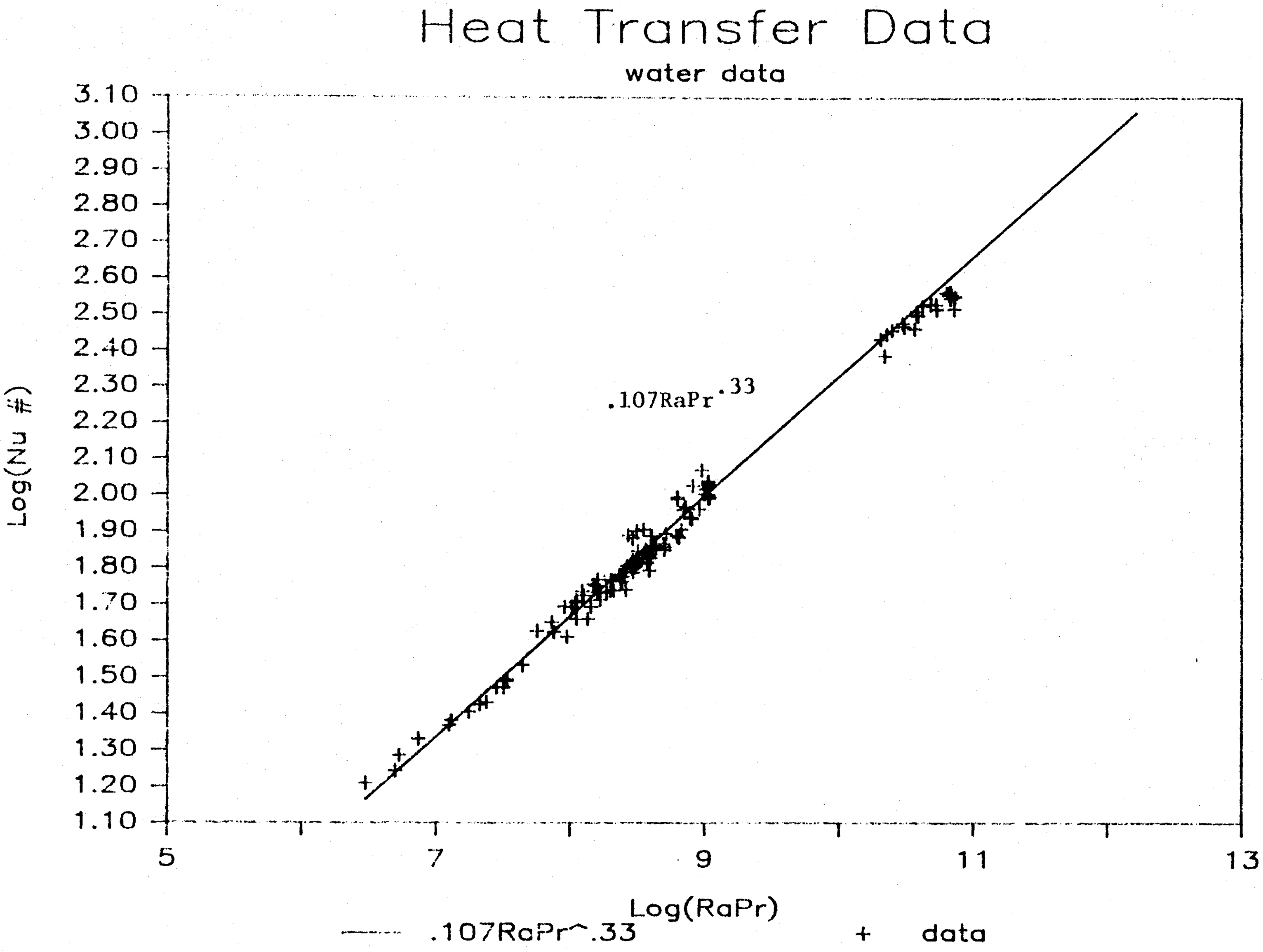
Heat Transfer Data
water data
3.10
3.00
2.90
2.80
2.70
2.60
2.50
2.40
2.30
2.20
2.10
2.00
1.90
1.80
1.70
1.60
1.50
1.40
1.30
1.20
1.10
Log(Nu #)
5
7
9
11
13
Log(RaPr)
.107RaPr.33
.107RaPr^.33
+ data

Figure 6.8

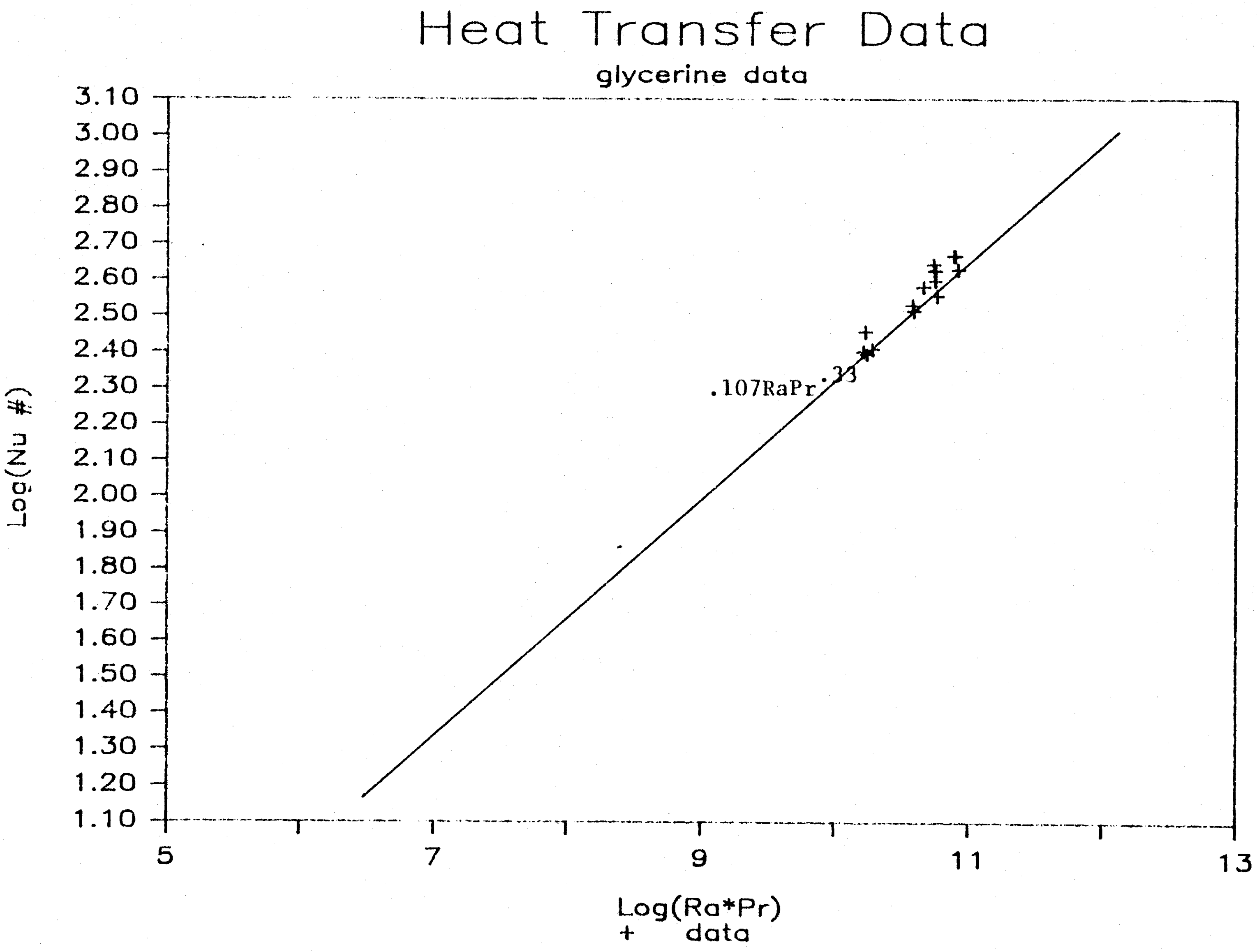
Heat Transfer Data
glycerine data
3.10
3.00
2.90
2.80
2.70
2.60
2.50
2.40
2.30
2.20
2.10
2.00
1.90
1.80
1.70
1.60
1.50
1.40
1.30
1.20
1.10
Log(Nu #)
.107RaPr^.33
5
7
9
11
13
Log(Ra*Pr)
+ data

Figure 6.9

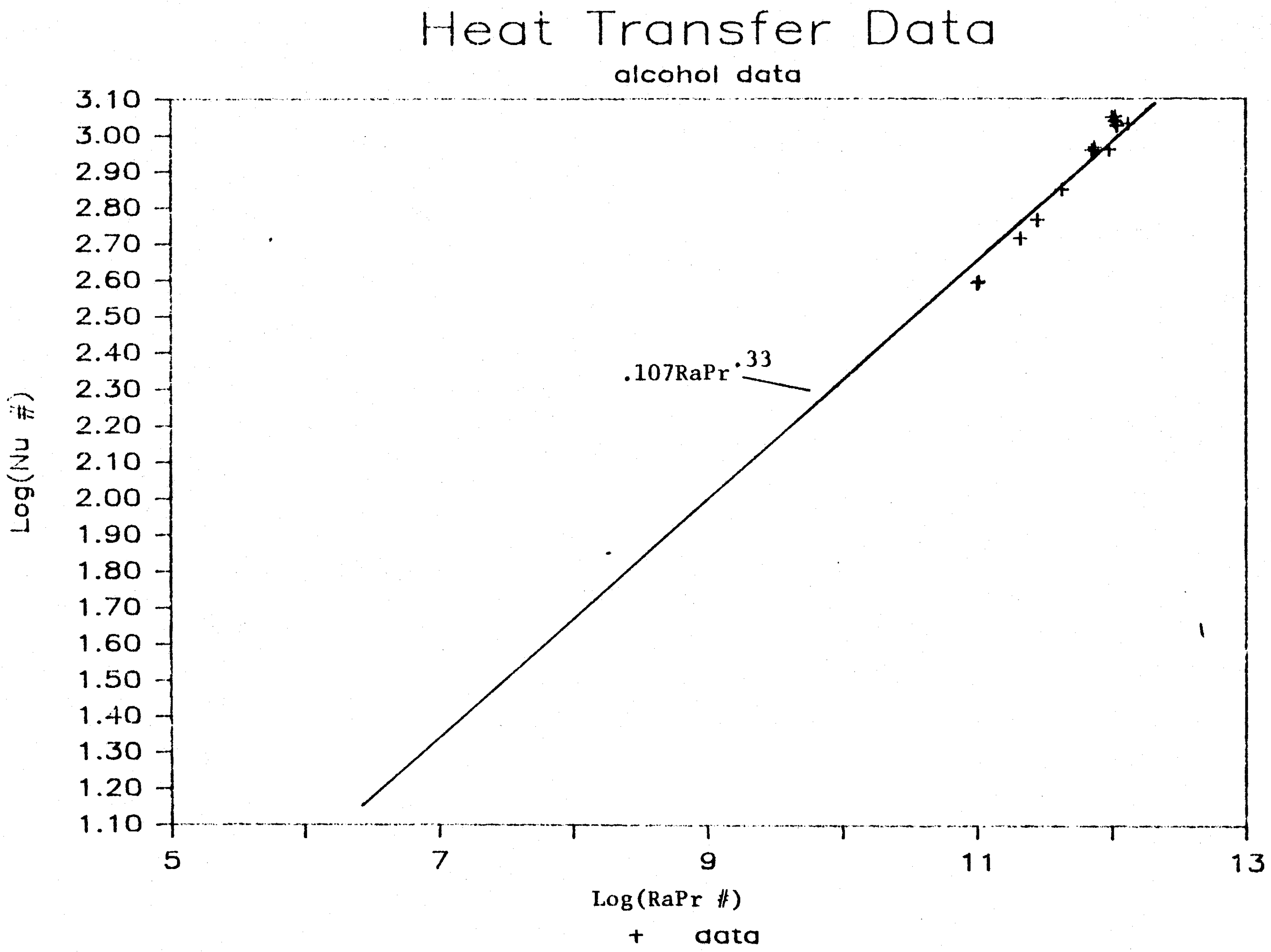
Heat Transfer Data
alcohol data
3.10
3.00
2.90
2.80
2.70
2.60
2.50
2.40
2.30
2.20
2.10
2.00
1.90
1.80
1.70
1.60
1.50
1.40
1.30
1.20
1.10
Log(Nu #)
.107RaPr^.33
5
7
9
11
13
Log(RaPr #)
+ data

Figure 6.10

boundary layer embedded within and much smaller than the observed fluid boundary layer. If one bases an average thermal boundary layer thickness on the surface heat transfer coefficient in the following manner:

$$\delta_t = k/h \qquad (6.b.8)$$

the thermal boundary layer thicknesses established at these Rayleigh number is of order 0.01cm to 0.001 cm. The photographs in Chapter 4 show the considerable extent of fluid motion at high Rayleigh number, a fluid boundary layer an order of magnitude greater than the apparent thermal boundary layer. This tends to corroborate the notion that the heat transfer rate is controlled primarily by conduction. The result receives further confirmation when the transient heat transfer data is examined in the next chapter.

VI.D Natural convection heat transfer coefficient in a non-rotating container

To test the instrumentation and the fluid properties data used to obtain the correlation of the previous sections, several experiments were performed without rotation. Fig. 6.11 shows the container removed from the turntable and positioned so that the curved lexan window was perpendicular to the direction of gravity. With the electronics package cooled by a fan, a heater taped to the lexan window was energized and surface temperatures measured. Fig. 6.12 shows the results plotted along with the usual correlation for laminar natural convection. All the one-g natural convection tests were done with the same heater (heater #3 in Table A.I.1). A correction to the surface heat transfer coefficient is required at such low Nusselt number to account for conduction losses into the lexan,

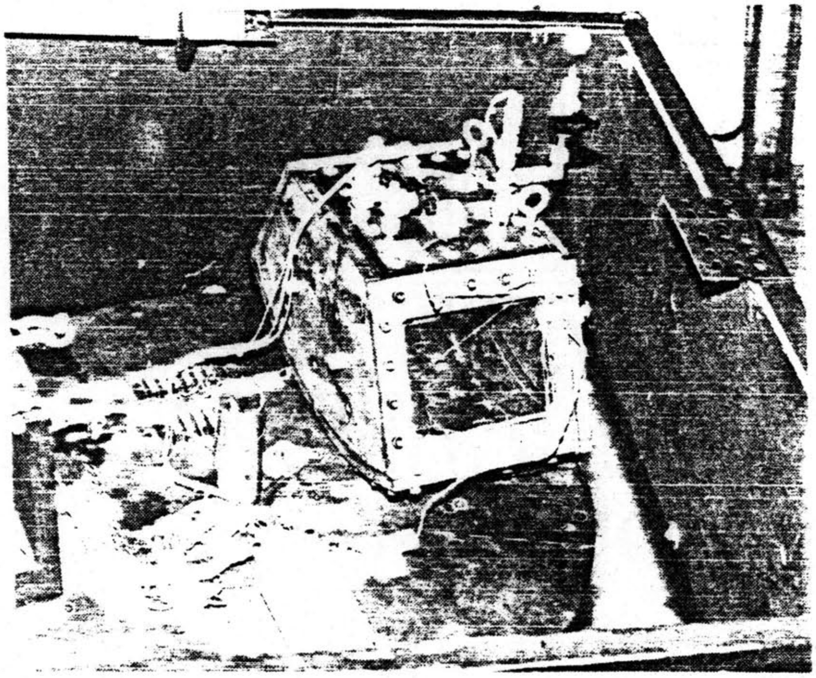

Figure 6.11 Container oriented so that gravity is perpendicular to heater surface.

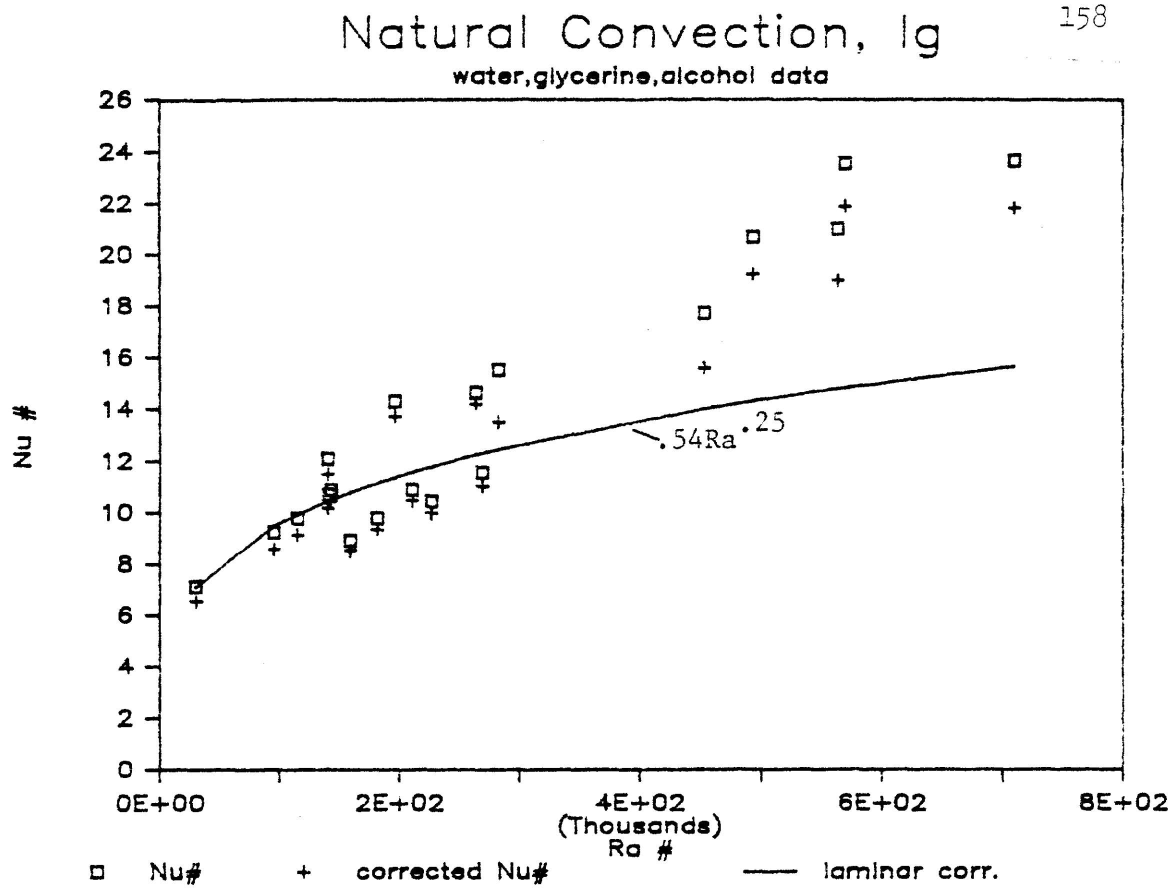

Figure 6.12

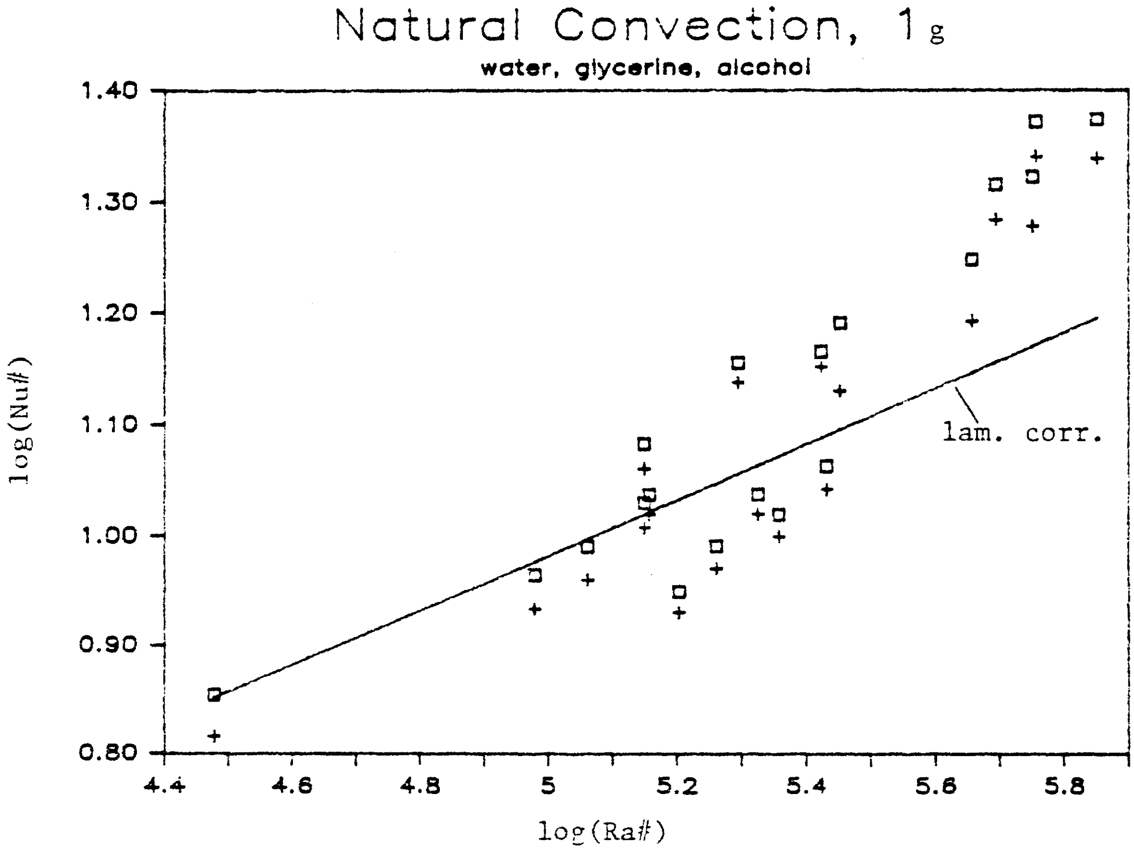

Figure 6.13

and the corrected data is indicated by a +. The length scale used in the Rayleigh and Nusselt numbers is half the smallest dimension of the heater. The thermocouples were placed away from the ends of the heater where the flow would be clearly three dimensional and the latter length scale inappropriate.

The glycerine and water data correlate well with the standard correlation. The corrected alcohol data does not. A plot of the surface temperature history (Fig. 6.14) for the alcohol tests shows strong oscillations on the surface of the heater indicating, perhaps, that at these high Rayleigh, boundary layer instabilities have resulted in shorter effective boundary layers and higher h. Despite the alcohol data, it appears that the natural convection data in 1g is reasonable and that the instrumentation is working properly.

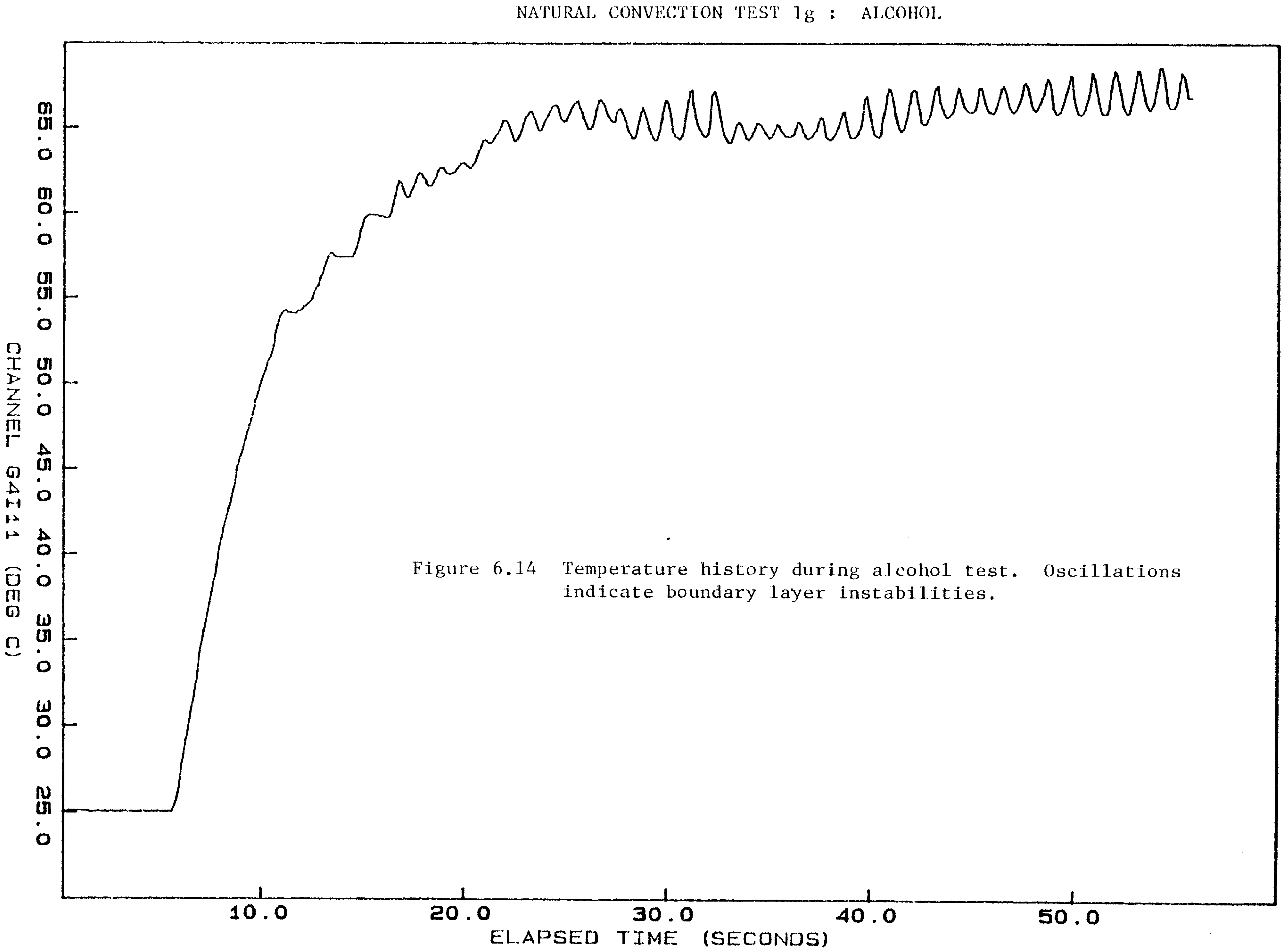

Figure 6.14 Temperature history during alcohol test. Oscillations indicate boundary layer instabilities.

CHAPTER 7

SPIN-UP IN SYMMETRIC AND NON-AXISYMMETRIC FLUID CONTAINERS

> The initial fluid motion relative to the walls of an arbitrary, non-axisymmetric container impulsively accelerated is calculated. Spin-up flow field and decay time constant are confirmed by experiments.

VII.A. Introduction

When an arbitrary, non-axisymmetric fluid filled container is suddenly made to rotate about some axis, the fluid within the container aquires some motion relative to the container . Over time, however, that relative motion decays and the fluid comes completely to rest relative to the walls of the container. At this time the fluid is said to be in solid body rotation. It has been suggested that the relative motion generated in the liquid helium bath surrounding the field winding following the impulsive acceleration of the airborne superconducting rotor would help to remove the ramp-up heat load since the field current is increased during the spin-up period. Experiments to actually measure the surface heat transfer coefficient during a fluid spin-up will be discussed in the next chapter. This chapter describes the theoretical and experimental work undertaken to understand the general physics of spin-up in a non-axisymmetric container. Specifically, the time constant associated with spin-up in an arbitrary container was sought as well as some estimate of the scale of the velocities induced in the fluid when the container is first accelerated. This information was then used to estimate the extent and duration of any surface heat transfer enhancement.

The organization of this chapter is as follows. A simple, elegant mathematical model by Wedemeyer [27]is presented describing spin-up from rest in a right circular cylinder. The model contains the essential physics of the spin-up process. The boundary conditions for the original model are then altered and the model equations resolved to show that the spin-up time constant in a similar geometry remains the same even if the fluid within the container is initially spinning at some finite, though smaller, rotation rate. The issue arises because an airborne rotor is idling at some low rotation rate before being accelerated to 6,000 rpm and the spin-up time constant for the on-board helium is an important parameter. The general problem of spin-up around a vertical axis in a non-axisymmetric container with vertical symmetry is considered next. An example of one of the geometries considered is the experimental apparatus shown in Fig. 1.5. The container is pie shaped in the horizontal plane and is uniform in shape in the direction parallel to the spin or vertical axis. Another geometry examined is a right circular cylinder impulsively accelerated off the axis of vertical symmetry as shown schematically in Fig. 1.9. Conservation of initial fluid angular momemtum is used to calculate the two dimensional (horizontal) relative flow in the rotating reference frame within each container following the impulsive acceleration of the container. When observed in a rotating coordinate frame with rotation rate ω, the container is motionless and the two-dimensional relative flow field consists of a counterrotation of fluid particles about the horizontal geometric center of the container at a rate equal to $-\omega$. The velocites associated with this motion relative to the walls of the container are thus found to scale with the characteristic horizontal radius of the container and not with the distance of the rotor from the actual axis of rotation. Furthermore, delineation of the relative motion flow also establishes the pressure distribution within the container in the horizontal plane . Since the fluid very close to the horizontal boundaries of the container is constrained by viscosity at each radius to have the container velocity, the imbalance between the pressure gradient in the regions away from the horizontal boundaries and the centrifugal acceleration of fluid near to the horizontal boundaries is calculated. It is subsequently found that the net imbalance in pressure forces which drives the spin-up secondary flow field is identical to that in a right circular cylinder spun-up on axis. It is then shown that the spin-up process in a right circular cylinder spun-up off axis is identical to its on-axis counterpart. Spin-up in a non-axisymmetric container, however, starts out in a similar fashion though it quickly evolves into a flow that is quite different from that in a circular cylinder. The flow field though, is still two-dimensional and the time constant for its' decay is the same as that for the relative flow in a circularly symmetric container.

VII.B. Spin-up of a homogeneous fluid in a circularly symmetric cylinder

In the discussion to follow the designation "interior" fluid will be used to describe all the fluid in the container except for fluid in regions very close to the horizontal and vertical boundaries of the container. The horizontal boundaries are those surfaces of the container perpendicular to the axis of rotation, or whose normal is parallel to the axis. The words axial and vertical will be used interchangeably to refer to the directions parallel to the spin-axis. The "spin-up" process itself is the means by which this interior fluid comes to know of the rotation of the container.

Figures 7.1a,b schematically show a right circular cylinder impulsively accelerated from rest about its' vertical axis at two different stages during the spin-up process. When the container is first accelerated fluid very near to the top and bottom endplates is immediately thrown outwards because there is no pressure gradient in the interior fluid regions to balance the viscous induced centrifugal acceleration. The fluid being thrown outward forms a thin boundary layer of order $\sqrt{(\nu/\omega)}$ known as the Ekman boundary layer. This thickness is determined by a balance of viscous shear stresses and an integrated coriolis force. Because the boundary layer is so thin it forms quite quickly, within two revolutions of the container. It is worthwhile noting at this point that because these Ekman boundary layers are so thin that the radial pressure gradient in the boundary layer is established by the radial pressure gradient in the interior fluid. When the container is first accelerated the interior fluid is at rest and the interior pressure gradient is zero. As time evolves and the fluid in the interior slowly becomes rotational, the pressure distribution in the interior changes as well. This simultaneously causes changes in the flux of fluid thrown outwards in the bottom Ekman layers. The flux in the boundary layer readjusts to each new distribution in interior fluid tangential velocity or radial pressure distribution.

The flux of fluid outwards in radius within this boundary layer of nearly uniform thickness causes fluid to be drawn downwards from the interior. The fluid thrown outwards is turned vertically in the sidewall boundary layer regions and is ultimately drawn inwards radially to complete the fluid circuit. The sidewall boundary layers, as indicated in Figure 7.1a, are of thickness $Ek^{.25}$. These boundary layers completely form in a time determined by ordinary viscous diffusion which is a time of order τ_E. Once formed, this boundary layer detaches from the outer wall and begins to move inwards slowly leaving behind a smaller boundary layer of order $Ek^{.33}$ as shown in Figure 7.1b. This detached shear layer is a wave front seperating non-spinning fluid infront from spinning fluid behind. The fluid behind the front is spinning because it has come from regions close

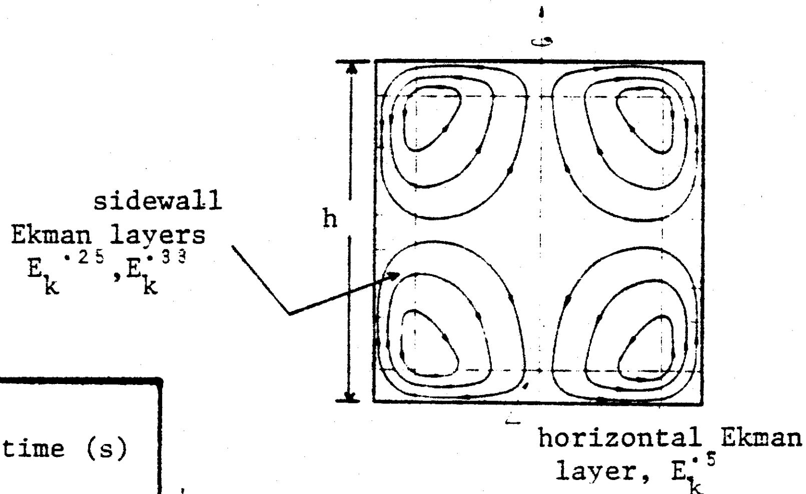

Figure 7.1a Spin-up flow field at time of order E_k time constant.

$\tau_E = \frac{h}{2\sqrt{\nu\omega}}$ = Ekman time (s)
Ek = Ekman number
$= \frac{\nu}{\omega h^2}$

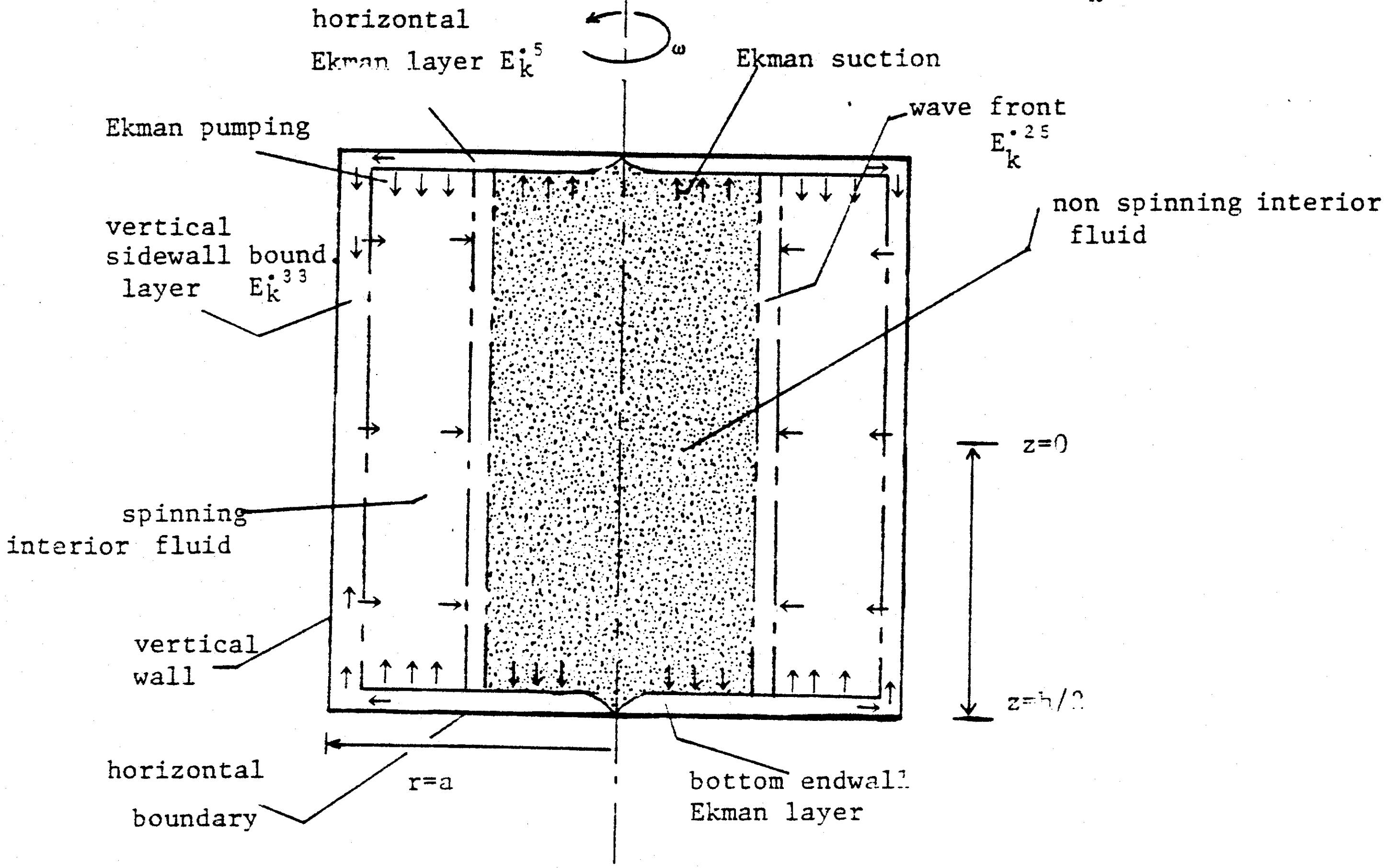

Figure 7.1b Spin-up flow field after sidewall boundary layer has detached from outer wall. Time is of order several E_k time constants.

enough to the wall to have been acted upon by viscous stresses. The wave front is shown in Fig. 7.1b. All viscous effects are confined within the boundary layers shown here and in the detached shear layer. Since these boundary layers comprise such a small fraction of the contained fluid, the spin-up process itself is essentially inviscid. Consequently, as this column of fluid behind the wave front advances inwards its' motion is torque free and the fluid conserves its' angular momentum by spinning faster. In addition, the wave front also seperates regions of Ekman suction from Ekman blowing. Fluid before the front is being pulled downwards slowly in the Ekman layers as mentioned previously, but the Ekman boundary layers are actually expelling fluid slowly behind the front. The fluid behind the wave front can thus be thought of as an expanding cylindrical ring of fluid which started out with zero width. The ring is expanding because it is drawing fluid out of the top and bottom Ekman layers. The tangential flow field in this expanding ring is consequently a superposition of a vortex flow and a solid body rotation. This is a subtle point which is essential to understanding Wedemeyer's model and will be discussed further. As the advancing wave front approaches the centerline, the rotation in the interior is evolving in such a way as to exactly match the rotation of the container and the radial pressure gradient imbalance driving the spin up is becoming negligibly small. The whole spin-up process takes roughly $5\tau_E$. Again, it must be noted that the dominant pressure gradient during the spin-up process is in the radial direction, and the pressure gradient in the z direction is an order of magnitude less. The absence of any z pressure dependence in this rotational system leads directly to the Taylor-Proudman condition which states that the interior inviscid fluid motion is constrained to be uniform in the z direction.

In summary then, the spin-up process is essentially inviscid. The motion of the horizontal boundary drives fluid outwards in a thin, viscous dominated boundary layer. Some of this fluid returns to the interior from the sidewall boundary layer and the rest comes from the Ekman layers behind the wave front. The fluid behind the wave front is simultaneously expanding in mass and spinning up at the rate necessary to conserve its' original angular momentum. The expanding mass is responsible for the fact that the tangential velocity in the interior never exceeds the tangential velocity at the endplates until the spin-up is completed. The pressure gradient in the interior fluid is zero infront of the wave front and increases like $\rho v^2/r$ from the wave front on out to the outer radius. Viscous effects in the Ekman layer drive fluids outwards at a rate proportional to the difference between the tangential velocity in the interior and the endplate velocity, ωr, at the same radius. This spin-up process is a secondary flow and all motions are of order $Ek^{.5}$, which is very small. The time constant for this spin-up is τ_E, which is the time required to flush all the interior fluid once through the bottom endplate boundary layers.

All of the previous information is neatly contained in Wedemeyer's inviscid analysis, which incorporates the behavior of the boundary layers implicitely. To first order, as has already been mentioned, the flow in the interior is a balance between tangential velocity and pressure gradient since all radial motions are slow:

$$(\partial p/\partial r)=\rho v^2(r,t)/r \quad . \qquad (7.b.1)$$

In the azimuthal direction, however, the first order, inviscid, slow flow is given by the following equation:

$$\frac{\partial v}{\partial t} + u\left(\frac{\partial v}{\partial r} + \frac{v}{r}\right) = 0 \quad . \qquad (7.b.2)$$

It is important to note that there is no z dependence in Eq. 7.b.2. The interior flow is uniform in height because the pressure gradient in the radial direction is much greater than the pressure gradient in the z direction. If there is no pressure dependence in z, it can be shown that:

$$\frac{\partial u}{\partial z} = \frac{\partial v}{\partial z} = 0 \quad . \tag{7.b.3}$$

Since the total mass flux in the vertical direction from one endplate to the other at any radius must be zero, the radial velocity in the interior region can be related to the Ekman flux at each endplate as follows:

$$uh/2 = \int u d\delta \tag{7.b.5}$$

where the latter integral is taken over one Ekman thickness and will be referred to as the Ekman flux. Wedemeyer noted that the Ekman flux divided by radius was nearly a linear function of the rotation rate fraction in the case of an infinite spinning disk in an unbounded spinning fluid, namely:

$$[\int u d\delta]/r = k_1(1- \omega_1/\omega) \tag{7.b.5}$$

where ω_1 is the rotation rate of the unbounded fluid above the spinning disk rotating at a rate ω and k_1 is $(\sqrt{\nu\omega})/2$. Wedemeyer uses this result in his analysis of a contained spinning fluid by noting that the Ekman flux is a function of radius only and then substituting $v(r,t)/r$ for ω_1, where v is the slowly evolving tangential velocity in the interior fluid region. This assumption implies that an Ekman flux could be determined locally for any given distribution of v(r) outside of the Ekman layer and that the finite container geometry does not affect the boundary layer flux. The radial velocity in the interior is thus coupled to the tangential velocity in the interior by the mismatch in tangential velocities between the interior and the endplate fluid and when $v(r,t) = \omega r$, the Ekman flux goes to zero as expected.

Substituting Eq. 7.b.5 into Eq. 7.b.4 and nondimensionalizing by dividing through the equation by ωa results in a linear relationship between the radial velocity in the interior and the tangential velocity:

$$u = -k(r-v) \tag{7.b.6}$$

where $k=(1/h)/(\sqrt{\nu/w})$ and the radial velocity in the interior is towards the centerline during the spin-up. Now, combining Eq. 7.b.6 with Eq. 7.b.2 results in the following equation:

$$\frac{\partial v}{\partial t} + k(v-r)\left(\frac{\partial v}{\partial r} + \frac{v}{r}\right) = 0 \tag{7.b.7}$$

subject to the nondimensional boundary conditions:

$$v(r,0) = 0 \tag{7.b.8}$$
$$v(1,t) = 1 \tag{7.b.9}$$

where $r=r/a$, $v=v/\omega a$, $u=u/\omega a$, and $t=\omega t$. A solution of this first order partial differential equation can be found using the method of characteristics after first transforming Eq. 7.b.7 into an angular momentum equation in the new variable vr. The result is shown in fig. 7.2. The radial position of the front seperating spinning from non-spinning fluid is represented by:

$$r_c = e^{-k\omega t}$$

with $v=0$ for $r <= r_c$ the fluid ahead of the wave front in Fig. 7.1b, and

$$v = [r-(1/r)e^{-2k\omega t}]/[1-e^{-2k\omega t}] \tag{7.b.11}$$

for $r >= r_c$ which represents the fluid behind the wave front which is rotational. The Ekman time scale appears directly in this solution since $2k\omega = (\tau_E)^{-1}$. It is interesting to note that v is almost a superposition

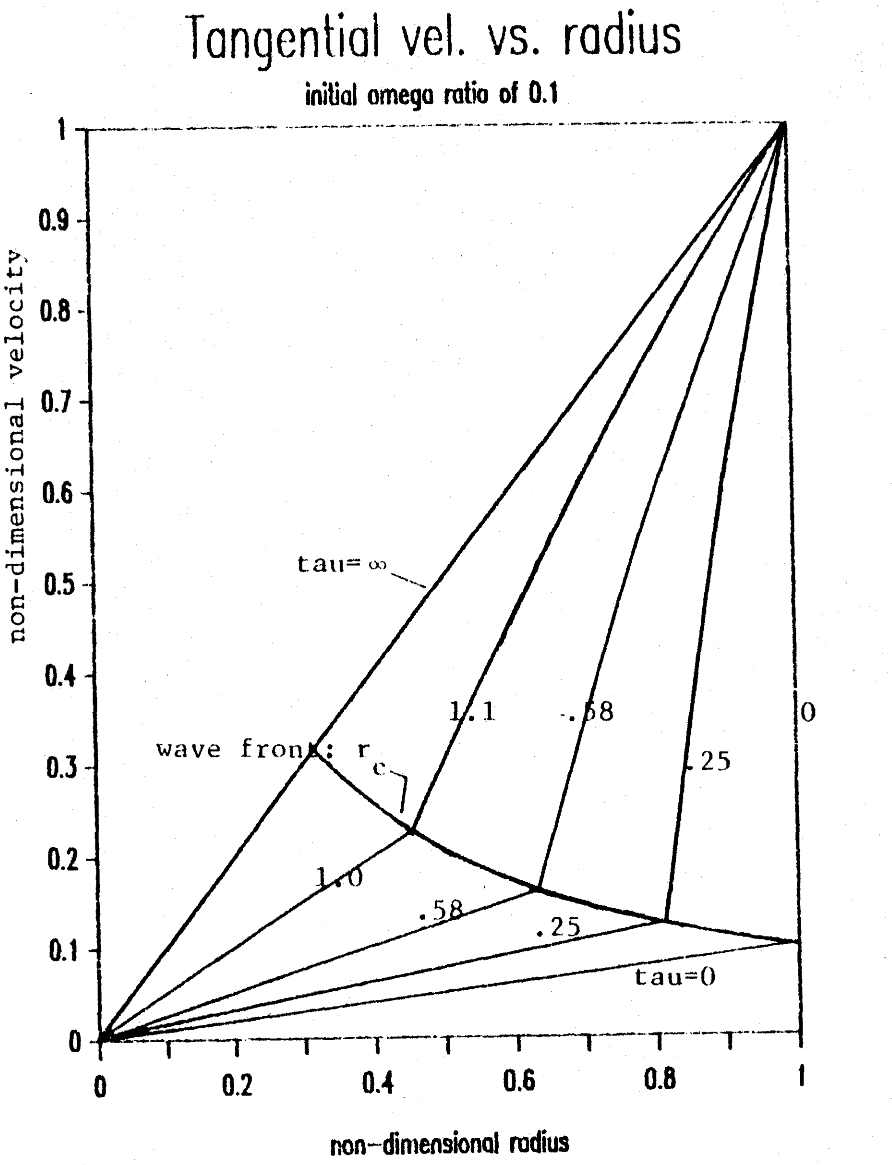

Figure 7.2b Tangential velocity versus radius when the fluid initially rotates at a slower speed. Velocity is always linear with radius ahead of the wave front, shown as r_c above.

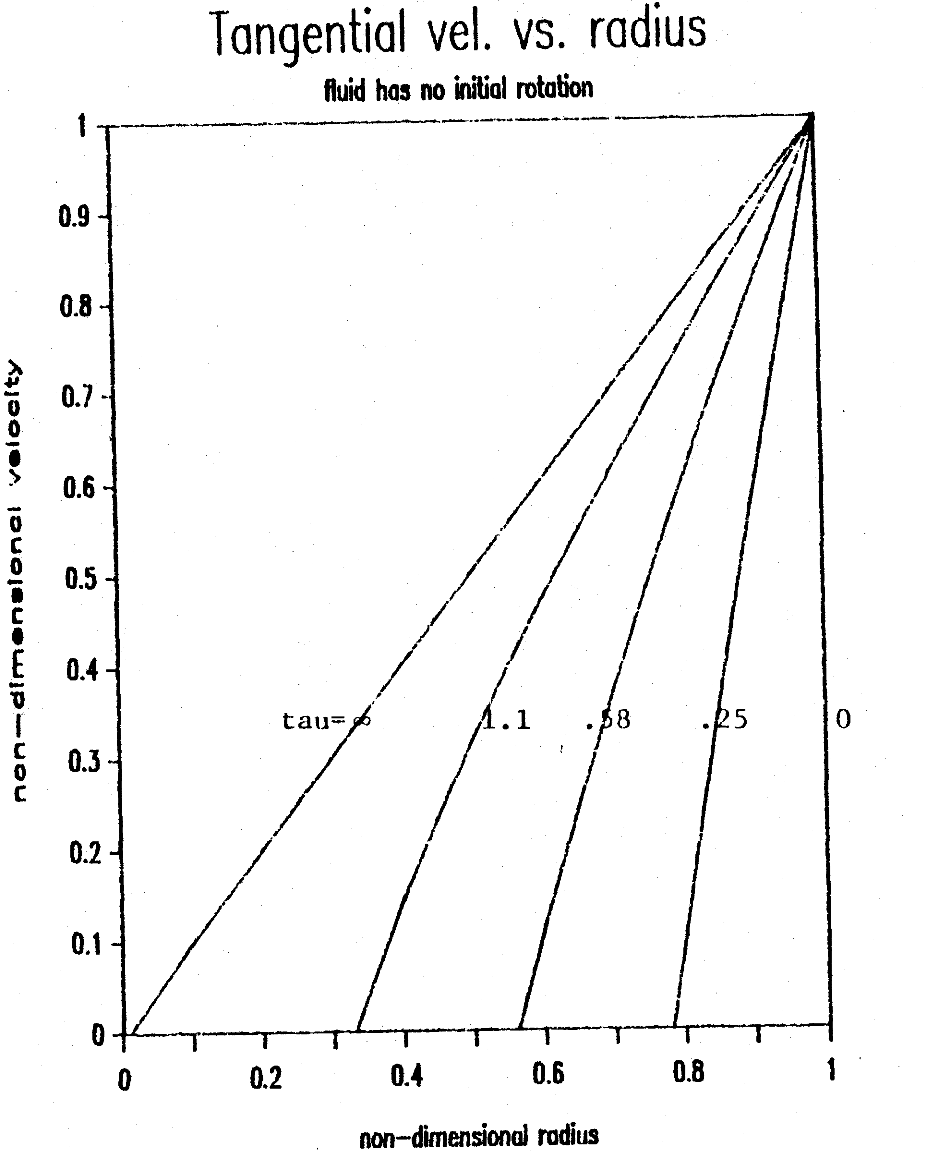

Figure 7.2a Tangential velocity versus radius for different t. Velocity varies nearly linearly with radius behind the front, and is zero infront of it.

of a solid body rotation and a vortex (1/r) like flow. Furthermore, using the latter equation and the continuity equation for the interior fluid region, the axial velocity into the Ekman layer ahead and behind of the wave front can be calculated. Because of symmetry in this circular geometry, the nondimensional equation of continuity in the interior is:

$$\frac{\partial ru}{r\partial r} = -\frac{\partial w}{\partial z}\frac{(2a)}{h}. \tag{7.b.12}$$

This equation can be easily integrated between z=0 and 1 since u is not a function of z, and w is zero at container midheight (z=0) by symmetry as well:

$$\frac{\partial ru}{r\partial r} = -w_E(2a/h) \tag{7.b.13}$$

where w_E is axial velocity into the Ekman layer if the gradient in radial velocity is positive, a is the container radius and h/2 is half the container height. Combining Eqs. 7.b.6, 7.b.11 with Eq. 7.b.13 gives the interesting result that:

$$w_E = +k(h/a), \qquad \text{for} \quad r <= e^{-k\omega t} \tag{7.b.14}$$

$$w_E = -k(h/a)/[e^{2k\omega t} - 1], \qquad \text{for } r >= e^{-k\omega t}. \tag{7.b.15}$$

The wave front in this approximate inviscid model thus clearly seperates a region of uniform Ekman pumping from a region of uniform Ekman blowing behind the wave front. If the axial velocity (w_E) did not reverse sign behind the wave front the tangential velocity distribution would have had to be a pure vortex.

The analysis just presented can also show that the spin-up time constant is the same even if the fluid is already spinning when the container is accelerated to a higher rotational speed. The issue arises for the following reason. A rotating airborne helium system will be idled at a low speed when it is not producing electricity to insure phase seperation of the coolant and uniform structural temperatures. Ekman pumping cannot increase the vorticity of fluid filaments in the interior regions if the fluid is not spinning to begin with and the Ekman time constant is the time required to flush the interior fluid through the endplate boundary layer where the fluid is acted on by viscous stress. But Ekman pumping can certainly increase the vorticity if the interior fluid is already spinning so it is natural to wonder if the Ekman time constant is still relevant. The spin-up time constant, it turns out, remains an Ekman time based on the final rotational speed even though the fluid is originally rotating with lower ω_1. The rate at which Ekman pumping pulls fluid into the Ekman layers is proportional to the difference in velocity between fluid in the interior ($\omega_1 r$), and fluid in the Ekman layer ($\omega_2 r$). Though pumping increases vorticity immediately the rate of pumping is that much less than it would have been with the interior fluid at rest.

The result is shown by solving Eq. 7.b.7 with the following revised nondimensional boundary conditions:

$$v(r,0) = r\omega_1 \qquad v(1,t) = 1 \tag{7.b.16}$$

where ω_1 is the initial rotation fraction ω_1/ω_2. The nondimensional solution falls out once more using the method of characteristics. The dividing characteristic (the cylindrical wave front radius as a function of time) turns out to be

$$r_c = [\omega_1+(1-\omega_1)e^{-2k\omega t}]^{.5} \tag{7.b.17}$$

$$\text{and for } r <= r_c: \qquad v= r\omega_1/[\omega_1+(1-\omega_1)e^{-2k\omega t}]$$

$$r >= r_c \quad v= [r-(1/r)e^{-2k\omega t}]/[1-e^{-2k\omega t}]$$

where $-2k\omega = \tau_E^{-1}$. This result is graphed in Fig. 7.2b. Notice that for $r>r_c$ (fluid behind the cylindrical wave front), the spin-up is identical to spin-up from rest (Fig. 7.2a). It is also interesting to note that the wave front moves only to a final radius of $\sqrt{\omega_1}$ which goes to zero if the spin-up is from rest.

It will be shown in the next few sections that the mechanics of spin-up in a circular cylinder hold for other geometries as well. To demonstrate this fact it is first necessary to describe the relative motion flow field in non-symmetric containers following an impulsive acceleration. The relative motion flow determines the pressure distribution in the fluid which drives the ensuing secondary flow (spin-up).

VII.C Instantaneous flow field in a non-axisymmetric container

The analysis of the previous section was applicable to fluid in a circular, axisymmetric container. In this section, the principle that fluid that is initially irrotational can acquire vorticity only through viscosity is used to determine the instantaneous flow field following an impulsive acceleration of a non-axisymmetric container. An example of such a non-axisymmetric container is a vertical, circular cylinder rotated about an axis other than, but still parallel to its original vertical axis. No attempt is made to describe the spin-up process that follows once this initial flow field is established for reasons that will become obvious.

The analysis to follow requires that the container acceleration be impulsive. The criteria for an impulsive acceleration can be established if one assumes without proof that the spin-up time constant in a non-axisymmetric container is also τ_E. The acceleration time scale, τ_α, is $(\omega_2-\omega_1)/\alpha$ where α is the acceleration rate of the container. In order to neglect absolute vorticity changes in the fluid which occur while the container is still accelerating it is required that

$$\tau_\alpha/\tau_E = [\sqrt{\nu\omega}/(\alpha h)]\Delta\omega \ll 1. \tag{7.c.1}$$

Now consider an arbitrary, simply connected region with an incompressible fluid initially at rest (Fig. 7.3). The geometry of the container does not vary in the direction parallel to the rotation axis. The container is then given an impulsive angular acceleration about an arbitrary axis so that the container angular rotation is now ω. An observer rotating with the container will see that the fluid has instantaneously acquired some relative motion in response to the motion of the boundaries of the container. The walls of the container S are impermeable and may be thought of as a closed loop always consisting of the same fluid particles. Since the fluid within is incompressible and inviscid, the circulation round this loop must be conserved. In stationary coordinates Kelvin's circulation theorem is:

$$\frac{D}{Dt}\int U_I \cdot dS = 0 \tag{7.c.2}$$

where U_I is the inertial velocity of a fluid particle of fixed identity. Since it will prove to be more convenient to work in a rotating coordinate system, the inertial velocity of a fluid particle is related to the velocity of this same fluid particle relative to some convenient coordinate origin (in this case, the geometric center of the container) as follows:

$$U_I = \omega x R + \omega x r + q \tag{7.c.3}$$

where q is the relative velocity vector. Substituting 7.c.2 into 7.c.3 and noting that the circulation of the fluid was zero initially (the container being at rest) it follows that:

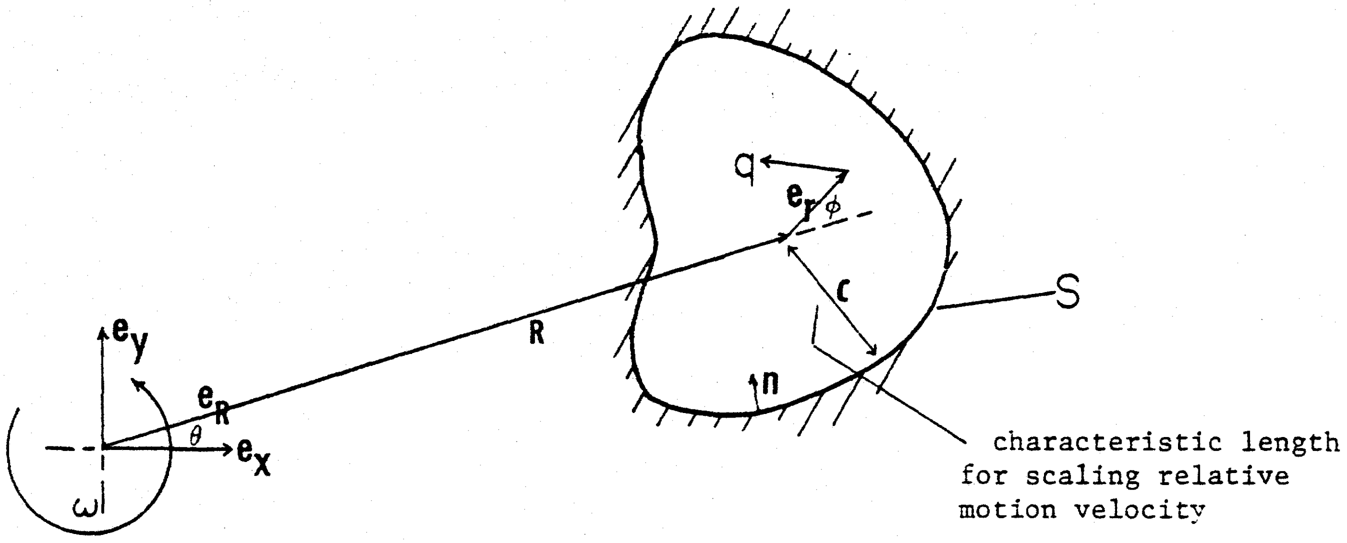

characteristic length for scaling relative motion velocity

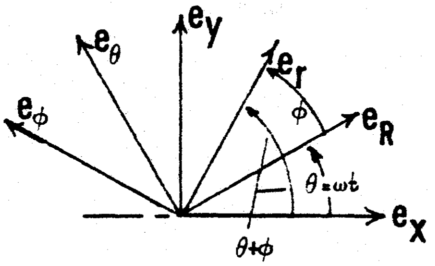

coordinate transforms:

$$\begin{bmatrix} e_r \\ e_\phi \end{bmatrix} = \begin{bmatrix} \cos(\phi) & \sin(\phi) \\ -\sin(\phi) & \cos(\phi) \end{bmatrix} \begin{bmatrix} e_R \\ e_\theta \end{bmatrix}$$

$$\begin{bmatrix} e_x \\ e_y \end{bmatrix} = \begin{bmatrix} \cos(\theta+\phi) & -\sin(\theta+\phi) \\ \sin(\theta+\phi) & \cos(\theta+\phi) \end{bmatrix} \begin{bmatrix} e_r \\ e_\phi \end{bmatrix}$$

Figure 7.3 Simply connected region and coordinate transform

$$\int((\omega x R + \omega x r) + q)\cdot dS = 0 \qquad (7.c.4)$$

for all time. The dot product of the first two terms enclosed by the parentheses in Eq. 7.c.4 with a vector tangent to the boundary of the container is equal to the inertial velocity of the boundary in that direction. It then follows that the integral of this velocity around the boundary must be twice the angular rotation rate of the container itself about its' center of geometry times the horizontal area, $2\omega A$. Hence

$$-2\omega A = \int q\cdot dS \;. \qquad (7.c.5)$$

Eq. 7.c.5 is true whether or not the region is simply connected. It is equally true for the circulation around the outer boundary of the cylinder in Fig. 7.4. However, the usefulness of the circulation theorem is that for the simply connnected region in Fig. 7.3, Eq. 7.c.5 and Stokes' theorem lead directly to a unique determination of the flow field. In a multiply connected region the flow field is not unique. According to Stokes' theorem:

$$\int q\cdot dS = \iint n\cdot(\nabla x q)dA \qquad (7.c.6)$$

where n for this presumed two-dimensional flow is a unit normal in the z direction, parallel to ω. Examination of Eqs. 7.c.6 and 7.c.5 shows that Eq. 7.c.6 is satisfied if:

$$\nabla x q = -2\omega e_z \qquad (7.c.7)$$

everywhere in S.

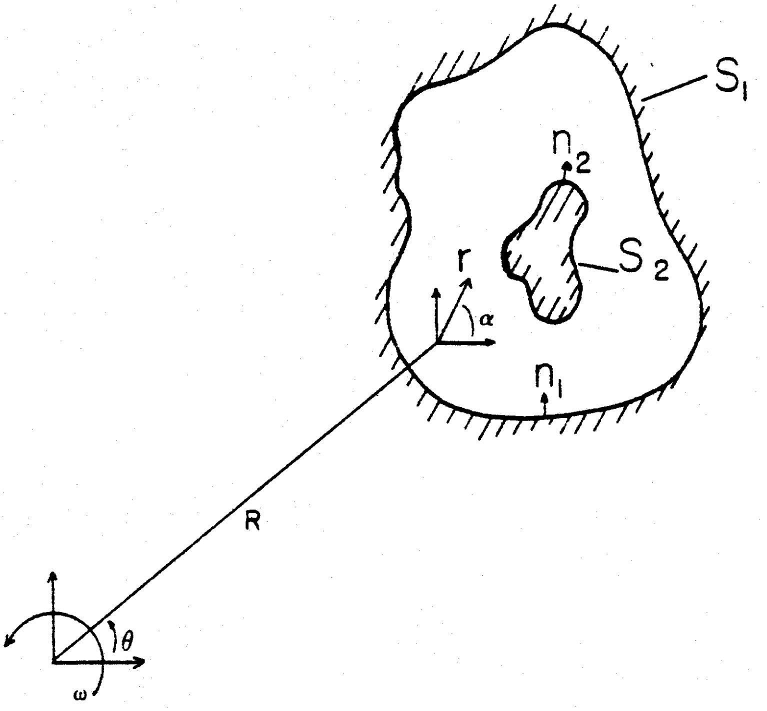

Figure 7.4 Doubly connected region

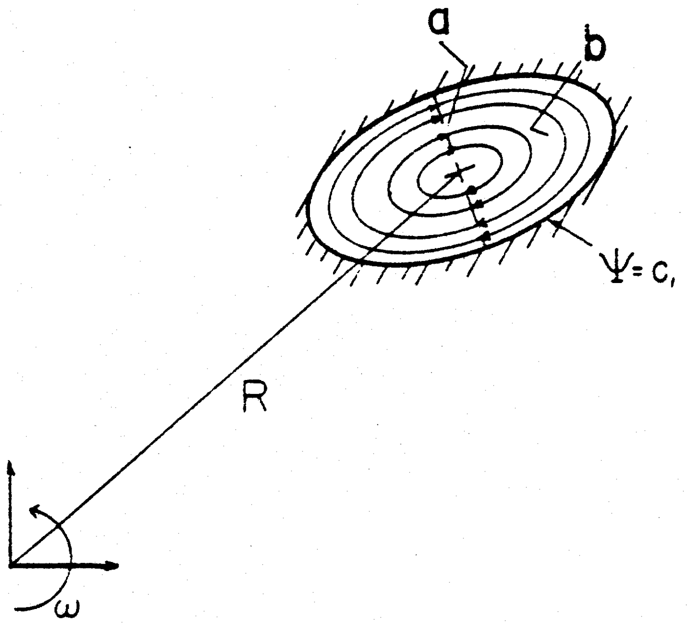

Figure 7.5 Relative motion streamlines in an elliptical container following an impulsive acceleration.

Equation 7.c.7 shows that if a fluid system is to conserve its absolute circulation, an observer rotating with the container will observe a fluid motion which has a uniform relative vorticity equal to -2ω. This result is independent of R, the distance to the axis of rotation. It will now be shown that Eq. 7.c.7, the incompressibility condition (which leads to the definition of a stream function) together with the boundary condition that the fluid velocity normal to the boundaries is zero is sufficient to uniquely determine the relative flow field q everywhere in S. The flow field in S is found by simultaneously solving the following two equations:

$$\nabla x q = -2\omega \qquad (7.c.7)$$

$$\nabla \cdot q = 0 \qquad (7.c.8)$$

with the boundary condition

$$n \cdot q = 0 \text{ on } S \qquad (7.c.9)$$

where n is a horizontal normal to the surface S.

It should be pointed out that the previous result holds even if the container had not started from rest. If the container had some initial rotation ω_1, and the fluid is in solid body rotation when the fluid is accelerated then

$$\nabla x q = -2(\omega_2 - \omega_1) . \qquad (7.c.10)$$

Eqs. 7.c.7,7.c.8 can be rewritten in terms of a stream function since the fluid is incompressible,

$$\begin{aligned} u &= -\partial\Psi/r\partial\phi \\ v &= \partial\Psi/\partial r \end{aligned} \qquad (7.c.11)$$

and Ψ automatically satisfies the incompressibility condition $\nabla . q=0$. Substituting 7.c.7 into 7.c.8 yields Poisson's equation,

$$\nabla^2\Psi = -2\omega \qquad (7.c.12)$$

with the boundary condition that $\Psi = 0$ (or any arbitrary constant) on S. The solution to Eq. 7.c.12 together with the boundary condition on S is simply a flow field counterrotating at a rate equal to $-\omega$ on streamlines which have the same shape as the container boundary S. The equation is analogous to the heat conduction equation in a domain with uniform heat generation and an outer boundary held at a uniform temperature. Ψ in Eq. 7.c.12 is then analogous to temperature, and -2ω is analogous to the rate of internal heat generation divided by the thermal conductivity of the medium. Just as the point of maximum temperature is located at the geometric center of the region (if the thermal conductivity is isotropic), the relative motion flow field just described is a rotation of fluid elements about the geometric center of the area enclosed by S. Furthermore, since the relative motion is centered about the c.g. of S, the net imbalance in pressure forces caused by this irrotational flow in the interior must also be centered about the c.g. of S. This point has implications for the spin-up process itself, and will be discussed further in the next section.

To illustrate the calculation of a relative motion flow field, consider a fluid filled elliptical cylinder (Fig. 7.5) with semi-axis a and b suddenly accelerated from rest. Since the equation for the bounding surface, S, of an ellipse is:

$$S(x,y) = (x^2/a^2 + y^2/b^2) \qquad (7.c.13)$$

and S is a known streamline of the flow, the solution for the relative motion streamfunction in this container is quickly found to be:

$$\Psi = -\omega S\ . \qquad (7.c.14)$$

A quick substitution shows, $\nabla^2 S=2$, thus $\nabla^2\psi=-2\omega$ proving that ψ is indeed the relative motion stream function for this geometry. In an appendix at the end of this thesis, the inertial velocity and potentional function associated with the relative motion is calculated- proving that the flow is irrotational and unique .

VII.D The Navier Stokes equations in the rotating frame

The previous section was used to show that the circulation of an inviscid, incompressible fluid is constant for all time. This fact together with the Stokes' theorem uniquely determined the 2-D flow field in an arbitrary simply connected region whose boundaries are given an impulsive acceleration. In this section, this same flow field will be deduced from the Navier Stokes equations themselves. In this manner it will be shown that the origin of the axis of rotation for the container affects the pressure distribution on the walls of the container, but has no effect on the relative flow field. This is obscured in the previous analysis. This fact is equivalent to saying that if the relative flow field has a uniform vorticity equal to -2ω then the relative flow field is steady.

The velocity of a fluid particle of fixed identity relative to the geometric center of the container S, is related to its inertial velocity as follows,

$$U_I = \omega R e_\theta + \omega r e_\phi + q \qquad (7.d.1)$$

where q has components in the radial and azimuthal directions, ue_r and ve_ϕ . Since we are tracking a fluid particle of fixed identity it is understood that q is also equal to $D(re_r)/Dt$, (D/Dt being the substantial derivative). In the local r,ϕ coordinate system Eq. 7.d.1 becomes,

$$U_I = (\omega R\cos\phi + \omega r)e_\phi + \omega R\sin\ e_r + q\ . \qquad (7.d.2)$$

Since dr/dt is ue_r, and rde_ϕ/dt is the negative of the azimuthal relative velocity, $-ve_\phi$, the acceleration of this fluid particle can be written as:

$$\begin{aligned}\frac{DU_I}{Dt} = &-[\omega^2R\cos\phi+\omega^2r - R(\partial\omega/\partial t)\sin\phi]e_r \\ &+[\omega^2R\sin\phi+R(\partial\omega/\partial t)\cos\phi + r(\partial\omega/\partial t)]e_\phi \\ &+\frac{Dq}{Dt} \ +2\omega xq\end{aligned} \qquad (7.d.3)$$

where, it should be noted, the equation includes acceleration terms $(\partial\omega/\partial t)$ as well. The inviscid Navier Stokes equation for this sytem is thus

$$\begin{aligned}\frac{Dq}{Dt} &-[\omega^2R\cos\phi+\omega^2r - R(\partial\omega/\partial t)\sin\phi]e_r \\ &+[\omega^2R\sin\phi+R(\partial\omega/\partial t)\cos\ + r(\partial\omega/\partial t)]e_\phi \\ &+2\omega xq \ = -\nabla P/\rho\ .\end{aligned} \qquad (7.d.4)$$

It is more useful, however, to incorporate the acceleration terms into the pressure gradient. Eq. 7.d.4 is equivalent to

$$\begin{aligned}\frac{Dq}{Dt} &+2\omega xq + r(\partial\omega/\partial t)e_\phi = \\ &-\nabla(P/\rho-\omega^2Rr\cos\phi+Rr(\partial\omega/\partial t)\sin\phi-\omega^2r^2/2 \\ &+q^2/2)\ .\end{aligned} \qquad (7.d.5)$$

It is already apparent that since R only appears as part of the gradient of the body force, the distance to the axis of rotation will not affect the relative flow field. Nondimensionalizing Eq. 7.d.5 by dividing thru with ωa and collecting terms gives the following:

$$\partial q/\partial t + (2\omega+\xi)xq + r(\partial\omega/\partial t) = -\nabla(P')$$

$$\text{where } P' = \nabla(P/\rho - \omega^2 Rr\cos\phi + Rr(\partial\omega/\partial t)\sin\phi$$
$$-\omega^2 r^2/2 + q^2/2)/\omega^2 a^2) \qquad (7.d.6)$$

and $\xi = \nabla xq$.

Taking the curl of Eq. 7.d.6 and noting that $(\nabla)xr=2$ yields the important result:

$$\frac{D}{Dt}(\xi+2\omega) + (\xi+2\omega)\cdot\nabla q = 0 \quad . \qquad (7.d.7)$$

Examination of Eq. 7.d.7 shows that fluid vorticity ξ equal to -2ω is a solution. In inertial space the flow is irrotational and a potential function exists such that:

$$\nabla\Phi = \omega xR + \omega xr + q \quad . \qquad (7.d.8)$$

Taking the partial of the previous equation with respect to time and substituting into 7.d.6 gives the appropriate Bernoulli equation in this non-inertial coordinate system:

$$\nabla(P/\rho - \omega^2 Rr\cos\phi - (\partial\Phi/\partial t) - \omega^2 r^2/2 + q^2/2) = 0 \quad . \qquad (7.d.9)$$

In the case of an impulsive acceleration, the pressure field can be found from Eq. 7.d.9 without the unsteady potential function. By studying the pressure field it is possible to determine likely areas of flow seperation. Flow visualization experiments will confirm that the flow seperates wherever the fluid deccelerates abruptly outside a wall boundary layer.

The fact that the flow field has a uniform relative vorticity equal to $-2\omega(t)$ merely restates the results of the previous section. The flow field is uniquely determined by the dual requirements of incompressibility and uniform vorticity, with a boundary condition of impermeability or zero velocity normal to the container boundary. With q known everywhere in the container, Eq. 7.d.9 determines the pressure distribution on the walls of the container necessary to balance the acceleration of the fluid particles inside the container. The pressure distribution on the wall has no effect on the relative flow field. It merely adjusts to whatever it needs to be inorder to balance the acceleration of the inertial flow field.

In an appendix at the end of this thesis the relative flow field in three typical geometries is calculated. The simplest case, that of solving Poisson's equation in a circle is presented in order to reinforce the intuitive feeling that the fluid inside the circular container responds to a rotation of the off-axis cylinder as though it were a solid cylinder mounted in a frictionless bearing at the end of a rotating crankshaft. As the crank starts to rotate, the cylinder will maintain its original angular momentum (zero in this case) in the e_r, e_ϕ coordinate system since the bearing cannot exert a torque on the cylinder. The center of gravity of the cylinder will move in a circular path but the cylinder itself will not rotate.

The flow field in the interior of an ellipse is also calculated along with a calculation of the total relative kinetic energy of this system . It will be shown in the next section of this chapter that the spin-up losses as this original flow decays into solid body rotation depends only on the relative kinetic energy (not the total fluid kinetic energy). This suggests a means to minimize kinetic energy losses upon spin-up.

The final flow field described is that of a pie shaped sector. This geometry is more relevant to the actual rotor reservoir. An approximate solution is derived which shows where the inviscid, steady, two dimensional flow field will seperate.

VII.E The change in internal energy of the fluid from spin-up to solid body rotation.

The relative motion following an impulsive acceleration will decay during the spin-up process and using the results just obtained it is possible to calculate the change in internal energy between these two well defined states. This calculation will show that the change in the internal energy of the fluid depends only on the kinetic energy of the fluid relative to the container. This is the energy dissipated as the fluid comes to solid body rotation. The spin-up losses are consequently independent of the axis of rotation of the container and depend only on its' geometry.

The total kinetic energy relative to the rest state in the system at any time t is calculated using inertial velocities:

$$KE(t) = 1/2\iint U_I \cdot U_I dA \qquad (7.e.1)$$

where U_I is given in Eq. 7.d.1. The change in kinetic energy of the system over time as the fluid comes into solid body rotation is

$$KE(\infty) - KE(0^+) = 1/2\iint (\omega x(R+r)\cdot\omega x(R+r)) - ((\omega x(R+r)+q)\cdot(\omega x(R+r)+q))dA \qquad (7.e.2)$$

since there is no relative velocity as t goes to ∞. The vector products can be expanded and subtracted. Using the vector identity $AXB\cdot C=(BXC)\cdot A$ Eq. 7.e.2 becomes

$$KE = -1/2\iint (2(R+r)xq\cdot\omega + q\cdot q)dA \qquad (7.e.3)$$

where $q=q(0^+)$. As the fluid evolves into the state of solid body rotation there is a concommitant change in the angular momentum of the system. In order to keep the container rotating at constant speed a torque must be supplied equal to the rate of change of angular momentum of the system

$$T = \frac{\partial}{\partial t} \iint (R+r) x (\omega x R + \omega x r + q) dA . \qquad (7.e.4)$$

The rate at which work is done on the system is $-(T.\omega)$. Since ω is constant throughout this process, the total work done on the system is:

$$W = - \iint (R+r) x (q \cdot \omega) dA \qquad (7.e.6)$$

recalling that $q=0$ at $t=\infty$. Eq. 7.e.6 describes the work added to the system inorder to counteract the tendency of the system to slow down as more fluid spins up. The first law for the adiabatic rotating control volume is:

$$-W = \Delta E + \Delta KE \quad . \qquad (7.e.7)$$

Combining the previous equations yields the result:

$$\Delta E = 1/2 \iint (q \cdot q) dA \ . \qquad (7.e.8)$$

The latter equation says that the dissipation during the transition to solid body rotation depends only on the relative kinetic energy at $t=o^+$.

It has already been shown that the relative flow field is the solution to Poisson's equation (Eq. 7.c.12), in effect, a fluid counterrotation about the geometric center of the container with an angular frequency of $-\omega$. Several important points can be made. First, since the initial relative flow field depends on the shape of the container, a fluid will undergo the same change in internal energy whether the cylinder is spun on axis or off . (This does not say that the external shaft work is the same in both cases, but the fluid cannot tell the difference between a spin-up on axis or off.) Second, it can be shown that viscous losses during the spin-up can be minimized by breaking up the liquid bath into several small simply connected baths rather than having one large liquid bath of the same total volume. For a system composed of n small areas , A_i (i=1 to n), the sum of all the n kinetic energies, or the total viscous loss is proportional to $n\Sigma((1/2)(q^2)A_i)$. The container geometry determines the initial relative motion so the initial kinetic energy scales with the product $(r\omega)^2$, where r is the characteristic dimension of each small area A_i. A_i is of order A/n where A is the sum of the A_i (or nA_i), hence r is of order $(A/n)^{.5}$. The total viscous loss is thus

$$\Delta E \sim \frac{n(A\omega^2)(A)}{n \quad (n)} \sim \frac{(A\omega)^2}{n} \; . \qquad (7.e.9)$$

Another conclusion related to the above is that for a given area, the circle has the greatest initial relative kinetic energy hence the greatest spin-up losses. This will be demonstrated in an appendix. However, since the relative motion flow in all geometries except circular geometries is unstable- it will also be shown in a later chapter that a circular geometry is less advantageous for heat transfer.

VII.F Flow visualization of spin-up in off-axis cylinder

The pressure forces on the vertical walls of a non-axisymmetric cylinder have no effect on the initial relative motion flow field. However, the imbalance in pressure forces between fluid near the boundaries and fluid away from the boundaries sets in motion a secondary flow which drives the spin-up. In this section it will be shown that the imbalance in pressure forces is independent of the axis of rotation and is centered at the c.g. of the container. In the case of simple geometries like a right circular cylinder this results in a spin-up off-axis which is identical to the on-axis case. For more complicated geometries the inviscid analysis shows that the initial counterrotation of fluid elements is bound to produce regions of seperated flow. In this section experiments will be described which demonstrate that spin-up off-axis in a circular geometry is no different than spin-up on axis, but that spin-up in a pie-shaped container, or a baffled right circular cylinder is dramatically different from the unbaffled on-axis counterpart .

In the first chapter of this thesis an elegant experiment by Prof. Greenspan was described which enabled an observer to detect the evolution of solid body rotation in a right circular cylinder . Figure 1.9 shows how the motion of the horizontal boundaries pull fluid into the end wall boundary layers, drawing a vertical column of fluid inwards from the vertical side walls. An observer positioned at right angles to a thin, collimated light source will see a dark column of spinning fluid advancing slowly towards the axis, as the non-spinning, sharply reflecting column of particles is pulled downwards into the endplates. Fluid is also moving upwards in the spinning regions, but this motion is small and not so easily seen.

Suppose instead that the fluid cylinder is mounted off of the axis of rotation. The lab apparatus for experiments in off-axis spin-up is shown in Fig. 7.6 . The resulting imbalance in pressure forces accompanying spin-up can be calculated using the results of chapter VII.E. Bernoulli's equation for a cylinder impulsively rotated off axis is:

$$\nabla(P/\rho - \omega^2 Rr\cos\ \ - \omega^2 r^2/2 + q^2/2)=0. \qquad (7.f.1)$$

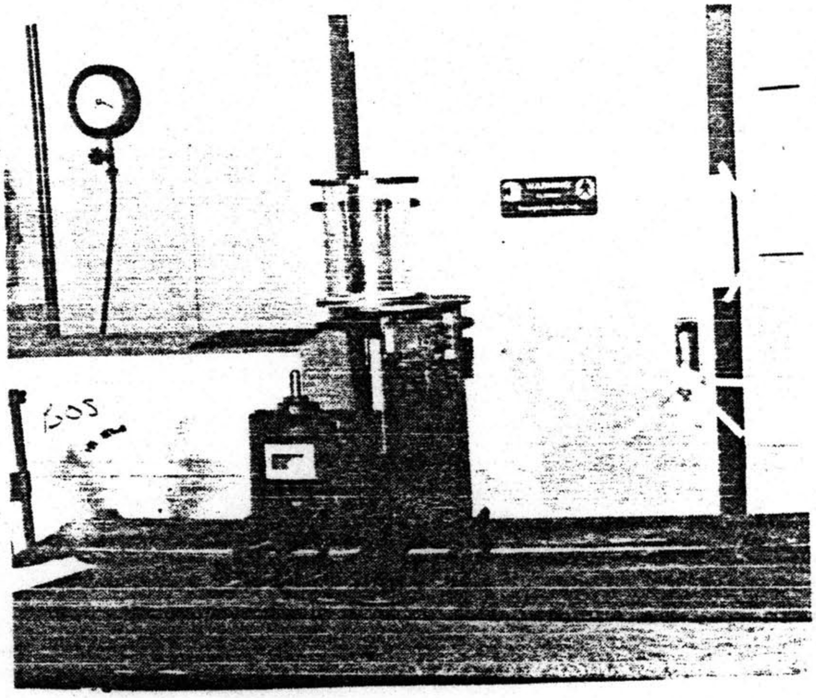

Figure 7.6 Apparatus for off-axis spin-up flow visualization experiments. The pictures in Figure 1.10 were taken using this apparatus. Shown here is plexiglas cylinder mounted off the axis of an aluminum turntable. Not shown here is the vertical slit light source.

In the interior of the container the relative fluid velocity is everywhere equal to $-\omega r$. Near the top and bottom horizontal endplates, the fluid velocity is effectively zero. The pressure gradient in the radial direction near the endplate region of the container is:

$$\left.\frac{\partial p}{\rho \partial r}\right|_W = \omega^2 R\cos\phi + \omega^2 r \ . \tag{7.f.2}$$

The pressure gradient in the radial direction in the interior fluid region is:

$$\left.\frac{\partial p}{\rho \partial r}\right|_W = \omega^2 R\cos\phi + \omega^2 r - \frac{\partial}{\partial r}(\omega^2 r^2/2) = \omega^2 R\cos\phi \ . \tag{7.f.3}$$

The net pressure gradient which will then generate a secondary flow is approximately equal to the difference between Eqs. 7.f.3 and 7.f.2:

$$\Delta\left(\frac{\partial p}{\rho \partial r}\right) = \omega^2 r \ . \tag{7.f.4}$$

Since the pressure difference increases outward from the c.g. of the container, fluid will be thrown outwards near the bottom of the container. The Ekman layer will then be identical to the Ekman layer in an on-axis spin-up. The fluid pressure gradient caused by the location of the axis, R, exists everywhere in the fluid system and has no effect on the secondary flow.

Figures 7.7a-d illustrate this point. A camera has been synchronized with the motion of the turntable in Fig. 7.6 to take a picture when the container center passes through the narrow vertical light beam. Shown here are a sequence of shots taken every few revolutions as the cylinder passed through the light source. The motion of the cylindrical front is clearly visible in these pictures. The last 4 pictures in this sequence (Figures 7.8a-d) were taken with the turntable stopped. The spin-down, however,

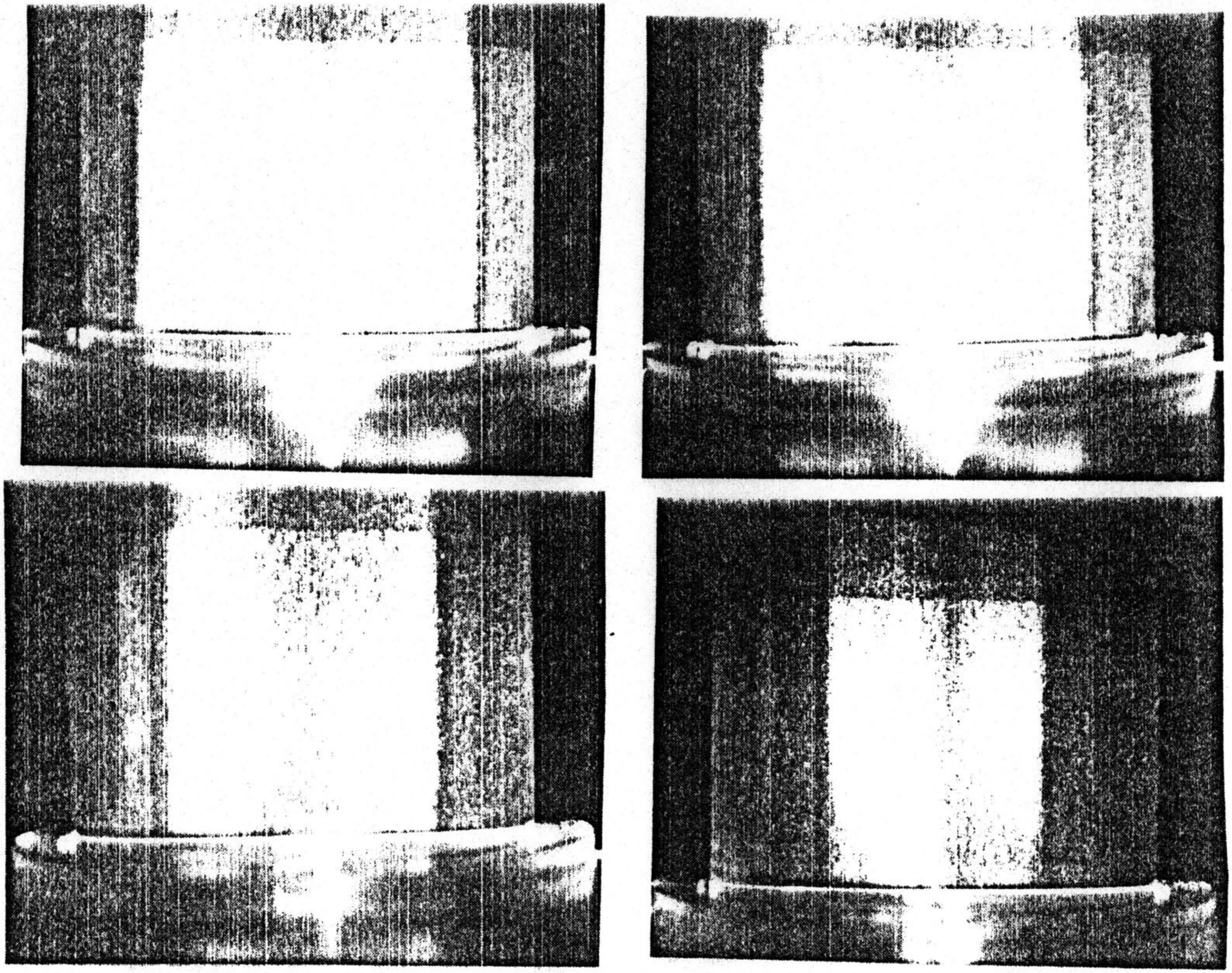

Figure 7.7a-d Sequence of pictures showing columnar evolution of spin-up in an off-axis cylinder. Bright column of fluid is non-spinning.

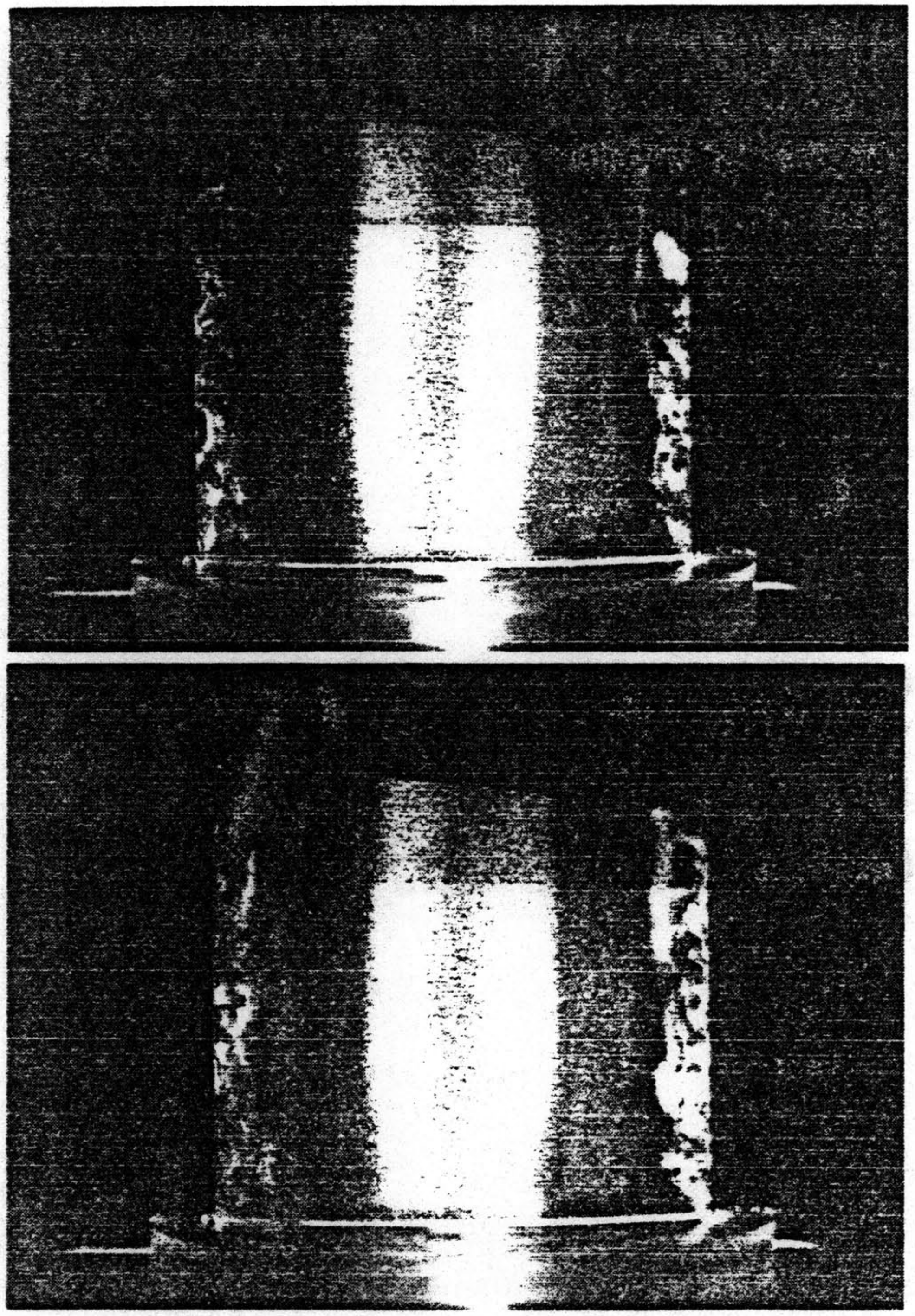

Figure 7.8a,b Spin-down in a circular container. The turntable was stopped and spin-down was photographed. In addition to visible roll cells at the outer radius, the inner core actually pulsates as Ekman pumping now pushes fluid up into this region from the end plate boundary layers.

is unstable. Very soon after the cylinder is stopped roll-cells develop on the outer wall. This does not obscure the fact that there is clearly a core of non-rotating fluid surrounding the center of the cylinder. The rotational speed in these pictures is 20 rpm. The spin-up time constant for this particular geometry was 80s.

In summary, if an appropriate local coordinate system is chosen the equations of motion describing spin-up in an off-axis container are identical to those for the on-axis container. The effect of the position of the axis of rotation is an additional pressure distribution on the container walls, which has no effect on the relative flow in the container and thus has no effect on the ensuing spin-up process.

VII.G Unstable spin-up in non-circular containers

The flow obtained earlier is bound to separate wherever the fluid motion near the boundaries deccelerates. This has been borne out by flow visualization experiments. It was also found, unexpectedly, that these seperated flow regions come to completely dominate the spin-up flow . Figures 7.9 thru 7.16 are a sequence of spin-up pictures taken at 20 rpm using the pie shaped container filled with liquid and seeded with mica flakes. In Figure 7.9 the container is impulsively accelerated from right to left (clockwise). In Fig. 7.10 (two revolutions later) two large seperated flow regions are evident in opposing corners. (If one examines these pictures closely, there are smaller separated flow regions in the other corners as well). The rest of the fluid is rotating in a counter-clockwise direction. As the spin-up progesses those two vortices grow until they possess sufficient rotational energy to move out of the corners. It is interesting to note that those two irrotational vortices, with a distinct core of concentrated vorticity (the dark centers of each vortex)

Figure 7.9

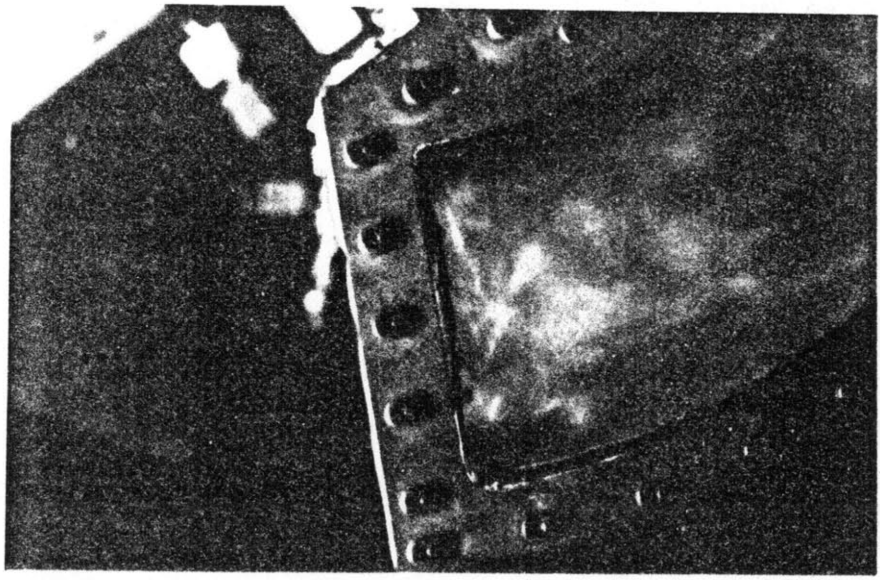

Figure 7.10

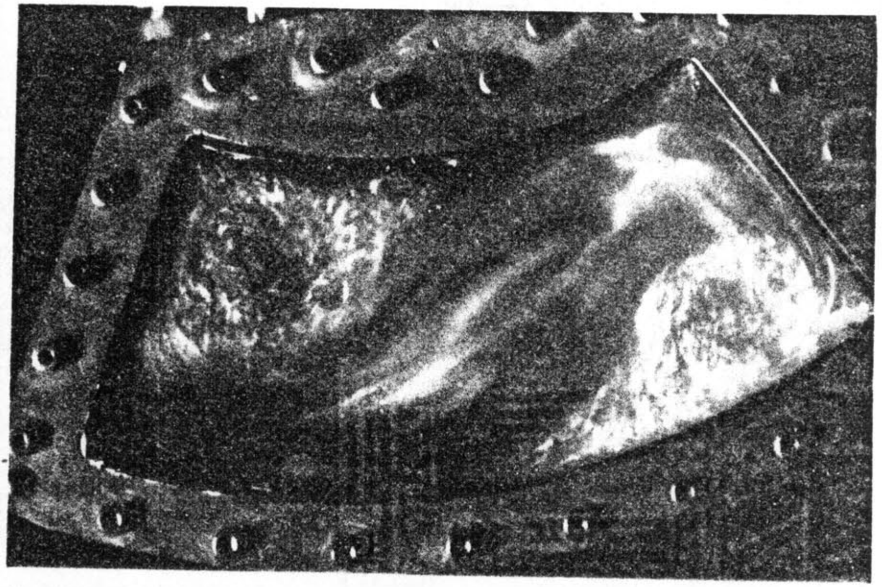

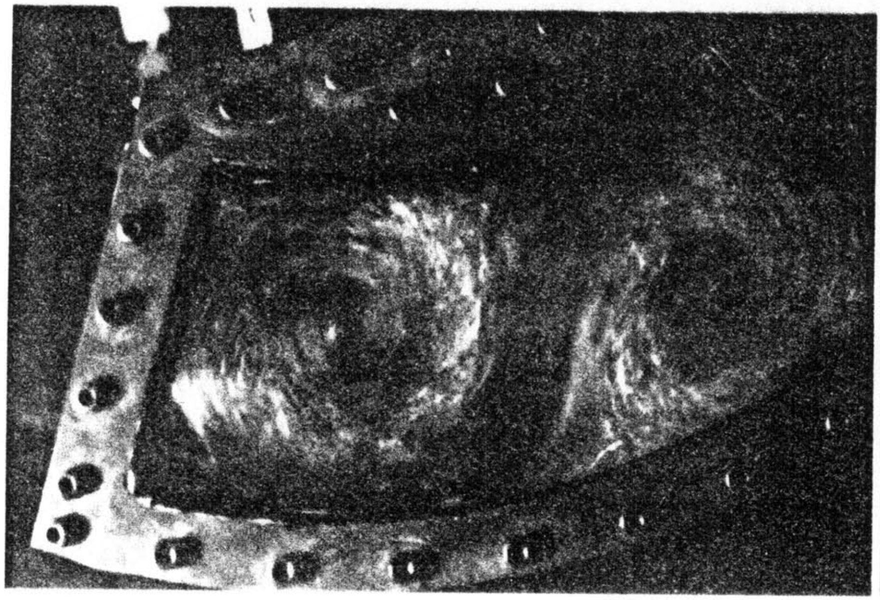

Figure 7.11

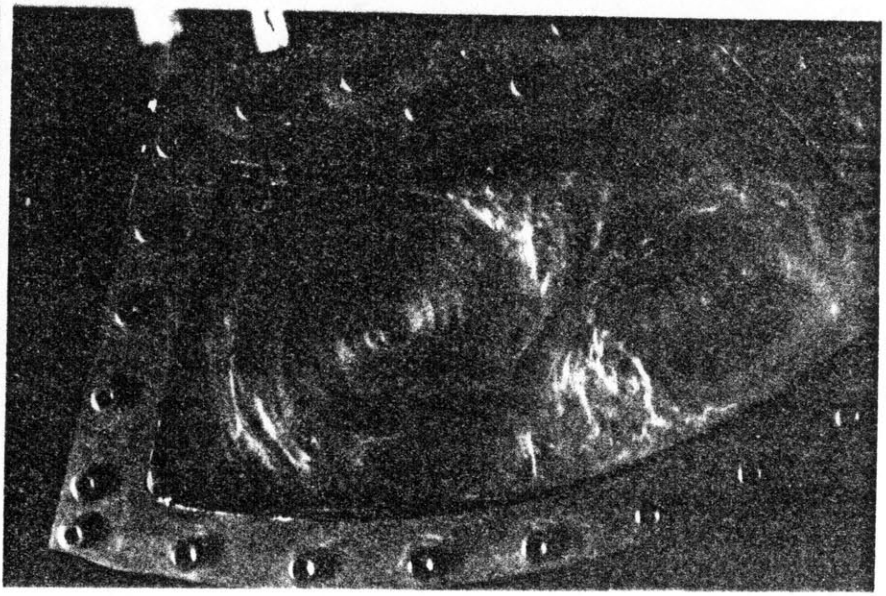

Figure 7.12

Figure 7.13

Figure 7.14

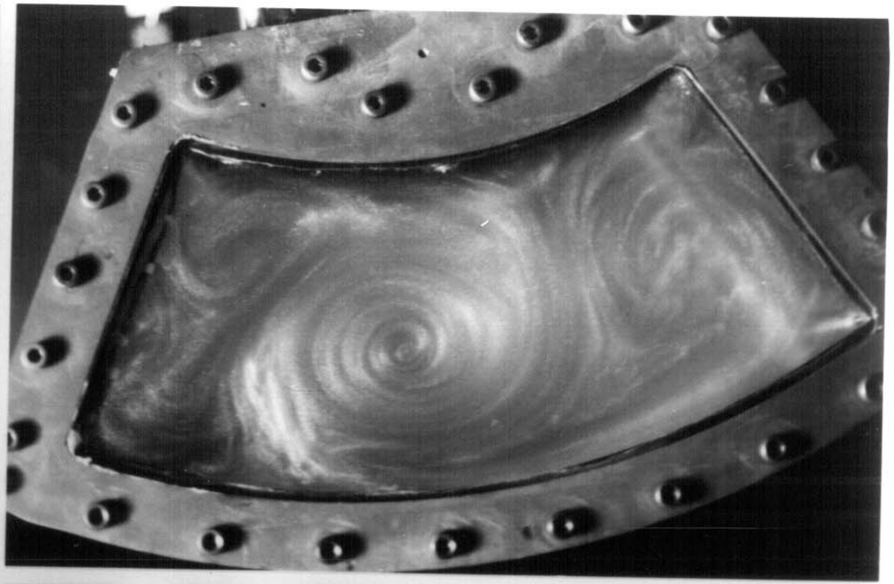

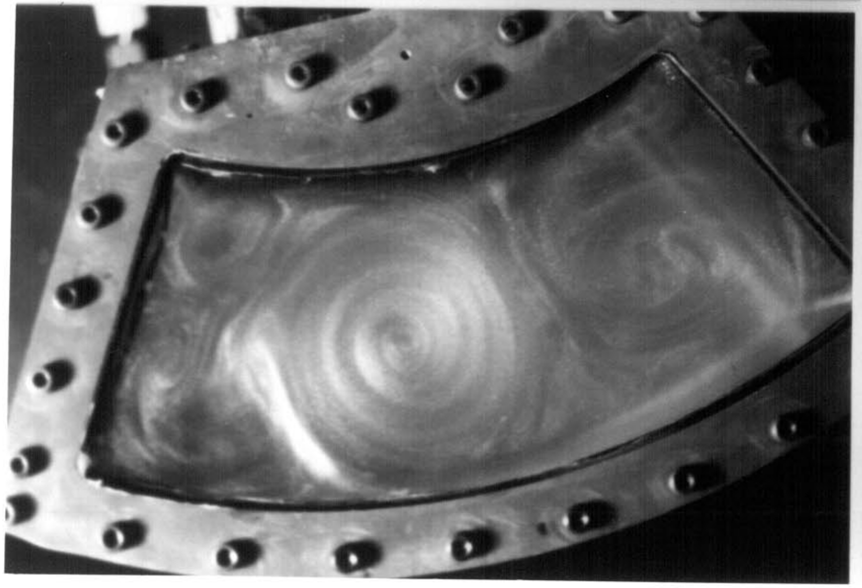

Figure 7.15

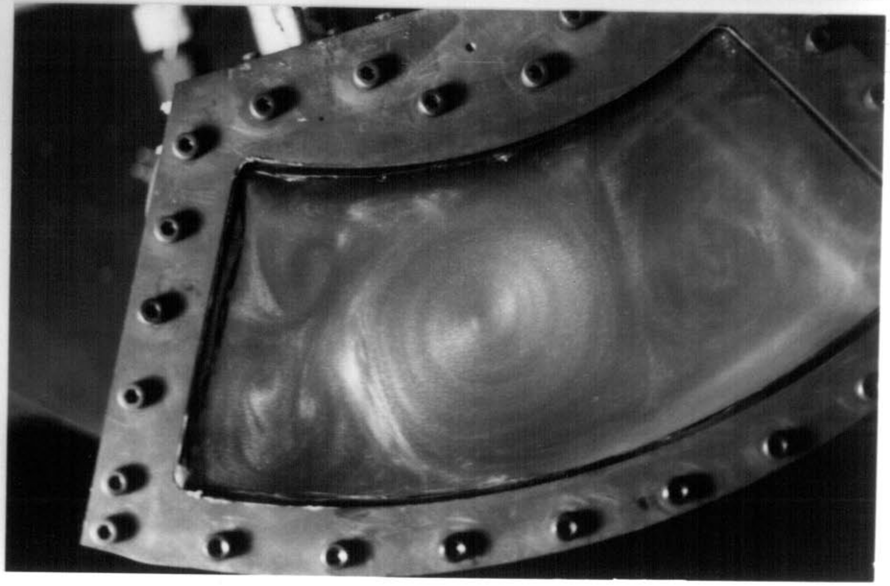

Figure 7.16

are rotating in the same direction, clockwise, the original direction of container rotation. In other words, the initial counterclockwise relative rotation of the bulk fluid is very quickly transformed into two clockwise vortices because of viscous effects in corners. Furthermore, because the two vortices are rotating in the same direction they exert an attractive force on each other. The velocity induced by one vortex on the other causes these vortices to sweep by each other. In Fig. 7.14 they have actually changed places. As these vortices interact they tend to scour the walls of the container creating high surface heat transfer coefficients in the process. This will be discussed in the next chapter. Once these vortices have switched places there no longer appears to be any other great fluid movement, and the flow field of Fig. 7.15 persists for the remainder of the fluid spin-up. As far as can be observed from repeated experiments, the spin-up time constant is still of order τ_E, even for such disordered spin-up flow fields. It is likely that an Ekman like flow is set up by each vortex, drawing fluid in the endplate regions in a fashion similar to, but not the same as the Ekman flow in a right circular cylinder. Here the velocity is of order 1/r measured outward from the vortex core, rather than of order r in a circular cylinder.

Another sequence of spin-up flow field pictures, Figures 7.17 thru 7.20 illustrate the vortex formation in a baffled circular cylinder impulsively accelerated to 500 rpm. The cylinder used is shown in Fig. 4.3. There are at least seven distinct eddies in Fig. 7.18. The largest and strongest eddies are those in the upper left hand corner of container rotating clockwise (same direction as the container), and one immediately to the right of the baffle, rotating counterclockwise. The clockwise vortex clearly originated in the seperated flow region in the corner between the baffle and the container wall though the origins of the others

Figure 7.18

Figure 7.17 First of a sequence of spin-up pictures showing eddy flow-field in baffled right circular cylinder.

Figure 7.19

Figure 7.20 As spin-up nears completion, eddies become less and less distinct.

are not so apparent. The vortex pattern is more stationary at these high rotational speeds than at the low speeds (probably because there are more pairs of vortices rotating in opposite directions), but it seems that the number of vortices is more likely a function of geometry than rotational speed. It is also found that the time constant for the decay of this energetic vortex flow field is still τ_E.

CHAPTER 8

TRANSIENT HEAT TRANSFER TEST RESULTS

VIII.A. Transient heat transfer

In this chapter, the results of heat transfer experiments during liquid spin-up are examined. These experiments will be referred to as transient heat transfer tests since the heater power is on while the fluid in the container is still being spun-up. The results of these tests are summarized as follows:

1. in tests with water, alcohol and glycerine/water- a heat transfer coefficient enhancement is found to last a time of order $(\alpha t)^{.5}/\delta_t$ and for high surface heat flux this time is short compared to τ_E,
2. the magnitude of the enhancement to h is a function of the fluid relative velocity, although the complex interaction of the spin-up vortices prevents verification of a simple model,
3. flow visualization confirms that the transient plume is two dimensional and that the plume gets swept along by whatever vortices are in the vicinity of the heater.

The bulk of the transient heat transfer testing was conducted in the following manner. The rotor was idled at some low rotational speed (usually 250 rpm) for a period of time sufficiently long to insure that all thermocouples were in temperature equilibrium (no instrumentation transients) and that the fluid was in solid body rotation as well. The data collection software was enabled for a short period (roughly 5s). At this moment a step change was introduced into both the DC motor voltage and the container heater voltage which caused the rotor to accelerate while a plume was forming inside the container. Surface temperature change as a function of time was recorded on disk and the test was stopped when a steady surface temperature was reached. Tests were also done with the rotor accelerated slowly rather than impulsively. The DC motor voltage was adjusted slowly by hand inorder to produce a desired acceleration rate.

Figure 8.1 and Figures 8.3 thru 8.5 are the results from a sequence of tests performed at constant heater power with varying acceleration rates. In the first curve in Fig. 8.1 the heater was energized with the rotor at 500 rpm and the fluid in solid body rotation. This test provides a datum for interpreting the affect of fluid relative motion. If the fluid is in solid body rotation the surface temperature time history is determined by the thermal inertia of the heater and the time constant of the developing thermal and momentum boundary layers . The second curve in Fig. 8.1 is a plot of surface temperature history at the same heater power following an impulsive acceleration. It is obvious that a quasi-steady state arrives in a time short compared with the Ekman spin-up time ($3\tau_E \approx$ 30 s). Though the surface temperatures are lower for the first 5 seconds than they would have been had there been no fluid transient, it is surprising to find that the surface temperature becomes steady while there is still considerable fluid relative motion. Fig. 8.2 shows a heater plume spiralling inwards during a spin-up. The trajectory of the plume is dictated by the near presence of vortical flow . However, at the time this picture was taken the temperature at the heater surface had already reached a quasi-steady value. The reason for this is straightfoward. The bulk fluid spins-up slowly but the fluid very near to the wall spins up quickly by viscous diffusion. A radial pressure gradient of order ($\rho\omega^2R$) is quickly established even though the absolute pressure on the outer wall is still well below its final value. At the heater power levels used in these experiments the thermal boundary layers are very thin, thin enough to be within the viscous dominated regions of the spin-up flow field. As soon as the side-wall spin-up boundary layers grow to sufficient size, the temperatures on the heater surface are no longer affected by vortex interactions in the interior, and because the pressure gradient at the wall

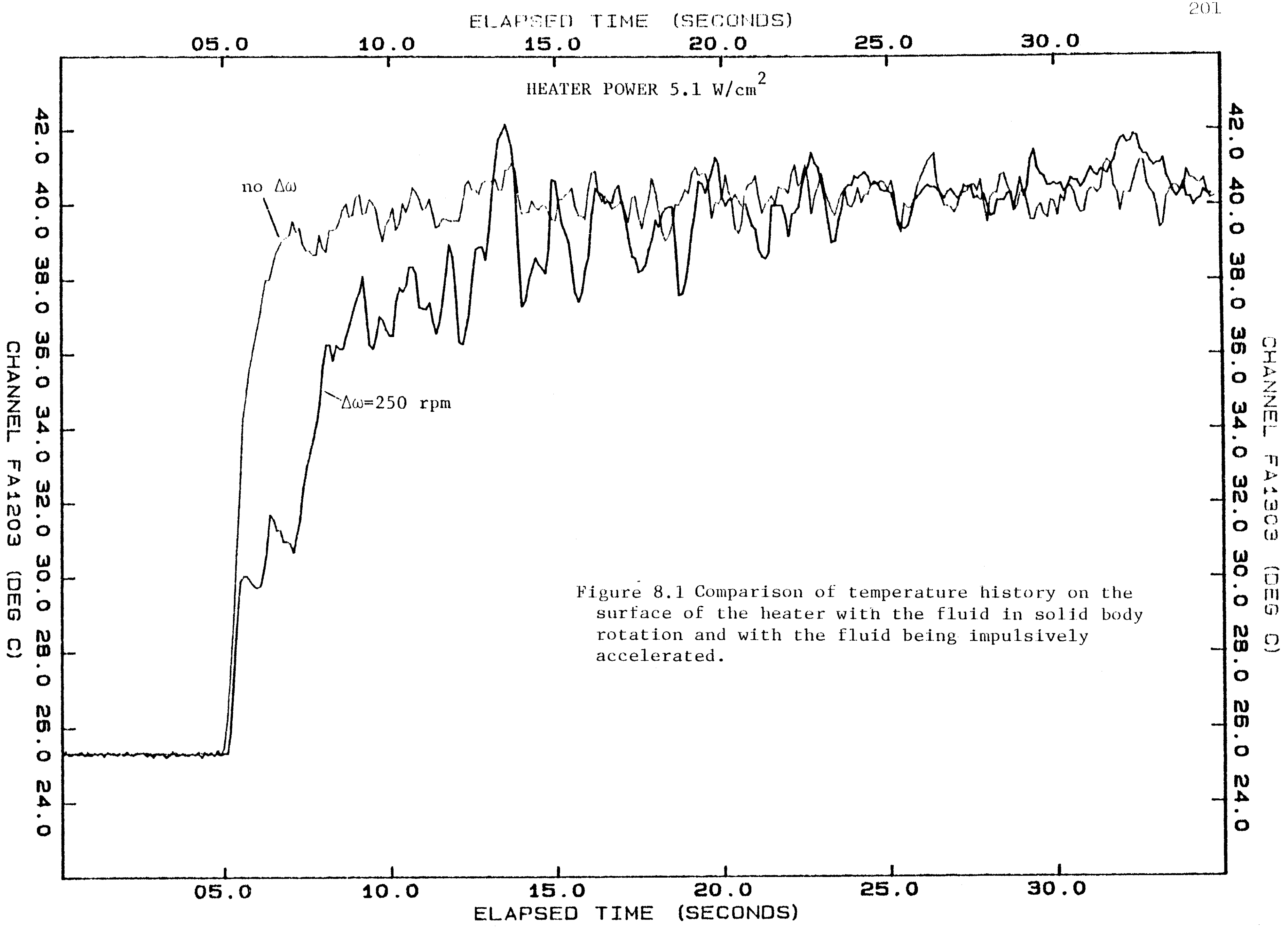

Figure 8.1 Comparison of temperature history on the surface of the heater with the fluid in solid body rotation and with the fluid being impulsively accelerated.

is nearly at the steady state value the surface temperatures are steady as well. This arises from the fact that the bouyant terms near the wall are based upon the local centrifugal acceleration acting over the density difference. Since the wall fluid has been spun up to the steady state ω the centrifugal acceleration will have achieved its final value.

The behaviour of the surface temperature during slower accelerations can be explained in a similar fashion. Surface temperatures will be higher while the rotor is accelerating and drop down later to reflect the quasi-steady conditions at the final rotational speed. There is some lag in thermal response because of the inverse relationship between thermal boundary layer thickness and rotational speed. The fluid relative motion has a greater impact on surface temperature early on in the acceleration. The results of varying acceleration rates are shown in Figures 8.3 thru 8.5. The circled region in the graph of Fig. 8.4 shows the scouring action of a vortex moving around in the interior fluid. In the spin-up pictures of the previous chapter these vorticies were shown to have originated in the corners of the pie shaped container. The vortices tended to grow in size and moved out of the corners, sweeping along the outer wall and sweeping some fraction of the hot fluid off of the heater.

One would expect then that the spin-up will affect the surface h only until the momentum boundary layer developing concurrently with the inviscid spin-up in the interior has grown to a distance of the order of the plume boundary layer thickness. It also seems reasonable to assume that if the thermal boundary layer thickness is large then the period of time that the relative motion will affect the surface temperature will also be longer. This assumption is confirmed in the temperature histories shown in Figures 8.6 thru 8. The output shown here follows a series of impulsive accelerations with diminishing heater power. The heater power used in

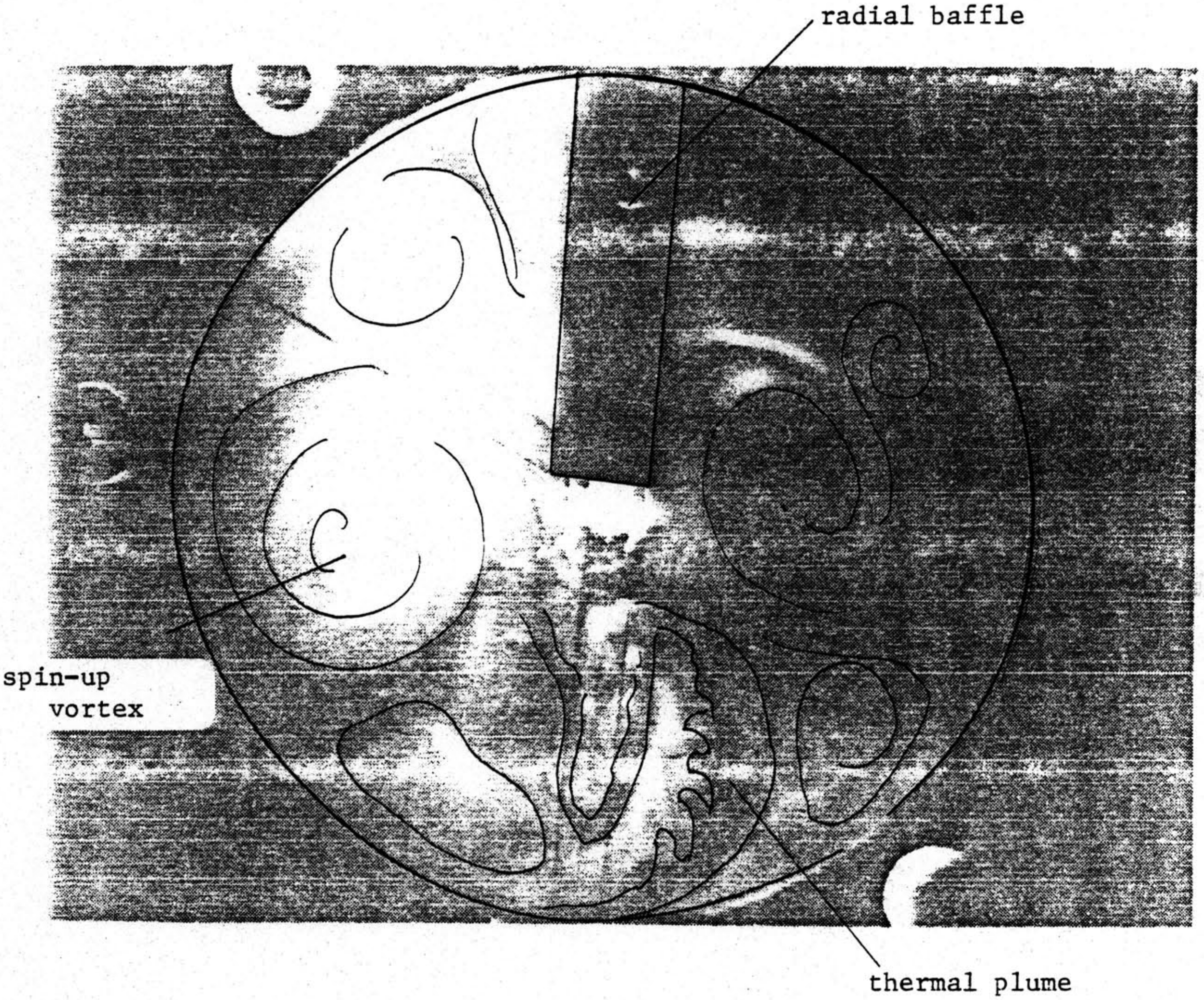

Figure 8.2 Thermal plume during spin-up. Plume is swept along by a local vortex.

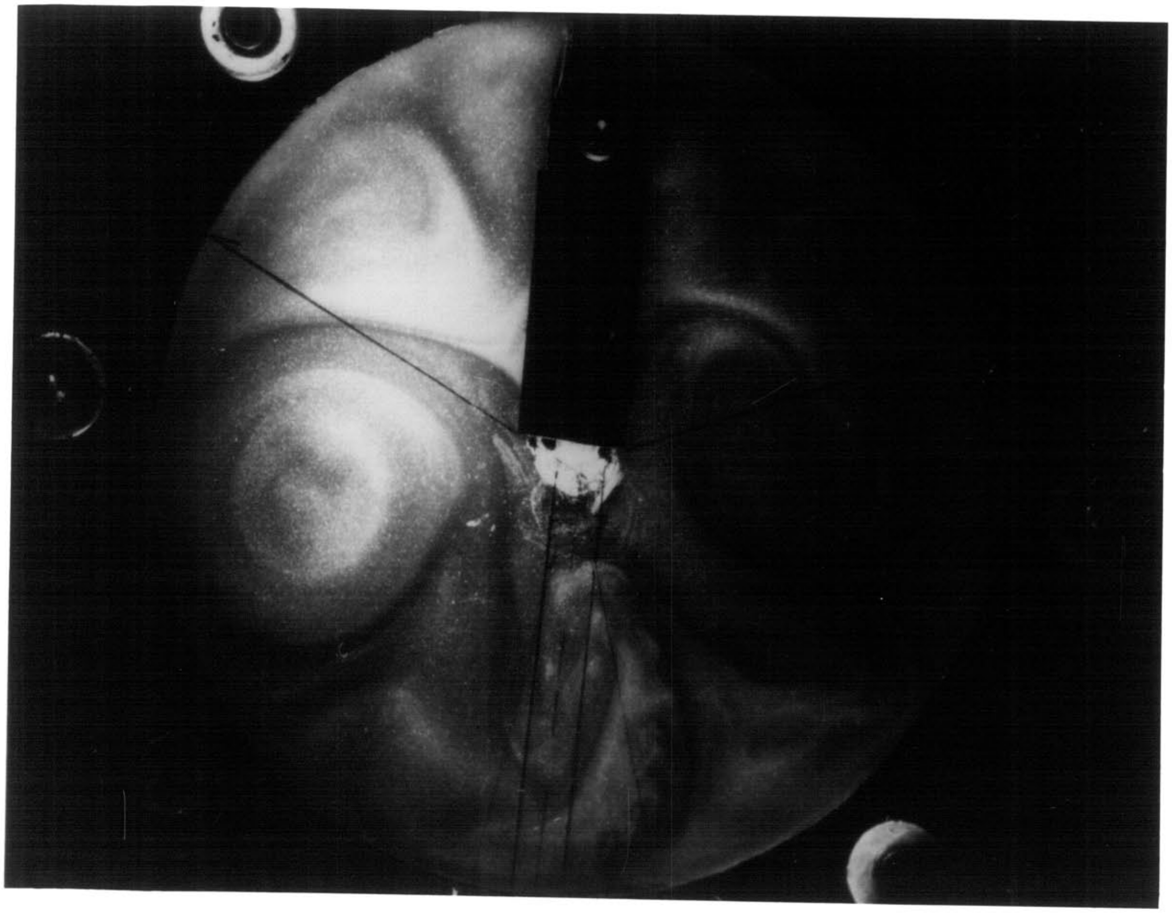

Figure 8.2

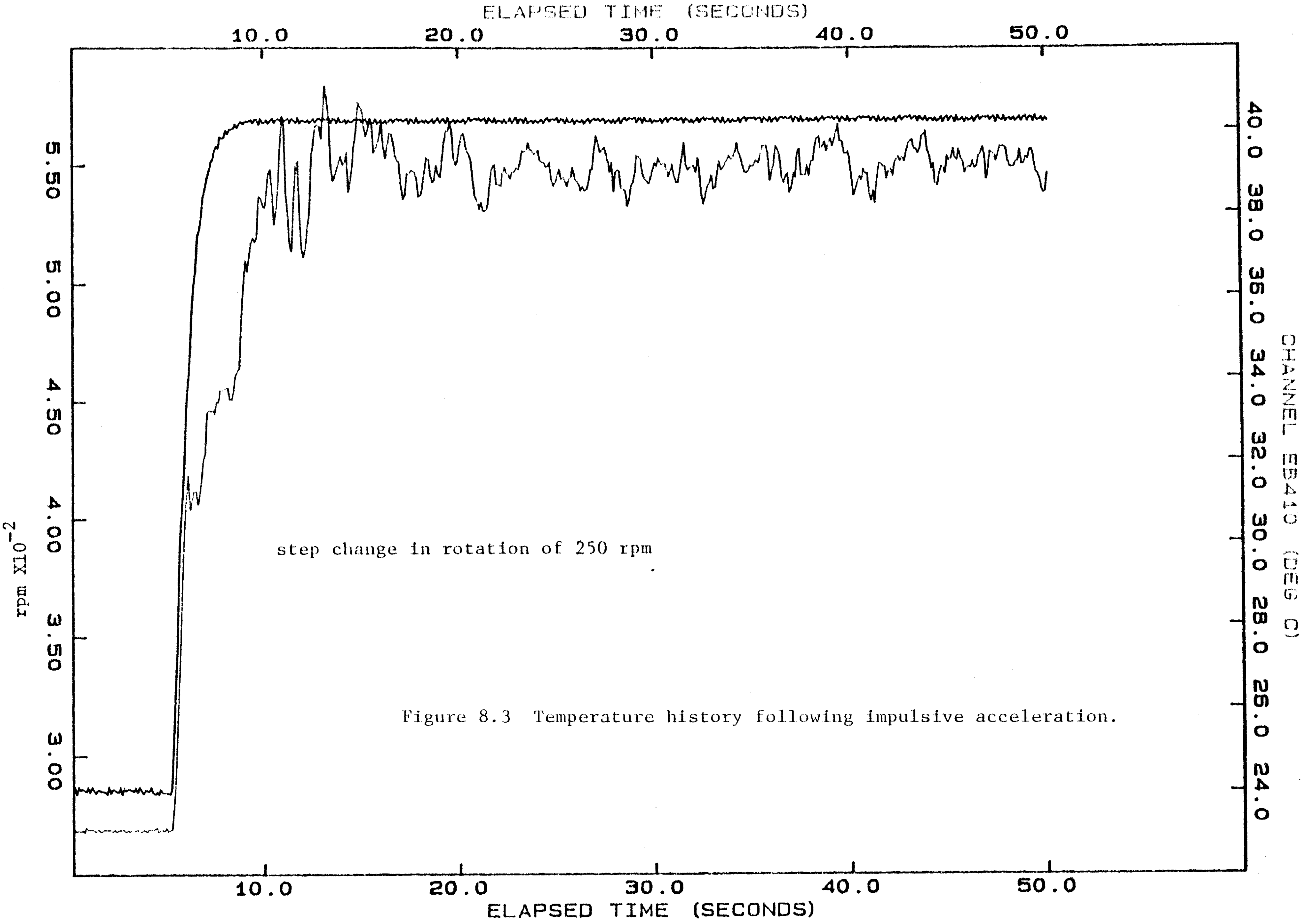

Figure 8.3 Temperature history following impulsive acceleration.

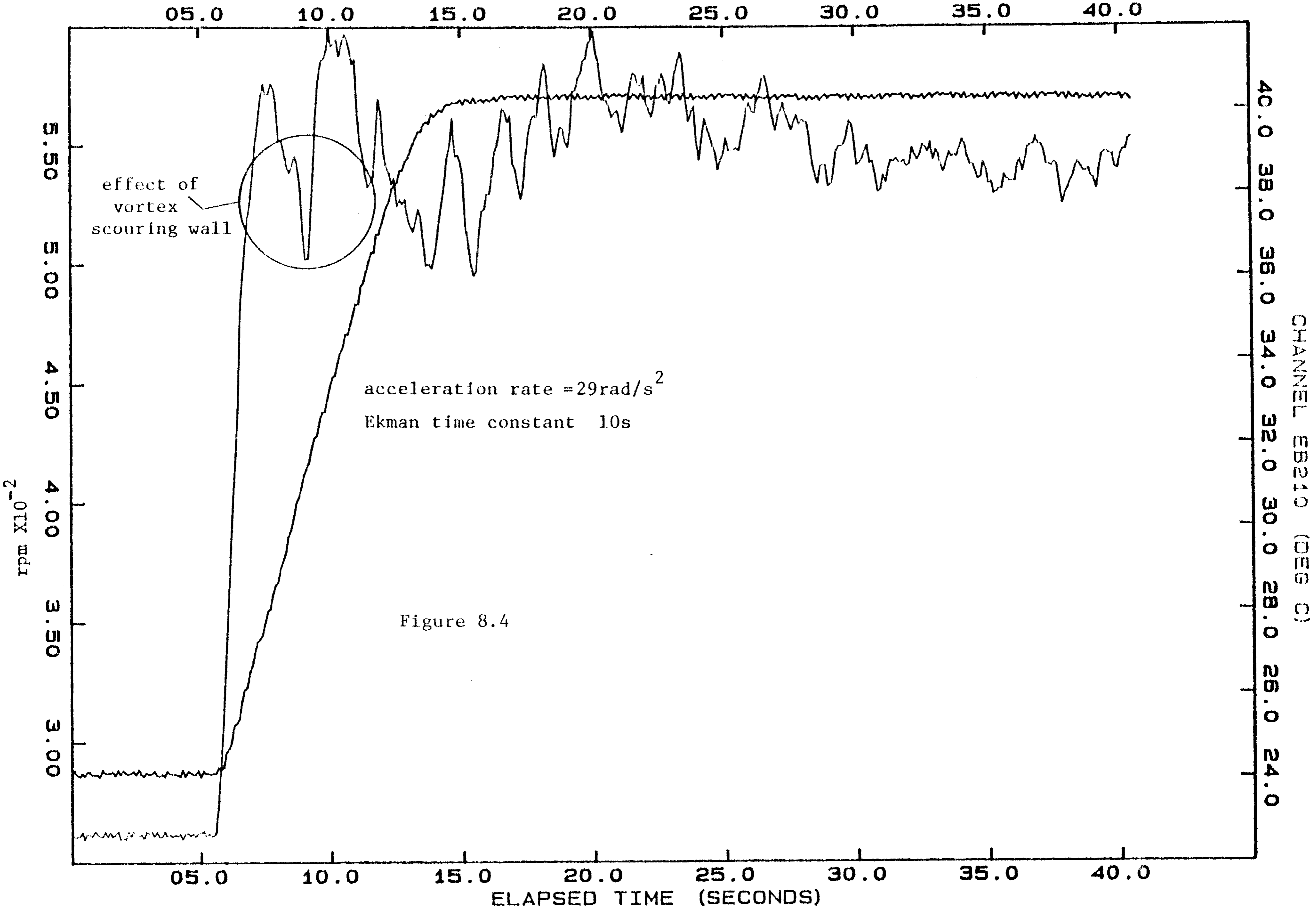
05.0
10.0
15.0
20.0
25.0
30.0
35.0
40.0
5.50
5.00
4.50
4.00
3.50
3.00
rpm X10^{-2}
40.0
38.0
36.0
34.0
32.0
30.0
28.0
26.0
24.0
CHANNEL EB210 (DEG C)
effect of vortex scouring wall
acceleration rate =29rad/s^2
Ekman time constant 10s
05.0
10.0
15.0
20.0
25.0
30.0
35.0
40.0
ELAPSED TIME (SECONDS)

Figure 8.4

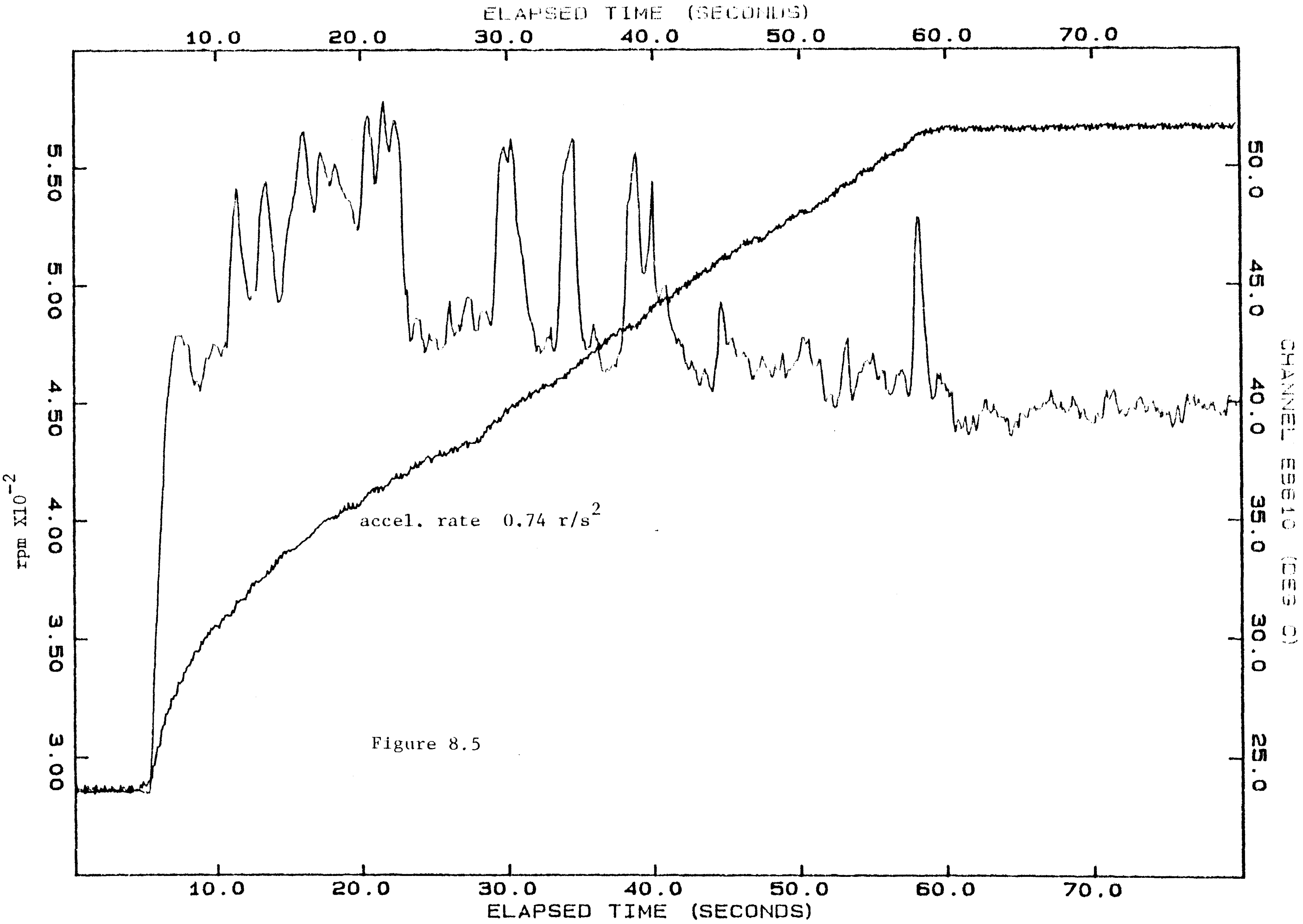
ELAPSED TIME (SECONDS)
10.0
20.0
30.0
40.0
50.0
60.0
70.0
rpm X10^{-2}
5.50
5.00
4.50
4.00
3.50
3.00
CHANNEL ES610 (ES3 C)
50.0
45.0
40.0
35.0
30.0
25.0
accel. rate 0.74 r/s^2

Figure 8.5

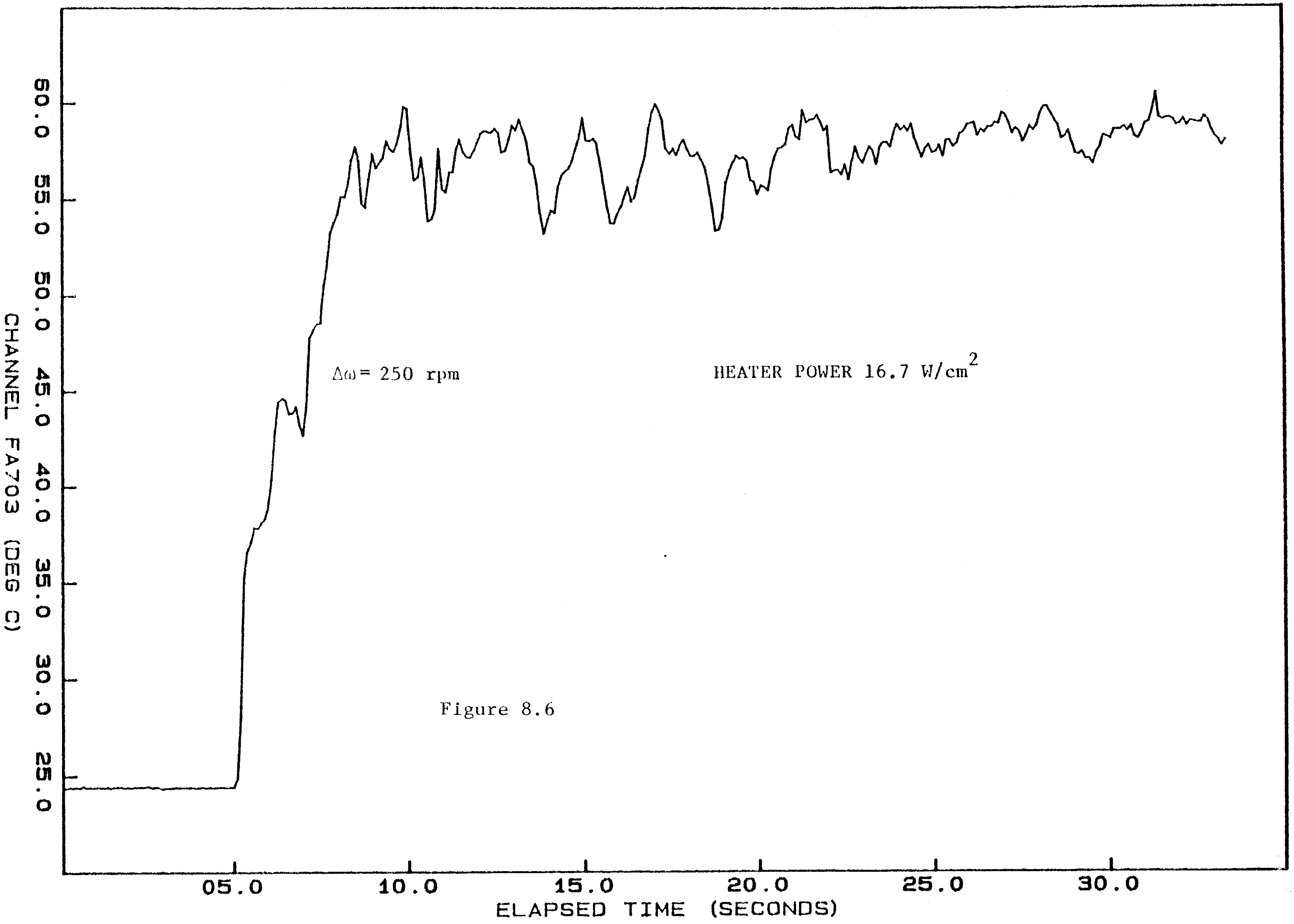

Δω = 250 rpm

HEATER POWER 16.7 W/cm^2

Figure 8.6

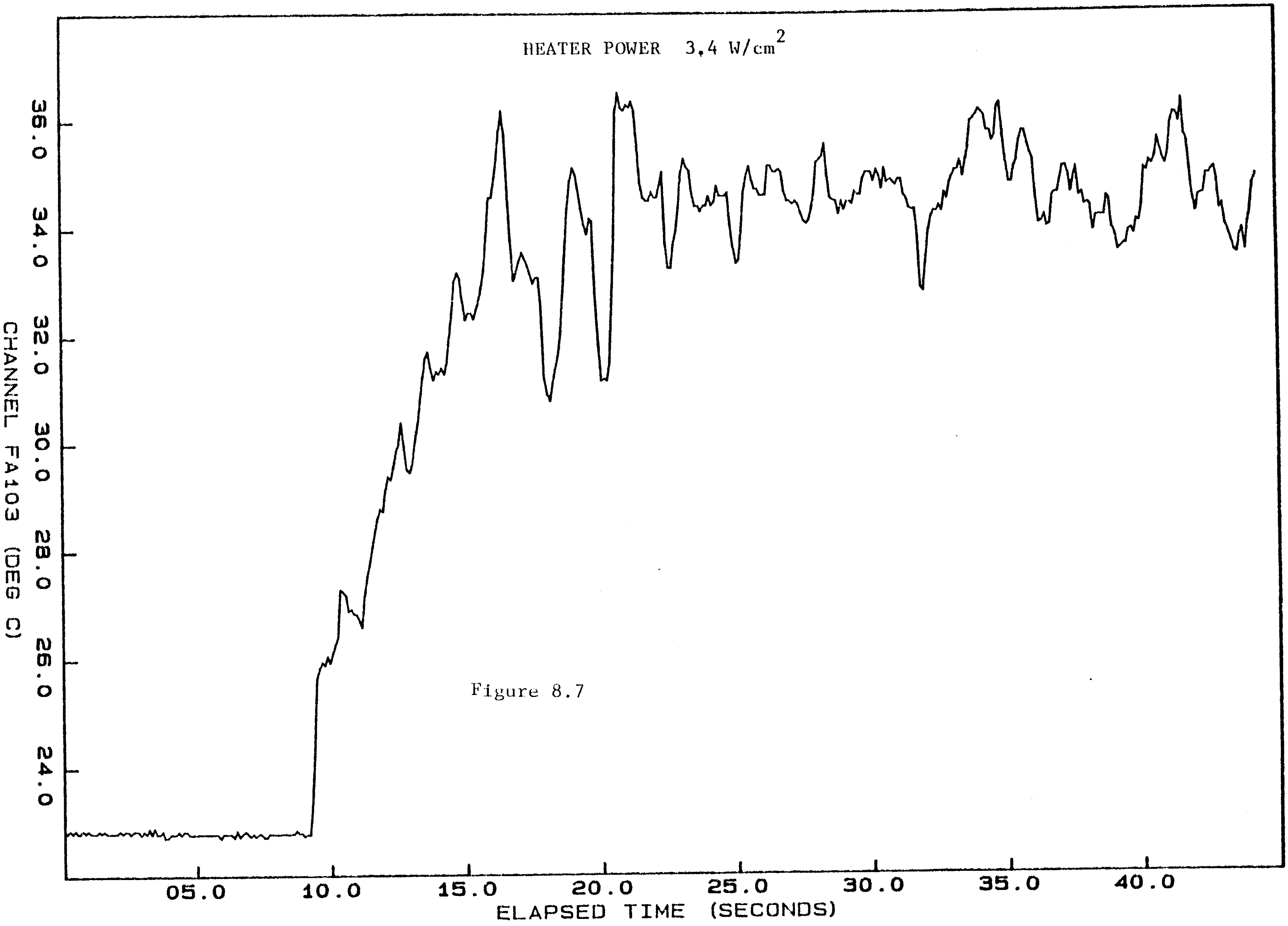
HEATER POWER 3.4 W/cm^2

Figure 8.7

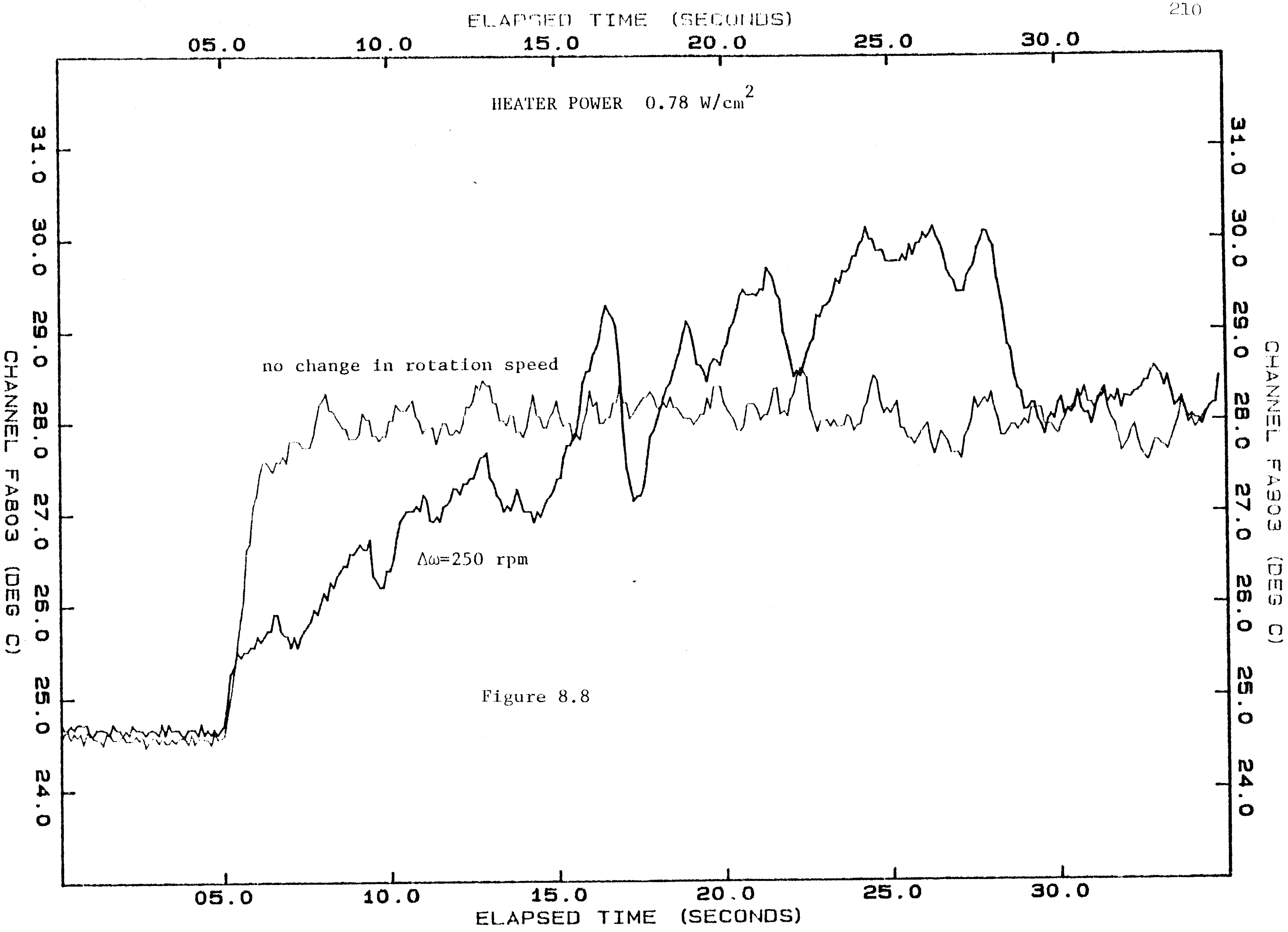
ELAPSED TIME (SECONDS)
05.0
10.0
15.0
20.0
25.0
30.0
HEATER POWER 0.78 W/cm^2
31.0
30.0
29.0
28.0
27.0
26.0
25.0
24.0
CHANNEL FA803 (DEG C)
no change in rotation speed
Δω=250 rpm
CHANNEL FA803 (DEG C)
05.0
10.0
15.0
20.0
25.0
30.0
ELAPSED TIME (SECONDS)

Figure 8.8

these tests ranged from 17 W/cm^2 down to 0.78 W/cm^2 with the same final rotational speed. The thermal boundary layer thicknesses in these tests varied by a factor of 2 from 0.009 cm. to 0.016 cm. (boundary layer thickness varies like $(F_o)^{-.25}$). The figures show that the enhancement in h follows inversely with surface heat flux F_o .

The first attempt to correlate all the data taken during the transient tests using water, alcohol, and water/glycerine into a single graph of $\Delta T/\Delta T_{ss} = f(\tau_{ht})$ where τ_{ht} is a dimensionless time was unsuccesful. The dimensionless time was based on the ratio of the diffusive boundary layer thickness to the quasi-steady thermal boundary layer thickness at the final rotational speed:

$$\tau_{ht} = \delta_v/5\delta_t = (\sqrt{\nu t})h/(5k) \quad .. \qquad (8.a.1)$$

This dimensionless time reflects the assumption that so long as fluid relative motion existed close to wall that natural convection at a low pressure gradient would be augmented by forced convection. But once the momentum boundary layer had grown sufficiently large, say 5 times the thermal boundary layer thickness, not only would the surface heat transfer boundary layer be unaffected from fluid motion in the interior, but a nearly quasi-steady pressure gradient would exist to increase the surface natural convection h.

The dimensionless time (Eq. 8.a.1) was succesful in reducing all water temperature histories to a single curve and the glycerine tests to a single curve- but did not allow for correlating both sets of tests together. This immediately suggested that a Prandtl number effect was being overlooked. The similarity solutions for natural convection flows of Prandtl number fluids >1 were used as a guide and a new dimensionless time was chosen based on the conduction boundary layer thickness times $Pr^{.5}$, which is effectively the associated momentum thickness layer:

$$\tau_{ht} = \delta_v/(Pr)^{.5}/\delta_t \qquad (8.a.2)$$

$$\text{or } \tau_{ht} = (\alpha t)^{.5}/(h/k) \qquad (8.a.3)$$

where it is noted that τ_{ht} is now independent of fluid viscosity.

Figures 8.9 thru 8.16 are plots of the temperature difference ($T_s - T_a$) normalized by the quasi-steady temperature difference at the end of the test vs. the dimensionless time of Eq. 8.a.3. All tests followed impulsive accelerations from 250 rpm to 550 rpm (the maximum allowable change in speed). All three working fluids were used in these tests and both the long and short heaters. Several features of these curves are worth noting. The enhancement in transient heat transfer coefficient for this step change in speed lasts to about $10\tau_{ht}$. If it were possible to give the system a greater impulsive acceleration, this enhancement would probably last longer. (It should be noted, though, that the Ekman time decreases as ω increases, and that the enhancement will last only through a time of order τ_E). There also appears to be little difference between the data for long and short heaters (factor of 5 different in length) suggesting again, that the transient h is also independent of length.

A simple model for establishing a reasonable estimate of surface heat transfer enhancement is motivated by observations of plumes such as the one in Fig. 8.2. Following an impulsive acceleration there is essentially slug flow of order ($\Delta\omega c$) over the heater of length l as indicated in Fig. 8.17. The simplified one-dimensional energy equation for this problem is:

$$\frac{\partial T}{\partial t} + (\Delta\omega c)\frac{\partial T}{\partial x} = \alpha\frac{\partial^2 T}{\partial y^2} \qquad (8.a.4)$$

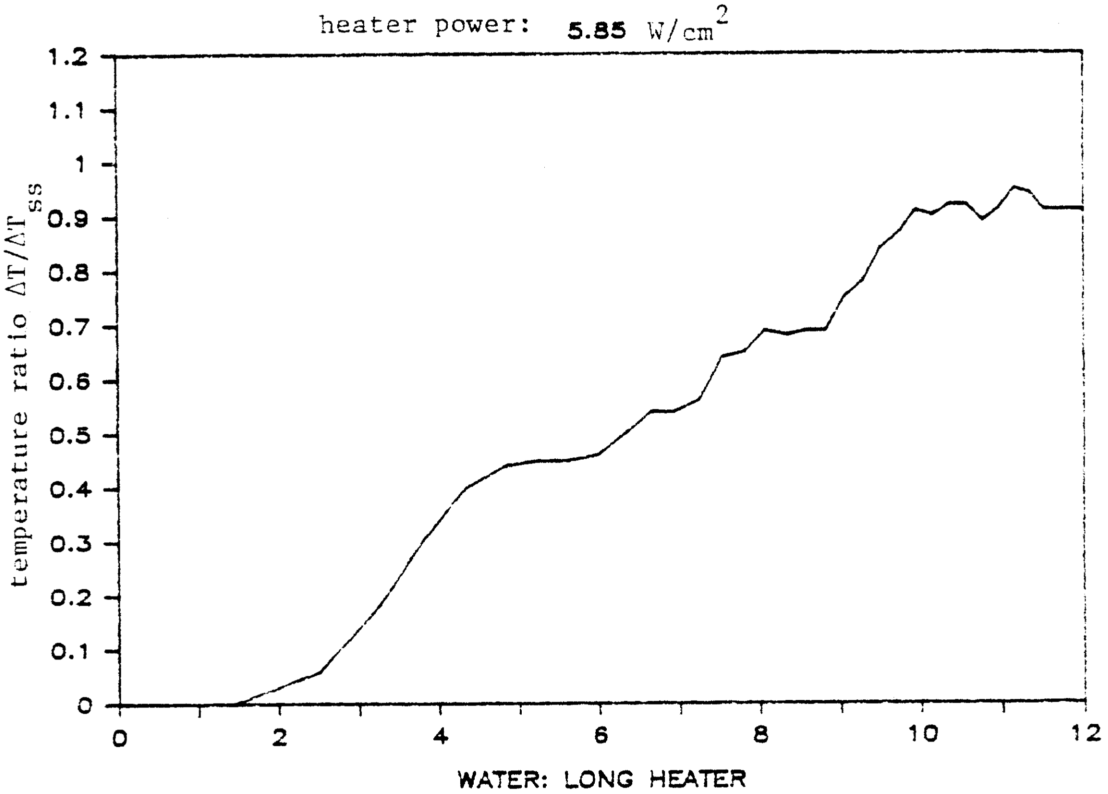

Figure 8.9

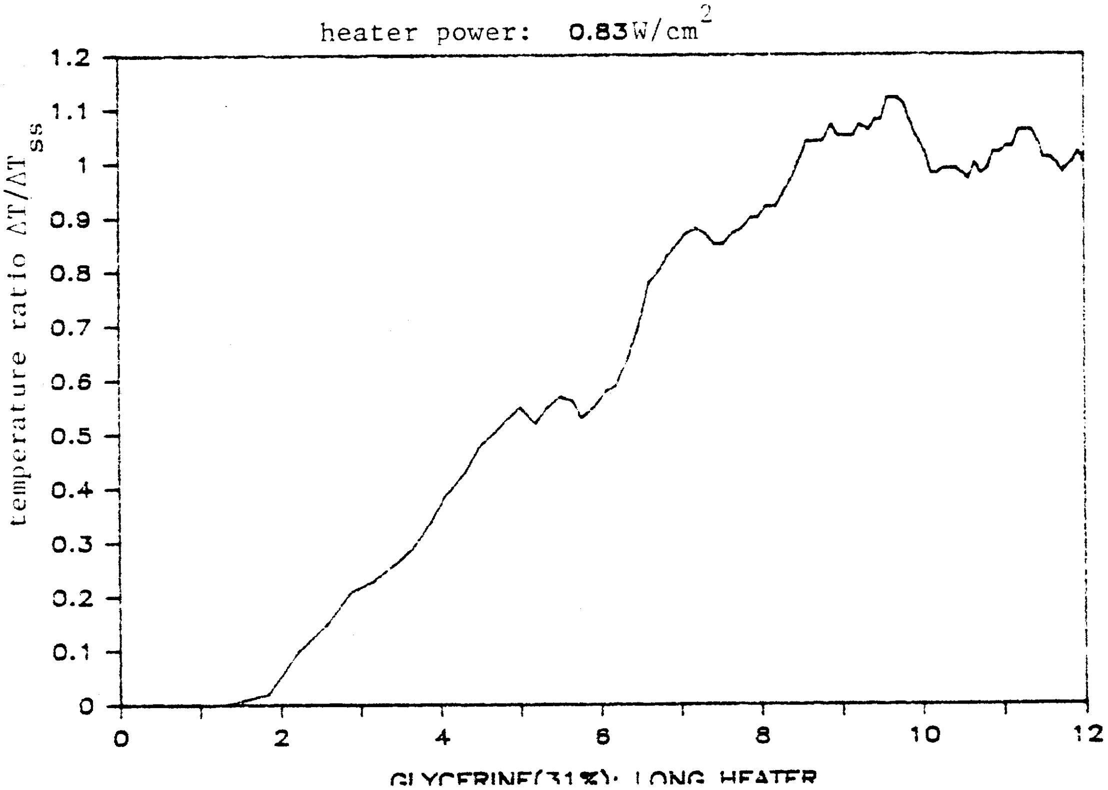

Figure 8.10

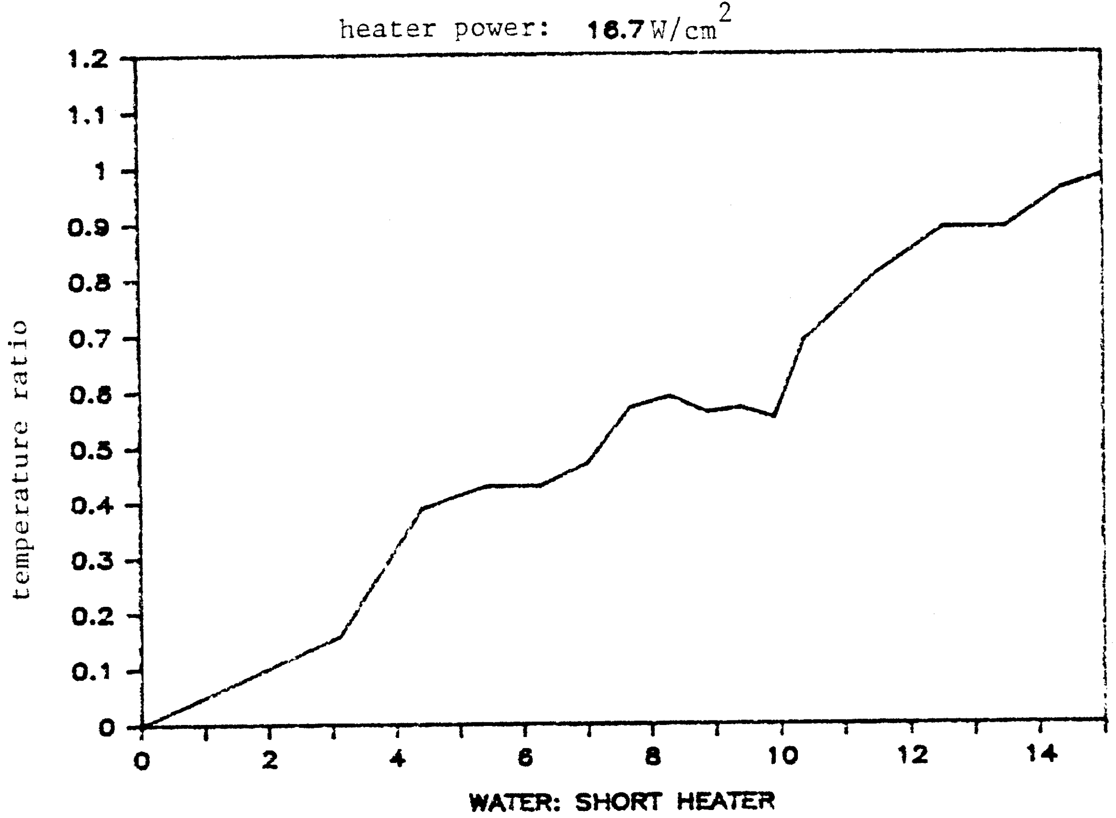

Figure 8.11

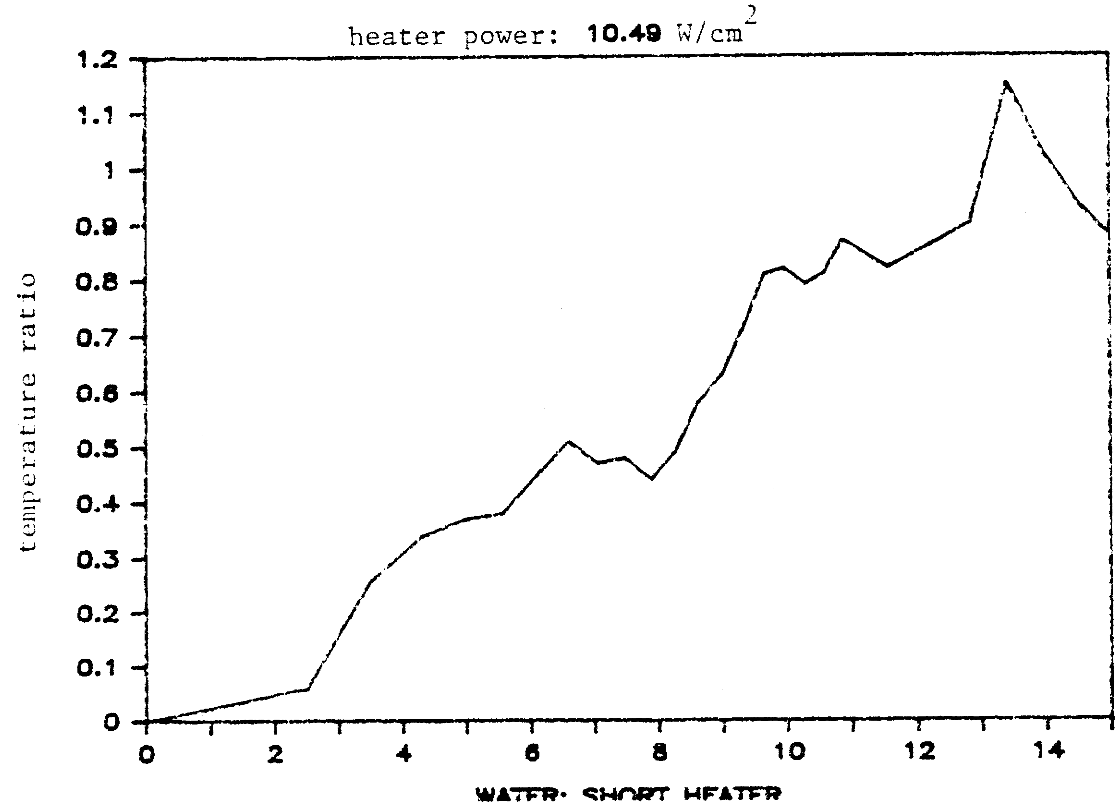

Figure 8.12

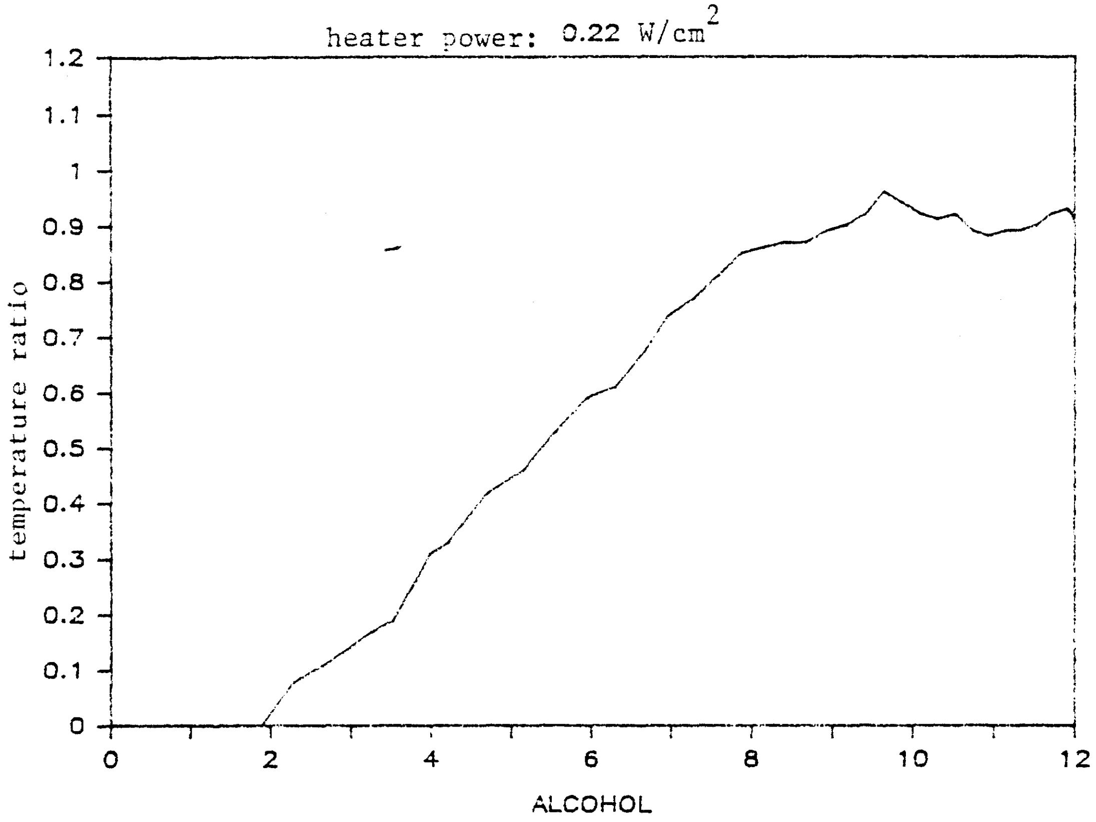

Figure 8.13

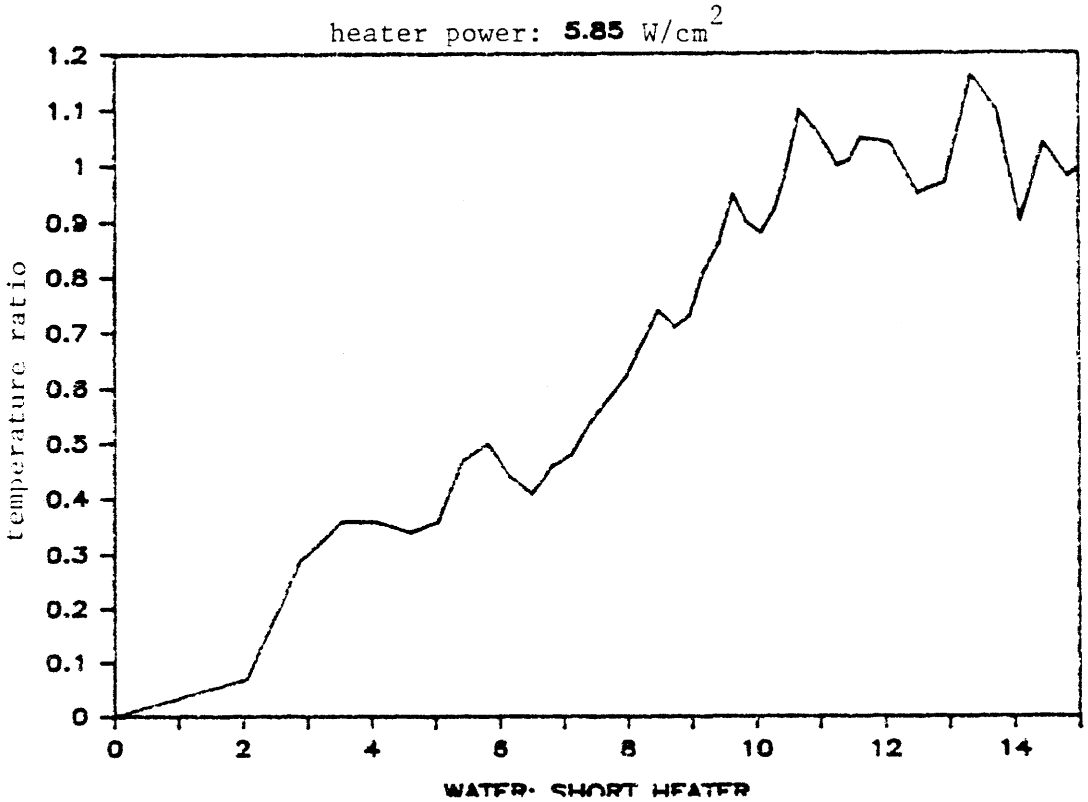

Figure 8.14

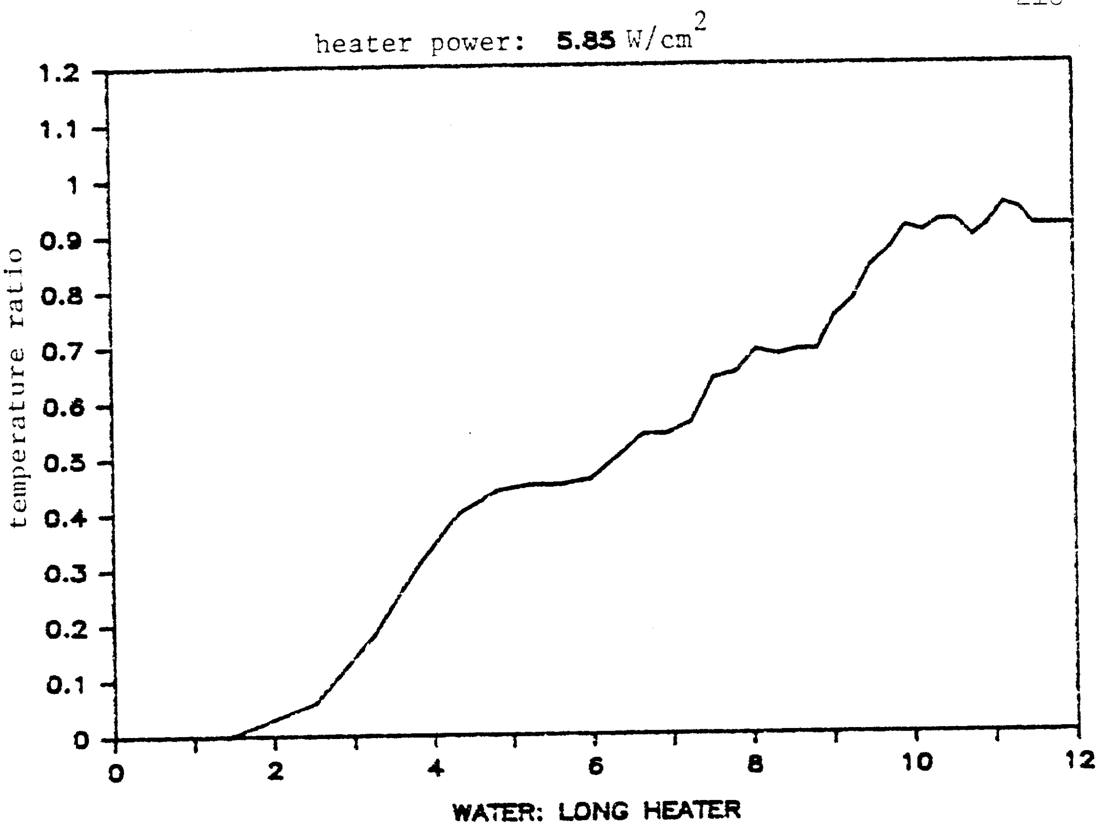

Figure 8.15

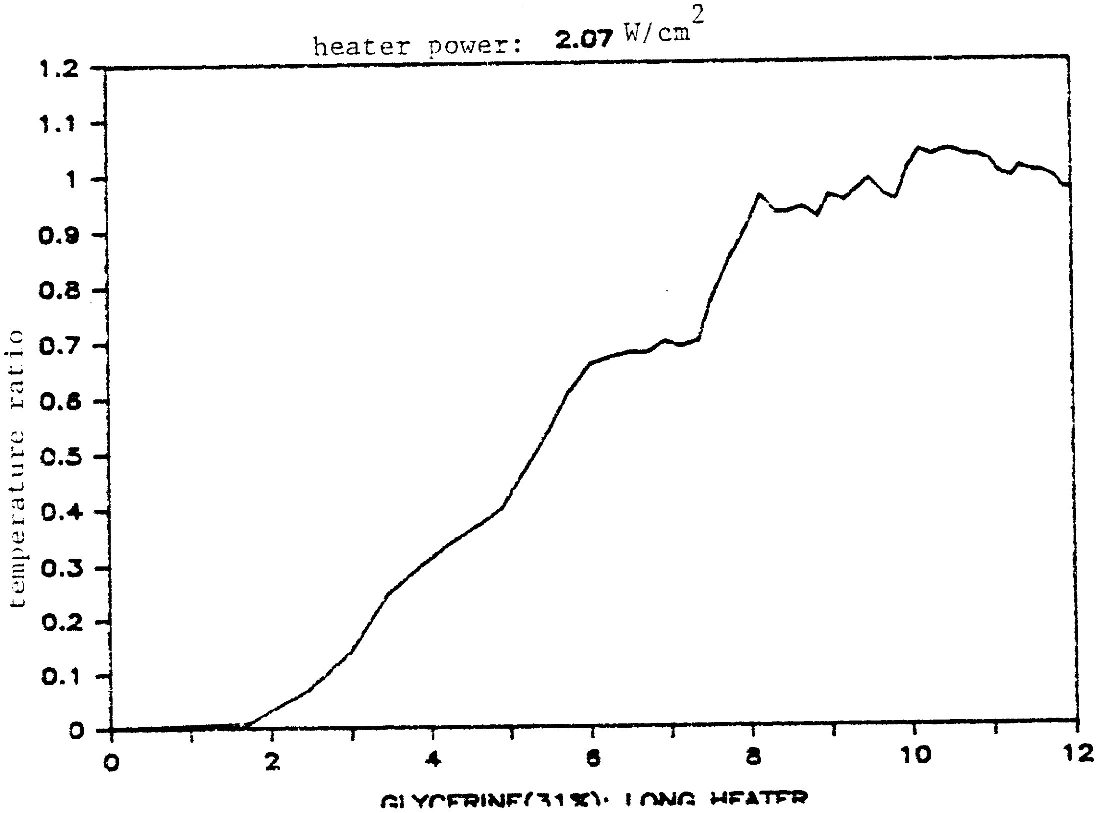

Figure 8.16

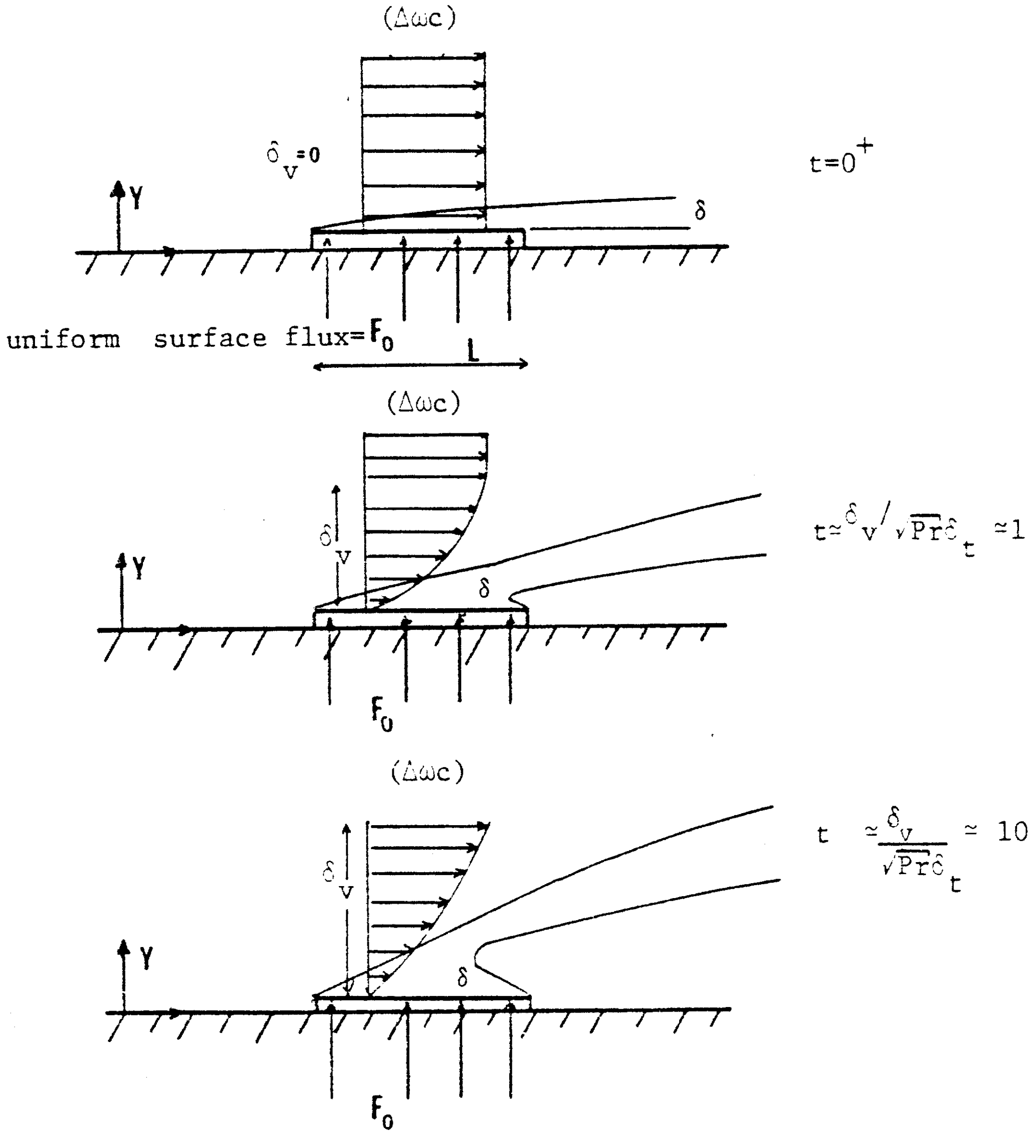
(Δωc)
$\delta_v = 0$
$t=0^+$
Y
δ
uniform surface flux= F_0
L
(Δωc)
δ_v
Y
δ
$t \approx \delta_v / \sqrt{Pr}\,\delta_t \approx 1$
F_0
(Δωc)
δ_v
Y
δ
$t \approx \frac{\delta_v}{\sqrt{Pr}\,\delta_t} \approx 10$
F_0

Figure 8.17

where $q=(\Delta\omega c)$. Now for $t \gg 1/\Delta\omega c$, the thermal boundary layer is quasi-steady and the first term is neglected. It can be shown that a solution of Eq. 8.a.4 for constant heat flux (F_0) boundary condition is:

$$T-T_A = \frac{2Fo\sqrt{(\nu x)}\,e^{-\eta^2}}{k\sqrt{(q\pi Pr)}} - y/2\mathrm{erfc}(\eta)$$

$$\text{where } \eta = y/2(1/\sqrt{(\nu x/qPr)} \qquad (8.a.5)$$

and $$T_S - T_A = \frac{2F_0}{k}\frac{\sqrt{(\nu x)}}{\sqrt{(q\pi Pr)}} = \frac{1.13F_0 x}{k\sqrt{(qx/\alpha)}} \quad . \qquad (8.a.6)$$

The surface heat transfer coefficient is thus:

$$h = \frac{k\sqrt{(qx/\alpha)}}{1.13} \qquad (8.a.7)$$

and $$h_{av} = 1.77k\sqrt{(q/l\alpha)} \qquad (8.a.8)$$

and the average Nu is:

$$Nu = 1.77\sqrt{(ql/\alpha)} \qquad (8.a.9)$$

where $q \approx \Delta\omega c$.

Over time the spin-up boundary layer on the side wall diffuses outward and the bulk flow over the heater diminishes. Again, using an error function model for the rate of outward momentum diffusion the order of magnitude of the fluid velocity a distance δ away from the heater is roughly

$$q = (\Delta\omega c)\mathrm{erf}(\delta/(2\sqrt{\nu t}) \qquad (8.a.10)$$

If one chooses a length δ based on the steady state momentum thickness: $\sqrt{Pr}\delta_t$, then the average transient heat transfer coefficient on the heater surface due to forced convection is approximately:

$$h_{tr} = 1.77k\left(\frac{(\Delta\omega c)}{\alpha l}\mathrm{erf}(\delta_t/(2\sqrt{\alpha t})\right)^{.5} \quad . \qquad (8.a.11)$$

Now the Nu, Ra correlation derived in Chapter 5 can be rearranged to relate h and F_0 directly:

$$h=(.11k)^{.75}(g\beta F_0/\alpha^2)^{.33} \quad . \qquad (8.a.12)$$

A nondimensional $\Delta T(t)$ can then be found from the following ratio-

$$\Delta T/\Delta T_{ss} \approx h/(h_{tr}+h) \approx 1/(h_{tr}/h + 1) \quad . \qquad (8.a.13)$$

Figure 8.18 shows Eq. 8.a.13 plotted alongside some measured data in a test with glycerine/water. The model would probably fit the measured data better if the test container were circular rather than pie-shaped. The jaggedness of the temperature curve makes it clear that it is the interactions of the spin-up vortices that dominate the surface heat transfer enhancement. Eq. 8.a.13 also goes to zero like $^1/\sqrt{t}$ which is much slower than the rate observed in practice. The problem is that the relative motion on the heater surface enhances heat transfer over half of the heater, but probably hinders heat transfer on the other half. The steady state (bulk fluid is in solid body rotation) momentum boundary layers generated by the heaters have been observed to meet at the center of heater which means that the spin-up relative motion which is sweeping across the heater in one direction only short circuits heat transfer over half of the heater (Fig. 8.17c). The usefulness of such a model, then, is in conservatively predicting the order of magnitude of h during the early part of the transient which in this case is around twice the steady state heat transfer coefficient.

Nonetheless, using Eq. (8.a.12) it is possible to estimate the heat transfer enhancement time. Since:

$$h = (.11k)^{.75}(g\beta F_o/\alpha^2)^{.33} \qquad (8.a.12)$$

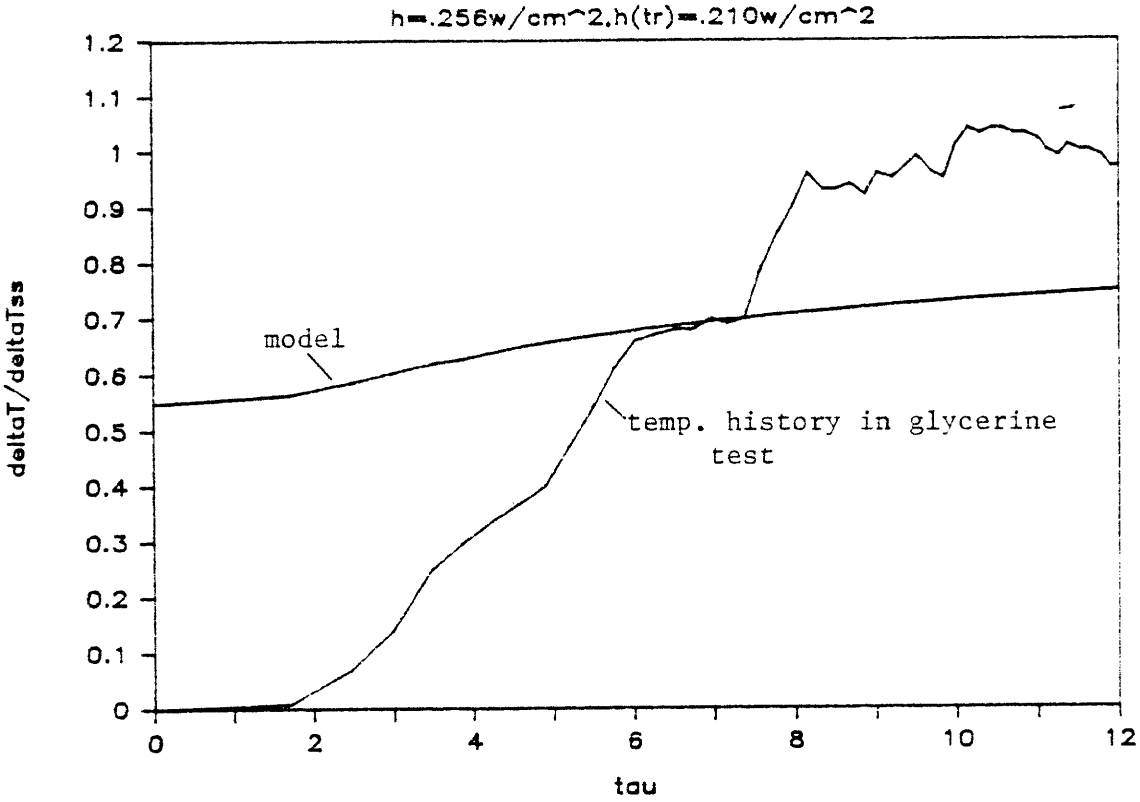

Figure 8.18 Comparison of transient test with glycerine and model for spin-up flow enhancement. Steady state heat transfer coefficient is rougly twice the maximum predicted transient heat transfer coefficient.

and δ_t is of order k/h it can be shown by substituting Eq. 8.a.12 into Eq. 8.a.3 that:

$$\tau_{ht}=(g\beta F_0/k)^{.25}(t)^{.5}/5.24 \ . \qquad (8.a.13)$$

The value of τ_{ht} at which a quasi-steady state is reached most likely depends on either a relative motion Reynolds number $(\Delta\omega(c)l/\nu)$ or on a relative motion RePr# product $(\Delta\omega(c)l/\alpha)$. The larger the value of this dimensionless group, the larger the dimensionless time required to reach quasi-steady conditions. It is presumed of course that τ_{ht} is small compared to τ_E otherwise it is improper to consider the magnitude of the relative motion as a function of $(\nu t)^{.5}$. It was not possible, however, to determine the functional dependance of τ_{ht} on Re or RePr because not enough is known of the motion or the velocity field associated with these vortices. Furthermore, additional tests with a lower Prandtl number fluid are required before Eq. 8.a.13 could be reasonably used as universal correlation for the effects of irrotational flow on heat transfer.

CHAPTER 9

SPIN UP OF INHOMOGENOUS FLUIDS, UNUSUAL PHENOMENA

IX.A Observations of spin-up with a free liquid surface

At various points during experiments with plumes and spin-ups in baffled and unbaffled cylinders on the horizontal lathe new phenomena of interest were observed. As a class, the phenomena are all related to the coupling of earths' gravity and centrifugal forces. Furthermore, these phenomena were all observed in mixtures of air and water. Some of these phenomena may explain aspects of curious behaviour of superconducting rotors (which are horizontal) and it is for this reason that they are briefly mentioned here.

When an unbaffled cylinder filled partly with soapy water is suddenly accelerated from rest, the turbulent mixing of air with the low surface tension water in the initial moments during spin-up generates a great amount of sudsy bubbles or foam. This foamy fluid mixture initially comprises a core of fluid centered around the origin and extending out radially far in excess of the air core radius that remains when the suds ultimately collapse. Figure 9.1 shows this foamy core and the spin-up flow field in the rest of the fluid. This picture was taken at a time that was long compared to the usual spin-up time for a homogeneous mixture. In fact, this foam core takes an order of magnitude longer to spin-up than either liquid or vapor alone. This is due to the surface tension of the bubbles resisting the centrifugal forces trying to separate the two fluids. What is also interesting is that this foam core is not exactly on center. Due to the coupling of the bouyancy of the core due to gravity and due to

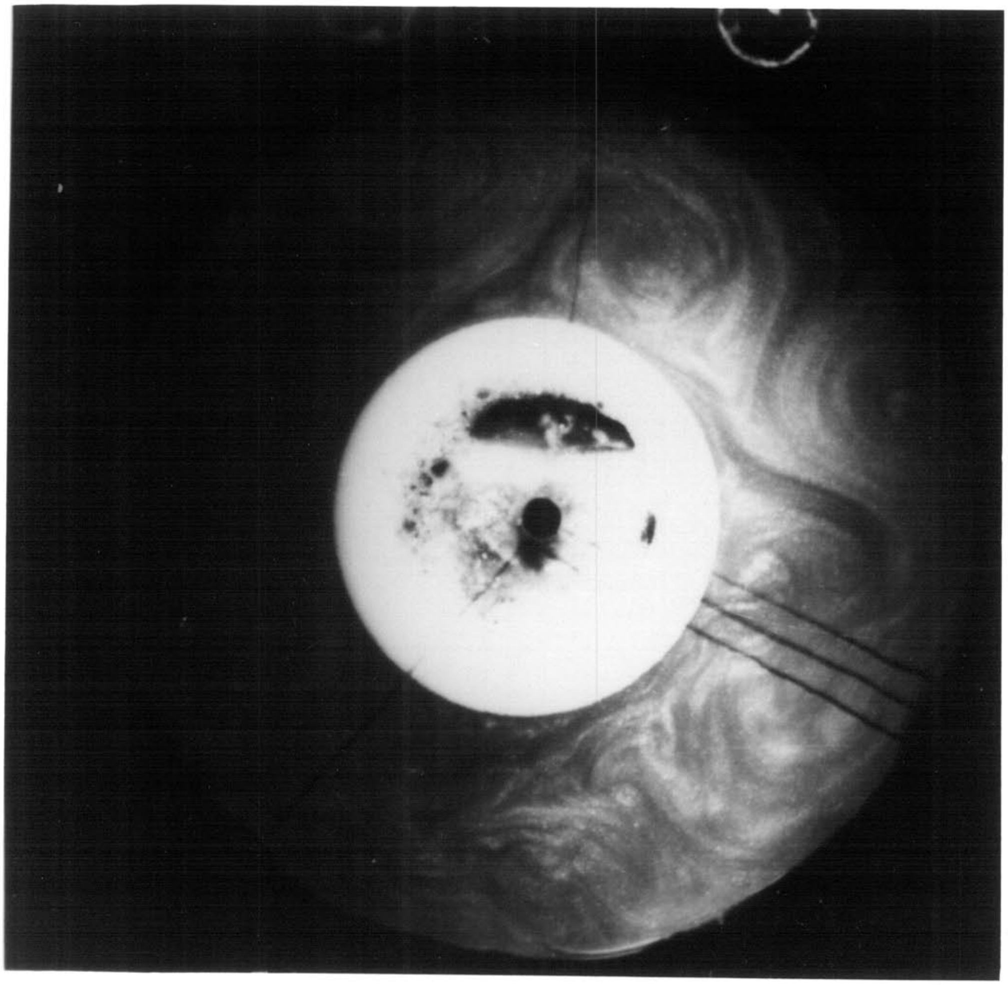

Figure 9.1 Foaming in the interior of a partially filled cylinder impulsively accelerated. The flow field in the liquid regions indicated by the mica-flakes illustrates the interior flow generated by the collapsing core of foam on the centerline.

centrifugal forces, the core finds its' equilibrium displaced from the horizontal axis of rotation. This sudsy core is also rotating slowly relative to the rotation of the core as a whole. This sort of phenomena has been explored by Gans [28]. However, this phenomena is significant to superconducting rotors for two reasons. Since it is well known that helium foams very easily it is likely that accelerating rotors without reservoir baffles and with continuous inlet jets of liquid helium will generate a great deal of foam and that a distinct separation of the phases may take a great deal of time. The density of these suds is certainly greater than that of vapor, and a torque tube inlet filled with sudsy helium might create enough of a centrifugal head to account for the blowout phenomena experienced during superconducting generator operation [29]. The heat transfer coefficient in a sudsy solution might also be sufficiently high to prevent the liquid level gages in the reservoirs of superconducting generators from working properly.

The spin-up process in a baffled cylinder with a baffle extending to the centerline also exhibits unusual phenomena when there is air present in the container. Figures 9.2 and 9.3 show a spinning container with two different air/void fractions. The pictures, again, were taken a few minutes after an impulsive acceleration of the container. The mica flakes attest to the persistence of an energetic motion in the interior which is not a spin-up flow field. The interior motion is a response to surface waves at the water/air interface. In both figures, a foamy region can be found on the high pressure side of the baffle (the container is rotating counterclockwise). In Fig. 9.3, a rotating hydraulic jump is also visible. The shape of the interface in each case is not steady, but

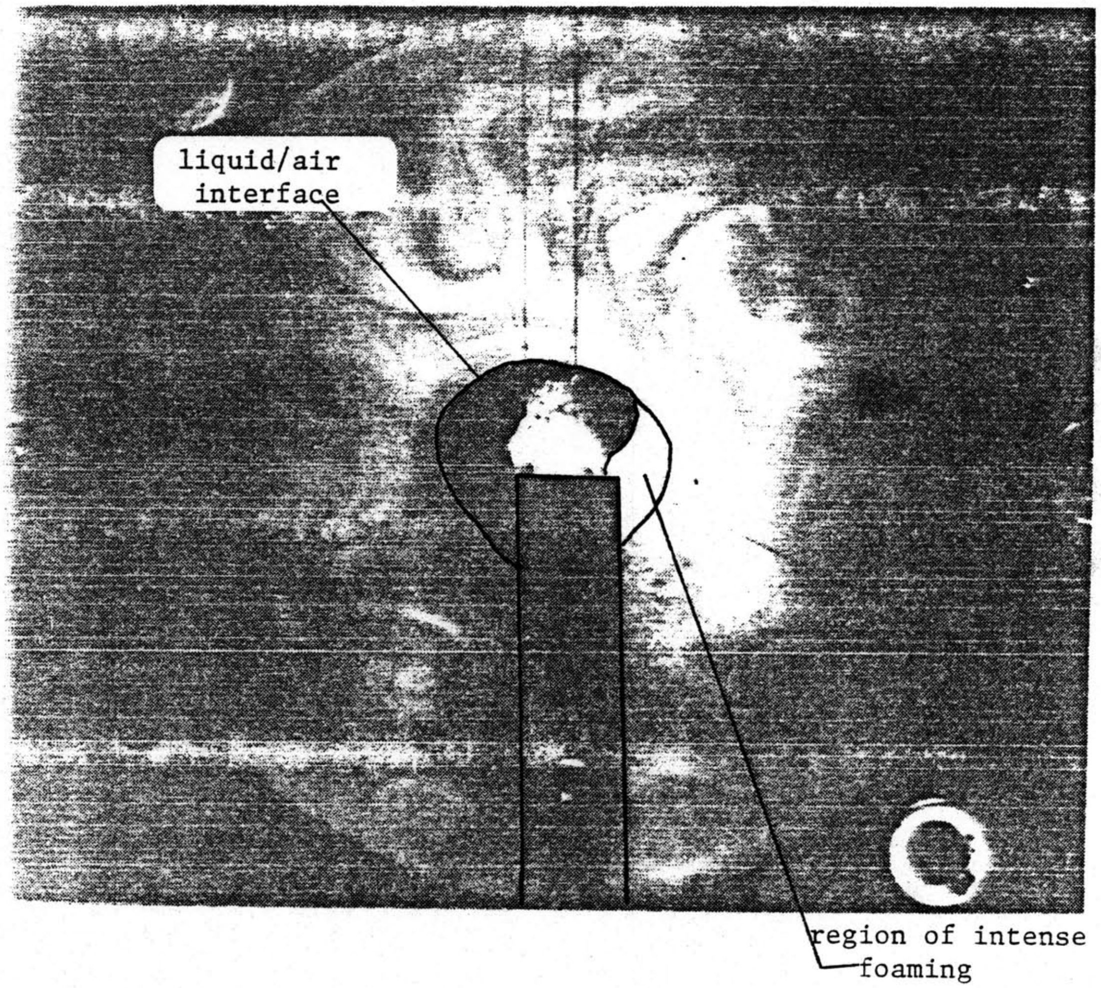

Figure 9.2 Surface waves generate interior motion which persists indefinitely.

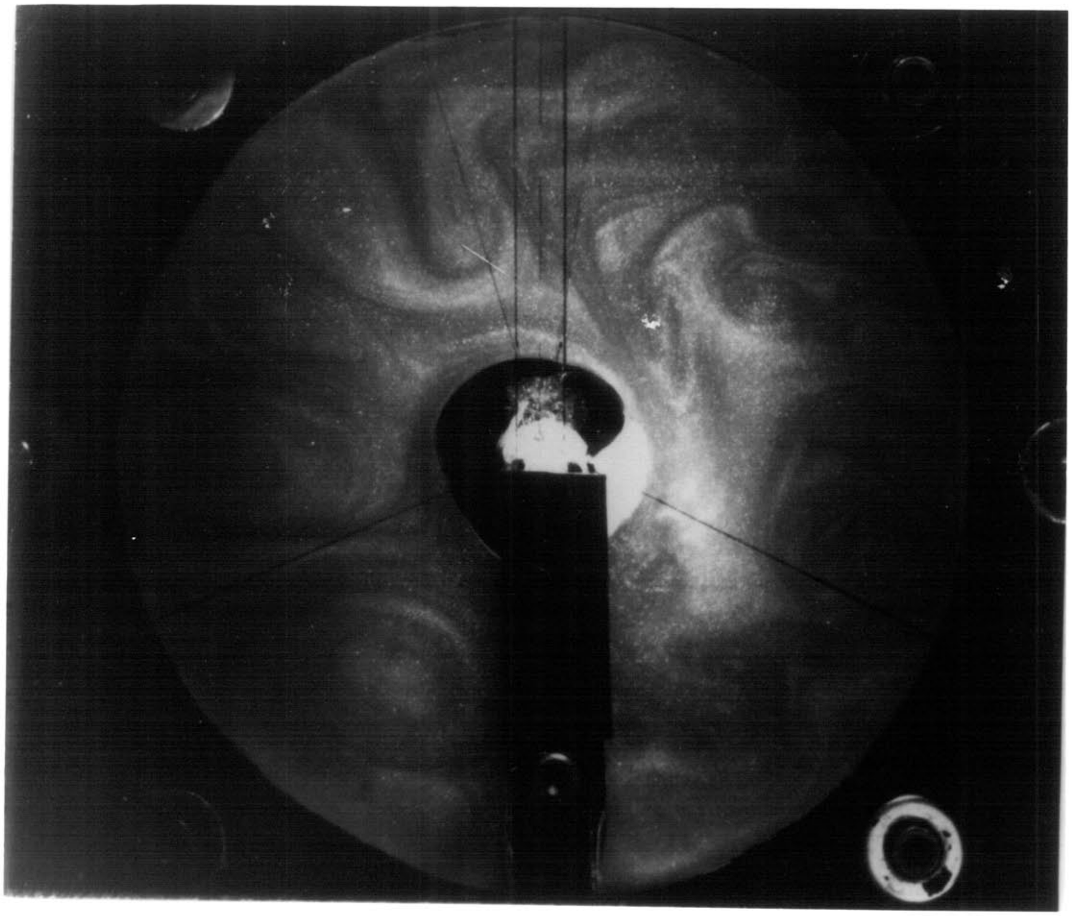

Figure 9.2

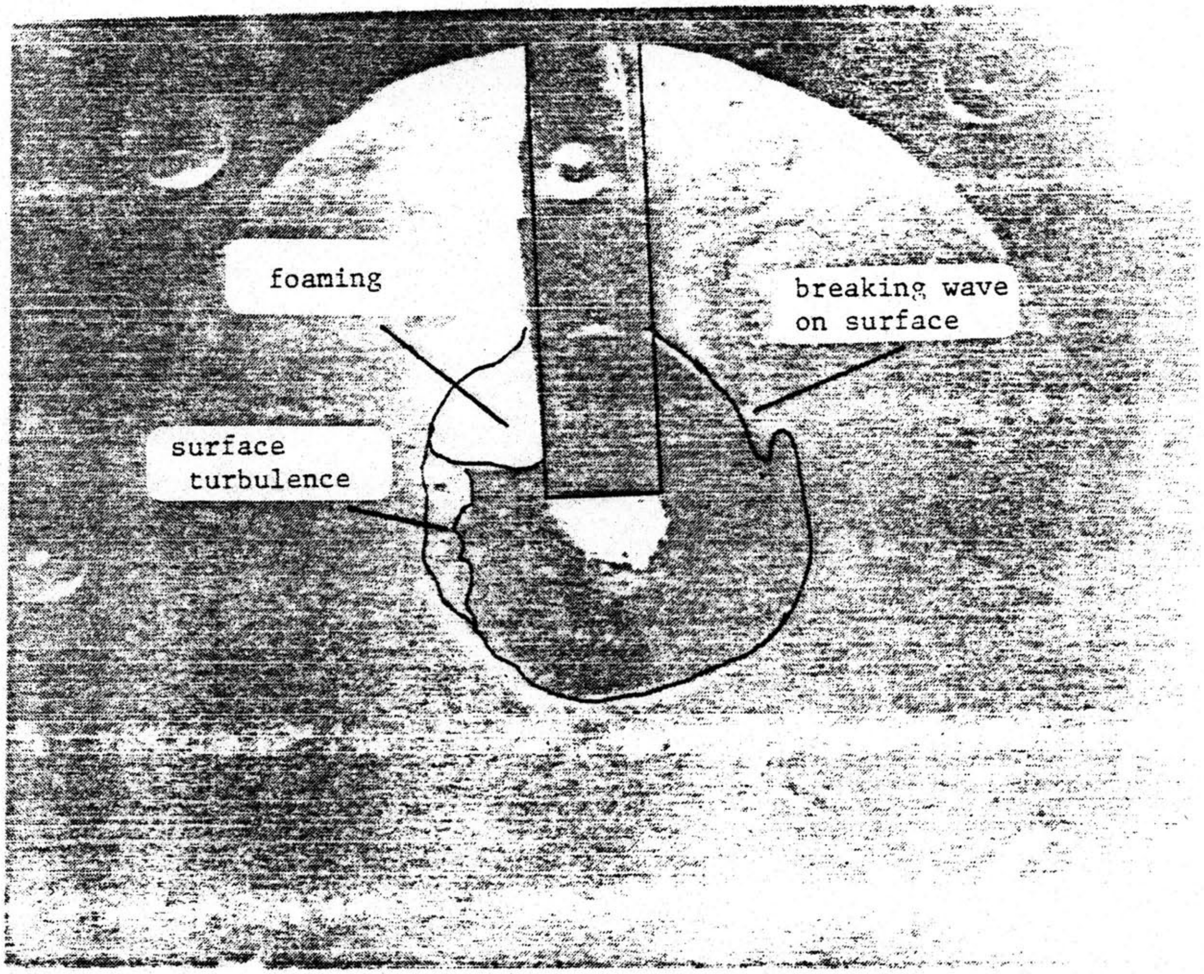

Figure 9.3 Surface waves in a baffled cylinder with a larger air fraction. foaming occurs on high pressure side of baffle only.

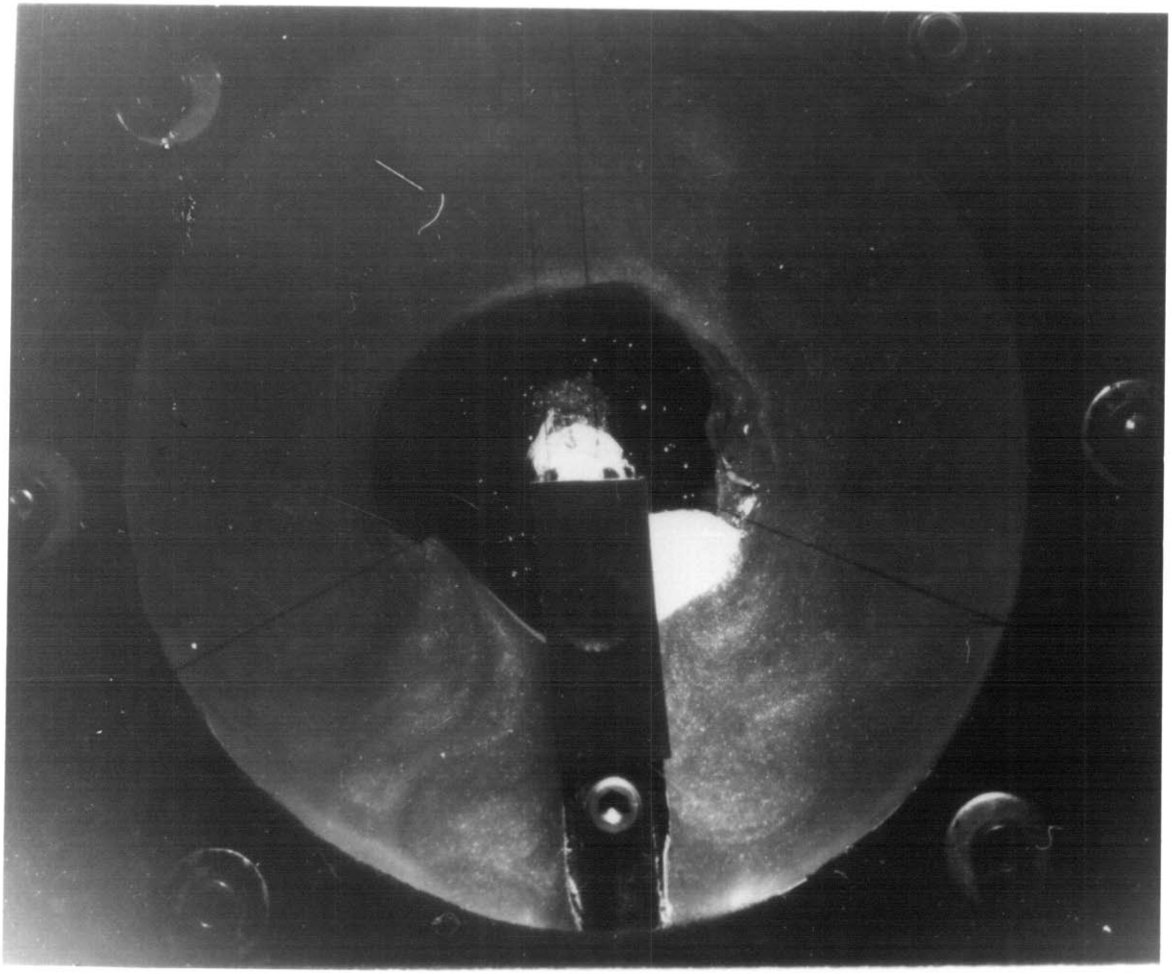

Figure 9.3

varies as the container rotates. Figures 9.4 and 9.5 were pictures taken with the container rotated 180°. In the bottom picture the baffle is pointing downwards. In the top picture, the baffle is pointed upwards. The observed phenomena is most certainly related to the cross coupling of gravity and rotation, vividly illustrated by the different liquid levels on either side of the baffle in Fig. 9.5. As the ratio of $g/\omega^2 r$ gets smaller so does the distrubance level at the air/water interface. With the container only slightly filled with water- $g/\omega^2 r \sim 1/25$, the surface is nearly ripple free. Therefore, it does not seem possible that an energetic interior fluid motion caused by liquid/vapor interfacial waves can be responsible for any significant additional helium boiloff. These experiments, however, do illustrate the utility of baffles in seperating phases.

Early on in the course of flow visualization experiments, plume pictures were marred by the presence of large scale two-dimensional fluid disturbances apparently coming from the centerline of the rotating container. The disturbance was found to have originated in the erratic motion of small, discrete air bublbes on the centerline. These bubbles were found to bounce up and down due to the coupling, again, of gravity and rotation- pumping a steady stream of liquid outwards from the centerline in the process. Figure 9.6 is a sequence of photos which not only illustrate the self-similar structure of a bouyant starting plume, they also show this reverse plume phenomena. This reverse plume not only spreads outwards, it also rotates slowly in the opposite direction of the container . The disturbance was eliminated by putting a rectangular piece of plastic foam along the centerline- held in place by a thin rod

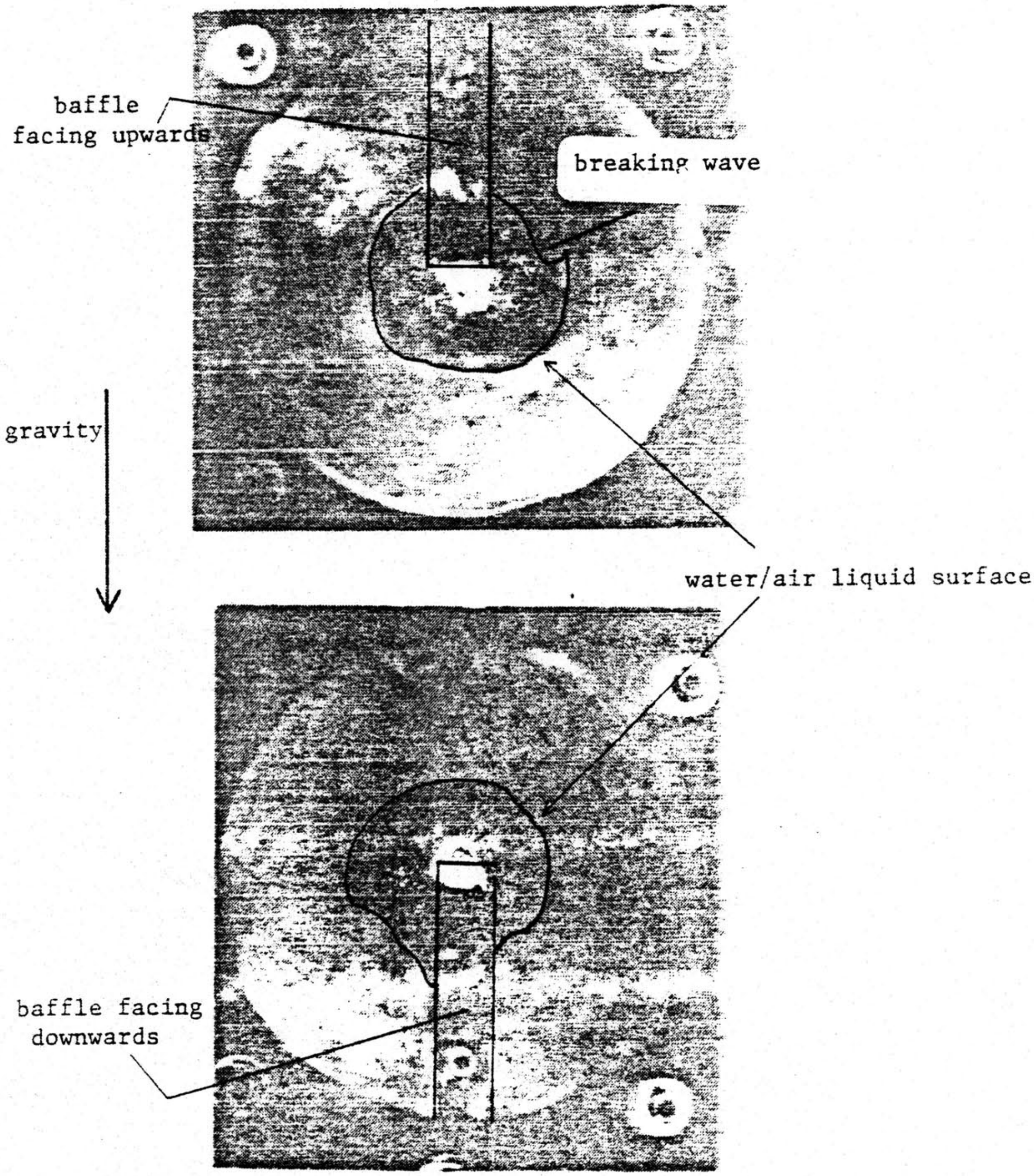

Figure 9.4 (above), Figure 9.5 (below) The surface wave pattern varies with theta. In these two pictures the container is frozen in two positions 180° apart. Notice the difference in liquid levels on either side of the baffle in fig. 9.5.

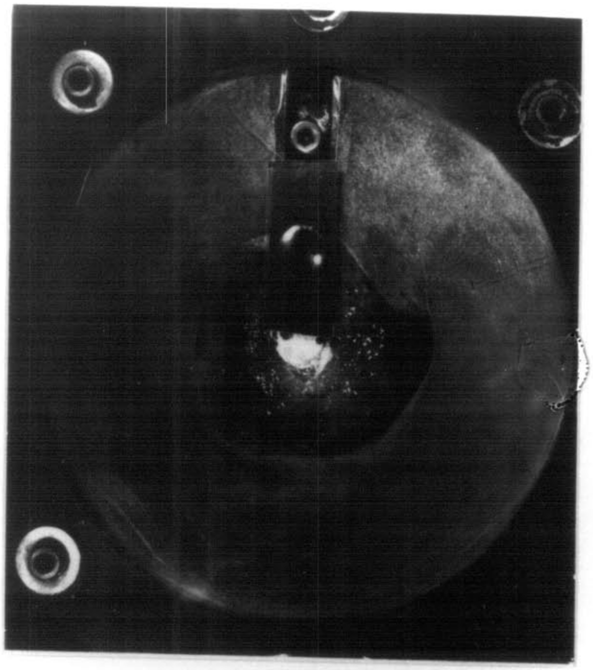

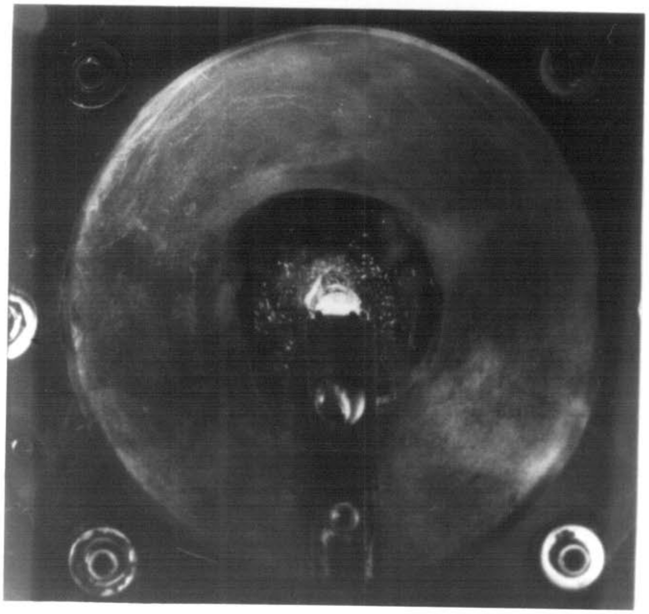

Figure 9.4 (above)
Figure 9.5 (below)

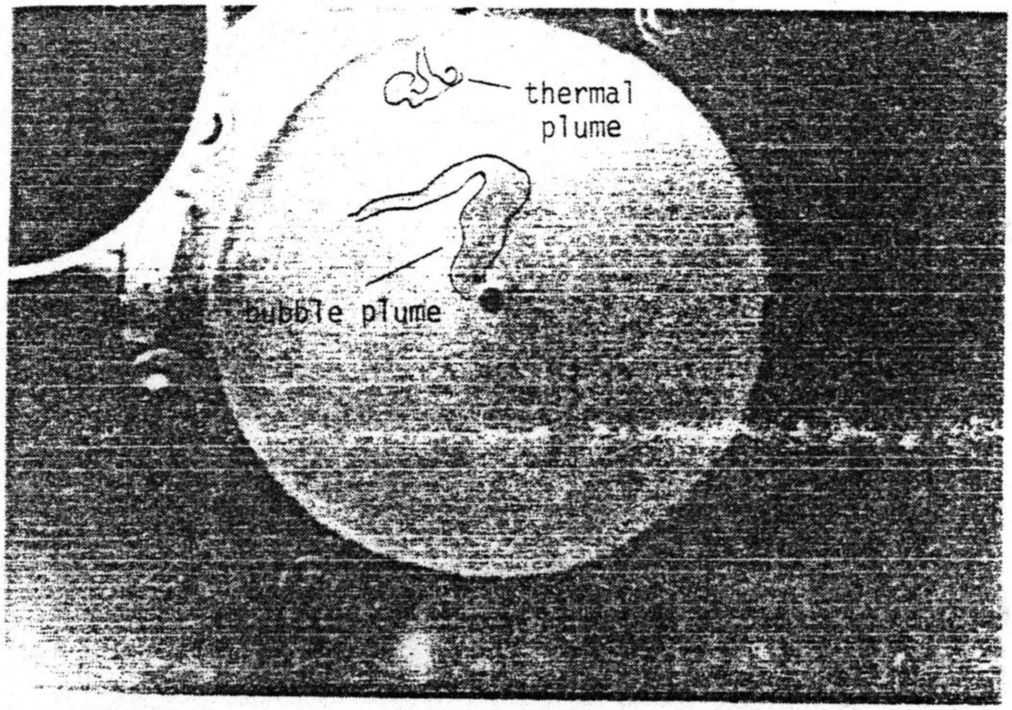

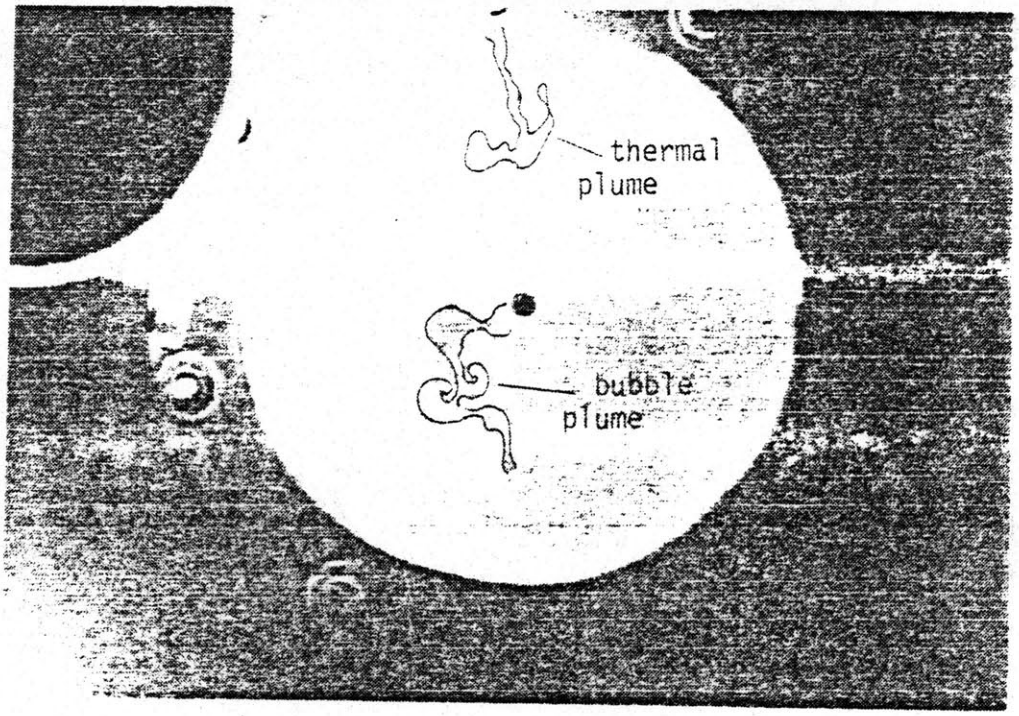

Figure 9.6a (above) Container is rotating counterclockwise
Figure 9.6b (below)

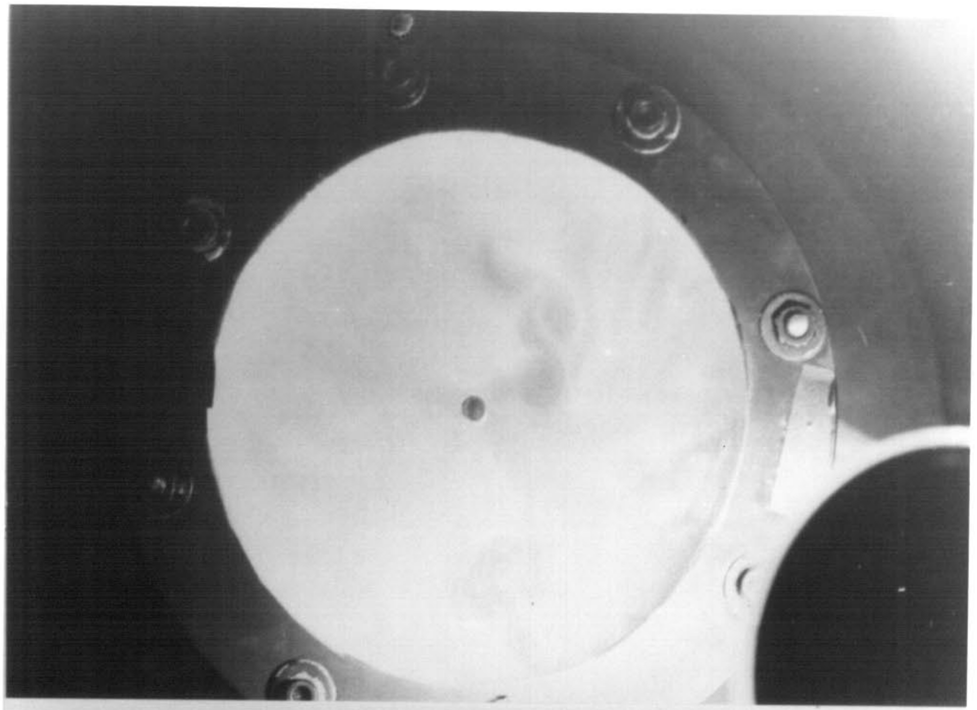

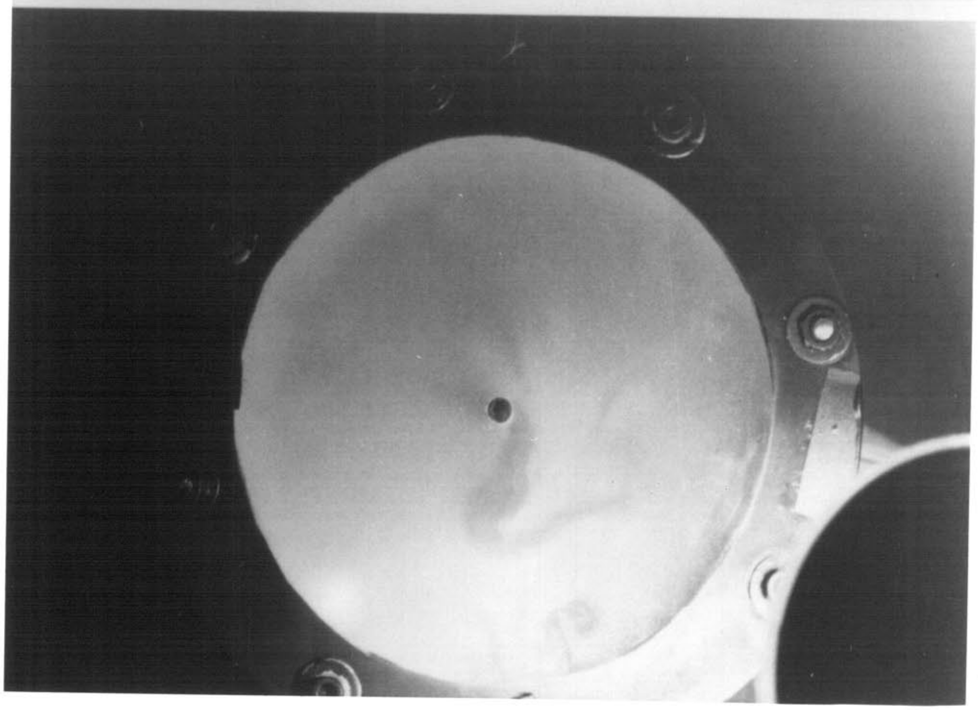

Figure 9.6a (above)
Figure 9.6b (below)

which was glued into the endplate. This plastic foam trapped the air bubbles preventing them from bouncing. Interestingly, small bubbles created a similar effect in the baffled cylinder (the baffle did not extend all the way to the centerline of the container). In a baffled cylinder, however, a strong plume was generated 270° from the high pressure side of the baffle originating at the centerline and moving straight radially outwards. The problem was also remedied by taping plastic foam to the inner edge of the baffle.

Except for the foaming, the small ratio of gravity to rotational acceleration at the liquid surface to be found in high speed superconducting rotors makes these experiments just mentioned interesting but not particularly relevant.

Appendix A.I
Experimental Data Summary

Table A.I.1
Heater Specification Table

l: length used in Rayleigh number calculation is 1/2 the length in the azimuthal direction, (1/2)/l
w: width of heater, dimension in axial (z) direction

h#	l cm.	w cm.	A cm^2	R ohms	type
1	1.79	2.2	3.94*	19.5	short heater
4	2.36	1.67	3.94	19.5	short heater
2	1.14	12.9	14.9	18.6	long heater
3	12.9	1.14	14.9	18.6	long heater

*heaters are not quite rectangular, area of heater where leadwires attach is not included in surface area

Table A.I.2
Data Table Abbreviations

exp#:	experiment number gly=glycerine tests iso,alc =alcohol tests everything else is water
h#:	heater number (see Table A.II.1)
Nu#:	Nusselt number (based on l/2 in Table A.II.1)
Ra#:	Rayleigh number (based on l/2 in Table A.II.1)
RaPr#:	Rayleigh number times Prandtl number

Data summary

Table A.I.3

Experiment Data Summary #1

exp#	h#	Nu#	Ra#	Pr#	Ra*Pr
a10	1	64.0	6.42E+07	4.80	3.09E+08
a11	1	65.3	6.61E+07	4.80	3.17E+08
a12	1	65.4	6.58E+07	4.79	3.15E+08
a13	1	63.0	6.02E+07	4.88	2.93E+08
a14	1	34.2	7.41E+06	5.95	4.41E+07
a15	1	45.7	2.23E+07	5.03	1.12E+08
a16	1	49.2	2.81E+07	5.13	1.44E+08
a17	1	51.5	3.24E+07	5.18	1.68E+08
a18	1	53.9	3.65E+07	5.15	1.88E+08
a19	1	54.6	4.08E+07	5.15	2.10E+08
a20	1	58.1	4.61E+07	5.17	2.39E+08
a21	1	63.3	6.23E+07	4.86	3.03E+08
a22	1	59.6	5.14E+07	4.79	2.46E+08
a23	1	58.1	4.40E+07	4.69	2.06E+08
a24	1	54.1	3.53E+07	4.56	1.61E+08
a5	1	40.8	1.58E+07	6.03	9.55E+07
a6	1	45.7	2.35E+07	5.75	1.35E+08
a7	1	58.5	3.29E+07	6.10	2.00E+08
a8	1	61.4	5.91E+07	4.97	2.94E+08
a9	1	64.7	6.55E+07	4.86	3.19E+08
alcb2	3	1061.0	4.21E+10	25.80	1.09E+12
alcb3	3	1096.0	4.11E+10	26.00	1.07E+12
alcb4	3	906.3	2.62E+10	28.50	7.47E+11
alcb5	3	706.8	1.36E+10	31.30	4.26E+11
alcb6	3	518.0	6.09E+09	34.30	2.09E+11
alcb7	3	1076.0	3.76E+10	35.00	1.32E+12
alcb8	3	911.9	2.48E+10	38.50	9.55E+11
b1	1	54.6	3.51E+07	5.69	2.00E+08
b2	1	57.8	4.45E+07	5.50	2.45E+08
b3	1	65.0	5.82E+07	5.23	3.04E+08
b4	1	67.3	6.94E+07	5.00	3.47E+08
b5	1	70.6	7.47E+07	4.89	3.65E+08
b6	1	69.3	7.45E+07	4.72	3.52E+08
c1	2	19.4	8.25E+05	6.46	5.33E+06
c10	2	29.6	5.06E+06	5.62	2.84E+07
c11	2	29.7	5.84E+06	5.44	3.18E+07
c12	2	31.2	6.21E+06	5.45	3.39E+07
c2	2	21.4	1.18E+06	6.30	7.42E+06
c3	2	16.2	4.84E+05	6.19	3.00E+06
c4	2	17.5	8.22E+05	6.09	5.00E+06
ga7	4	72.5	9.79E+07	4.05	3.96E+08
ga8	4	78.2	1.24E+08	4.14	5.13E+08
gb1	3	242.5	4.48E+09	4.88	2.19E+10

Experiment Data Summary #2 (cont.)

exp#	h#	Nu#	Ra#	Pr#	Ra*Pr
c5	2	23.3	2.24E+06	5.62	1.26E+07
c6	2	24.1	2.33E+06	5.58	1.30E+07
c7	2	25.4	3.13E+06	5.59	1.75E+07
c8	2	26.7	3.79E+06	5.60	2.12E+07
c9	2	27.0	4.25E+06	5.60	2.38E+07
d1a	1	50.7	2.55E+07	4.29	1.10E+08
d1b	1	68.1	7.82E+07	4.91	3.84E+08
d2a	1	56.5	3.53E+07	4.38	1.55E+08
d2b	1	71.5	9.02E+07	4.83	4.36E+08
d3a	1	51.3	2.72E+07	4.11	1.12E+08
d3b	1	72.7	8.65E+07	4.80	4.15E+08
d4a	1	53.0	3.03E+07	4.16	1.26E+08
d4b	1	61.2	5.66E+07	4.47	2.53E+08
d5a	1	54.4	2.94E+07	4.19	1.23E+08
d5b	1	66.1	6.36E+07	4.58	2.91E+08
d5c	1	70.7	1.06E+08	4.69	5.00E+08
d6a	1	58.5	3.73E+07	4.31	1.61E+08
d6b	1	71.3	8.78E+07	4.67	4.10E+08
d6c	1	60.3	5.34E+07	4.36	2.33E+08
ea1	4	100.6	2.37E+08	4.22	1.00E+09
ea2	4	117.0	2.24E+08	4.24	9.50E+08
eb1	3	362.3	1.19E+10	5.32	6.31E+10
eb4	3	364.4	1.29E+10	5.23	6.75E+10
fa1	4	55.0	4.66E+07	5.59	2.60E+08
fa10	4	100.1	2.62E+08	4.06	1.06E+09
fa11	4	97.7	2.70E+08	3.98	1.07E+09
fa12	4	62.1	7.65E+07	5.05	3.86E+08
fa13	4	65.1	7.37E+07	5.08	3.74E+08
fa2	4	67.0	7.57E+07	5.26	3.98E+08
fa3	4	72.0	1.01E+08	4.96	5.02E+08
fa4	4	76.5	1.38E+08	4.66	6.43E+08
fa5	4	80.3	1.46E+08	4.61	6.73E+08
fa6	4	86.0	1.84E+08	4.37	8.04E+08
fa7	4	91.5	2.17E+08	4.21	9.14E+08
fa8	4	42.0	1.29E+07	5.89	7.60E+07
fa9	4	44.9	1.23E+07	5.92	7.31E+07
ga1	4	68.4	8.32E+07	4.51	3.75E+08
ga2	4	64.8	6.95E+07	4.41	3.06E+08
ga3	4	73.4	1.09E+08	4.53	4.94E+08
ga4	4	77.3	1.37E+08	4.55	6.23E+08
ga5	4	86.2	1.83E+08	4.30	7.87E+08
ga6	4	86.8	1.81E+08	4.30	7.78E+08

Data summary- Page 2 Table A.I.3

Experiment Data Summary #3 (cont.)

exp#	h#	Nu#	Ra#	Pr#	Ra*Pr
gb2	3	291.5	6.16E+09	4.99	3.07E+10
gb3	3	288.4	7.33E+09	4.98	3.65E+10
gb4	3	312.8	7.72E+09	5.02	3.88E+10
gb5	3	336.5	9.60E+09	5.03	4.83E+10
gb6	3	333.0	8.33E+09	5.02	4.18E+10
gly1	3	395.0	4.32E+09	13.00	5.62E+10
gly10	3	380.0	3.36E+09	13.63	4.58E+10
gly11	3	252.0	1.08E+09	15.15	1.64E+10
gly12	3	422.0	4.19E+09	13.21	5.53E+10
gly13	3	438.0	4.18E+09	13.11	5.48E+10
gly15	3	420.0	4.32E+09	13.08	5.65E+10
gly16	3	285.0	1.13E+09	14.90	1.68E+10
gly2	3	425.0	6.79E+09	12.27	8.33E+10
gly3	3	359.0	4.47E+09	13.01	5.82E+10
gly4	3	462.0	6.42E+09	12.30	7.90E+10
gly5	3	256.0	1.29E+09	14.80	1.91E+10
gly6	3	464.0	6.26E+09	12.40	7.76E+10
gly7	3	326.0	2.79E+09	13.98	3.90E+10
gly8	3	337.0	2.71E+09	14.03	3.80E+10
gly9	3	248.0	1.16E+09	15.00	1.74E+10
isob1	3	1089.0	3.93E+10	26.80	1.05E+12
isob2	3	1127.0	3.95E+10	26.80	1.06E+12
isob3	3	908.0	2.44E+10	28.90	7.05E+11
isob4	3	582.0	8.28E+09	33.80	2.80E+11
isob5	3	394.0	2.84E+09	36.10	1.03E+11
isob6	3	390.0	2.71E+09	37.20	1.01E+11
isob7	3	1120.0	3.70E+10	27.10	1.00E+12
isob8	3	926.2	2.50E+10	29.80	7.45E+11
110a	4	77.1	1.12E+08	3.59	4.03E+08
110b	4	91.1	1.74E+08	4.00	6.96E+08
110c	4	98.7	2.62E+08	4.18	1.09E+09
111a	4	80.5	9.67E+07	3.62	3.51E+08
111b	4	92.8	1.82E+08	3.96	7.19E+08
111c	4	103.7	2.45E+08	4.19	1.03E+09

Experiment Data Summary #4 (cont.)

exp#	h#	Nu#	Ra#	Pr#	Ra*Pr
16a	3	298.2	5.83E+09	5.10	2.98E+10
16b	3	326.3	1.03E+10	5.20	5.36E+10
16c	3	358.2	1.29E+10	5.31	6.86E+10
17a	4	75.8	8.30E+07	3.52	2.92E+08
17b	4	105.9	1.97E+08	4.16	8.20E+08
17c	4	108.9	2.52E+08	4.22	1.06E+09
18a	4	77.5	7.84E+07	3.45	2.71E+08
18b	4	98.5	1.55E+08	4.05	6.28E+08
18c	4	107.6	2.52E+08	4.19	1.06E+09
19a	4	79.6	8.89E+07	3.52	3.13E+08
19b	4	97.4	1.59E+08	3.98	6.32E+08
19c	4	105.8	2.59E+08	4.14	1.07E+09
sa1a	1	49.3	2.05E+07	4.45	9.12E+07
sa1b	1	63.9	5.42E+07	4.90	2.65E+08
sa2a	1	42.4	1.38E+07	4.09	5.66E+07
sa2b	1	64.8	5.77E+07	4.88	2.82E+08
sa3a	1	56.9	3.45E+07	4.34	1.50E+08
sa3b	1	70.2	6.75E+07	4.73	3.19E+08
sa4a	1	49.3	2.47E+07	4.21	1.04E+08
sa4b	1	66.5	6.47E+07	4.76	3.08E+08
t1	2	30.9	6.10E+06	5.52	3.36E+07
t2	2	31.2	6.16E+06	5.48	3.38E+07
11a	3	285.2	4.66E+09	5.30	2.47E+10
11b	3	353.8	1.38E+10	5.28	7.26E+10
12a	3	315.4	7.07E+09	5.35	3.78E+10
12b	3	327.0	1.32E+10	5.45	7.21E+10
13a	3	321.7	7.14E+09	5.29	3.78E+10
13b	3	356.7	1.23E+10	5.39	6.63E+10
14a	3	278.7	4.45E+09	5.09	2.27E+10
14b	3	360.7	1.24E+10	5.35	6.65E+10
15a	3	269.5	4.09E+09	5.02	2.05E+10
15b	3	337.7	1.01E+10	5.26	5.28E+10
15c	3	349.0	1.24E+10	5.45	6.77E+10

Table A.1.4 Natural Convection Data Summary

Natural convection data summary

exp#	Nu#	Ra#	corr.	Nu#*
g4g	7.15	3.01E+04	8.50%	6.54
g5g	9.24	9.54E+04	7.00%	8.59
g1g	9.79	1.15E+05	6.60%	9.14
g1g*	12.10	1.41E+05	5.00%	11.50
g3g	10.71	1.41E+05	5.10%	10.17
g1w	10.89	1.44E+05	4.00%	10.45
g6w	8.91	1.60E+05	4.40%	8.52
g5w	9.79	1.82E+05	4.50%	9.35
g2g*	14.30	1.97E+05	4.00%	13.73
g3w	10.89	2.11E+05	4.00%	10.45
g4w	10.45	2.27E+05	4.50%	9.98
g2w	14.63	2.65E+05	3.00%	14.19
g2g	11.55	2.70E+05	4.70%	11.01
g1i	15.51	2.83E+05	13.00%	13.49
g2i	17.71	4.54E+05	12.00%	15.58
g5i	20.68	4.93E+05	7.00%	19.23
g3i	21.01	5.64E+05	9.70%	18.97
g6i	23.54	5.71E+05	7.00%	21.89
g4i	23.65	7.10E+05	7.80%	21.81

corr.: conduction error
*: corrected Nu#
i: alcohol tests
w: water tests
g: glycerine tests

Appendix A.II

CONDUCTION ERROR ESTIMATE

If it is assumed that the heat flux into the lexan wall from the heater is proportional to the temperature on the surface of the heater, a reasonable estimate is made of conduction errors in the surface heat transfer coefficient. A fraction of the heater power diffuses into the lexan walls of the container at a rate proportional to $\Delta T/\ t$, where ΔT is the difference between the temperature in the middle of the heater package and ambient temperature (the initial temperature) of the lexan. If one neglects the conduction gradient in the heater itself and assumes that the maximum ΔT is twice the ΔT based on the measured temperature at the surface of the heater and the ambient water temperature, the heat flux back into the lexan window is of order:

$$F_e = k(2\Delta T)/(2\sqrt{\alpha t}) = 0.0548\Delta T/\sqrt{t}\ \mathrm{W/cm^2} \quad . \qquad \text{(A.II.1)}$$

All properties in the above equation are those of lexan, and are listed in Appendix A.III.1. (Based on the thermal diffusivity of lexan, $13\text{X}10^{-4}\ \mathrm{cm^2/s}$, it takes 20 min. for the thermal boundary layer to propagate to the outside of the lexan window.) Now ΔT can be related to heater power at high Rayleigh numbers using the correlation obtained in Chapter 6. Given that

$$Nu = .11(RaPr)^{.33} \qquad \text{(A.II.2)}$$

$$\text{then } h = .11k(g\beta\Delta T/\alpha^2)^{.33} \qquad \text{(A.II.3)}$$

and in terms of surface heat flux:

$$F_o = h\Delta T \qquad \text{(A.II.4)}$$

$$\text{such that } F_o = .11k(g\beta\Delta T/\alpha^2)^{.33}\Delta T \quad . \qquad \text{(A.II.5)}$$

The ratio of the heat conduction into the lexan to the heat carried away by the natural convection is thus of order:

$$F_e/F_o = .5((\sqrt{t})k(g\beta\Delta T/\alpha^2)^{.33})^{-1} \quad . \qquad \text{(A.II.6)}$$

Some tabulated results are given below. Eq. (A.II.6) is evaluated for a rotor at 500 rpm, and using the thermal properties of water. At 300 rpm the data in the table is roughly 40% larger. The conduction correction to the natural convection data in Chapter 6 was obtained by replacing the laminar natural convection correlation for the high Ra# correlation used here in Eq. A.II.2.

Table A.II.1

Conduction error as a percentage of F_0

t\ΔT	10°C	20°C	40°C
10s	5.0%	4%	3.0%
40s	2.4%	2%	1.4%

Appendix A.III
Thermal properties of water, alcohol and water/glycerine.

Water data [ ]

(C)	J/gm/K	gm/cm^3	gm/cm/s	cm^2/s	W/cm/K	cm^2/hr	1/K	
T	Cp	ρ	μ	μ/ρ	k	α	$\beta*10^3$	Pr #
15.56	4.19	1.00	1.12E-02	1.12E-02	5.95E-03	1.42E-03	0.18	7.88
21.11	4.18	1.00	9.79E-03	9.83E-03	6.04E-03	1.44E-03	0.23	6.78
26.67	4.18	1.00	8.59E-03	8.62E-03	6.14E-03	1.47E-03	0.27	5.85
32.22	4.18	1.00	7.64E-03	7.69E-03	6.23E-03	1.50E-03	0.32	5.13
37.78	4.18	0.99	6.81E-03	6.86E-03	6.30E-03	1.52E-03	0.36	4.52
43.33	4.18	0.99	6.15E-03	6.22E-03	6.37E-03	1.55E-03	0.40	4.04
48.89	4.18	0.99	5.62E-03	5.68E-03	6.44E-03	1.55E-03	0.43	3.65
54.44	4.18	0.99	5.12E-03	5.21E-03	6.49E-03	1.57E-03	0.49	3.30
60.00	4.18	0.98	4.71E-03	4.80E-03	6.54E-03	1.60E-03	0.52	3.01
65.56	4.19	0.98	4.30E-03	4.39E-03	6.59E-03	1.63E-03	0.56	2.72
71.11	4.19	0.98	4.01E-03	4.10E-03	6.64E-03	1.63E-03	0.59	2.53

Alcohol data [ ]

(C)	J/gm/K	gm/cm^3	gm/cm/s	cm^2/s	W/cm/K	cm^2/hr	1/K	
T	Cp	ρ	μ	μ/ρ	k	α	$\beta*10^3$	Pr #
20	2.37	0.785	2.39E-02	3.10E-02	1.40E-03	7.53E-04	1.03E-03	40.5
30	2.37	0.776	1.76E-02	2.30E-02	1.40E-03	7.61E-04	1.03E-03	29.8
40	2.37	0.772	1.33E-02	1.70E-02	1.36E-03	7.43E-04	1.03E-03	23.2
50	2.37		1.07E-02	1.40E-02	1.35E-03			18.8
60	2.37		8.00E-03	1.00E-02	1.33E-03			14.3

30% glycerine solution [ ]

(C)	J/gm/K	gm/cm^3	gm/cm/s	cm^2/s	W/cm/K	cm^2/hr	1/K	
T	Cp	ρ	μ	μ/ρ	k	α	$\beta*10^3$	Pr #
20	3.25	1.05	1.76E-02	1.68E-02	5.19E-03	1.53E-03	3.10E-04	11.0
30	3.23	1.04	1.35E-02	1.29E-02	5.32E-03	1.58E-03	3.60E-04	8.2
40	3.30	1.04	1.07E-02	1.03E-02	5.40E-03	1.57E-03	4.10E-04	6.5
50	3.36	1.04	8.79E-03	8.49E-03	5.53E-03	1.59E-03	4.60E-04	5.3

40% glycerine solution [ ]

20	3.03	1.07	3.72E-02	3.47E-02	4.48E-03	1.38E-03	4.10E-04	25.2
30	3.01	1.07	2.66E-02	2.48E-02	4.52E-03	1.40E-03	4.50E-04	17.7
40	2.90	1.09	2.07E-02	1.90E-02	4.61E-03	1.46E-03	4.80E-04	13.0
50	3.14	1.09	1.62E-02	1.49E-02	4.69E-03	1.38E-03	5.10E-04	10.8

31% glycerine (interpolated values)

20	3.23	1.05	1.98E-02	1.88E-02	5.11E-03	1.51E-03	3.21E-04	12.6
30	3.21	1.05	1.49E-02	1.42E-02	5.23E-03	1.56E-03	3.70E-04	9.2
40	3.26	1.04	1.18E-02	1.13E-02	5.31E-03	1.56E-03	4.18E-04	7.3
50	3.34	1.04	9.60E-03	9.20E-03	5.44E-03	1.57E-03	4.66E-04	5.9

Appendix A.III.
Important thermal properties

material	thermal conductivity W/cm/K	density gm/cm^3	specific heat c_p J/gm/K
kapton	0.36E-2	1.43	1.3
teflon	0.21E-2	2.14	1.2
RTV	0.23E-2	1.6	?
Cu	3.5	8.96	0.38
lexan	0.2E-2	1.2	1.255

Appendix A.IV

RELATIVE MOTION STREAM FUNCTION

In this appendix, the relative motion flow field following an impulsive acceleration is calculated for three representative container geometries: a circle, an ellipse and a pie shaped container.

A.IV.1 Circle

If the simply connected region in Fig. 7.3 is circular, the relative motion stream function is the solution to Poisson's equation in cylindrical coordinates:

$$\frac{1\partial\psi r\partial\psi}{r\partial r\ \partial r} = -2\omega \qquad (A.IV.1)$$

such that:

$$\psi = -1/2\omega r^2 \qquad (A.IV.2)$$

and the relative velocities are:

$$u = -\frac{1\partial\psi}{r\partial\theta} = 0 \qquad (A.IV.3)$$

$$v = \frac{\partial\psi}{\partial r} = -\omega r \quad . \qquad (A.IV.4)$$

The relative motion flow field consists of circular streamlines centered at the origin of the container. The inertial velocity of any fluid particle is thus:

$$U_I = \omega Re_\phi + \omega re_\theta - \omega re_\theta = \omega Re_\phi \ . \qquad (A.IV.5)$$

In a non-rotating coordinate system, the inertial velocity is :

$$u_x = -\omega R\sin(\omega t) \qquad (A.IV.6)$$

$$u_y = \omega R\cos(\omega t) \qquad (A.IV.7)$$

The position of a given fluid particle at any instant of time is found by integrating the latter two equations (see Fig. A.IV.1):

$$x - x_o = R\cos(\omega t) - R \qquad (A.IV.8)$$

$$y - y_o = R\sin(\omega t) \qquad (A.IV.9)$$

$$(x - (x_o - R))^2 + (y - y_o)^2 = R^2 \qquad (A.IV.10)$$

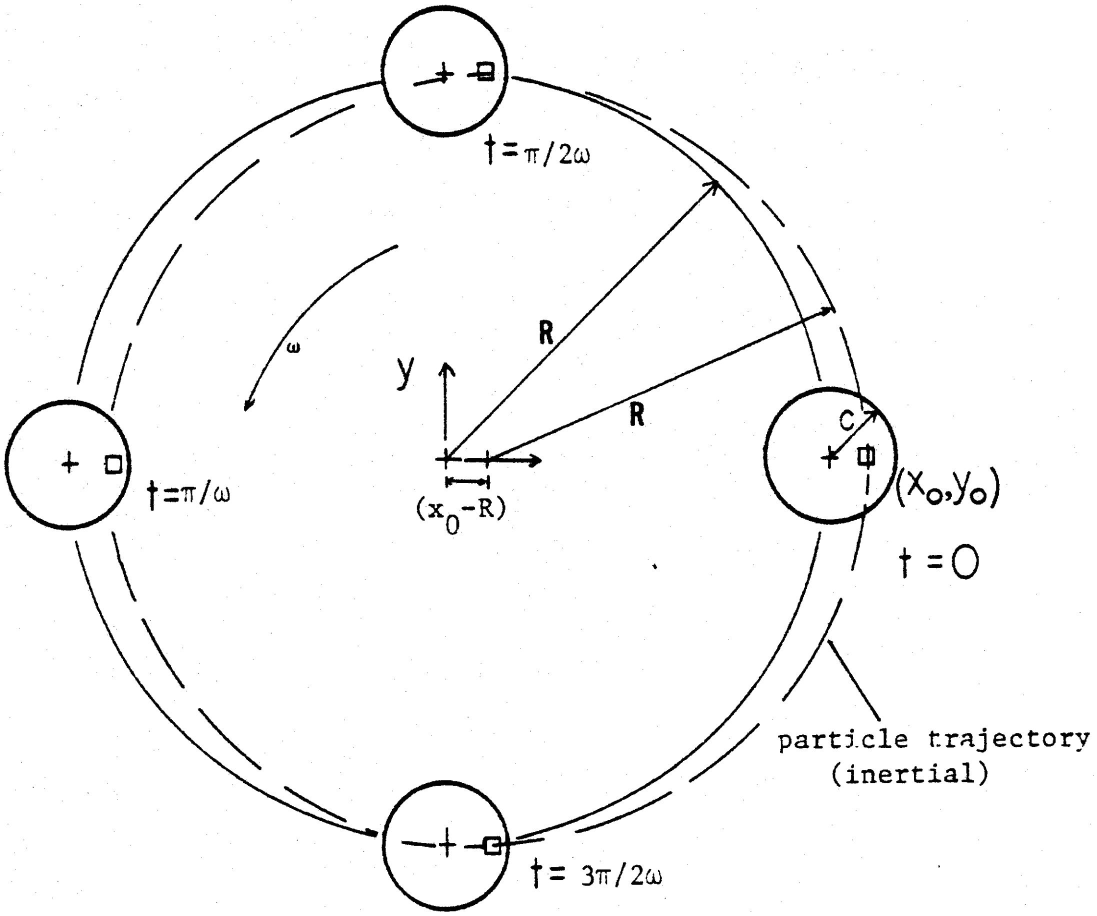
t=π/2ω
ω
y
R
R
c
(x₀,y₀)
t=0
t=π/ω
(x₀-R)
particle trajectory (inertial)
t= 3π/2ω

Figure A.IV.1

The trajectory of a given fluid particle is the same as the motion of any point on a cylinder of radius c mounted in a frictionless bearing and which is made to rotate about a centerline a distance R away (see Fig. A.IV.1) . Just as it is not possible to change the angular momentum of this cylinder without exerting a torque, the fluid motion described by Eq. A.IV.5 is one of zero rotation. In the local r,θ coordinate system, the inertial velocity is:

$$U_I = (\omega R\cos\phi + \omega r)e_\phi + \omega R\sin\phi e_r - \omega r e_\theta \qquad \text{(A.IV.11)}$$

$$U_I = \nabla(\Phi) \qquad \text{(A.IV.12)}$$

where

$$\Phi = \omega Rr\sin(\phi) \ . \qquad \text{(A.IV.13)}$$

The existence of the velocity potential confirms that the flow is irrotational and unique.

A.IV.2 Ellipse

The relative flow within an elliptical container was calculated in Chapter 7.C. It was also shown in Chapter 7.E that the viscous dissipation that occurs as the fluid spins-up is proportional to the relative kinetic energy. Since

$$\Delta E = 1/2 \iint (q \cdot q)\, dA \qquad \text{(7.e.8)}$$

for an ellipse such as the one shown in Fig. 7.3, then:

$$\Delta E = 1/2 \int_0^b \int_0^a \left(\frac{\partial\psi}{\partial x}\right)^2 + \left(\frac{\partial\psi}{\partial y}\right)^2 dxdy \qquad \text{(A.IV.14)}$$

$$\Delta E = \frac{\omega^2 \pi a^3 b^3}{a^2+b^2} \qquad \text{(A.IV.15)}$$

$$\Delta E = \omega^2 \frac{A(a^2 b^2)}{a^2+b^2} \ . \qquad \text{(A.IV.16)}$$

It is interesting to note that the kinetic energy losses are a maximum for a/b=1, a circle. As the ratio of a/b or b/a gets very small then the kinetic energy goes to zero.

A.IV.3 Pie shaped sector

In this section, the calculus of variations will be used to approximate the streamlines of an impulsively accelerated fluid in a pie shaped container. This exercise gives mathematical form to streamlines whose shape is the same as that of the container itself. The stream function shows that fluid particles are rotating around the center of geometry of the container. The stream function, however, is not realizable in practice. The local pressure gradient in the vicinity of abrupt changes in container geometry in the fluid outside the boundary layers gets very large (of order $1/\rho$ where ρ is the local radius of curvature of the container) and the momentum in the fluid boundary layer is insufficient to balance this pressure gradient increase. The flow separates in the corner boundary layers and a strong local vortex develops readjusting the streamline of the fluid outside the boundary layer into a more navigatable curvature (see Fig. 7.13).

The pie shaped container is sketched in Fig. A.IV.2. Taking advantage of container symmetry one finds that the stream function for this flow is the solution to the following equation:

$$\frac{1}{r^2}\frac{\partial^2\psi}{\partial\theta^2} + \frac{1}{r}\frac{\partial}{\partial r}\frac{r\partial\psi}{\partial r} + 2\omega = 0 \quad . \qquad \text{(A.IV.17)}$$

Transforming Eq. A.IV.17 into a variational problem results in:

$$\delta\int_0^1\int_{-\alpha}^{\alpha} -1/2\left(\frac{(\partial\psi)^2}{(\partial r)} + \frac{1}{r^2}\frac{(\partial\psi)^2}{(\partial\theta)} + 2\omega\psi\right) r\,dr\,d\theta = 0 \qquad \text{(A.IV.18)}$$

Performing the indicated variation results in the following equation:

$$\int_0^1\int_{-\alpha}^{\alpha}\left(-\frac{\partial\psi}{\partial r}\delta\left(\frac{\partial\psi}{\partial r}\right) + \frac{1}{r^2}\frac{\partial\psi}{\partial\theta}\delta\frac{\partial\psi}{\partial\theta} + \omega\delta\psi\right) r\,dr\,d\theta = 0 \qquad \text{(A.IV.19)}$$

which is then integrated by parts where possible to give:

$$\int_{-\alpha}^{\alpha} -\frac{\partial\psi}{\partial r}\delta\psi\Big|_{r=0}^{r=1} - \int_0^1 \frac{\partial\psi}{\partial\theta}\delta\psi\Big|_{-\alpha}^{\alpha} + \iint\left(\frac{1}{r^2}\frac{\partial^2\psi}{\partial\theta^2} + \frac{1}{r}\frac{\partial\psi}{\partial r}\frac{r\partial\psi}{\partial r} + \omega\right)\delta\psi\, r\,dr\,d\theta = 0 \quad .$$

$$\text{(A.IV.20)}$$

The first two terms are zero because the streamfunction is specified on the boundaries of the container. The variational problem to solve, after nondimensionalizing the latter equation, is

$$\iint \left(\frac{1}{\alpha^2 r^2}\frac{\partial^2\psi}{\partial\theta^2} + \frac{1}{r}\frac{\partial}{\partial r}r\frac{\partial\psi}{\partial r} + 1\right)\delta\psi\, r\,dr\,d\theta = 0 \qquad \text{(A.IV.21)}$$

$$\begin{aligned} \psi &= \psi/(\omega a^2) \\ r &= r/a \\ \theta &= \theta/\alpha\ . \end{aligned} \qquad \text{(A.IV.22)}$$

Using the Kantorivich method, a function in r is chosen which automatically satisfies the boundary conditions at **r=0,r=1.** The stream function is then a product of this function in **r** and an undetermined function of θ only. A suitable function is:

$$\psi = r(1-r^2)\Theta(\theta)\ . \qquad \text{(A.IV.23)}$$

Substituting the latter equation into Eq. A.IV.22 and integrating with respect to **r** gives the following

$$\int_{-1}^{1}\int_{0}^{1} \left(\frac{r(1-r^2)\Theta''}{\alpha^2 r^2} + \frac{\Theta(1-9r^2)}{r} + 1\right) r(1-r^2)\,\delta\Theta\, r\,dr\,d\theta = 0 \qquad \text{(A.IV.24)}$$

$$\int_{-1}^{1}\left((\Theta''/(6\alpha^2) - \Theta/2 + 2/15\right)\delta\Theta\, d\theta = 0\ . \qquad \text{(A.IV.25)}$$

The optimal functional dependence of the stream function on   is the solution to the second order differential equation enclosed within the parenthesis, subject to the boundary conditions :

$$\begin{aligned} \Theta(-1) &= 0 \\ \Theta(\ 1) &= 0\ . \end{aligned} \qquad \text{(A.IV.26)}$$

The complete solution to this equation is

$$\Theta = 4/15\left(1 - \cosh((\surd 3)\alpha\theta) - \frac{(1-\cosh((\surd 3)\alpha))}{\sinh((\surd 3)\alpha)}\sinh((\surd 3)\alpha\theta)\right)) \qquad \text{(A.IV.27)}$$

and the stream function can now be approximated as:

$$\psi = (4/15)r(1-r^2)(1-\cosh((\surd 3)\alpha\theta)-\lambda\sinh((\surd 3)\alpha\theta))$$

$$\text{where} \qquad \lambda = (1-\cosh((\surd 3)\alpha))/\sinh((\surd 3)\alpha\ )\ . \qquad \text{(A.IV.28)}$$

It is a simple matter to show that the stream function is a minimum at $\theta=0$, $r=1/\surd 3$ which is the geometric center of this pie shaped sector. In figure A.IV.2 three streamlines were calculated for ψ =0.135,0.384, and 1.0.

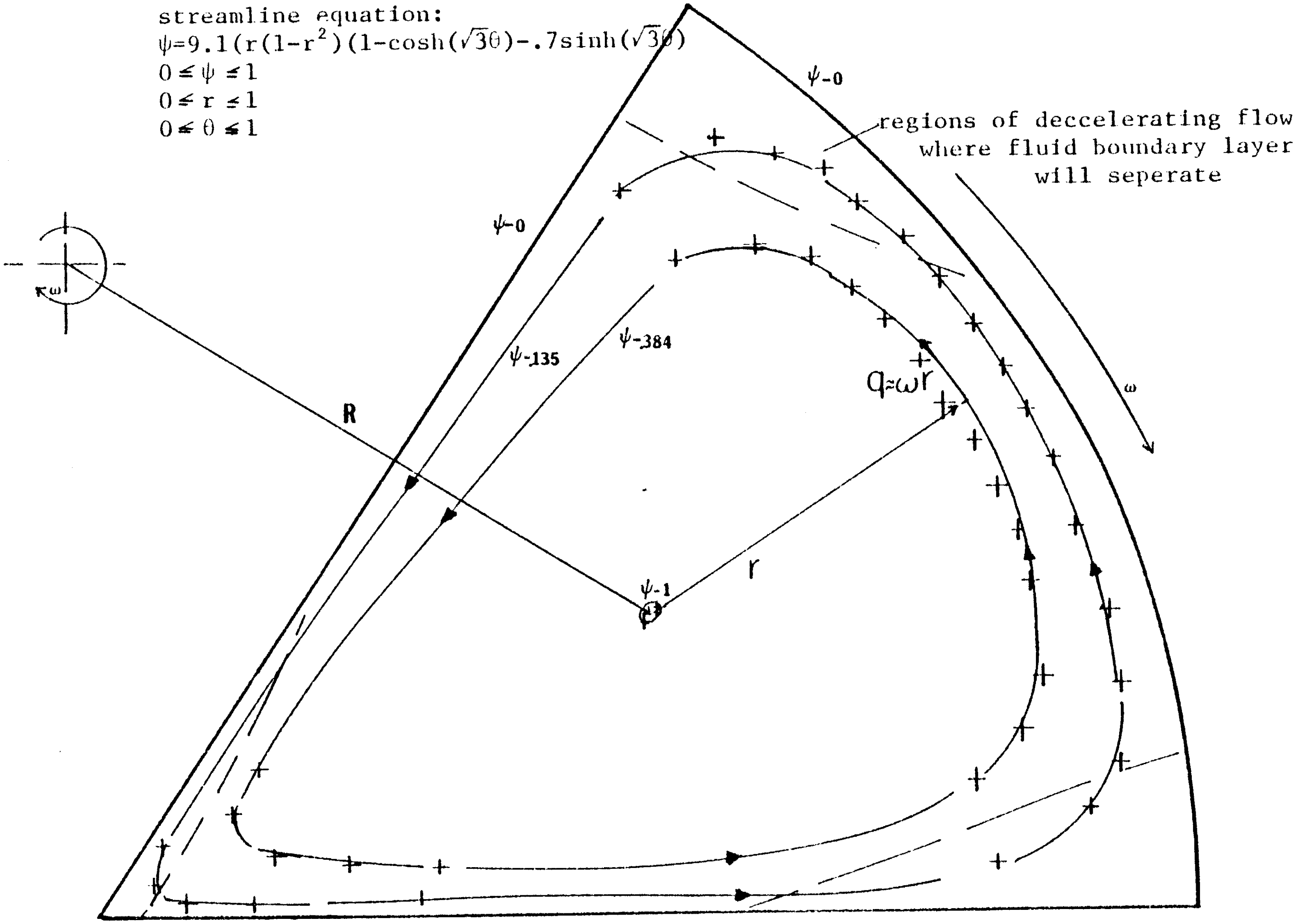

streamline equation:

$$\psi=9.1(r(1-r^2)(1-\cosh(\sqrt{3}\theta)-.7\sinh(\sqrt{3}\theta))$$

$0 \leq \psi \leq 1$

$0 \leq r \leq 1$

$0 \leq \theta \leq 1$

regions of deccelerating flow where fluid boundary layer will seperate

Figure A.IV.2

List of References

1. Taylor, G.I. "Experiments on the Motion of Solid Bodies in Rotating Fluids" (1923), pp. 213-218, from The Scientific Papers of Sir G.I. Taylor, Vol. IV, Ed. G.K. Batchelor, Cambridge University Press, 1971.

2. Greenspan, H.P. , The Theory of Rotating Fluids , Chapter 1, Cambridge Unievrsity Press, Cambridge, 1980.

3. J. L. Smith, Jr., et al, "MIT-DOE Program to Demonstrate an Advanced Superconducting Generator", IEEE Trans. on Magnetics, Vol. MAG-15, No. 1, p. 727 (Jan. 1979).

4. Sobel, L. D., "Experimental Results of a High Speed rotating Liquid Helium System" , M.Sc. thesis, January 1980, (MIT Thesis)

5. Gamble, Bruce B., and Thomas A. Kaim, "High Power Density Superconducting Generator" , 15th Intersociety Energy Conversion Engineering Conference, Seattle, Washington (August 18-22, 1980).

6. C. E. Oberly, IEEE Trans on Magnetics, MAG-13, 260 (1977).

7. Ken Tepper, "Mechanical Design of the Rotor of a Fault-worthy, 10MVA Superconducting Generator", PhD Thesis, MIT (1980).

8. Eckels, P. W., J. H. Parker, Jr., A. Patterson, and J. H. Murphy, "Heat Transfer Correlations for a Cryostable Alternator Field Winding", unpublished, Westinghouse Electric Corporation, Research and Development Center, Pittsburgh, Pennsylvania 15235, Sept., 1981.

9. Morris, W.D., Heat Transfer and Fluid Flow in Rotating Cooling Channels, Research Studies Press, Chichester, New York, 1981.

10. Ogata, H., "Heat Transfer to Subcritical and Supercritical Helium in Centrifugal Acceleration Fields", Free Convection Regime and Boiling Regime, Cryogenics, pp. 461-470, August 1977.

11. Schnapper, C., "The Convection and Transfer of Heat by Helium in Rotating Channels" , PhD Thesis, Univ. (TH) Karlsruhe, Stuttgart, 1978.

12. Scurlock, R. G. and G. K. Thornton, "Pool Heat Transfer to Liquid and Supercritical Helium in High Centrifugal

Acceleration Fields", Int. J. Heat Mass Transfer, Vol. 20, pp. 31-40, Pergamon Press, 1977.

13. Gill, A. E., 'The Boundary-layer Regime for Convection in a Rectangular Cavity,' J. Fluid Mech., vol. 26, pp. 515-536.

14. Al-Homoud, Adnan A. and Adrian Bejan, " Experimental Study of High Rayleigh Number Convection in Horizontal Cavity with Different End Temperatures", University of Colorado, College of Engineering, CUMER-79-1, based on Masters Thesis, May 1979.

15. Hudson, J. L., Tang, D. and Abell, S., "Experiments on Centrifugally Driven Thermal Convection in a Rotating Cylinder" , J. fluid Mech., Vol. 86, Part 1, pp. 147-159, 1978.

16. Homsey, G. M., and Hudson, J.L., "Centrifugally Driven Thermal convection in a Rotating Cylinder" , J. Fluid Mech., vol. 35, part 1, pp. 33-52, 1969.

17. Abell, S., and Hudson, J.L., " An Experimental Study of Centrifugally Driven Free Convection in a Rectangular Cavity", Int. J. Heat Mass Transfer, Vol. 18, pp. 1415-1423, Pergamon Press, 1975.

18. Gray, V.H. " Feasibility Study of Rotating Boilers for High Performance Rankine Cycle Power Generation Systems", Nasa Tech Note N67-23313, 1967.

19. Taylor, G.I., " The Path of a Light fluid When Released in a Heavier fluid Which is Rotating", The Scientific Papers of Sir G.I. Taylor, pp. 139-145, Vol. IV. Ed. G.K. Batchelor, Cambridge University Press, 1971.

20. Taylor, G.I., "Motion of Solids in Fluids When the Flow is Not Irrotational ", reprinted from Proceedings of the royal Society, A, vol. XCIII (1917), pp. 99-113, from The Scientific Papers of Sir G.I. Taylor, Vol. IV, Ed. G.K. Batchelor, Cambridge University Press, 1971.

21. Turner, J. S., Buoyancy Effects in Fluids , Chapter 6, Cambridge University Press, 1979.

22. Baxter, Richard, "Slow Transverse Motions of a Body in a Finite rotating Fluid", USNA TSPR No. 11, NASA Tech. Note N72-12240-H2/12, 1972.

23. Baker, D.J., "A Technique for the Precise Measurement of Small Fluid Velocities," Journal of fluid Mechanics, Vol. 26, 1966, p. 573.

24. Wreski, James, "Design and Construction of a Turntable for Rotational Fluid Flow Experiments", Bachelors Thesis, MIT, May, 1983.

25. Otten, David, "Demonstration of an Advanced Superconducting Generator", Interim Report #4, MIT Cryogenic Engineering Laboratory and Electric Power systems Engineering Laboratory, E(49-18)-2295-T.O. #11, IR4, pp. 124,136.

26. Turner, J. S., Buoyancy Effects in Fluids , Chapter 7, p. 220, Cambridge University Press, 1979.

27. Wedemeyer, E. H. "The unsteady flow within a Spinning Cylinder", J. Fluid Mech., Vol. 20, pp. 383-399, 1964.

28. Gans, R.F. " On Steady Flow in a Partially Filled Rotating cylinder", J. Fluid Mechanics, Vol. 82, p. 415, 1977.

29. Private communication, P. W. Eckels (Westinghouse Corp.) to Larry Sobel, October 1983.